12-2023

Design, fabrication, and integration of robotic skin sensors for human robot interaction.

Olalekan Olakitan Olowo
University of Louisville

DESIGN, FABRICATION, AND INTEGRATION OF ROBOTIC SKIN SENSORS FOR HUMAN ROBOT INTERACTION

.

By

Olalekan Olakitan Olowo
B.S., Ekiti State University, 2013
M.S., Covenant University, 2017

A Dissertation
Submitted to the Faculty of the
J.B. Speed School of Engineering of the University of Louisville
in Partial Fulfillment of the Requirements
for the Degree of

Doctor of Philosophy
In Electrical Engineering

Department of Electrical and Computer Engineering
University of Louisville
Louisville, Kentucky

December 2023

DESIGN, FABRICATION, AND INTEGRATION OF ROBOTIC SKIN SENSORS

FOR HUMAN ROBOT INTERACTION

.

By

Olalekan Olakitan Olowo

B.S., Ekiti State University, 2013

M.S., Covenant University, 2017

A Dissertation Approved on

August 14th, 2023

by the following Dissertation Committee:

_____

Dr. Dan O. Popa

_____

Dr. Kevin Walsh

_____

Dr. Tommy Roussel

_____

Dr. Cindy K. Harnett

DEDICATION

This thesis is dedicated to my Lord and Savior, Jesus Christ, who granted me the privilege, opportunity, and strength to persevere. I am eternally grateful.

To my beloved mother, Omolara Olowo, whose unwavering support and prayerful encouragement sustained me through challenging times.

To my dearest uncle and his wife, Oluwatoyin and Odunayo Folorunsho, who have served as my parental figures in the US. Your sacrifice and love are debts I can never fully repay.

I extend my appreciation to my siblings, Olanrewaju and Olaoluwa, and to my extended family, including uncles, aunties, cousins, my awesome grandmother, uncle Deji and family. Your support has been invaluable, thank you for being a part of my journey.

.

ACKNOWLEDGMENTS

I would also like to thank Dr. Dan O. Popa my supervising professor for his constant guidance, support, and the knowledge and wisdom he has imparted on me. Without his teachings, this work would not have progressed, and I am indebted to his wisdom and support throughout this period of my life. I would also like to thank Dr. Ruoshi Zhang and Dr. Andriy Sherehiy for their experience in leading the project and allowing me to help. I would also like to thank Dr. Kevin Walsh, Dr. Thomas Roussel and Dr. Cindy K. Harnett for serving on my committee and teaching me during my time at the University of Louisville.

I would also like to thank all other members working in the NGS KAMPERS project. Dr. Ji-Tzouh Lin, Bryan Harris, Douglas J. Jackson, Danming Wei and Brian Goulet. Their work helped this thesis and allowed me to complete it. I would also like to thank members outside of the KAMPERS project who helped me, Dr. Moath Alqatamin, Dr. Sumit K. Das, Jordan Dowdy and Daniel Sills. All of them have assisted throughout this work and all has been greatly appreciated.

I would also like to thank the National Science Foundation(NSF) for their support through the following project: #1849213 RII Track-1: Kentucky Advanced Manufacturing Partnership for Enhanced Robotics and Structures.

Finally, I would like to thank my family and friends, both in DMV and Lagos. Without their support, I would not have been able to complete this work and my life

would be incredibly different. This page wouldn't be complete without mentioning an amazing lady in person of Youngsoon Takei who came into life towards the tail end of my studies bringing peace, love and happiness.

ABSTRACT

DESIGN, FABRICATION, AND INTEGRATION OF ROBOTIC SKIN SENSORS FOR HUMAN ROBOT INTERACTION

Olalekan Olowo

14TH August 2023

Supervising Professor: Dan O. Popa

Enhancing physical human-robot interaction in modern robotics relies on refining the tactile perception of robot skin sensors. This research focuses on crucial aspects of the development process, including fabrication techniques, miniaturization, and integration for a more efficient collaborative human-robot interface.

The fabrication process of robot skin sensors, designed to mimic human skin, is explored both within and outside cleanroom environments. An enhanced technique is presented to increase fabrication yield and create more miniaturized sensor designs with feature sizes in the tens of microns. These sensors function as piezoresistive arrays using organic polymers like PEDOT: PSS as the pressure-sensing medium. Various deposition techniques, such as cleanroom spin coating and direct-write inkjet printing with Aerosol inkjet printers, are discussed.

A NeXus microfabrication platform is introduced to eliminate errors, simplify the cleanroom process, and reduce production time for sensor arrays. This platform is

employed for the prototyping of tactile strain gauges, integrating an Aerosol jet printer station for patterning sensor electrodes on flexible substrates and a piezo-electric fluid dispenser for PEDOT:PSS deposition, bypassing cleanroom photolithography.

The post-processing phase is detailed, highlighting the sintering of patterned silver traces using an oven or intense pulse light (IPL). The curing process determines the resistance and conductivity of printed samples, with IPL offering flexibility and efficiency compared to traditional ovens.

Cured samples undergo testing on a specialized testbench equipped with an indenter, force feedback control, motorized stage, and computer vision functionality. LabVIEW Programs synchronize testing components, producing tangible results for each tactile sensor test. Test quality influences the integration of tactile sensors with a robotic arm.

A novel tactile fingerprint design, realizable in the NeXus, is proposed and characterized based on performance and reliability. Sensitivity, indentation cycles, and spatial resolution studies contribute to a comprehensive understanding of the proposed design.

The research's ultimate goal is to integrate tactile sensors, including commercially available options like Flexiforce sensors and robot skin sensor patches, with a robot to enhance direct interaction. The effective use of the Robot Operating System (ROS) and local area connectivity to implement the robot's response to physical touch on the skin sensors marks a significant stride in advancing human-robot interaction. The abstract encompasses the critical elements of improved fabrication, miniaturization, and integration, making strides toward more effective and adaptable physical human-robot collaboration.

TABLE OF CONTENTS

LIST OF FIGURES

LIST OF TABLES

CHAPTER 1

INTRODUCTION

1.1 Motivation

The earliest prototype of a robot is a reprogrammable manipulator called “Unimate” invented and patented to a Louisville, Kentucky native known as George C. Devol in the 1950s[1]. It became an industry success upon the patent acquisition and modification by Joseph Engleberger, also regarded as “the Father of Robotics” a decade later[2]. Their primary objective was to aid people working on the assembly line. Several decades later, we have seen a wide variety of uses of robots to carry our automated tasks replacing or aiding human labor.

And the exponential increase for robots has reached a record in recent times, especially during the 2020-2021 pandemic. In 2021 almost 40,000 industrial robots were installed by North America firms, 28% more than the previous year, and amounting to more than $2 billion in purchases[3].

Recently, a new of type of robot has emerged, distinct from the industrial use in manufacturing, and with collaborative capabilities to work alongside people in less organized settings like homes, schools, and even hospitals. This new type of robot is also known as a Co-robot or “Cobot”[4].Despite the fact that current technology enables robots to achieve great levels of accuracy, precision, and repeatability of movement far above

human capabilities, they are still not apt in responding to external stimuli to trigger a change of motion or trajectory to enhance collaboration within the same shared space. Collaborative robotic application requires that robots be able to learn on their own and interact safely within a changing and dynamic environment imitating the level of perception seen in humans[5, 6]. Using vision sensors, many researchers have investigated how humans and robots interact with their surroundings, and use machine learning to recognize objects, localize themselves in the environment, and interact with people.

However, during physical human-robot interaction (pHRI), the impression of contact connection between the robot and environment also plays a big role. A little over four decades ago the idea of replicating the haptic response of human skins on robots has been introduced, as this is imperative for robots to interact safely with humans within a shared workspace [7]. Sensitive skin provides quantifiable, measurable measurements of all these near contacts that can be located. Skin also conveys information regarding encounters with one's own physical body. These self-experiences contribute to the development of knowledge about the body schema, one's own sensory-motor embodiment. The tactile sense is essential for self-acquiring a kinematic and volumetric body model, together with proprioceptive sense. This means in comparison to robots equipped with visual 2D/3D vision or joint sensing, the artificial skin will offer a more rich, direct, and informative data set. Overtime, several researchers overtime investigated varying modalities of sensing, providing mediums for analyzing physical variables such as temperature, proximity, normal and shear forces, light pressure contact, and torque required to make a robot more intuitive and collaborative [8, 9]. This investigation of haptic response to the artificial tactile perception of the environment has yielded studies showing

the development of sensors based on the working principles ranging from capacitive sensing, optical fiber sensing, inductive sensing, and piezoelectric sensing phenomenon[10-12]. The application of tactile perception provide by robot skins sensors will makes possible the ability for contact control, full body monitoring and touch/object classification. We foresee a future where new age industrial robot's teach pendant will eventually fizzle out to give way to direct tactile interaction.

The continuous development of this technology is expedient, as science and engineering seek to further push the boundaries to abound the future of a safer and more collaborative partnership between humans and robots, both for industrial and domestic purposes[8]. This research is focused on varying aspects tailored toward engineering suitable materials for fabrication, adequate fabrication techniques, electronic circuits, hardware, and software interfaces to achieve optimum tactile feedback. In the work presented in our thesis we sought to improve fabrication techniques, generate more intuitive designs with better spatial resolution, reduce manufacturing time and integrate tactile skins with robots.

1.2 Challenges

The challenges involved in the creation of robot skin sensor arrays encompasses technological hurdles along the areas of spatial resolution designs of skin sensors, optimizing fabrication processes, scaling of these sensors over large surface area, multiple signal conversions and processes, timely extraction of information for reactive control and low power consumption. Determining material specifications along the lines of compliance and durability featuring soft, flexible, impact absorbing textures, high temperature and chemically inert properties are regarded crucial components to an ideal robot skin outlook.

In the past several years, we have been investigating and developing robotic skin sensor arrays based on semiconductor organic materials, and addressing challenges in design, simulation, fabrication, packaging, algorithms for human-robot interaction, electrical transducers, and interfaces to robot controllers. Studies overtime have evaluated sensing mediums with varying methods used to capture physical variables such as temperature, proximity, and sense contacts due to force, pressure, and torque[2, 3]. This artificial perception of the environment in contrast to human skin has been investigated by many researchers depicting modalities based on optical fiber sensing, inductive sensing, capacitive sensing and the use of piezoelectric[4-6]. At the University of Louisville, the Next Gen Systems (NGS) group at LARRI (Louisville Automation Research & Robotics Institute has developed robotic sensor patches over the last decade. The organic semiconductor polymer Poly (3, 4-ethylenedioxythiophene)-ploy(styrenesulfonate), or PEDOT: PSS, is the base sensing material employed in our research. It has been printed over flexible Kapton substrate utilizing a variety of methods.

There are a couple of challenges in the way of developing robot skin sensor arrays, including those related to design, manufacturing, robot integration, and control. These difficulties include:

1. Spatial Resolution: One of the main challenges is improving the spatial resolution of skin sensors. Improved sensitivity requires achieving a more densely packed and dense arrangement akin to human fingertips, which has tactile nerve receptors with millimeter spacing.

2. Fabrication Optimization: One of the biggest challenges is making high-resolution designs a reality using cleanroom fabrication methods. Through careful attention to detail,

photolithography can produce designs smaller than 10 microns. Although cleanroom technique achieve high design resolution in tens of microns, the processes involve are time consuming and cumbersome requiring all factors(human and machine) involved in the process are in optimal condition to obtain a repeatable outcome.

3. Cost of Fabrication: Cleanroom fabrication can be costly, influenced by equipment, tools, and chemicals used. The expense is independent of the quality of the fabricated skin sensor batches, making the process financially demanding.

4. Data collection and Testing: To assess the functionality of the robot skin sensor, data collecting and testing are essential after manufacturing. Finding paired matches for lamination is aided by this step. It is becoming a challenge to provide test stations that could evaluate, assess and analyze large streams of data in real time.

5. Integration with Robots: Signal routing and packing become more difficult when integrating the manufactured tactile sensor with a robot. In signal processing, the response of the sensor is calibrated to account for drifts caused by the irregular properties of materials such as PEDOT: PSS (poly (3,4-ethylenedioxythiophene)-poly(styrenesulfonate)). More importantly is the ability to configure the tactile sensing information into useful kinematic orientation of the robots.

6. Mechanical Enclosure and Encapsulation: Two more challenging tasks are keeping the sensor patches stable in relation to the robot and housing the circuitry. Building a placeholder extension to safely contain the sensor patches is part of this.

In general, overcoming these obstacles in the development of robot skin sensors is essential to progressing the area and improving the sensitivity and performance of these sensors, especially in applications that call for artificial environmental perception.

1.3 Contributions of this dissertation

The work detailed in this thesis covers several aspects of robot skin fabrication, characterization, and application to the Resquared arm. The research contributions of this thesis are:

1. Improved cleanroom fabrication techniques for touch-sensitive robotic skin arrays: In order to custom make sensor arrays containing piezoresistors deposited in flexible substrate, I contributed a novel wet-etching fabrication technique to the fabrication process that has been established at the University of Louisville cleanroom[13-15]. The new approach involves the introduction of gold etchant between the photolithography process eliminating the delicate use of two photoresists to create robot skin sensor microstructure patterns. it has the following advantages: it improves the process of realizing small microstructure patterns in the tens of micron. The novel gold etching technique eliminates bubbles that are often present during the application process of two photoresists used to pattern the microstructures. Finally, the novel wet-etching fabrication technique completely dissolve gold particles in undesired regions of the microstructure taking care of the issue of short circuit between gold electrodes. This arises as a result of lifting-off materials in the previous technique using the acetone sonicated baths, this leaves on the surface of the structure tiny gold particles that causes the short circuit.

2. Robot skin sensor fabrication using additive manufacturing outside the Cleanroom: One major disadvantage to robot skin sensor fabrication using cleanroom technique is the long processing times, and the reduced yields. An average of 6-7hours is required for the complete fabrication process within the cleanroom, followed by additional time to prepare PEDOT: PSS colloidal solution, and completing the sensor using a double-sized lamination process. As a result, I proposed, developed, and tested a completely new additive manufacturing process for the sensors using our NeXus robotic system[16]. Specifically, I worked to substitute the deposition and isolation techniques of leaving the PEDOT: PSS (poly (3,4-ethylenedioxythiophene)- poly(styrenesulfonate) on the sensing regions, which was previously done in the cleanroom with a direct write inkjet process, cutting down the average 4-5hour period of PEDOT: PSS application alone to within minutes. Sensor patterns have been obtained using deposition tools of the NeXus, in particular piezoelectric inkjet dispensing, or aerosol jet dispensing. Process parameters were tuned for both deposition and also curing of the jetted conductive and piezo-resistive films using a curing oven as well as a novel Intense Pulse Light Technology. Results demonstrated that the robot skin sensors increased in sensitivity from 1158nV/N to 1.7μV/N[15, 16].

3. We also designed and printed a novel fingerprint tactile structure:

A new fingerprint design is proposed and fabricated completely with the additive manufacturing tool heads in the NeXus. cutting the duration of time-consuming cleanroom procedures from 10 hours to less than 2. Producing a unique "fingerprint" design, as small 3.8 x 3.8 mm footprint. Silver electrodes and an organic polymer film PEDOT:PSS coated in layers are both present in the sensor. To enhance the center of force's consistency and

detecting resolution, the sensor array is encircled by two layers of silicone elastomer with precise protrusions and inner chambers.

Performance testing and evaluation of 4x4 “Skin Cell” arrays to determine its reliability, resolution and sensitivity. These tests use multiple indentation cycles totaling over 180,000 cycles, in addition to single force and ladder force. The data, which have an average spatial resolution of 827 microns, demonstrate the sensor's ability to record tiny spatial features.

Developed novel models for sensor arrays: dynamic and spatial responses. System identification analysis is used in the study to gain further understanding of the sensor's behavior and response to outside stimuli. This analysis, which displays a time constant of 63 ms, describes the dynamic relationship between applied forces and sensor output.

4. Experimental characterization of robot skin samples:

A new set of tactile sensors have been fabricated in the NeXus instead of in the cleanroom and is characterized showing we can completely transfer the fabrication process from the cleanroom to the Novel micro-Fabrication platform known as NeXus. A new testing procedure and reduced-order system identification models of the sensors have been obtained in order to characterize the dynamic relationship of the tactile sensor response with respect to applied strain. Sensors were packaged as individual tactels, or 4x4 “Skin Cell” arrays. Characterization of the cured sample in oven and IPL was carried out, and a new curing process for our tactile sensor thin films was established.

We worked on new sensor packaging designs to improve performance, concentrating applied load to the precise sensing area. These improvements have increased the performance of our SkinCell tactile arrays.

5. Integration of tactile sensors with a robot and physical human-robot interaction strategies.

Both custom fabricated sensor arrays, and commercially available tactile sensors have been integrated with a robotic arm, which was programmed in a guiding motion as a result of physical pushing and pulling. An algorithm for moving the robot in the direction of contact was proposed as a proof of concept. In addition, after fabrication, characterization, and testing of the robotic skin sensor, they were integrated with the robot using a structural electronic object named Octocans. An OctoCan contains eight 4x4 SkinCell sides, data acquisition electronics, power, and a microcontroller unit (MCU) that can transfer the tactile information from up to 128 sensors to the robot controller at a rate of 150Hz. The virtual modeling of the sensor patch embedded in the Octocan with robot arm was obtained in RVIZ and Gazebo prior to prototyping.

1.4 Thesis Organization

Chapter 2 provides information about background and literature survey on robot skins and sensor fabrication methods. In Chapter 3 the skin sensor fabrication procedures in cleanroom and NeXus are explained along with interfacing with electronics. In Chapter 4, a sensor testing analysis and system identification is described with results from the tactile sensors. Chapter 5 describes the deployment of the sensors and its application on robots using the pressure sensing capability. In chapter 6, a novel fingerprint tactile structure design is discussed, the fabrication, lamination, static, dynamic, reliability, spatial resolution and sensitivity profile of the sensor patch is described and evaluated. Finally, Chapter 7 provides a conclusion and some of the future work. Listed in appendix A is the list of journal and conference publications.

CHAPTER 2

BACKGROUND AND LITERATURE SURVEY

The future of robotics is seeing the emergence of a new generation of robots that are collaborative, and intuitive with increasing levels of environmental awareness and perception. These collaborative robots are beginning to find application in virtually any sector of human endeavor. These include manufacturing industries, health care sectors, offices and even homes. It is therefore a major focus of today's research to enhance the collaboration frontier between man and machine to create a safe working environment for everyone. It is to this realization that robotic skins are fabricated and integrated to enhance the physical human-robot interaction. These robot skin sensors provide sensory input by mechanical stimulation based on contact with the environment. Acquiring a "sense of touch" or tactile perception is defined by the observation and response to perpendicular forces within a predefined or determined region and this can include the interpretation of spatial data. And this is with regards to extrinsic sensor arrays located or placed on the robot for cutaneous sensing.

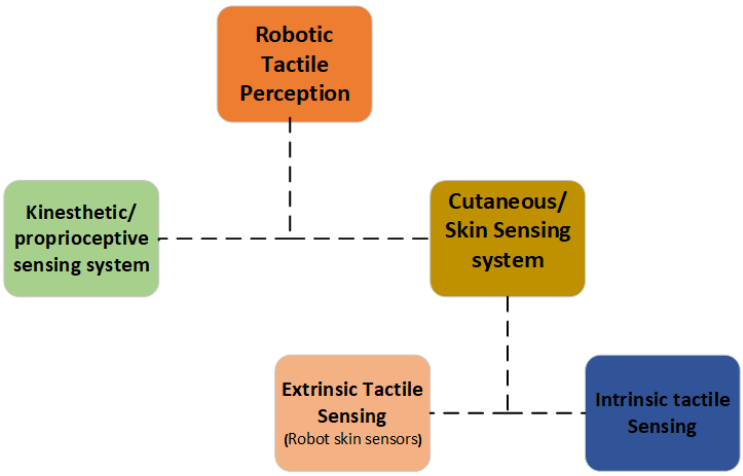

Figure 1 Robotic Tactile Perception

2.1 Tactile Perception (Sense of Touch)

As we've seen increasing demand of robots primarily for manufacturing purposes so are we starting to witness the varying and increasing applications in all works of life. These mechanical knights as fondly used by Leonardo Da Vinci in 1495 A.D, referring to these mechanical creatures, have since evolved in shapes, sizes, nomenclatures and even imitation of our very human frame otherwise known as humanoids[7].

For robots to be completely and intuitively aware to their immediate environment it is important they are equipped with sensing modalities for autonomous learning, sensory guided motor control, safe interactions amongst other things. But what happens if robots embody every form of sensing without the ability to sense touch. To have an understand of what this feels like as humans, an experimented conducted with anesthesia apply to the hands of a group of people shows the difficult and inability to maintain stability while grasping object[8]. This also means the loss of the sense of touch would be practically seen in the inability to profile object properties such as texture, size and temperature, resulting in direction and spatial disorientation and loss of awareness of the body[9]. For this reason,

the sense of touch would determine the extent and quality of what is sensed or perceived. Several sensing technologies have been explored but the most common challenges revolve around manufacturing of tactile sensors. Although creative and inventive ideas in terms of design progresses but they mostly still don't meet expectations either because they're too large to be utilized, compromising dexterity or because they are sluggish, delicate, elastically rigid, mechanically rigid, and lacking robustness. Taking the human skin as the relevant biological prototype for artificial replication of tactile sensing, studies have shown its multilayered structure is viscoelastic , nonlinear, and nonhomogeneous. This complex structure is supported by a system of tissues that are conformable and distortable as well[10]. Different skin layers are defined by their rigidity and stiffness. With a Young's modulus 10–100 000 times greater than that of the dermis, the base epidermis layer in comparison to the dermis layer is significantly stiffer. Skin mechanics will undoubtedly be crucial in the tactile perception given these characteristics. Skin's epidermis and dermis layers physically interlock, which serves to prevent any inclination for them to slide over one another and forms a filtering system that disperses forces and stresses away from the source of application[11, 12]. Tactile perception can be classified in two main sensory modalities, which is the skin sense(cutaneous) and proprioceptive sense(Kinesthetic) as shown in Figure 1. The skin sense and the kinesthetic sense both receive sensory information from receptors that are located in the skin and muscles, tendons, and joints, respectively. It should be remembered that sensory inputs include varying stimuli that cause pain in addition to mechanical stimulations like heat and cold. In respect to the task meant to be achieved, robotic tactile sensing can be further classified to “perception for action” to imply dexterity in manipulation during human-robot collaboration or “action for

perception” in line with exploration and object recognition. Based on these, the tactile sensors for acquiring sensory are placed. These placements could either be intrinsic or extrinsic. By intrinsic, we refer to robot tactile perception built from within the mechanical frame of the robot structure while extrinsic sensors are those mounted on the surface of the robot at specific location for precise purpose intended [17]. So, based on the physical nature and working principle of these embedded sensory system within a robot, it can be further classified along the working operation of tactile sensing which be piezoelectric, capacitive, inductive, piezoresistive, ultrasonic, magnetoelectric and so on. A few of these working principles are in section 2.3.

2.2 Physical human-robot interaction

Physical human-robot interaction is an aspect of Human-robot interaction(HMI) that requires direct physical communication and engagement with collaborative robots (also known as Co-bots) enabling the accomplishment of tasks with Humans and robots working side by side within the same shared space. Investigation into the interaction of forces applied as depicted by[18] [19] describes a method of direct physical communication implemented in the past. Rajruangrabin used an Extended Kalman Filter to combine surface mounted force sensor data with joint data, as opposed to Kanda's approach, which needed a human to engage with the end effector. It was demonstrated that the positioning of the surface-mounted sensor was the only restriction on the location of interaction[19].

Currently, efforts are being made to develop sensorized artificial skin for application in pHRI in both commercial and research contexts. There are now surfaces with flexible, non-flat capacitive touch sensor arrays[20-23]. There has been demonstrated a stretchable

sensing fabric with embedded piezoelectric sensors, epitaxially layered conducting polymer, and carbon-filled rubber[24]. It has also been demonstrated that thin film bendable polyimide sensor arrays are feasible[25].

2.3 Tactile Sensor Survey

Robotic skin has long been considered a “holy grail” sensor for modern robots. It is a key type of heteroceptive sensor inspired by nature that could eventually enable “co-Robots” to haptically perceive their environment and share their workspace with humans. Despite considerable progress in that last 35 years, numerous fabrication techniques, integration schemes, dynamic performance limitations, reliability, and cost challenges remain in realizing robotic skin, thus the need for the research proposed here. Lumelsky, Shur, and Wagner were among the first who proposed the idea of using large-area, flexible arrays of sensors with data processing capabilities, which they call “sensitive skin” and can be used to cover the entire surface of a robot[26]. Other early work to develop robotic skin organic thin film transistors (OTFT) and a-Si:H TFTs fabricated on flexible plastic substrates at University of Tokyo and elsewhere[27], PVDF tactile sensors at Tohoku University[28], work at Univ. Nebraska with nanoparticles, and force, temperature, and electric field sensors at MIT Media Lab. Later on, modular robotic skin designs, such as ROBOSKIN [29] and HEXOSKIN [30] were custom developed by European robotics labs in Italy and Germany but are not available commercially. Concurrently, several other commercial pressure sensitive arrays have been commercialized in the US, however, the main application of these products is in biomechanics, rather than robotics. Perhaps the most “integrated” skin-robot effort to date has gone into sensitive surfaces for manipulation with robotic hands and fingertips. For example, a recent commercial product from

SYNTOUCH provides finger “modules” for commercial robotic hands. The modules detect heat, vibration (for texture) and pressure sensing using a combination of thermistors and fluidic pressure sensors, with a spatial resolution of 3mm, a vibration bandwidth of 1KHz, a thermal/pressure bandwidth of 50Hz, a dynamical range 30mN-30N, and sensitivity/hysteresis below 5%. While these sensors have been tuned for installation on fingers, it is difficult to see how they can be scaled to other parts of the robot, how they will be cost-effective for home use, or rugged enough if subjected to daily “wear and tear” of prosthetics.

Over the last 3 decades, hundreds of research papers have been published describing tactile sensors based on various principles of transduction, including piezoresistive, capacitive, piezoelectric, optical, resistive, Triboelectric. In this document, we summarize the types of sensors reported and their performance tradeoffs for applications in robotic skins:

Piezoresistive tactile sensors: The piezoresistive phenomenon happens when the electrical resistance of an interface material changes in response to external stimuli. A wide variety of materials, including metals, semiconductors and polymers exhibit this property, and have been incorporated in devices that have low energy consumption, simple read-out mechanisms, and wide range of detection. The figure of merit often used to characterize performance of these sensors is the “Gauge Factor (GF)”. However, the most sensitive piezoresistive sensors are based on doped silicon (Si) with reported GF>100, however, they are non-flexible, and thus non-conformable to 3D surfaces often found on a robot.

Capacitive tactile sensors: By using specifically created porous dielectric materials, it is possible to detect forces by altering the relative static permittivity of dielectric layers

between substrates. With the capacitive pressure sensors, normal and shear forces are commonly measured by observing changes in the distance between conductive electrodes. Capacitive tactile sensing technology has proven to be highly sensitive, compatible with static force measurement, and power efficient. However, devices are vulnerable to interference from approaching objects that change the fringe fields of the capacitor. This phenomenon can lead to ambiguous signals during measurement and significant hysteresis.

Piezoelectric tactile sensors: Another popular transduction technique for tactile sensing is piezoelectricity. Piezoelectricity is the term for a voltage that is generated in response to applied mechanical stresses for certain crystalline materials such as.... In their undisturbed form, the charge centers of anions and cations align with one another. However, when an external force is applied, the structure deforms. In that situation, the anions' and cations' charge centers split and create electric dipoles, which causes a piezopotential to arise. As a result, the external circuit is forced to conduct free electron flow in order to screen piezopotential and establish a new balanced state. A significant challenge in the use of piezoelectric sensors is their sensitivity to temperature.

Optical tactile sensors: The change in light intensity in mediums with different refractive indices is used by tactile sensors with optical modes of transduction to measure the pressure. Optical fiber-based taxel are flexible, sensitive, and quick, but they can occasionally be large. They can measure normal forces and are impervious to electromagnetic interference. Other problems with optical sensors include light loss from microbending and chirping, which distort the signal.

2.3.1 Tactile Sensors and a comparison of their sensing performance

The tables below summarize scientific papers describing tactile sensors for applications on robotic fingertips and as whole-body large area skin sensors.

Table 1: Robot Fingertip Sensors

Transduction Method	Materials/miniaturization technique	Sensitivity	Spatial Resolution	No of sensors	References
Piezoelectric	Si-micromachining	0.5V/N	1mm	32	Dahiya et al[31]
Piezoelectric	Si-micromachining	_____	0.7mm	8×8	Kolesar et al[32]
Piezoelectric	Si-micromachining	5.2mV/gm	0.07mm	8×8	Polla et al[33]
Capacitive	Si-micromachining	0.45pF/g	0.5mm	32×32	Suzuki et al[34]
Capacitive	Si-micromachining	0.13pF/g	2.2mm	3×3	Chu et al[35]
Capacitive	Si-micromachining	20μN	0.1mm	8×8	Gray et al[36]
Capacitive	Si-micromachining	100μN	500dpi	16×16	R.J. De souza et al[37]
Capacitive	Si-micromachining	13.5mV/kPa	0.24	8×1	Leineweber et al[38]
Resistive	Si-micromachining	_____	0.6mm	6×8	Raibert et al[39]
Piezoresistive	MEMS on Si	0.5-1V/N	0.42mm	6×6	Takao et al[40]
Piezoresistive			1mm	24	Choi et al[41]
Piezoresistive	MEMS on Si	1.59mV/kPa	0.3mm	64×64	Kane et al[42]
Piezoresistive	Si-micromachining	0.032mV/kPa	1mm	4×4	Liu et al[43]
Piezoresistive	Si-micromachining	0.02mV/kPa	0.25mm	32×32	Sugiyama et al[44]
Piezoresistive	ZnS:Mn particles (ZMPs)	10–50 MPa	100μm	500	X. Wang et al[45]
Optical	PDMS silicone	Detection at 100% up to 5cm in distance	10.8×10.8 cm^2	8×8	D.Hughes et al [46]

Table 2: Large Area tactile sensors

Transduction Method	Materials/ miniaturization technique	Sensitivity	Spatial Resolution	No sensors	References
Piezoelectric	On Polyimide	_____	2.5mm	6×7	Domenici et al[47]
Piezoelectric	P(VDF-TrFE)	0.41VPa^{-1}(max 20Pa)	3-6mm	2×10^7 fibres per mm^2	Persano et al[48]
Piezoelectric	P(VDF-TrFE)	2.3kPa^{-1}	1 × 1 cm^2	_____	Sharma et al[49]
Piezoelectric	ZnO nanowires	2.1μS kPa^{-1}	1 cm^2	92 × 92 (234 taxels per inch	Wenzhuo et al[50]
Piezoelectric	Polypropylene	0.001 kPa^{-1}(max 2Pa)	5mm	23×23	Gerda et al[51]
Piezoelectric	Graphene	GF=389	2.5 × 2.5 cm^2	4 × 4	Sun et al[52]
Capacitive	Alumina ceramic	0.0035 kPa^{-1}	41×90mm	_____	Qiulin et al
Capacitive	PDMS/air gap	0.7 kPa^{-1}	1 cm × 1 cm	5 × 5	S.Park et al[53]
Capacitive	PDMS/Rubrene	0.55 kPa^{-1}	64 mm^2	8×8	S.C. Mannsfeld et al[54]
Capacitive	Ionic conductor	0.01 kPa^{-1}	10 mm × 10 mm	2 × 2	J. Y. Sun et al[55]
Capacitive	Fluorosilicone/air gap	0.91 kPa^{-1}	4cm	_____	L. Viry et al[56]
Piezoresistive	Pt/nanofibers	GF=11.5	8 × 5 cm^2	64	C. Pang et al[57]
Piezoresistive	PDMS/SWNTs	1.8 kPa^{-1}	2 × 2 cm^2	_____	X. Wang et al[58]
Piezoresistive	Graphene/PU sponge	0.26 kPa^{-1}	7 × 9 cm^2	13 × 11	H. B. Yao et al[59]
Triboeletric	PDMS/Ag nanowires	28 mV N^{-1}(40-140N)	2mm	_____	T. Li et al.[60]
Triboeletric	PDMS/ZnS	6 MPa^{-1}	5 cm × 8 cm	_____	Z. L. Wang[61]
Triboeletric	PDMS/PET	0.06 kPa^{-1}	2.5mm	16×16	X. Wang et al.[62]
Optical	FBG	1mN	5mm	3×3	J.-S Heo et al [63]

State of the art commercially available Tactile sensors:

There are few tactile sensor patches that are commercially available. The following table lists some of the characteristics of the tactile sensors and their cost as well.

Table 3: Commercially available Tactile sensors

Sensor Product Name	Pressure range	Linearity	Contact surface material	Sensor thickness	Cost
Tekscan	648kPa	N/A	N/A	0.1mm	~$27k
PPS-Conformable Tact array System	3-75 PSI	99.8%	Conductive cloth	1mm	~$30k
First Sensor K-series STARe A/G	6kPa-40MPa	99%	Silicon	0.1mm	unknown
TakkStrip (TakkTile Sensors)	50kPa-150kPa	99%	Vytaflex20 Rubber	3.5mm	~$300
SynTouch-BioTac SP	100kPa	N/A	Silicone Elastomer	10mm	~$18k
OptoForce-OMD-20-SE-40N	40N(Fz), 10N(Fx,y)	98%	N/A	17mm	~$5K
Novel emed® A50	10kPa-1270kPa	N/A	Silicone	15.5mm	~$32K

2.4 Robot Skin Research Studies

The body's principal means of communication with the outside world is through the skin. By replicating nerve receptors and sensors, recent technical developments have begun to produce electronic skin for robotics[64]. Animals with biological skin transmit important information to the brain using a variety of nerve receptors located beneath the skin. Each skin receptor translates a variety of information, including temperature, discomfort, and mechanical stimuli, which are then transmitted directly to the brain[65]. Electronic skin

has been created to attempt to duplicate these receptors in the shape of various sensors, however these signals cannot be sent directly to the brain. To transmit this information, data communication protocols, signal encoding and processing, and signal transmission must all be created[66].

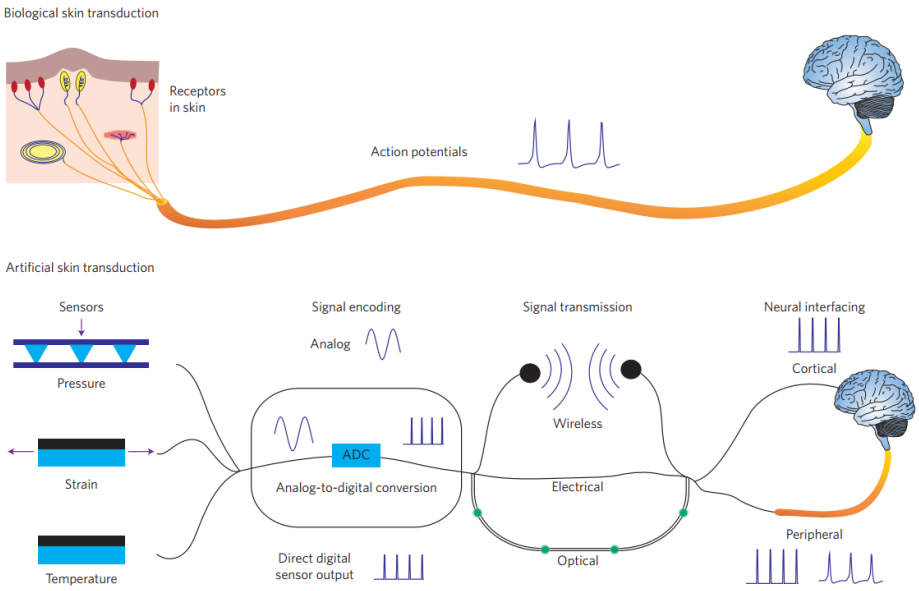

Figure 2: Comparison of sensory stimulation procedures for both natural and artificial stimuli[18]

As the likelihood of deploying service robots in our homes, workplaces, and industries increases, physical human-robot interaction must be improved to guarantee safety. Future collaborative robots will require the development and integration of tactile sensing technology, which is now a gap in the market. Robotic "skins" that are flexible and bending are necessary to accommodate touch sensors on the robot body and end-effectors, as these components have curved surfaces. The last ten years have seen tremendous advancements in the field of flexible electronics, leading to increases in the conformability and bendability of a wide range of sensors and electronics. Robotic skin has been investigated for many years and has to have similar characteristics to human skin in order

to interact with human settings[67]. As it has been extensively discussed in[68], tactile feeling is one of the crucial components among all the sensing abilities. Research on robotic tactile "skins" focuses on the best ways to fabricate them, choose the right materials, package them, and analyze the electrical designs that go along with them in order to analyze feedback from the sensors. Certain design criteria have been discussed to guide the required expectation for optimum tactile perception as regards operations in a robotic system some of which are reported in[69-73] . Some of which are, the robot tactile sensors should be able to respond quickly to contacts giving prompt feedback similar to the human skin responding as fast as 1ms. Based on the body site, the spatial resolution of the touch sensors should be dispersed or placed in an array. It should be around 1 mm for fingertips, which corresponds to a grid of roughly 15×10 elements on the size of the fingertip, and it can be as high as 5 mm for less sensitive areas like the palm and shoulders. Because skin is flexible and conforms to objects, biological sensors may gather information such as precise shapes of objects. Therefore, Robotic taxels should consequently be strong, flexible, conformable, elastic, and soft so that they can survive challenging environmental factors like high temperatures, high humidity, chemical stressors, electric fields, abrupt forces, etc. They shouldn't considerably increase the width or thickness of a robot connection or part when spread throughout the body. Additionally needed are linearity and little hysteresis. Inverse compensation can handle nonlinearity, but hysteresis is more difficult to handle. Taxels should produce output that is reproducible, monotonic, and stable. The fact that human touch perception is hysterical, nonlinear, time-varying, and sluggish is interesting to observe. Several other design criteria as regards tactile feedback information processing,

embedded coverings and multifunctionality of tactile sensors have also been put into consideration.

Outlined In section 2.1 is the several operation modes of various type of tactile sensors or otherwise known as mode of transduction. Describing resistive tactile sensors as presented in [74]based on a resistive mode of transduction, shows varying resistance values depending on the applied force at a contact location. This could be term piezoresistive tactile sensing, the application of materials whose resistance varies with changes in force/pressure, a typical example is the PEDOT: PSS used in [14, 75], spin coated on flexible substrate to make tactile sensors. These piezoresistive sensing technology is widely used in microelectromechanical systems with silicon based tactile sensors, employed as force sensing resistors (FSR) to create position and direction sensing in joysticks[76, 77]. These types of sensors are widely known to be economical, generally sensitive but could require a lot of power[78].

Describe in the equation below is the relationship between change in resistance and other parameters, showing that piezoresistive material response is indicated by a change the material resistivity and geometrical shape.

$$\varepsilon(1 + 2v) + \Delta\rho/\rho = \Delta r/r_o \qquad (2\text{-}1)$$

where v Poisson's ratio, ε applied strain, r_o stands for resistance without pressure, and $\Delta\rho$ is the change in resistivity ρ.

Tactile sensors with capacitive mode of transduction have been employed in the robotics. The advantages capacitive tactile sensors are capability of constructing dense sensor arrays, it has very high sensitivity however, stray capacity and extreme hysteresis are significant

disadvantages[36, 79, 80]. Peter A. Schmidt et al reports an array of capacitive sensor that connect or couples to the substrate using tiny fiber brushes the sensor elements on the array are strong enough to endure stresses experienced during gripping and are extremely sensitive (with a threshold of roughly 5 mN). Thus describes an 8×8 capacitive tactile sensing array with a $1mm^2$ area and spatial resolution at least ten times better than humans[80].

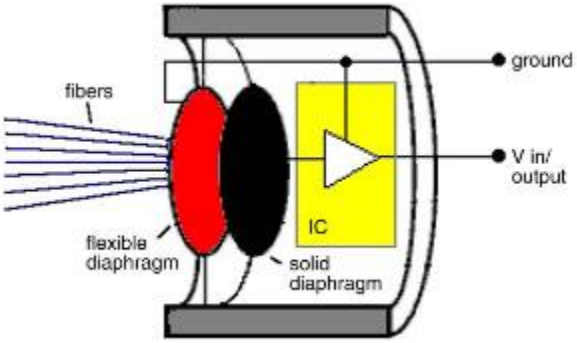

Figure 3 Sensor element with fibers, capacitor and IC schematic illustration[9]

Piezoelectric mode of transduction has been employed in the creation of robot skin sensors, producing measurable charge in proportion to the influence of a deformation or force. For dynamic tactile sensing, piezoelectric materials like PZT, PVDF, etc. are appropriate. Despite having greater piezoelectric capabilities than quartz and ceramics (such as PZT), polymers like PVDF are favored for touch sensors because of their exceptional qualities like flexibility, workability, and chemical stability[81]. The first report on the use of PVDF for tactile sensing was made in [71], and since then, reports on several works based on PVDF or its copolymers have appeared in [32], [82], and [41, 83-85]. The sensitivity of piezoelectric materials to temperature drifts is a significant source of worry**.** E.S Kolesar et al, describes 64 tactile sensors fabricated on 40μm thick PVDF arranged in an 8×8 matrix using complementary metal-oxide semiconductor (CMOS) technology[32]. The

well-established piezoelectric effect, which states that the mount of surface charge generated on a piezoelectric material is proportionate to the magnitude of the externally applied force, can be used to explain the functionality of piezoelectric-based touch sensors. The relationship between the generated finite surface charge (Q) and the applied force (F) can be expressed as Q = SF, where S is the piezoelectric material's charge sensitivity constant. The ideal capacitance (C), using a piezoelectric material as the dielectric medium and excluding edge effects, for a parallel plate capacitor design is:

$$C = \frac{\varepsilon_o \varepsilon_r A}{d} \qquad (2\text{-}2)$$

where ε_o is the relative dielectric constant parallel to the direction of the applied force (ε_r= 11 for PVDF), ε_r is the permittivity of free space, and A is the electrode's surface area. The open-circuit voltage (V) produced at the capacitor's terminals can be calculated using Gauss's Law as follows[32]:

$$V = \frac{Q}{C} = (\frac{S}{C})F \qquad (2\text{-}3)$$

A self-organizing multimodal sensing module that can detect temperature, pressure, acceleration, and force known as HEX-O-SKIN or CellulARSkin, was created by a renowned research team in Germany [52]. While incorporating existing commercially available sensors into modules, they created their own pressure sensor. Each module has a distinct ID and local intelligence to preprocess data, which lowers the network message overhead. Each module includes four ports for communication with nearby modules, and an accelerometer tracks the modules' relative position in relation to the robot host. Of the four ports for communication, one serves as the

master, while the others are the slave ports. The sensor runs two internal timers at a high oversampling rate to retrieve analog and digital signals for processing, this processed signal with control commands are forwarded in data packets from the master port to the slave ports. The slave ports then broadcast control messages decoded in accordance with their specific ID[86]. Mittendorfer, Philipp, et al used the multi-modal sensor HEX-O-SKIN patches on HRP-2 humanoid robot to demonstrate a tactile grasping sequence[30]. Figure 4 shows the picture with the informative labeling of the HEX-O-SKIN.

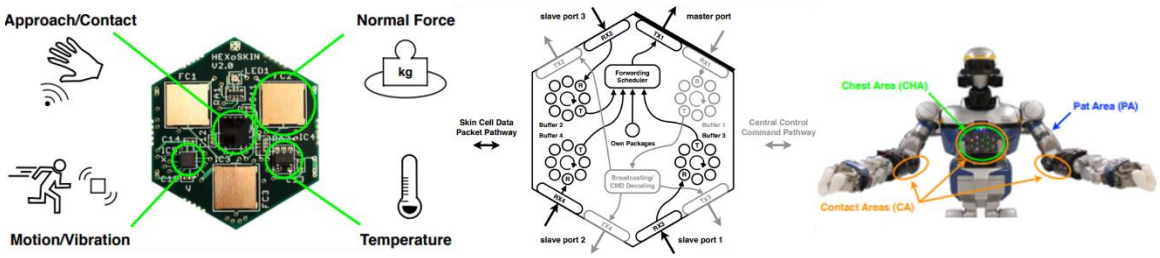

Figure 4 HEX_O_SKIN tactile patch and implementation[30, 86]

Another artificial robot skin is the Roboskin, The system is built on a triangular-shaped conformable mesh of sensors that are coupled to create a networked framework. With 12 taxels based on capacitive transducers, each sensor is supported on a flexible substrate, enabling the sensor to adapt to smooth curved surfaces. created by an Italian team, the Roboskin made up of twelve capacitive pressure-sensing taxels, uses two of taxels to offset the temperature drifting of the other ten taxels. They are set up on a bendable PCB with a triangle shape so it may be attached to any portion of a robot. There is also an off-the-shelf capacitance-to-digital converter integrated circuit in the module to detect the variation in capacitance, which is one of thirteen that are linked together by an I2C bus.

Robots named iCub, Kasper, and Nao were used to test the skin[29]. Figure 5 belows shows Roboskin patch.

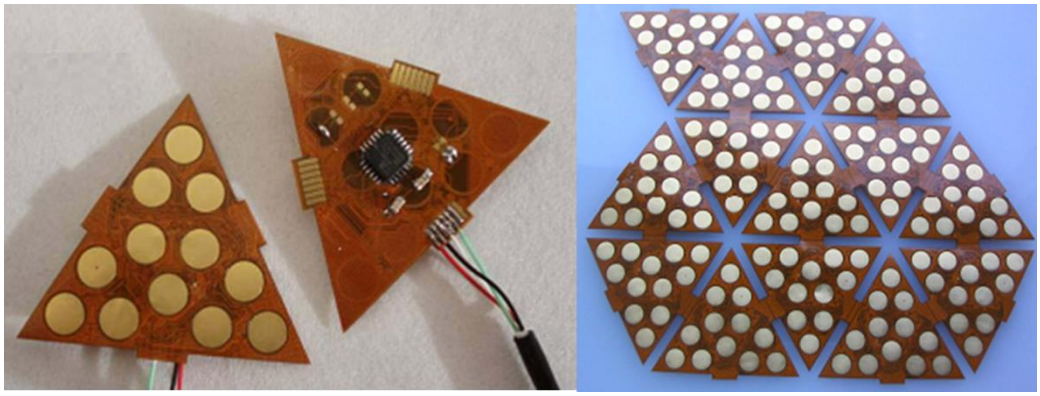

Figure 5 Roboskin patches and front and back view[29]

2.5 Requirements for Robotic Skin Applications

Although many tactile sensors have been developed, not all of them are suitable for application in robotics. Requirements for large area skin for robots includes spatial resolutions larger than 5mm, normal force detection range smaller than 50N, and max operating pressure greater than 1000psi. For these sensors, the measurement sensitivity does not need to exceed 0.1% of the range because they are used for robot physical guidance by a human or to implement safety behaviors when contacting an object. Other requirements include flexible/bendable with a bending radius varying from 1 to 10 cm, interconnection to other skin modules and the robot controller with a serial bus interface or a parallel bus interface not exceeding 32 pins, data transfer rates greater than 50 Hz, and ability to acquire sensor data within the Robot Operating System (ROS) programming environment. Requirements for robot fingertip applications are slightly different and include spatial resolution around 1mm, normal and shear force detection ranges smaller

than 10N, extremely low bending radius around 1cm, and data transfer rates greater than 500Hz. Many of the sensors tabulated above do not meet all of these application requirements, while others greatly exceed these requirements (overkill) leading to high cost. Many of these tactile sensors come with their circuitry and proprietary software and this software are not flexible or integrable to the Robot Operating System (ROS), and are compatible with Windows OS but not Linux OS, making them unusable on modern robots. Our lab recently purchased a PPS- Conformable TactArray system, with active areas ranging from 64 x 64 mm to 320 x 320 mm of capacitive sensors and a data acquisition sampling rate of 7-10kHz. While this commercial sensor has very high tactile sensitivity (0.0015 – 80 psi), it is not suitable for real time application, and we cannot integrate the sensor response to guide the motion of a robot. In terms of maintainability, the PPS sensor is packaged in a cloth-like material but cannot tolerate dust and liquid. Therefore, additional protection, such as wrapping in polymer layers is needed, thus affecting calibration accuracy and sensitivity. Other products, such as Tekscan arrays may be customizable to varying sizes and resolutions, produce sensor readings at higher rates, but are not conformable to 3D or curved surfaces.

In conclusion, although several commercial fingertip sensors have been integrated with robots, no robot-compatible large-area sensor is commercially available, thus motivating continued research in this direction.

2.6 Robot Skin Sensor Manufacturing Technology

Since silicon wafers and other hard substrates are often used in semiconductor integrated circuit technology today, they cannot be used for robot skin. Robot linkages need skin that has sensors on a flexible substrate that can be bent into many forms. Recently,

research has been done to develop sensors for flexible substrates. Considering its flexibility, chemical inertness, and resistance to high temperatures, kapton, often referred to as polyimide for flexible electronics, is an excellent substrate option when compared to other flexible polymers.

These flexible substrates that can accommodate tiny electronic circuitry on a nano scale have made it possible to develop new technologies like wearables and soft robotics. In previous years, the NGS group at UofL have developed, investigated the robot skin sensors, describing the fabrication of sensor microstructures on Kapton sheets using cleanroom microfabrication techniques to create tactile sensors[13, 16, 75]. Fu and colleagues used the combination of photolithography processes and inkjet printing techniques to facilitate the fabrication of microstructures of the printed interdigitated capacitors on Flexible Kapton[2]. Dahiya et. al. describes the transfer of fabricated crystal silicon micro-/nanostructures for tactile sensing ranging from 4 to 50microns in size on flexible Kapton substrate[31]. These tactile sensor microstructures fabricated on flexible polymers are built with specific sensing mediums to capture varying analog signals of physical variables such as pressure, force, temperature, strain, etc. The sensing mediums adopt transducing mechanisms for quantifying these signals detected into digital quantities for useful application. Optical fiber sensing, resistive, inductive sensing, capacitive sensing, and piezoresistive or piezoelectric actuating methods are some of the available sensing mediums available[4-8].

In [9], electro-hydro-dynamic printing was used to replace the cleanroom technique for the deposition of organic polymers PEDOT: PSS responsible for the piezoresistive phenomenon in the fabrication of tactile sensors used for robotic skin application. The high

voltage demands and diligent parameter scrutiny for nozzle requirement, viscosity, and recipe print formation make it rather cumbersome to make the process reliable for continuity. The Nordson EFD Pico Pulse equipment describe in[87] is the inkjet technique used to complete the fabrication of robot skin sensors, dispensing organic polymer PEDOT: PSS on tactile sensors. However, the aerosol jet printing technique in particular provides more flexibility in tuning printing parameters for desired feature size on flexible substrates, compatible with varying surfaces that may be complicated to achieve with cleanroom processes and on surfaces with uneven textures[88, 89]. Thus, increasing the operability of the users to easily adapt and control the size of the printed circuits with respect to photolithographic processes carried out in the cleanroom based on the modified printing recipe[90]. The aerosol inkjet printing process involves the formation of mist from the ink with the help of an ultrasonic atomizer. Pressurized mist is transported then by a carrier gas (Nitrogen) to the printing head where it is focused into the aerosol and sheath gas (Nitrogen). This focused stream of the aerosol and sheath gas is directed towards the substrate. In this work, an aerosol inkjet printing system from Optomec® that capable of depositing solvent or water-based ink up to 1-10cp in viscosity[91].

CHAPTER 3

ROBOTIC SKIN FABRICATION AND INTEGRATION

In this chapter, we discuss the fabrication and evaluation of robotic skin sensor arrays based on semiconductor organic materials. In order to successfully deploy on robots, skin sensors must be designed, simulated, fabricated, packaged, connected to electronic transducers, fashioned as interfaces to robot controllers, and used via human-robot interaction algorithms. The organic semiconductor polymer in this work is Poly (3, 4-ethylenedioxythiophene)-ploy(styrenesulfonate) or PEDOT: PSS, which has been printed over flexible Kapton substrate utilizing a variety of processes, is the base sensing material employed in our research. A 20:1 gauge factor is compatible with the resistance change caused by strain in the active sensor material.

In this work, we adapt cleanroom techniques to fabricate the pressure sensitive robotic skin sensor with the organic piezoresistive material, Poly(3,4-ethylenedioxythiophene) polystyrene sulfonate. PEDOT:PSS, consists of two different ionomers. The positive-charged Poly(3,4-ethylenedioxythiophene) and the negatively charged Sulfonated Polystyrene were combined. In this chapter, for the purpose of evaluating our produced PEDOT:PSS inks, we created strain sensors. Utilizing micro structuring technology, conductive traces are created on the substrate using lithography, deposition, and lift-off. The fabrication techniques described were those employed in the cleanroom, and new novel-fabrication platform “NeXus”. The manufacturing process how

to automate printing processes and calibrate printing stations is discussed. Additionally, a data collecting system was developed using both commercially available gear and custom-

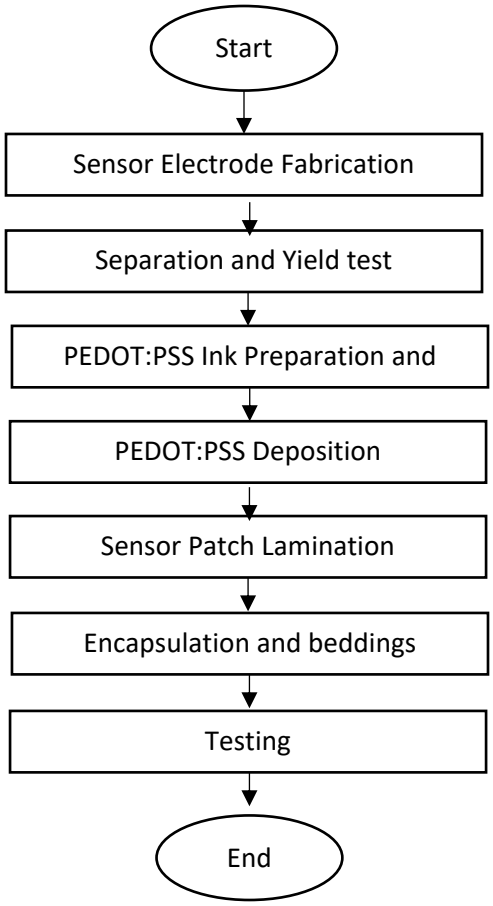

Figure 6 Sensor manufacturing steps

made hardware to verify the resulting pressure sensor arrays. As shown in Fig. 3, the entire procedure entails a few processes, from sensor microfabrication to testing.

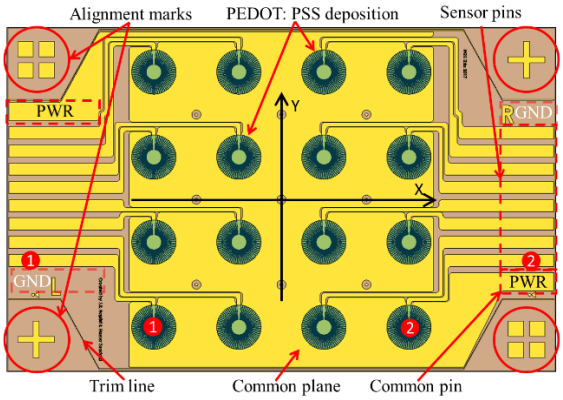

Figure 7 Diagram of Skin Sensor patch

.

3.1 Skin Sensor Cleanroom Fabrication Technique

3.1.1 Robot skin Sensor design

In recent years, sensor geometries based on a 4×4 interdigitated structure. In this work, two skin sensor design have been proposed, evaluated, and simulated using COMSOL® Finite Element Analysis (FEA). The fabrication process is refined based on the dimensional parameters of the sensor arrays used for simulation. The study employed two types of skin sensor design namely.

- Star-Shaped Sensor design: The diameter of each sensor is 3.65mm, separated from the neighboring sensor by a spacing of 7mm. 16 sensors are arranged in a single patch as 4×4 sensor array. Fig. 4 also shows the dimensions of a single beam in star-shaped structure, the electrical traces are 0.5mm apart and they are 1mm thick. Nine electrodes are interconnected from tactile sensors to both sides of the array. Eight electrodes are for signal lines, and one is for ground. The side electrodes will later be used for interconnection to the electronic circuit.

- Circular tree design: In this study, the other tactile sensor design employed is a circular tree structure that is fabricated in the cleanroom on a flexible polyimide substrate otherwise known as a Kapton Sheet. In comparison to traditional interdigitated or serpentine structured strain gauge sensor designs, the topology of the circular tree also known as unbalancing binary tree as depicted in Fig. 6 is made to avoid directional effect of strain on the sensor. That is, under the same amount of strain applied, the interdigitated or serpentine sensor topology will produce different values of resistance when measured at x and y axes of the sensors.

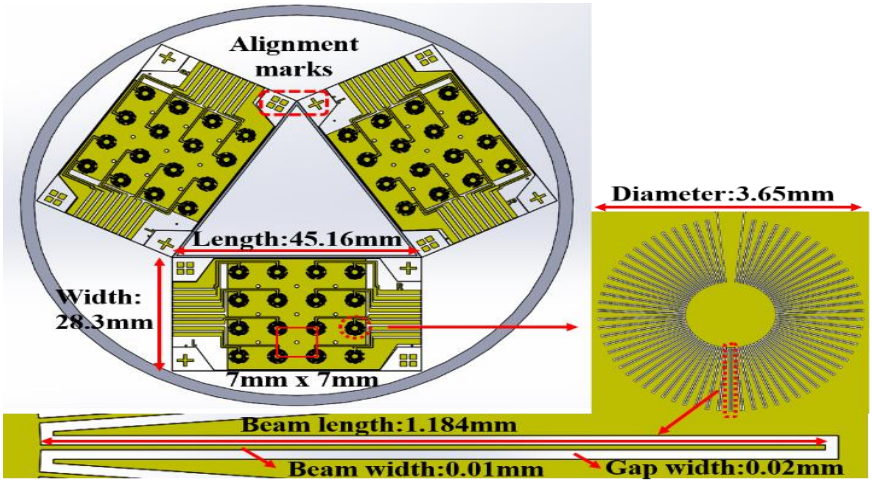

Figure 8 Star-shaped sensor arrays

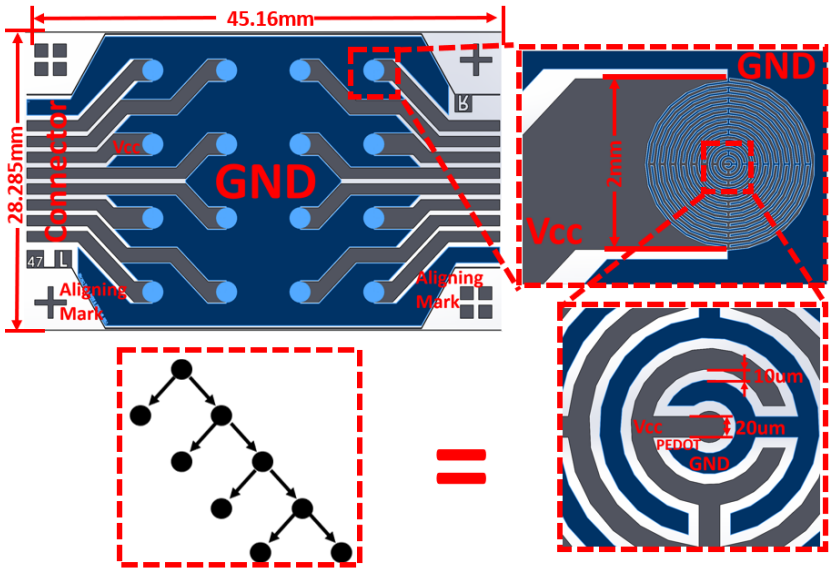

Figure 9 Circular tree shaped sensor array

In the previous design proposed, a star-shaped design, it reduces the directional effect, through simulation and experiment. The design proved effective but the constraint, microstructure patterning and spatial density efficiency proved hard to improve given the specific fabrication process. Hence, we introduced the circular tree design to improve on the spatial resolution of the star-shaped design, efficiently utilizing the space create with the center of the sensor geometry. This topology which expands recursively in circular patterns forms the sensor electrodes with the base sensing material, PEDOT: PSS, filling in the gaps.

Simulating this proposed sensor design at its center, the physical properties of the materials and simulation model dimensions used in the ANSYS and COMSOL simulation environment is the same as those described in. Fig. 8 shows the total deformation in respect to strain on a sensor patch, considering the complexity of the sensor geometry, a simplified geometry with three circular rounds of electrode was adopted. The width of the electrode is 0.1mm while the gap between the electrode meant for the filling of the PEDOT:PSS is

0.05mm. Fig. 7 Shows the simulation result of force load and resistance trend in color green and the corresponding experimental result of force and voltage profile in color blue. The simulating environment for convenience could only be depicted in a force-resistance relationship. The simulation result shows similar trend to the experimental result, but still displays marginal disparity and discrepancies resulting from a reduced order model, mashing, boundary conditions and uncertainty of material properties in the simulating environment.

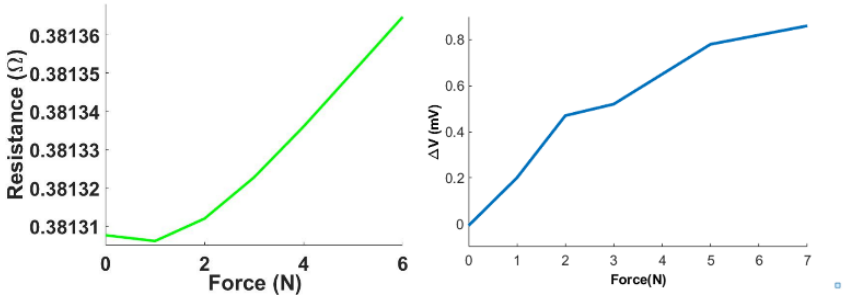

Figure 10 Resistance and Force load trend in green and experimental result in voltage and force profile in blue

The patterning of these robot skin designs can be fabricated in the cleanroom using two approaches which are wet liftoff photolithography combined with a dry etching procedure to isolate the sensing region leaving the organic pressure sensing medium (PEDOT: PSS) on only the sensing areas while the other approach uses wet etching technique that involves using a particular etchant in pattering the sensor designs. Fig. 9 illustrates these approaches, and the fabrication techniques are discussed in detail in this chapter.

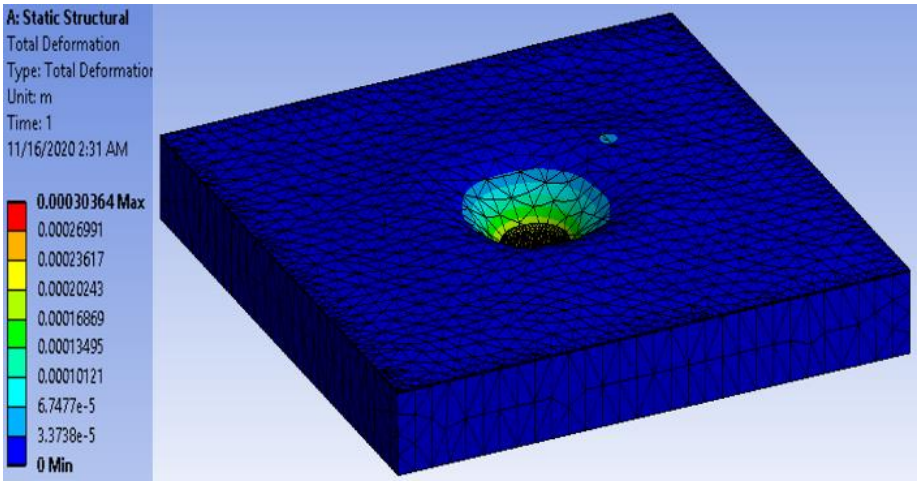

Figure 11 Deformation distribution due to normal load application on the sensor patch

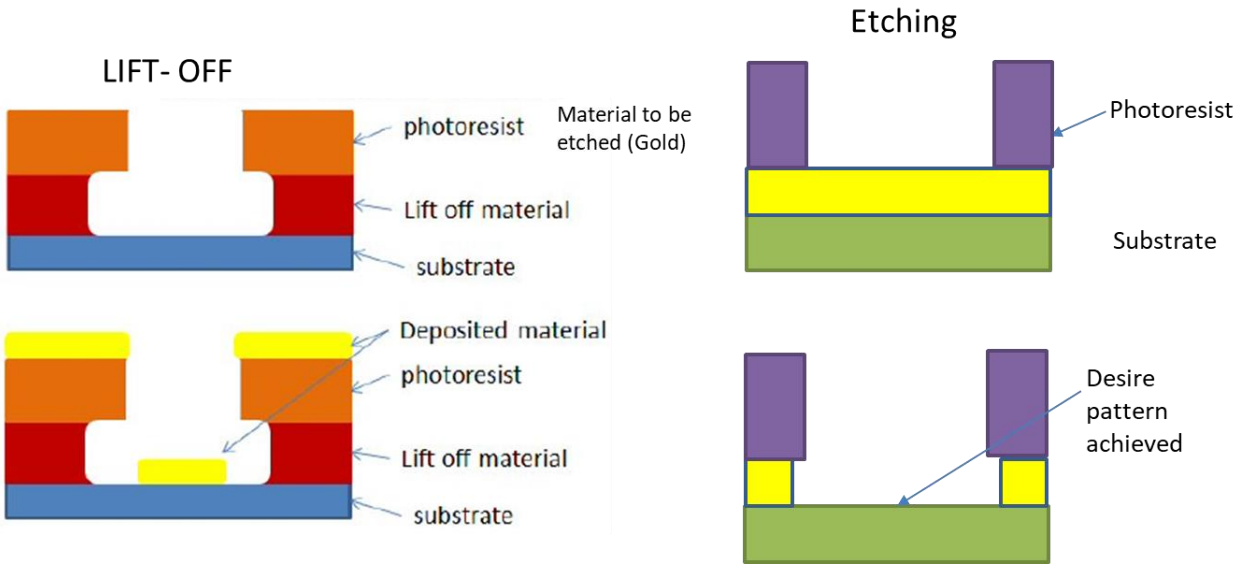

Figure 12 Fabrication approaches

3.1.2 Cleanroom Fabrication Technique [lift -Off]

We investigated a scalable, cleanroom compatible fabrication technique using Wet lift-off photolithographic with a dry etching photolithographic process to repeatably deposit PEDOT: PSS on the sensing areas of the fabricated sensor electrodes. The

patterning of the sensor features was carried on 50 microns thick Kapton® substrate otherwise known as polyimide. Fig. 3-7 depicts the steps taken for the lift-off fabrication process. Fabrication process to uniformly depositing the pressure sensing material PEDOT: PSS is described below.

1. A clean 4" silicon wafer is first ready to be used as a carrier, and MicroChem® SPR 220-3.0 photoresist is spun onto it.
2. After being cut appropriately to a size that is slightly less than the 4" wafer size, a Kapton® polyimide film is cleaned using acetone and isopropyl alcohol (IPA), in that sequence. After the film has been put into a 4-inch silicon wafer carrier and aligned, it is heated to 5°C for 60 seconds. A brayer is then used to laminate the thicker 6" by 6" Kapton® film onto the film. After a brief period of heating, the wafer and Kapton film are removed. Remove the thicker layer of Kapton® film, and then apply the skin sensor Kapton® substrate on the wafer.
3. To pattern the electrodes, two-layer photoresists made of MicroChem LOR3A and SPR220-3.0 are spun onto the wafer, respectively. Before proceeding, the wafer is soft baked for 120 seconds at 115°C and allowed to cool.
4. To begin photolithography, choose a desired electrode mask and use a Karl SUSS® mask aligner with a 16-second UV light exposure.
5. After that, the wafer is post-baked for 60 seconds at 115°C on the hotplate. The MF319 developer is used to develop the photoresist. The sample is then dried using a N2 cannon and cleaned using MARCH® Reactive Ion Etching (RIE), which is set to 50 watts of power and a 20 SCCM oxygen flow rate for 45 seconds at a pressure of 300 mTorr.

6. 300 nm of gold are sputter-deposited onto the patterned Kapton film using the Kurt J. Lesker® PVD75 sputtering deposition equipment. For liftoff, the coated Kapton® film and wafer are put in a beaker with acetone and immersed in a sonicated bath for around 20 minutes. After separating off the wafer, the Kapton® film is repeatedly cleaned with acetone and IPA before being dried with a N2 gun.
7. The resistance of every sensor is measured prior to proceeding with the production process. Since all sensors are open circuits, their recorded conductance values should ideally all be zero. Should any sensor exhibit a non-zero conductance value, RIE will either liftoff the Kapton® film again or clean it. Step 2 should be followed by adhering the modified film with interdigitated structures to a fresh carrier wafer.
8. The patterning windows over the interdigitated structures are covered with a semi-conductive material, and a PEDOT:PSS based solution is spun onto the Kapton® film. After that, the wafer is placed in a regular oven and dried for ten minutes at 80°C with a vacuum.
9. After cooling the wafer, a thin coating of 2g type C parylene particles is applied to the Kapton® sheet using a SCS Labcoter® 2 (PDS 2010) Parylene deposition machine, as seen in Fig. 3-8. After coating is complete, N2 is sprayed on the sensor surface to eliminate any remaining dust.
10. To spin two layers of the MicroChem LOR3A and SPR220-3.0 photoresists on the Parylene film, repeat step 3 one more.
11. Step 5 is repeated after exposing the sensor area to a second photolithography step in the mask aligner for 16 seconds under UV light using a second mask.

12. Each tactile sensor's top surface is sputtered with 300 nm thick titanium using the PVD75. Step 6's liftoff procedure is then repeated.
13. Ultimately, the Kapton® substrate is reached by repeatedly etching the surface of the film using a RIE machine operating at 200 watts of power and a 20 SCCM oxygen flow rate for five minutes each cycle.

3.1.3 Cleanroom Fabrication Technique [Gold Etching]

The gold etching technique is an upgrade to the wet lift-off photolithographic fabrication technique. This is because using sonicated baths filled with acetone to lift off materials from undesired regions still appears to leave tiny gold particles on the sensor areas not easily seen, causing short circuiting between the gold electrodes and the ground resulting in reduced yield. The lift-off technique appears to be less effective when dealing with sensor geometry having increasingly small microstructure patterns. Also, the use of two photoresists during the spin coating process in preparation for photolithography, interferes with the optimum outcome of achieving desired patterns. This is due to the presence of bubbles formed because of varying curing temperature and timing of the photoresists.

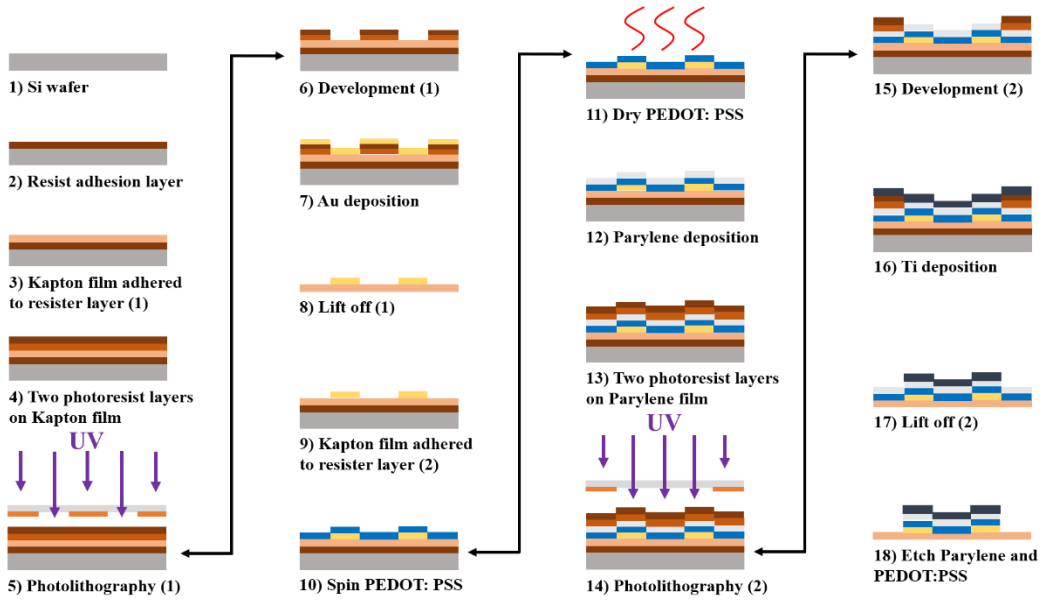

Figure 13 Lift-off fabrication Technique[50]

Potassium iodide is the gold etchant used to dissolve and etch off regions not protected by photoresist, leaving behind the desired pattern. Described below are the steps taken to achieve the desired pattern and increase the yield of the skin sensors using which is shown in Fig. 12.

1. A clean 4” silicon wafer serving as the support carrier for the Polyimide is spun with photoresist 1827
2. A Kapton substrate is cut to the size of the silicon wafer with little allowance from the edge of the wafer, cleaned from dust particle with Acetone and Isopropyl alcohol (IPA) simultaneously and dried with nitrogen gun. The Kapton sheet is then attached by aligning it to the wafer on a hot plate at 115˚C for 90secs. The flat glass plate is placed on the substrate for 30seconds and then smoothen with a brayer for the next 1minute to remove the bubbles underneath its attachment to the carrier

wafer. After which it is removed from the hot plate and cooled off, leaving the Kapton sheet adhered and straightened on the silicon wafer.

3. The next process is the sputtering of gold on the Kapton substrate using Kurt J. Lesker PVD75®, a sputtering deposition system. The parameters for the deposition of 300nm of gold includes 60 minutes pump time, 3.5 minutes deposition, a base pressure of 5milli torr.
4. The Gold-plated substrate in preparation for the photolithography is then spun with a less viscous and thin photoresist, 1805. After which it is post baked at 115 ˚C for 90 minutes.
5. A specific electrode mask with the required patterned is selected and installed in the Karl SUSS® mask aligner to initiate the first photolithography process. Choosing the program "Hard Contact" for the photolithography process takes place between the Photomask and the Kapton Substrate for a duration of 22 secs of exposure to UV light.
6. The substrate is then placed in the MIF219 developer solution for 60 seconds to develop the photoresist, revealing the patterned features. The substrate is rinsed with DI water, dried and post baked for about 1minute to remove moisture, cooled and then inspected under an electron microscope.
7. Moving over to the Chemical Bay, with the intent of etching off the gold portion which was created by a window opening through the photolithography process, the substrate is immersed in a gold etchant called potassium iodide. For 2 minutes, the solution is shaken over the immersed substrate to finally reveal the desired pattern.

The substrate is taken out afterwards, rinsed and then dried for 60 secs on the hot plate.

8. The resistance of the sensors is taken and verified to ensure its value measures as zero. This indicates it is an open circuit. If resistance values are gained it means it is short circuited and that will ultimately affect the yield.
9. A prepared colloidal PEDOT: PSS based solution is spun on the patterned Kapton sheet which is still adhered to the silicon wafer at 3000rpm for 30 seconds. The spin coating of the PEDOT: PSS covers the entire sensor patterned feature and then moved to a conventional oven to dry out under vacuum at 80 ˚C for about 20 minutes.
10. The substrate is cooled and moved over to the Parylene deposition system SCS Labcoter® 2 (PDS 2010) shown in Fig. 11. The wafer with 4grams of measured type C Parylene is placed in the system and operated under vacuum for about 2-3hours to evenly spread a fine layer of Parylene sealing the surface of the wafer. At this point the whole surface of the substrate is covered with both PEDOT: PSS and Parylene which increases the resistance overall, but it is required for it to be left on the sensor area. To achieve this, a dry etching technique is used to take off the PEDOT: PSS and Parylene in unwanted regions of the substrate and here is how the process is done.

Figure 14 SCS Labcoter2 Parylene Deposition System

.

11. Two photoresists (MicroChem LOR 3A and 1805) is spun on the substrate at 3000RPM for 45seconds. After the spinning of the first photoresist, it is post baked for 6 minutes at 150˚C and the second is also spin coated and post baked for 90 seconds.
12. A second photolithography process is carried with a second mask which is a window mask, it exposes the regions of the sensor for development. The exposure time is for 16 seconds and then we repeat step 6.
13. Using Kurt J. Lesker PVD75®, titanium is deposited on sensor area. With a process configuration of 35 minutes pump time and a deposition cycle for 4 times at 3 minutes interval and 1-minute rest time, 300nm titanium deposition thickness was achieved.

14. Finally, March RIE set at 200 watts, 100mtorr, and 20% SCCM oxygen flow rate for 32minutes, is used till Kapton film is revealed, etching off PEDOT: PSS and Parylene from the other regions of the substrate while the Titanium deposition protects PEDOT: PSS from been etched off the surface of the sensor patterned areas.

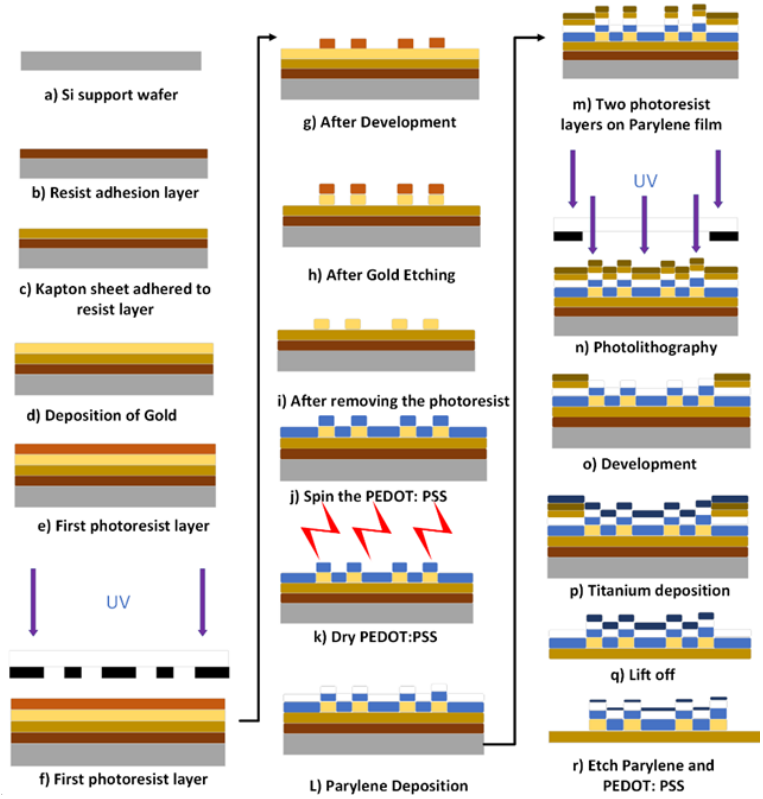

Figure 15 Gold etching fabrication technique

3.1.4 Formulation of PEDOT:PSS Collidal solution

To achieve the piezoresistive phenomenon of the robotic skin strain gauge, it is expedient that the PEDOT: PSS solution that is spin coated on the substrate has the desirable properties for the application. These properties are specific to its wettability, conductivity, and adhesion to the metal electrode in this case, the gold-plated substrate.

For the formulation of the PEDOT: PSS solution in our work, we obtained a stock from Sigma Aldrich with the following properties. A PEDOT: PSS sample gel like in appearance with concentration of 5% in water, a resistance of 50-150 Ω/sq, PH scale of 1.5-2.5 and a viscosity of 30,000-90,000 mPas (22 °C). To reduce its viscosity, make suitable for spin coating, increase its wettability and adhesion, the recipe in the ratio PEDOT: DMSO: PVP = 2g: 2g: 0.77g is used for its application on a supporting wafer carrying the Gold Patterned substrate. The PVP (Polyvinylpyrrolidone) which is amphiphilic, having both hydrophobic and hydrophilic properties serve as the surface stabilizer for the PEDOT: PSS colloidal solution to the substrate enhancing it adhesion and bonding it to the gold pattern on the Kapton substrate. DMSO (Dimethyl sulfoxide) solvent is used to dissolve the PVP which is in powdered form, allowing for proper miscibility with PEDOT: PSS. The DMSO also improves the morphology of PEDOT: PSS also enhancing its conductivity.

3.2 Skin Sensor Fabrication Upgrade using the NeXus

The fabrication of robot skin sensor using cleanroom technique appears to be cumbersome, time consuming and expensive. This requires several trainings on how to utilize tools, equipment, and chemicals for carrying out the photolithographic steps in the cleanroom. An attention to every minute detail and careful realization of procedures is crucial to ensure the successful yield of fabricated sensors but still cannot guarantee 100% repeatability either using lift-off or metal etch techniques in the cleanroom.

Due to these challenges, the NeXus novel micro-fabrication shown in [92] have been introduced to substitute one of the most important steps in sensor fabrication which is the deposition of PEDOT: PSS on the sensing regions in the NeXus [92].

The upgrade fabrication process involves the fabrication of the skin sensor electrode in the cleanroom and deposition of the PEDOT: PSS using the direct write ink jet printing tools (Aerosol jet printer, Pico-Pulse) which are present within the NeXus as shown in Fig. 13 below.

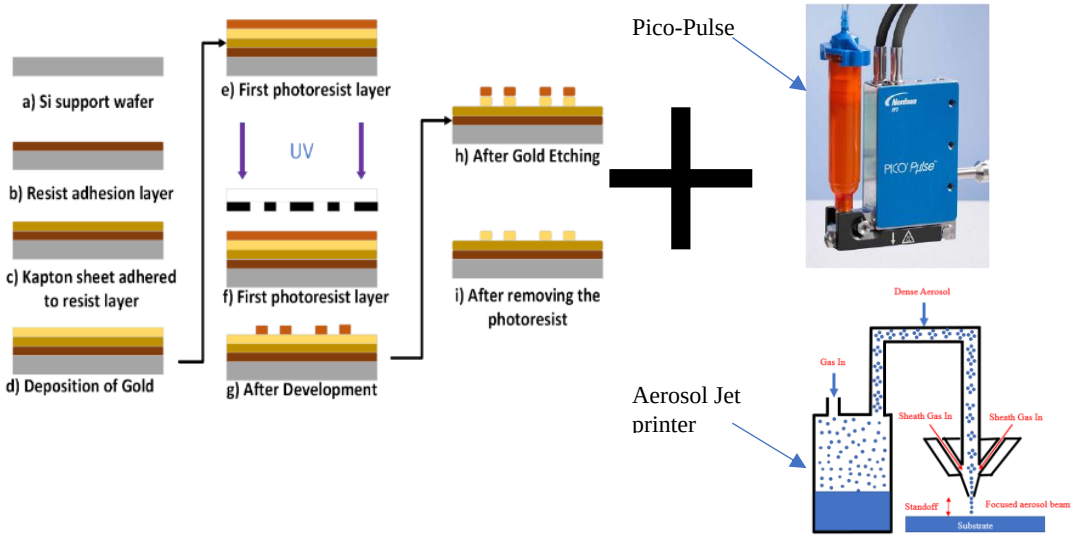

Figure 16 Upgrade Fabrication with Direct write inkjet printers (PicoPulse & Aerosol jet printer)

3.2.1 PICO PULSE® inkjet printing system

The deposition of the PEDOT: PSS is carried out through a custom-built direct-write Inkjet system that is part of the NeXus micromanufacturing platform (Figure 3-13) which consists of the following components:

- The Nordson EFD Pico Pulse® ink-jetting instrument with a piezoelectric actuator print head with 50micron nozzle and fluid syringe.
- Nordson EFD Pico Pulse® controller.
- 3 DOF positioner used to control height adjustment and sample displacement during the printing.

- Air pressure gauge.
- NI LabVIEW® based User Interface (UI) for motion control of the motorized stages.

The motion part of the printing system consists of three motorized precision stages from Newport - two linear stages M-ILS300LM-S for displacement in XY plane with 300 mm stroke and ±0.1 μm repeatability, and vertical stage GTS70VCC for Z direction with 70 mm stroke and ±1 μm repeatability. The motion control is realized through Newport XPS-D8 controller, National Instrument PXI platform with real-time PXIe-8861 controller, and NI LabVIEW UI allowing path and motion programming-based G-code. The sample chuck with a vacuum clamping mechanism for substrates is attached to the top of the Z stage.

The Pico Pulse® printing head is mounted above the sample chuck along with a camera for the inspection of the ink deposition process. All the dispensing parameters are controlled and adjusted with the help of the Nordson EFD Pico Pulse controller with proprietary UI. The following dispensing parameters are usually adjusted during the printing process:

- Waveform times (open/close/pulse).
- Cycle – droplet dispensing period corresponding to dispensing frequency, f_d. Determines the frequency of the droplet jetting during printing (1 – 250 Hz).
- Stroke – ink droplet jetting force. Expressed in %, where maximum force corresponds to 100%.
- Deposition Height, h (3 mm): Distance from the printer head's nozzle to the substrate.
- Temperature, T_i (40 °C): Temperature of the ink.

- Air Pressure, p_a (20psi): Fluid pressure in the printhead's valve assembly.

Based on results from our group's previous study of the inkjet deposition of high viscosity fluid (UV adhesive) with the help of the Pico Pulse system, we have determined a set of the dispensing parameters for PEDOT: PSS/DMSO/PVP solution. These parameters allow deposition of a PEDOT: PSS droplet (dot) with a specific diameter d_d on the Kapton substrate. The standard deviation $\mathbf{S_d}$ for the average diameter of the PEDOT: PSS droplet is placed next to the specified diameter (Table 4-3).

f_d [Hz]	Stroke	p_a [psi]	T_f [°C]	H [mm]	$\overline{d_d}$ (µm)	S_d (µm)
3.3	80%	20	40	3	400	10

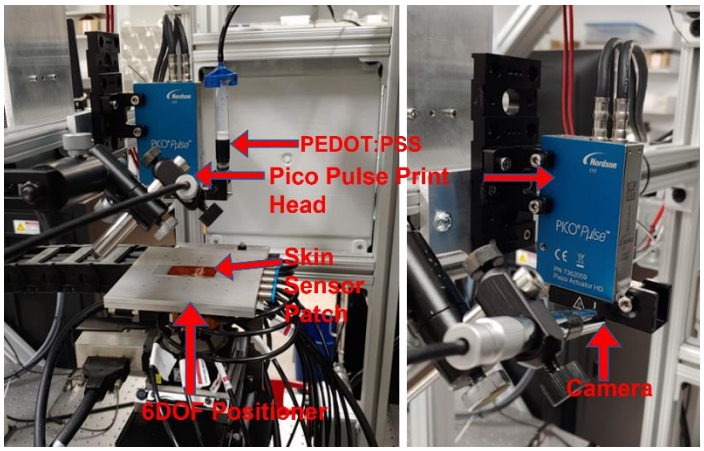

Figure 17 A) Pico Pulse Experimental Setup, B) Schematic View, Cross-Section of Valve Assembly, With Cartridge and Position of Its Piston In Closed And Open Mode

Table 4: Printing Parameters for the PEDOT: PSS Solution

Studies show that the formation of the continuous lines or films with a single nozzle inkjet printer requires control of the droplet overlap on the substrate with an adequate resolution. It is especially critical in the case of the various conducting materials, such as nano/micro particle inks, and conducting polymer composites, which often require post-processing, sintering, or thermal annealing respectively. Hence droplet overlap in a single printed line and line spacing for a film are the key parameters in the inkjet printing process that will determine the properties of the fabricated structure. As in the case of our PEDOT: PSS/DMSO/PVP solution, conductivity, and piezoresistivity will depend on the uniformity of the printed film – constant thickness of the film across the whole sensor area and its uniform distribution of the constituent organic polymer components: PEDOT: PSS and PVP.

To assure uniformity of the inkjet printed PEDOT: PSS films with Pico Pulse, we have adopted the method proposed by Gengenbach et al and Duineveld P et al. This approach enables synchronization between the dispensing process of the printhead and motorized stage motion, expressed by the following formula,

$$v_s(t) = f_d d_{dot} \tag{4-2}$$

where $v_S(t)$ is a motorized stage velocity, f_d is a deposition frequency, and $d_{dot}$is a spacing constant, a measure of the droplet overlaps. Here low values of d_{dot}would result in a high overlap of the droplets, and large values would produce an opposite situation.

To align the inkjet printing nozzle for the dispensing of PEDOT: PSS to the exact location of the skin sensors on the sensor patch, G-code is generated for precise sample displacement on the 6DOF positioner. A DXF drawing line corresponding to what will be

printed is created in a cad software and imported in a “manufacturing workspace of Autodesk’s fusion 360. Autodesk’s fusion uses a cutting operation for operations such as water jetting or plasma cutting, which provides a toolpath for the manufacturing process. In this case, a cutting operation is created that models the DXF sketch for the inkjet print head. Figure 15 shows the DXF sketch in the manufacturing workspace of Autodesk’s fusion 360. The cutting operation is set to a print speed of 600mm/min and the contours of the DXF files are selected as the profile to print. Thereafter, using a custom post-processor simulated within the manufacturing workspace, the G-code is generated from the contours selected in the cutting operation. The G-code generated is imported into a custom LabVIEW program, which is then parsed to extract X and Y coordinates as well as a feed rate (speed) to print the PEDOT: PSS. Each line of G-Code begins with a G-Code designator to instruct the program what kind of information will come next. For this use case, only the movement designators, G0 and G1 are needed. A G0 move represents a travel or non-printing move. A G1 command designates a printing movement. Both commands are followed by absolute cartesian coordinates for the 6-dof positioner of the NeXus system to move to. To summarize, the LabVIEW program takes the coordinates from each G-Code line, parses them into absolute X and Y positions, then instructs the Newport 6-dof positioner to move to those positions at a given feed rate, only depositing material if the coordinates were preceded by a G1 designator. An example of a simple square in G-Code: G0 X10 Y0 Z1 F600, G1 X10 Y20 Z1 F600, G1 X30 Y20 Z1 F600, G1 X30 Y0 Z1 F300, G1 X10 Y0 Z1 F600. Figure 3-15b shows the outcome of Inkjet printing PEDOT:PSS on a skin sensor patch.

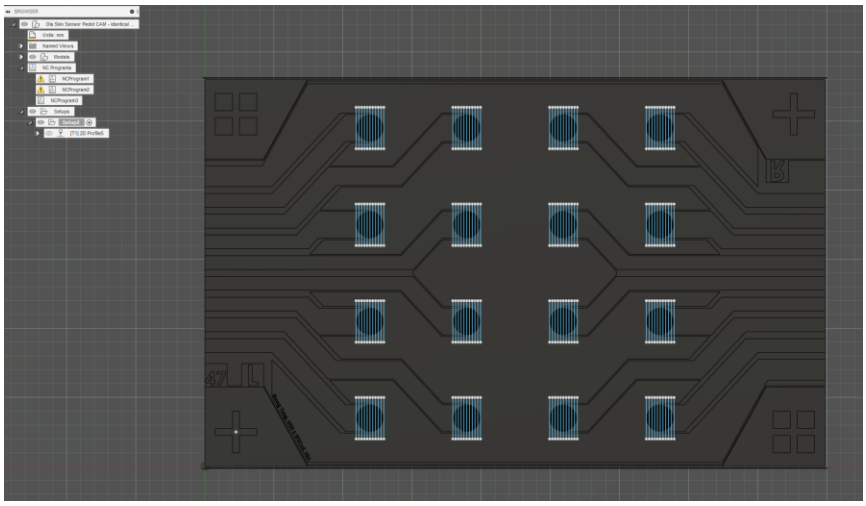

Figure 18 Autodesk's Fusion 360 Cutting Operation Contour Lines for The Generation Of G-Code Print Lines for The Circular Tree Skin Sensor Patch

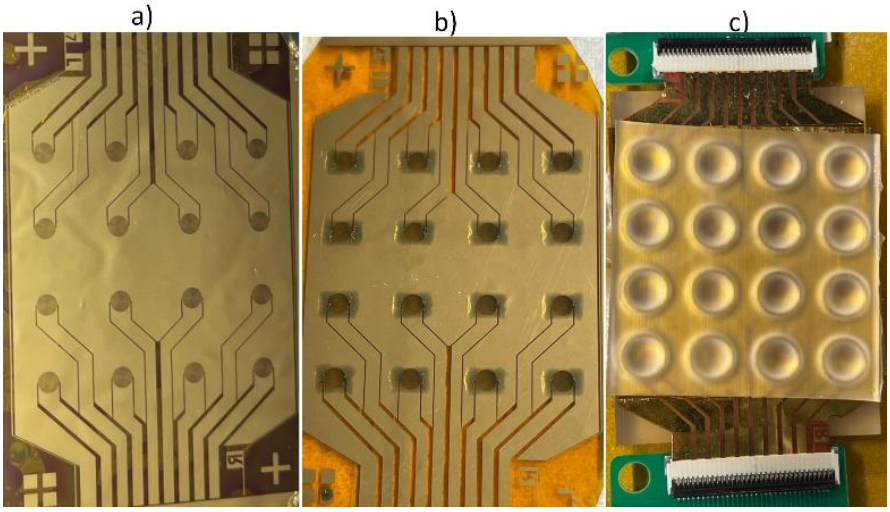

Figure 19 A) Skin Sensor Patch Without PEDOT: PSS B) Skin Sensor Patch with Inkjet-Printed PEDOT: PSS C) Encapsulated Skin Sensor Patch

3.2.2 Aerosol Jet printing process for PEDOT:PSS deposition

We investigated a new method of depositing PEDOT: PSS through aerosol jet printing, replacing the technically challenging and time-consuming techniques applied in the cleanroom. Aerosol jet printing reduces the number of steps and time required to realize the robot skin sensor fabrication process, reducing the process time from about 5 hours to

26 mins for a laminated paired skin sensor patch. It also diminishes the likelihood of human error in the patterning of the PEDOT: PSS on the skin sensor structures, as indicated in its characterized sensitivity of 6.2μV/N as compared to 0.4μV/N and 5.1μV/N of cleanroom fabricated ones.

3.2.2.1 Plasma Treatment of Sensor Electrodes

After the fabrication of sensor structures in the cleanroom, the resistance of each skin sensor on the sensor patch is inspected to determine the yield ensuring there is no short circuit occurrence within its links. After satisfying this requirement, the sensor is ready for PEDOT: PSS deposition process. This step begins with a plasma treatment of the substrate to improve the adhesion of the PEDOT: PSS ink to the surface. In previous studies, we have used PEDOT: PSS stock from Sigma Aldrich, but because of its high viscosity, it had to be mixed with other solvents to make it suitable for deposition. In this study, we used the PEDOT: PSS stock from Heraeus (CleviosTM®) and it has the following properties: 15-60mPa.s viscosity, the conductivity of 850S/cm, and solid content of 1.0%-1.3%. This ink has low viscosity allowing for direct application with an Aerosol Inkjet printer without the need to adjust its admissibility with other compounds. However, this type of PEDOT: PSS ink wouldn't adhere to the Kapton's surface, hence the need to introduce a plasma treatment of the substrate's surface to improve its wettability. The plasma treatment was carried out in a Harrick® Plasmer Cleaner device. The substrate was inserted into the chamber, and after evacuation and reaching low vacuum, the substrate was exposed to air RF plasma at 30W for a 2min period. With an effective period of 30mins, the skin sensor

patterned substrate is ready for inkjet printing of the PEDOT: PSS organic polymer using the Aerosol jet printer[93].

3.2.2.2 G-code Generation

Before commencing deposition of the PEDOT: PSS after plasma treatment of the substrate, it is important to feed the instructions in the form of precise coordinates to the aerosol jet print system. This enables precise displacement of the substrate during deposition of the ink onto the skin sensor patch. This was realized by generating G-code command lines, imported into the Inkjet print system. The Autodesk® Fusion 360 manufacturing workspace software was used to create printing patterns in DXF format based on the design of the imported CAD model. The Autodesk® Fusion 360 provides a library and capabilities that allow simulation of the printing process based on the designed pattern of trajectory. Once the design trajectory was confirmed through simulation in the software environment, the custom post-processor was activated to generate the G-code parsed in X and Y coordinates that also indicated the feed rate, which also represents the print speed. Figure 3-16a shows the Autodesk® Fusion 360 interface indicating the DXF contoured line drawings of regions over the skin sensor surface where the G-code should be generated.

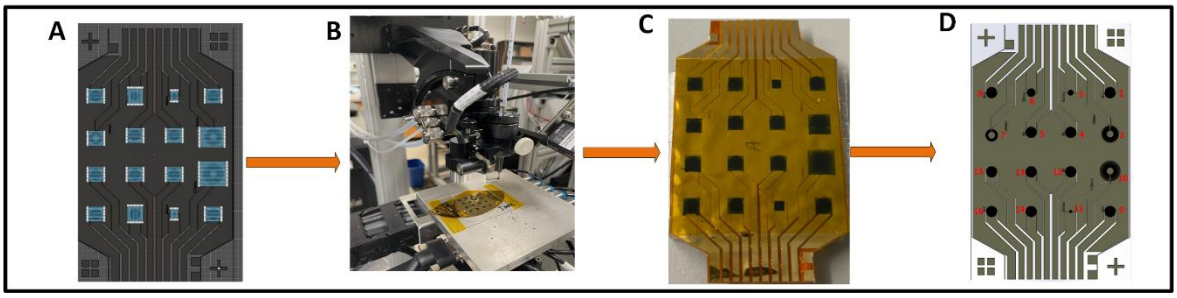

Figure 20 Figure 20 Illustration of the aerosol jet printing process of PEDOT: PSS unto a robot skin sensor. (A) shows Autodesk Fusion 360 interface for generating the G-code for the PEDOT: PSS deposition. (B) shows the Aerosol Inkjet printer used to deposit the organic polymer. (C) shows the PEDOT: PSS printed on the skin sensors. (D) shows the geometries of the different sensors numbered in order of their connections

3.2.2.3 Optomec Aerosol Jet Printing System

The OPTOMEC® Aerosol Inkjet print system is part of a custom-built NeXus micromanufacturing platform consisting of the following components: An Aerosol printer head equipped with a 300µm diameter nozzle, a process control cabinet, KEWA process control software, a 6DOF positioner for carrying sample and height adjustment and a NI LabVIEW® interface for synchronizing ink deposition process and motion control of the stages. The aerosol jet printing process works using aerodynamic principles to realize PEDOT: PSS ink deposition on the substrate. The ink placed into the ultrasonic atomizer is formed into a dense mist of aerosol droplets that are carried along the deposition path and focused with compressed nitrogen gas through the nozzle tip. The viscosity of the ink and the process recipe determining the atomizer flow rate, and morphology of the deposited PEDOT: PSS ink on the substrate are important criteria for achieving successful printing of the skin sensors. Figure 18A shows the printed lines at 100µm based on the inputted process recipe in Table 3-2. Figure 18B, shows the Dektak profilometer measurement of PEDOT: PSS indicating the thickness of about 100nm of the deposited ink.

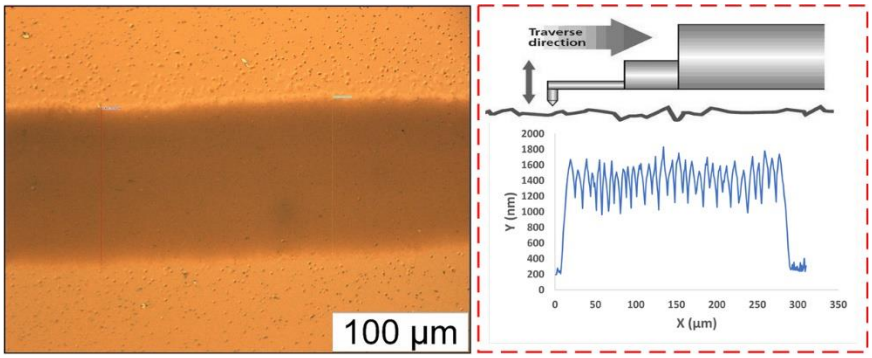

Figure 21 shows the width of the line is 60 microns. (B) illustrates profilometry measurement of the PEDOT: PSS film composed of ten layers which thickness is around 1.4 µm.

Table 5: Parameters for Printing for PEDOT:PSS Ink

Sheath Flow Rate	*50 sccm*	Print Speed	*10mm/s*
Atomizer Flow Rate	*20 sccm*	Atomizer Bath Temperature	*27℃*
Atomizer Current	*500mA*	Stand-off Distance	*3mm*

This Fabrication approach significantly reduced the time taken to manufacturing a complete skin sensor patch as shown in the pie chart description in Fig. 19.

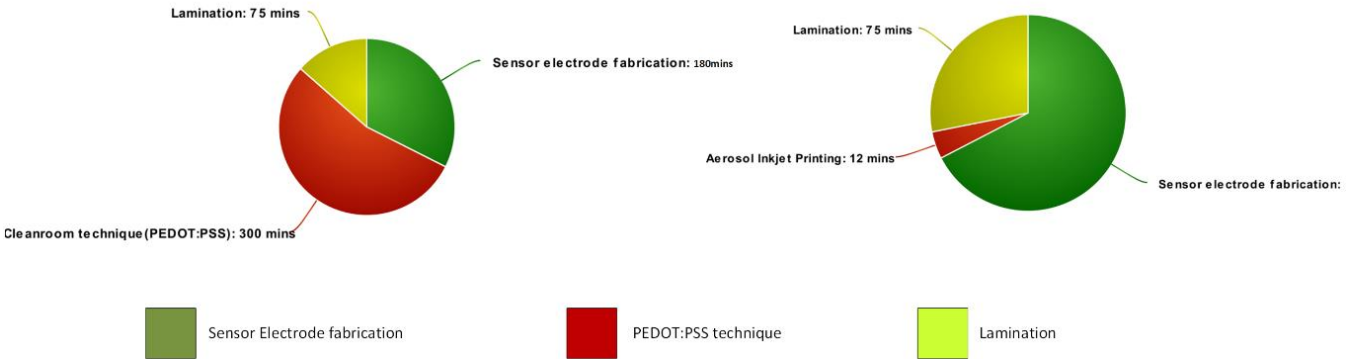

Figure 22 Cleanroom and NeXus fabrication technique comparison

3.3 Lamination of Skin Sensor Arrays

A functional fabricated robot skin sensor patch is a paired double-sided piece having two completely fabricated and laminated skin sensor patches. Each sensor patch is laminated with Kapton tape to ensure the ease of handling, preventing the breakage of the gold electrode links and wearing off of the PEDOT:PSS, also to seal the sensor area from exposure to atmospheric moisture. In this process, the two completely fabricated sensor patches are paired and aligned back-to-back with the sensor area facing outward. The reason for the double-sided attachment of the sensor patches is to compensate for temperature drift of sensors. Crucially, the lamination maintains a tight grip of the sensor patches within the circuit board connectors, allowing stable and steady feedback response

The process of lamination is described in detail below:

1. The circular Kapton sheet containing three fabricated sensor patches is cut to detach the three sensor patches to begin the process as shown in Fig. 20.
2. The samples are carefully handled and put using adhesive tape on a level table. Next, a broader piece of Kapton® tape is used to uniformly protect the samples. The electrode regions are shielded and both tapes are trimmed to size.
3. Two sensor arrays whose resistance values are most closely matched are chosen to form a lamination pair based on the measured resistance of the tactile sensors. Next, lay one of the two sensors—whose backs are facing up—onto the flat substrate. In order to form double layers on either side of the electrode connectors, another thin piece of Kapton® tape is applied. Lastly, we cut the excess tape away from the sensor array outline using a razor blade. Double layers of thin Kapton® tape are used to increase the electrode thickness of the double-side sensor array in order to

meet the ZIF connector space since the connection space of a zero-insertion-force (ZIF) connector is bigger than the width of two sensor array substrates laminated together.

4. After cleaning a pair of sensor arrays with acetone and IPA, the arrays were aligned back-to-back using the alignment markers positioned at the intersections of each sensor array. We clamped one side of the pair with a clip.
5. The double-layer sensor array is positioned on the flat substrate, and the pairs are separated by placing wiping paper in the middle of them. Next, we evenly sprayed 3M® contact glue between each pair.
6. After removing the wiping paper and closing the pair, the brayer was used to make a double-sided structure. Then, the clip was taken off and another wiping paper was placed on top of the laminated sensor arrays.
7. To cure the glue, a laminated double-layer sensor array is sandwiched between two flat substrates, topped with a hefty metal block, and placed in a normal oven set at 75°C and vacuum for ten minutes.
8. The laminated sensor array is then finally removed, and its outline is cut to make its edge flat with the bottom so that two ZIF connectors may be inserted. At this point, the components are prepared to connect to our conditioning electrical circuit[13].

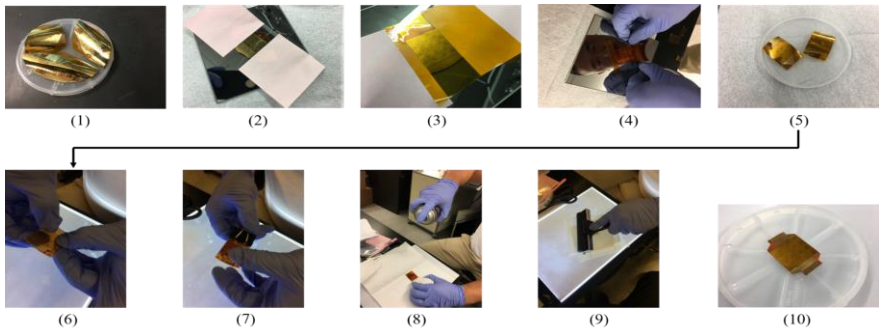

Figure 23 Lamination process for double-layer skin sensor array

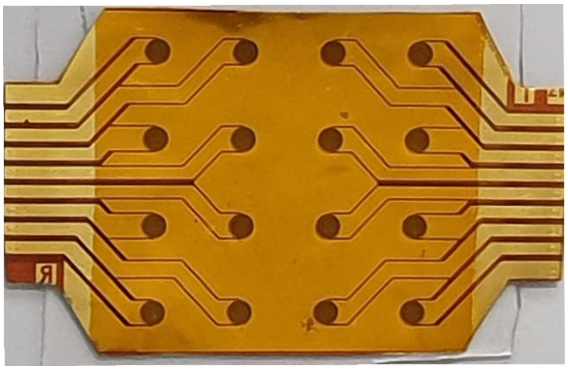

Figure 24 Laminated Circular tree Skin Sensor Array

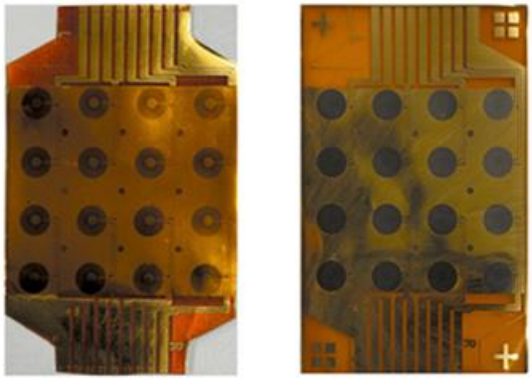

Figure 25 Laminated and Unlaminated Star-shaped Skin sensor array

3.4 Packaging and Encapsulation Interconnection of Sensors

Following the processes of manufacture and lamination, encapsulating the robot skin sensors is an essential part of packing the sensor patches to ensure the best possible

feedback during testing. The encapsulation consists of an extruded cover that is precisely fitted over the skin sensor patches in accordance with the sensor geometries, and a cavity that is intended to be positioned beneath the patches. The beddings and covers are made from silicone rubber with a molding process. SYLGARD ™ 184 Silicone Elastomer from Dow Inc. is selected due to its desired properties [citation], such as transparent finish to achieve better sensor to silicone alignment, long working time, controllable viscosity, elevated curing temperature, user-friendly stiffness, and good dielectric property.

Two-part molds are 3D printed to fabricate the silicone parts. After printing, the molds must be filed to remove as much surface irregularities as possible to achieve a smooth surface finish of the silicone, and to seal the gap between the molds. The elastomer base and curing agent are mixed by 10 to 1 ratio by volume in a mixing cup and stirred vigorously by a plastic coffee stir for as long as 10 minutes to achieve even mixing. The compound is then degassed in a vacuum chamber until no more bubbles merges from the liquid. The molds are treated with mold release agent (brand, model), then assembled and clamped while the silicone is degassing. A fresh syringe is used to transfer the mixture carefully and slowly into the mold through the opening at the top, to avoid bubble formation within. The complete sets are placed in a preheated scientific oven under 120°C for overnight to cure. This test-bedding prevents the slipping of the sensor patches from the circuit connectors and helps isolate responses of the individual sensors on the patch,

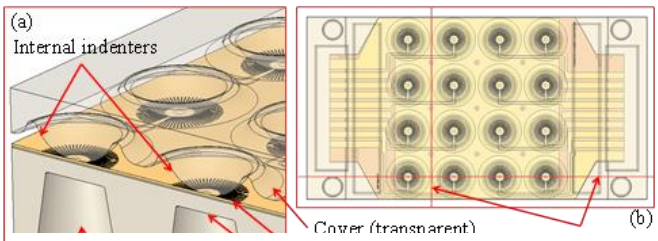

Figure 26 Cross section view of the sensor bedding and cover

confining the deformation of the sensor within the boundaries of its corresponding cavity. Hence, preventing the crosstalk with other neighboring sensors, thereby improving the overall skin sensor patch sensitivity.

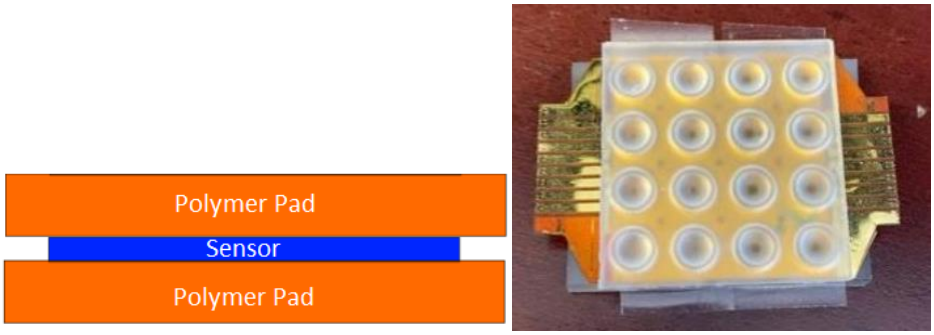

(a) (b)

Figure 27 (a) Sensor encasing (b) An example of encasing

Since each sensing element on the Skin sensor patch is a strain gauge sensor and they measure strain instead of contact force, thus a soft bedding needs to be placed underneath each sensing element. However, if a flat bedding is used, then strain response becomes indenter geometry dependent when same force been applied at the center of a tactile, if we are using a rigid spherical indenter. When applying pressure with finger, the fingertip flattens when it is in contact with the sensor patch. It pushes the entire sensor tactile down rather than strain it, hence the sensor may fail to recover the input force. Both effects would deteriorate detection spatial and force resolution of Skin sensor.

To clearly define the spatial and force resolution, we added cavities and spherical indenters into the rubber encapsulation. The cone-shaped cavity is a structural weak point under each tactile in the bedding, which provides space for the tactile to deform and strain when force is applied. The Skin sensor needs to be protected from physical damages with a soft cover on top of it, which allows us to integrate a spherical indenter in it to further “focus” the

tactile experiences. Thus, the sensor patch is sandwiched between the bedding and the cover, shown in Fig. 3-22a. The spherical indenter and the cone-shape cavity together improve force to strain transduction, thus improves sensing repeatability.

In this way, the entire sensor patch behaves like an array of FSRs. The cavity, sensor tactile, and the indenter can be seen and referred to as a "sensor unit". The size of each sensor unit, the distance between them, and the quantity determine the spatial resolution of a sensor patch. This design allows the sensor tactile to strain in a similar way regardless of the input shape, given the sensor patch closely adheres to the bedding. Fig. 3-23(a) illustrates a cross-section view of the bedding-sensor-cover unit. In this diagram, the cone's top and bottom diameters measure as 3.16 and 4.15 millimeters, and 3.8 mm tall. The diaphragm under the sensor tactile is 0.7 mm thick and the sensor tactile are 7 mm away from each other. On the cover, each indenter sits in a 0.75 mm deep and 5 mm diameter recess. Each indenter measures 4 mm in diameter from bottom and 1.25 mm tall. A circular fillet with 2 mm radius is applied at the edge of each indenter to create the spherical surface. The physical representation of the encapsulation and bedding is shown in Fig. 3-23b

3.5 Electronic Interface for Skin Sensor Array

An experimental testbench was designed to test the individual sensors on each patch at a variety of force loads using a plunger and load cell for measurement. Sensor response is measured using an ADC board then sent to a host PC that logs the current response value in a visualizer, for active test data reading, and a CSV file for post-processing.

3.5.1 Hardware Components

Hardware used in the test bench consists of the following: National Instruments Compact RIO (cRIO) model 9074, National Instruments 9205 Analog Input Module, National Instruments 9516 Motor Drive Interface Module, Transducer Techniques MLP-25 Load Cell, Transducer Techniques TMO-1 Load Cell Signal Conditioner, Newport M-UTM150CC1HL mid-range travel translation stage. The testbench system was controlled by the cRIO-9074 Real-Time controller with the 9205 and 9516 peripherals used in general-purpose I/O ports. Each 9516 was connected to a Newport travel stage to allow linear motion in a single direction. The first stage was aligned vertically, with the plunger and load cell fastened as shown in Fig. 3-24, a picture of the hardware setup.

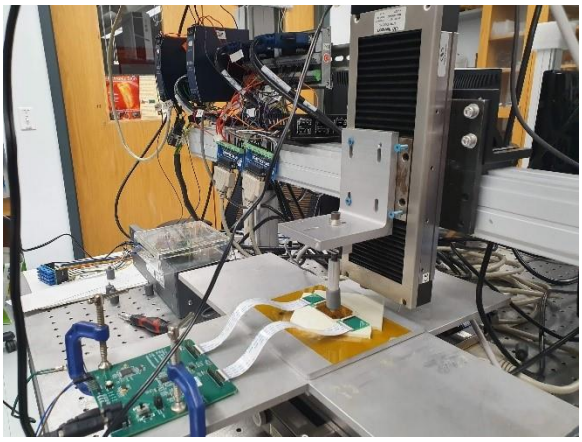

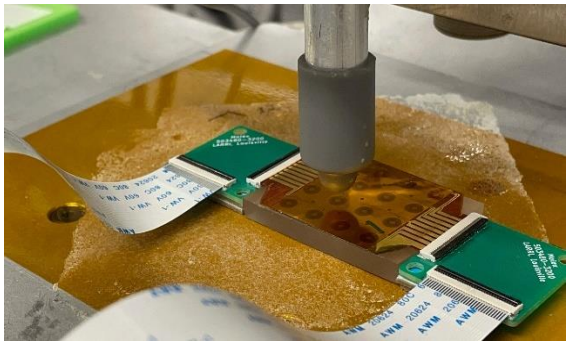

Figure 28 (a) Hardware setup of experimental Testbench (b) closer view of skin sensor testing

This allowed for force testing by controlling the motor positioning based on a feedback loop from the load cell. The other two stages were set up to emulate an XY coordinate space to allow the sensor to move to separate testing positions. The load cell reading was sent to the TMO-1 signal conditioning board before being sampled by the 9205-voltage input module. Once sampled, the reading is converted to the needed units in software. To ensure precise automated coordination of individual sensors during testing the Edmund Optics EO-1312C 1/1.8" CMOS Color USB Camera is selected to profiling sensors using computer vision as shown in Fig. 3-25 below. LabVIEW imaging processing techniques are employed to extract pixels from the mounted camera converting the pixels to coordinates for the precise movements of the motorized XYZ stage to measurable distance between the force actuator and the skin sensors. Figure 3-26 shows the testbench system data flow including the camera connected to LabVIEW 2014 via a micro-USB.The location of the camera placement is very important. The camera must be able to obtain the necessary information without interfering with any of the linear steps. The testbench table cannot accommodate a mount since the X and Y linear stages occupy the majority of the space. The same metal bar that the linear Z stage is fixed on also supports the mounting of the

camera. The camera system is secured in place by mounting on the metal bar. Straight down above the beginning location of the X linear stage, the camera records the scene. In order to bring the sensor starting point below the field of view of the camera, the Y linear stage is then moved back 100mm. Figure 3-27 shows the camera mount setup.

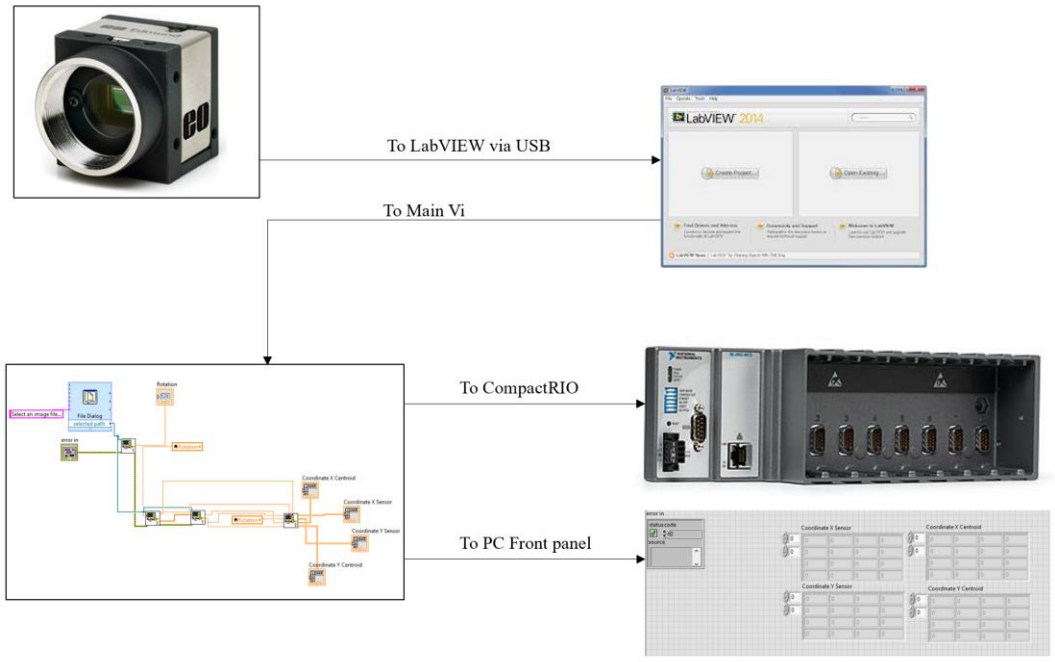

Figure 30 Data flow between Camera and Real-Time controller including LabVIEW[51]

Figure 29 Edmund Optics EO-1312C 1/1.8" CMOS Camera

Figure 31 A) Camera connected to mount B) Sensor underneath camera[51]

3.5.2 Software Components

LabVIEW program based on real-time was developed and deployed into the cRIO device. An automated system was designed to allow for consistency between tests run and repeatability for the test engineer. Software on the cRIO includes position control for the XY motor system coordinates. XY Coordinates were preprogrammed into the LabVIEW suite. This required a manual sensor lineup before each test could be performed. Coordinates were automatically moved through as each sensor was tested to provide a quick testing solution.

A control feedback loop was designed for Z motor positioning to take inactive force feedback from the test. The force is calculated using the following conversion.

(3-1)

$$F = -40 * V$$

Where -40 is the conversion factor in N/V. The control loop consists of a digital Proportional Derivative (PD) controller. A PD controller is a control loop feedback system that continuously calculates an error signal between the desired point and the measured point then adjusts the output with a corrected value to drive that error value to 0. LabVIEW discrete PD controllers can be mathematically modeled using the following equations.

$$e(k) = SP(k) - PV(k) \quad (3\text{-}2)$$

Where e(k) is the error signal, SP(k) is the desired setpoint, PV(k) is the measured value, k is the index of sampled time k*t. The setpoint and measured value are both set in newtons.

$$u(k) = u_p(k) + u_d(k) \quad (3\text{-}3)$$

$$u_p(k) = K_c * e(k) \quad (3\text{-}4)$$

$$u_d(k) = -K_c * \frac{T_d}{\Delta t}(PV(k) - PV(k-1)) \quad (3\text{-}6)$$

Where u(k) represents the controller output, u_d(k) represents the derivative term, u_p(k) represents the proportional term, K_c is the controller gain, T_d is the derivative time, and Δt is the change in time. For this test, K_c is set to equal 10 while T_d is set to equal 0.002. This primarily makes the error signal proportional dependent due to the gain magnitude difference but still considers the derivative term. Tuning the gains of the PD controller is out of this paper's scope.

The controller output is used to control the Z-axis motor positioning to change the measured value of the load cell before the control loop makes new adjustments to the Z-

axis positioning. This allows us to run dynamic load tests such as sine and triangle waves as well as static tests.

The PD controller is used sequentially for two testing portions. The first portion is to set the load cell to read a given force offset. The second portion is used for changing the motor positing compared to a mathematical function or holding the motor at the offset for a given period.

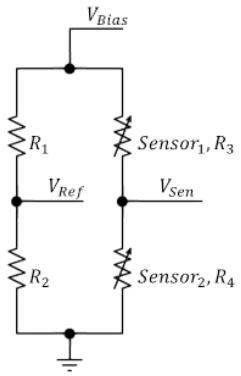

Figure 32 Sensor Skin Patch Measurement circuit

$$V'_{Sen} = V_{Bias} \cdot \frac{R + \Delta R}{2(R + \Delta R)} = \frac{1}{2} V_{Bias} \tag{3-7}$$

On each sensor sheet, the traces to each individual sensor are routed in a symmetrical way according to Y-axis, so that when two sheets are assembled back-to-back, the individual sensors and their associated pins and traces are aligned. However, this arrangement does not apply to the common pins, which only appear at top left and bottom right corners when observed in the direction shown in Fig. 29. For example, when the sheet is flipped according to the y axis, pin 1 and pin 2 and the sensor tactile they connected will be aligned. In this unique design, all sensor sheets can be fabricated in the same way yet

properly assembled. When interfacing with external circuitry, two FFC/FPC connectors from Molex® are used (part number: 5034803200). Their special locking mechanism clamps the sensor contacts like a claw, where connects top and bottom individual sensors.

Such arrangement creates a voltage divider circuit configuration on each sensing tactile where the common pins provide power and ground to the 16 pairs of voltage dividers in between. The rest of the sensor pins tap to the middle point of each voltage divider and fed into the ADC. The common plain is purposely made large to reduce undesired resistance on the trace. The gold electrodes are inspired by and modified from interdigitated finger pattern. Instead of parallel lines in a standard configuration, we twisted the lines into a star-shape. The advantage of such arrangement is it can sense strain evenly, regardless the location of indentation. This configuration resists temperature drift as well. Fig. 3-20 shows circle diagram of a sensor tactile, and it can be seen as a half-bridge circuit. R_1 and R_2 set reference voltage, R_3 and R_4 are the active sensors. Assume $R_3 = R_4 = R$ initially, and the temperature induced resistance drift ΔR can be cancelled, if both R_3 and R_4 experience similar temperature change.

$$\left|V_{Sen} - V_{Ref}\right| = V_{Bias} \cdot \left|\frac{R_4}{R_3 + R_4} - \frac{R_2}{R_1 + R_2}\right| \tag{3-7}$$

$$\Delta R = R_G \cdot k \cdot \varepsilon \tag{3-8}$$

k is gauge factor of the sensor in (3-9). Equations (3-10) and (3-11) indicate strain ε induced V_{Sen} change with quarter- and half-bridge configurations, respectively.

$$\left|V_{Sen} - V_{Ref}\right| = V_{Bias} \cdot \left|\frac{k \cdot \varepsilon}{4} \cdot \frac{1}{1 + k + \frac{\varepsilon}{2}}\right| \tag{3-10}$$

(3-9)

(3-11)

$$\left|V_{Sen} - V_{Ref}\right| = V_{Bias} \cdot \left|\frac{k \cdot \varepsilon}{2}\right|$$

In our setup, V_{ref}, V_{Bias} are generated from voltage reference and buffered. k is the gauge factor of the sensor. The left-hand-side of (3-11) is amplified by an instrument amplifier and digitized with an analog to digital converter (ADC).

3.6 Tactile Strain Gauge Fabrication

In this work, we investigated tactile sensor designs compatible with direct write ink jetting process of aerosol jet print. The parametric study of the tactile sensor performance is understudied using finite element analysis (FEA) to determine the influence of package geometry based on the sizes of the cavity design and indenter dimple size of the top cover. The design optimization results from the finite element analysis (FEA) in the realization of the fabricated tactile sensor carried in the NeXus using the aerosol inkjet printing and the molding of the soft silicone bedding for the encapsulation used for test purposes. Curing procedures using oven and Intense Pulse Light (IPL) at different parameter were crucial to determining the resistance value and sensitivity of the tactile sensors.

3.6.1 Tactile sensor design

The tactile sensor design presented in this study operates as a strain gauge. This implies that the strain or deformation induced directly on the fabricated structure based on the applied stress or force across its cross-sectional area results in the variation of electrical resistance.

Proposed in this study are two major components, a tactile strain gauge sensor with a circular star-shaped pattern of 10mm diameter, inspired by the conventional serpentine strain gauge sensor. The second component is the polydimethysiloxane (PDMS) unto which the tactile sensor is encapsulated in between a molded PDMS cavity and a cover bedding with dimple. It is important to note that the conducting structure of the tactile sensor is printed with the help OPTOMEC® Aerosol Jet printer. The circular pattern of the present tactile sensor design is shown in Fig 3-29(a). It avoids directional effect due to sensor topology of conventional serpentine structure in the x and y direction resulting in different resistance measurement along the x and y axes as described in. This makes the tactile sensor exhibit a similar level of sensitivity in all directions, with the PDMS bedding having a stiffness which can be engineered to fit a suitable design need providing a soft cushion for the easy deformation of the structure. The circular design pattern printed features conducting lines with 60-microns width, 3mm inner diameter, and 10mm outer diameter, respectively. Passing through the center of the circle connecting with the tangent segments is a long segment of the pattern. The long segment patterns paired is separated at a measured angle of 10° between them. With a total of 36 of such long segment patterns measured at 145.52mm, this increases the success rate for printing and suitable for the COMSOL® FEA analysis. This is with the understanding that the effectiveness for strain sensing is proportional to the lengths of the segments which are reported to be 87% of the total length[94]. The proposed design of the sensor encapsulation and bedding is illustrated in Figure 3-22(a).

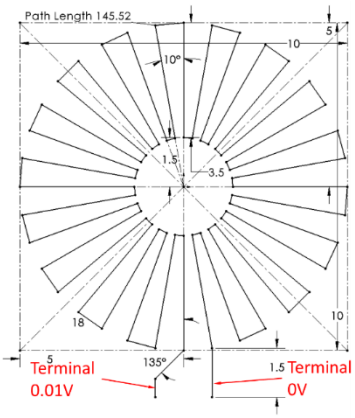

(a)

(b)

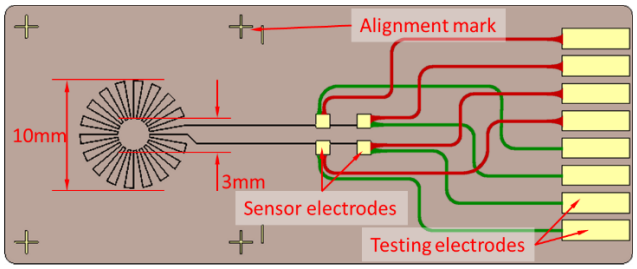

Figure 33 (a) Circular design pattern of the proposed tactile structure. (b) Illustration of a fabricated tactile sensor with a customized FPC substrate.

3.6.2 Fabrication and Printing Process

In this study, tactile sensor electrodes are made up of cured silver traces deposited on a customized FPC substrate using the aerosol inkjet printer. The silver ink used for this deposition is the NovaCentrix® silver ink which has a conductivity of 9.2× 10^5 S·m producing an average strain gauge resistance of 1.56kΩ. Derived below with Equation (1) using the total length of the tactile sensor measured at 180.39mm.

(3-12)

$$R = \frac{L}{\sigma \cdot W \cdot T}$$

From equation (1), W represents the width of the conductive silver line, T is the thickness of the deposited silver ink, σ is the conductivity of the silver ink, and L is the total length of the tactile structure. Fig.30(b). shows the proposed design of the star shaped pattern sensor structure on the flexible Kapton substrate.

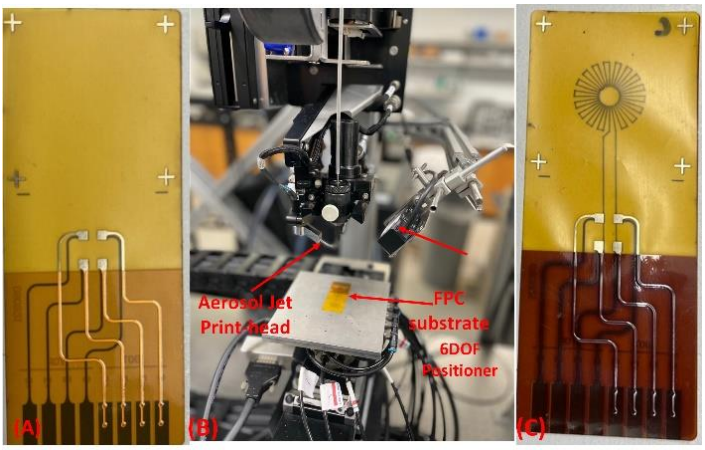

Figure 34 The fabrication process of tactile sensors with an FPC substrate. A) The customized FPC substrate. B) The OPTOMEC® Aerosol Inkjet printer system. C) Printed tactile sensors cured in an oven

The multiscale additive manufacturing platform known as the NeXus, a novel robotic system make host to a few sub-systems which includes the OPTOMEC® Aerosol inkjet print system, an inspection station, a 6 DOF positioner, a 3D FDM printing station, a PicoPulse® deposition station, intense pulse light (IPL) sintering station and industrial robot arms. The aerosol inkjet print sub system consists of KEWA process control software, a gas flow and atomization control system, and a 6 DOF positioner for aligning the substrate with the print head nozzle tip at a stand-off position of 3-5mm. The characterization of the NovaCentrix® JS-A426 silver ink has been conducted using the OPTOMEC® Aerosol inkjet print system and gauge factor is 1.85 closely matched to what

is obtainable commercially. Fig. 31 shows a blank Kapton substrate placed on the 6 DOF positioner in alignment with the OPTOMEC® print. Fig. 31(c) shows the characterized NovaCentrix® JS-A426 silver ink printed line at 60 microns width projected from a 300 microns diameter aerosol inkjet nozzle based on the process recipe shown in the Table below.

Table 6*:* Parameters for Aerosol Jet Printing

Sheath Flow Rate	***132sccm***	Print Speed	***10mm/s***
Atomizer Flow Rate	***18sccm***	Atomizer Bath Temperature	***27°C***
Atomizer Current	***400mA***	Stand-off Distance	***3mm***

3.6.2.1 Inkjet Trajectory for Tactile Sensor

The fabrication procedures adopted with the use of the OPTOMEC® Aerosol inkjet print system within the microfabrication Platform, NeXus allows for repeatability and increased yield of tactile sensors as reducing error prone cleanroom fabrication due to the complexity of the process. The aerosol inkjet subsystem within the NeXus adopts a process that requires the generation of path trajectory for the inkjet printing of the tactile sensor. The generated trajectory path is required to provide the substrate placed on the 6 DOF positioner the X and Y coordinates for the deposition of the silver ink streaming. This trajectory path precisely aligns the fixed nozzle print head of the OPTOMEC® Aerosol inkjet printer to blank substrate for the creation of the star shape tactile sensor pattern. The open-source computer aided-Manufacturing (CAM) tool required for the trajectory path

generation is called Inkscape. Inkscape has a G-code path generator extension, from which its vector-based graphics editor is translated. The star shaped tactile sensor design is uploaded into the Inkscape workspace and using the G-code extension tab the G-code file containing the trajectory path is feed into custom NI LabVIEW User Interface directing precise coordinates to Newport controller, which in turn commands XY motorized stages.

3.6.2.2 Sintering Process of the Tactile Sensor

After the deposition of the silver ink, there is a need to cure the printed ink, removing the solvent allowing for compactness of the silver nanoparticles. The curing process ensures the fusion of these particles, thereby increasing their conductivity. For the curing process, Xenon® Intense pulsed light (IPL) S-2210 device and a thermal scientific Lindberg vacuum oven was used. The IPL which delivers peak energies and frequencies within a controlled experiment can successfully sinister metallic ink at precise control variables which prevent damage to the substrate. Table 3-4 shows the process recipe used for the IPL curing process while Fig. 33(b) shows the tactile sensor thermally cured with IPL. For oven curing, the fabricated tactile sensor was placed in the oven for approximately 20 hours at 200°C. It is important to note that the duration of the thermal cure is dependent on the substrate. In this case, the substrate upon which the tactile sensor is fabricated is Kapton which is optimal for the intended purpose as regards the duration of the curing process within a specified number of cycles The tactile sensor is shown curing in the oven in Fig. 33. After oven drying, the substrate's color changes and turns darker as shown in Figure 33c, and we believe this is due to the prolonged curing schedule that altered the properties of the adhesive used to assemble the customized FPC.

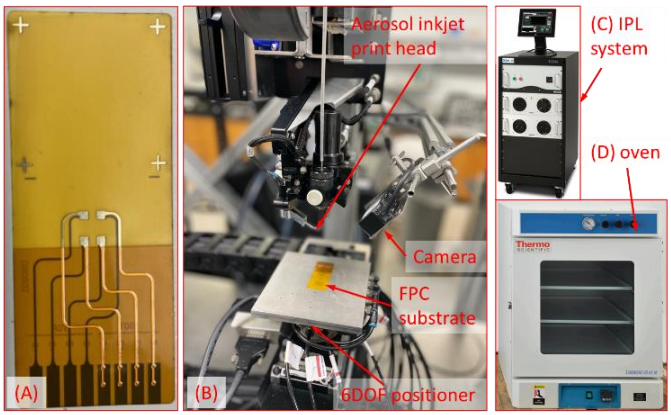

Figure 35 The fabrication process of tactile sensors with an FPC substrate. A) The customized FPC substrate. B) The OPTOMEC® Aerosol Inkjet printer system. C) The Xenon S-2210 IPL. (D) The Thermo Scientific Lindberg vacuum oven.

Table 7: Parameter for One IPL Curing Cycle

Duration (µs)	Delay(ms)	Pulses	Voltage (V)
100	*100*	50	*1500*
250	*100*	50	*1500*

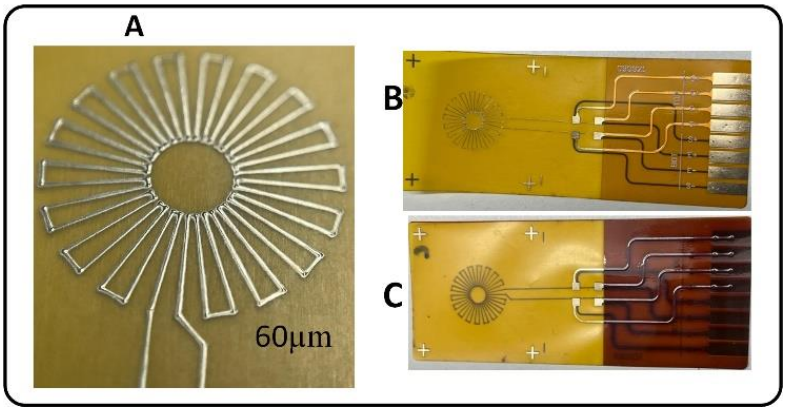

Figure 36 A) 60µm measured width of the silver printed lines. B) printed tactile sensors cured with IPL. C) printed tactile sensors cured in an oven

3.6.2.3 Tactile Sensor Encapsulation

Since strain rather than force is detected by the suggested tactile sensor, compliant bedding is required. We also incorporate a cover piece on top of the printed sensor to 1) shield the printed traces and 2) assist in concentrating strain by converting external force with an inbuilt dimple. The sensor will be tested on a piece of hard acrylic plastic that is 40 mm wide, 70 mm long, and 5 mm thick. The compliant surface, which has a thickness of 4.5mm, is created by pouring Sylgard® 184 Polydimethylsiloxane (PDMS) into a cylindrical cut-out that has been machined toward the detecting end as shown in Figure. 34a. The bedding has a diameter of 25.4 mm, which makes it big enough to cover the full sensor area and produce as even a deformation of the surface as feasible. The PDMS bedding is meticulously treated to ensure that its surface rests flat against the rest of the component. The testing electrodes land on the hard acrylic surface after the printed sensor sheet is directly placed on the testing bed with the circular sensor part visually aligned concentrically with the bedding. The sensor testing electrodes are fixed with spring-loaded testing pins so that the 4-point probe method can be used to measure resistance.

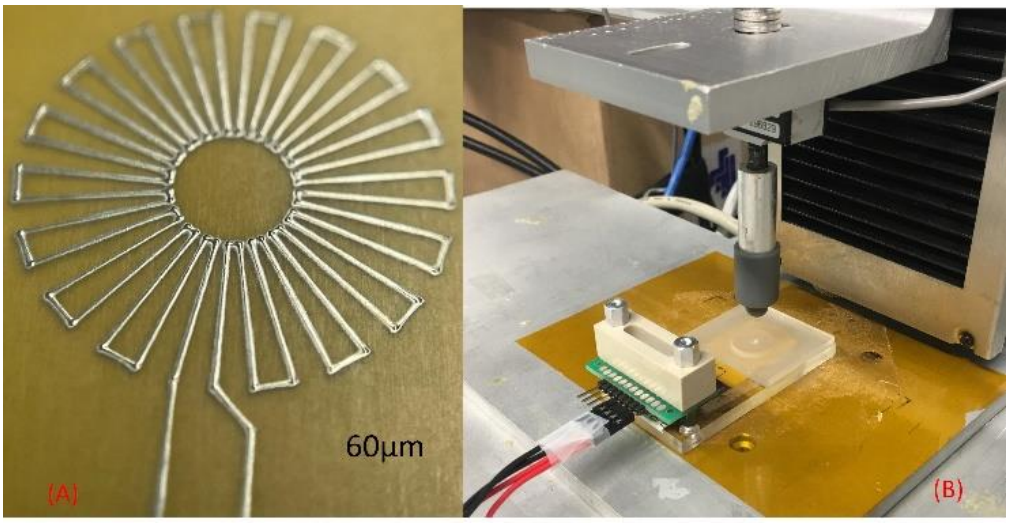

Figure 37 A) illustration of the tactile sensor setup with encapsulation. B) shows the experimental test setup

3.6.2.4 Experimental Test Setup

In order to compensate for intrinsic resistance across the testing probes and the testing pads, measurements are taken using an Agilent 34461A 6.5-digit multimeter with a 4-wire Kelvin connection to the printed sensor. To confirm that high contact resistance is not present, a 2-wire measurement is compared to the Kelvin measurement. The silver ink print to the copper contact on the FPC appears to be minimal, as evidenced by the observation of a difference of less than 2Ω between the two measurements. The sensor receives a continuous 1mA current from the meter, which was tuned to the 1kΩ range. The dissipation of power by a sensor varies between 60 and 400µW, depending on the resistance of each individual sensor. We don't observe any self-heating that would considerably affect the resistance reading. Fig. 27b shows an automated test bed for the generation of a force ladder profile as seen in chapter 4. Fig. 35(b) depicts the experimental test configuration. By mounting the acrylic plate fixture on a stand with a weighted rod that

is positioned directly above the sensor pattern, force is delivered to the sensor. The rod is stable and free to move, which is due to a plastic guide. In order to exert force in a controlled manner, standard weights are attached to the weight loader, and the sensor resistance is recorded.

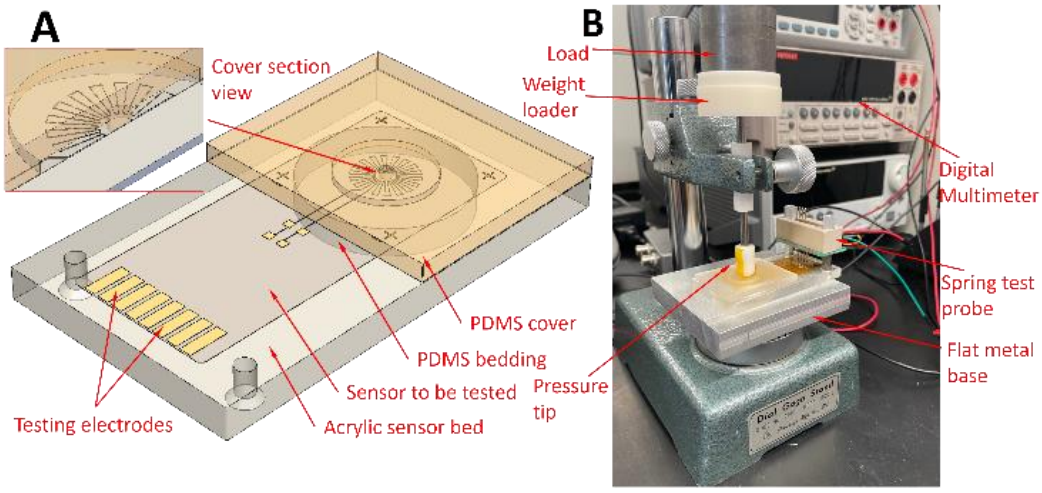

Figure 38 A) illustration of an encapsulated tactile sensor setup . B) shows the experimental test setup.

CHAPTER 4

ROBOT SKIN SENSOR DESIGN AND EVALUATION

In this chapter we described the testing approach used to evaluate robot skin sensors performance fabricated using the varying cleanroom techniques, and the NeXus. We investigated the sensitivities of tactile sensors solely fabricated using the NeXus and determined the dynamic relationship between input force load profile to the tactile system and the output sensor response. The force load profile applied on the test bench is between 0.5N – 2N, as this is the effective range of testing under which the creep nature of the Kapton sheet is still compliant. This section starts with the description of the testing methodology.

4.1 Testing Methodology

The objective of the testing station is to allow the user to choose within the software interface a testing profile and ensure its completion without interference. The option within the system allows the user to evaluate the performance of the tactile sensors through automated repetitive tests or rerun. Automated testing of samples is made possible through the motorized stage and computer vision, allowing for precise movements between each sensor cell and the testing plunger. This precise movement with incremental force control at a specific distance of velocity is coordinated by the LabVIEW Soft motion. Time stamp matching proves necessary as a different script file in python is used to collate the response

data from the system prevent lag between the actual time reading and that produced from the cRIO. Figure 39 depict the block diagram representing the testing methodology implemented.

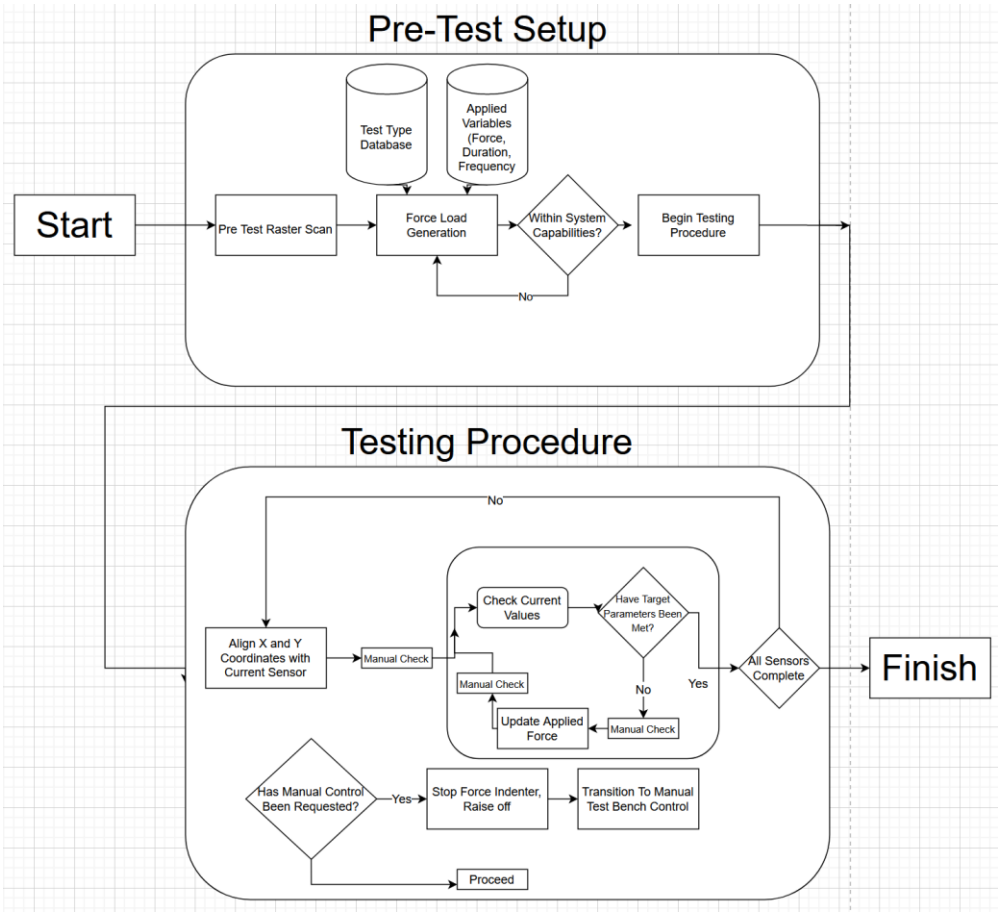

Figure 39. Block Diagram of the testing methodology[51]

Section 3.5 in chapter 3 describes the hardware and software components of the of the testing station. We made use of the LabVIEW software and the compactRIO (cRIO) real-time FPGA hardware from National Instruments. LabVIEW can be used to program the deterministic, reconfigurable hardware known as cRIO. It has eight swappable device slots and a 400MHz processor as shown in Figure 40.

Figure 40 NI cRIO-9074 [61]

With cRIO, two modules were utilized. NI9516, a servo motor controller with dual encoder feedback and position and torque control, and NI9201, an analog-to-digital converter with 32 single ended input channels, 12-bit resolution, and a range of 0V to 5V [62]. Our sensor and a load cell were used as sensors, and an ADC module was used to capture their data. A servo module was used to operate a Newport actuator, which applied pressure to our sensor. Figure 41 below shows the visual interface for the automated test profile used to carry out the test analysis of the robot skin sensors.

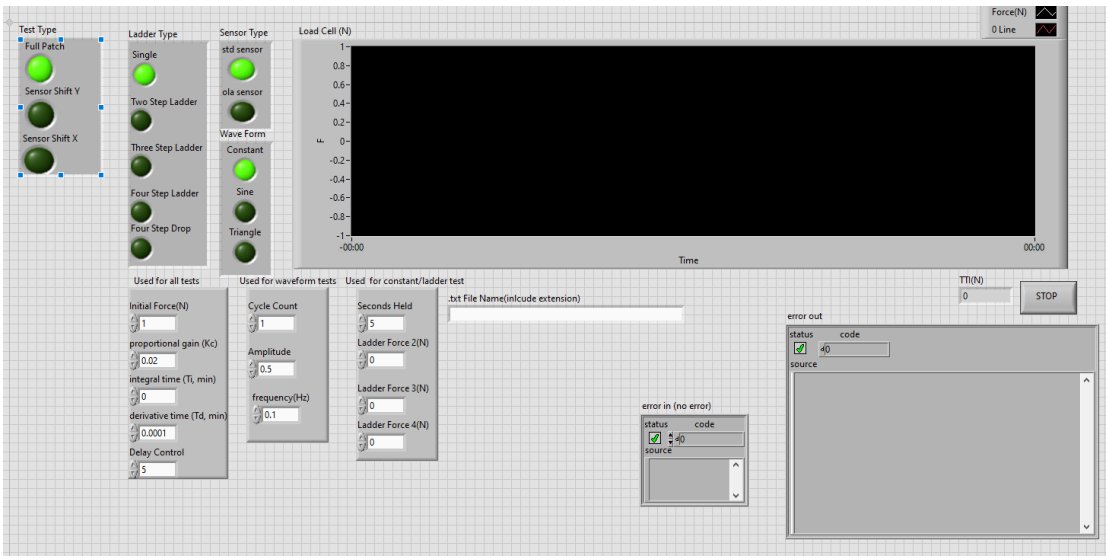

Figure 41 Automated Test setup Front Panel

4.2 Skin Sensors Test Analysis

Several tactile sensors have been developed in batches to investigate the sensitivities of different patterned geometries of each tactile structure. The fabricated structures testing, and analysis is discussed in this section.

4.2.1 Finite Element Analysis (FEA)

In this section, simulations of the skin sensor's PEDOT:PSS material and PDMS encapsulant are presented. The simulation software used for the finite element analysis is the COMSOL Multiphysics. Figure 42 illustrates the appearance of the simulated materials on the system interface.

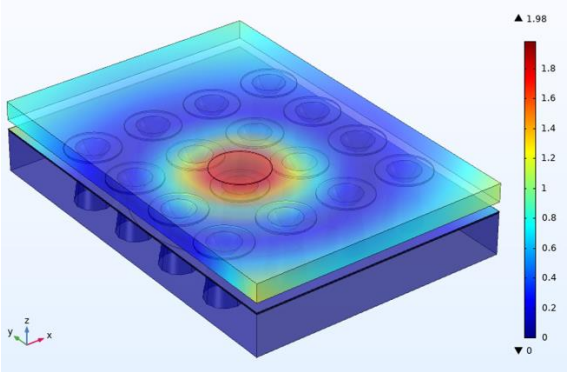

Figure 42 COMSOL simulation of input force on top of one sensor unit

4.2.1.1 Finite Element Analysis Setup

PEDOT: PSS is modeled using p-type silicon with empirical transverse and longitudinal piezoresistive coefficients of 4.6e-10 and -7.1e-10 (m2/N). The number density is between 5.5e15 to 8.86e15 (/cm3), they are implemented in COMSOL® for finite element analysis (FEA). Since gauge factor is independent of the sensor's thickness, to avoid high aspect ratio in the meshing that leads divergence and prolonged simulation time, 3 μm thickness of the PEDOT: PSS and gold electrode was used for the skin sensor simulation. The resistance value of the model was extrapolated to be 4 Ω at 150 nm of the PEDOT, compared to the measured average value of 30Ω. The discrepancies come from the uneven

thickness of the PEDOT: PSS and variation of the contact resistance between PEDOT: PSS and gold.

The bedding material involved is a type of Polydimethylsiloxane (PDMS), or commonly known as silicone with the commercial name Sylguard 184. The Young's modulus of the silicone is 2.2 MPa when cured at 125°C [34]. Also, importantly, our simulation includes the skin patch and its encapsulation that become the skin sensor package. The encapsulation includes a cover and a bedding that would provide complete conformance for the purpose of strain transfer from external force to the sensor patch. This encapsulation also serves as the interface between the sensor and human finger touch. The sensor would not be sensitive with human's finger size touch without the encapsulation which provides sensitivity compatible to that of a millimeter size indenter. The cover is equipped with discrete indenting bumps, which transfer and concentrate forces to the sensitive location of the tactile sensor. However, a flat bottom cylindrical bump is easy to slip in practice, instead, we used fileted bump and simulations show they are equally sensitive. The force applied on the encapsulation that sandwiches the sensor patch is show in Figure 42.

The bedding, on the other hand, was hollowed with cavities to provide location sensitive membrane that coincide with the sensor and the indenter above. The geometry of an individual sensor and the bump are arranged so it resembles a classic silicon pressure sensor, where the sensing elements center around the edge of the cavity. This way, the force was redistributed from the general area of the cover to the most sensitive area of the sensor to which the stress is applied, and maximum strain is induced.

4.2.1.2 FEA Simulation Results

The simulations yield three important insights for the integration of sensor and the encapsulation. The results include the effects of indentation sizes, the existence of cavities, and the back-to-back lamination of skin sensors.

The sensitivity depends on the size and location of the force contact point (indentation). Taking the center of a sensor tactile as the reference, the smaller the indentation size, the more sensitive the sensor.

First, the sensitivity increases as the indentation size decreases and peaks at the radius of 1mm. For example, there is an increase of sensitivity of 138% with the indentation radius at 1 mm from 1.5 mm. On the other hand, when the indentation size increases to 2 mm in radii, the sensitivity reduces to noise level, see Figure 43.

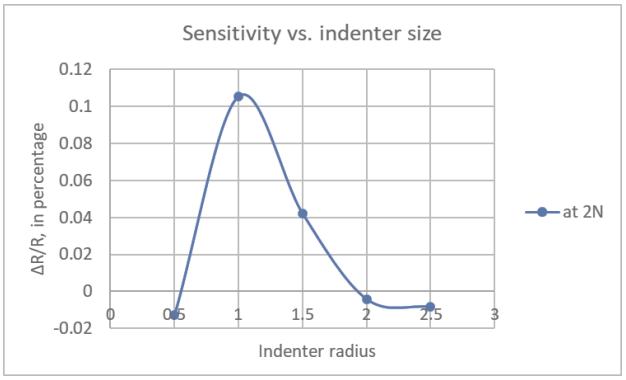

Figure 43 Indenter size and sensor tactile sensitivity with 2N input force

The resistance changes increase 33% with the sensor tactile on the top layer with a cavity in the bedding compared to without a cavity in the bedding. Meanwhile, the change increases 150% for the lower sensor sheet when the force is at 2N. The sensitivity for the upper layer and lower layer of the sensor sheet can be seen in Figure 44.

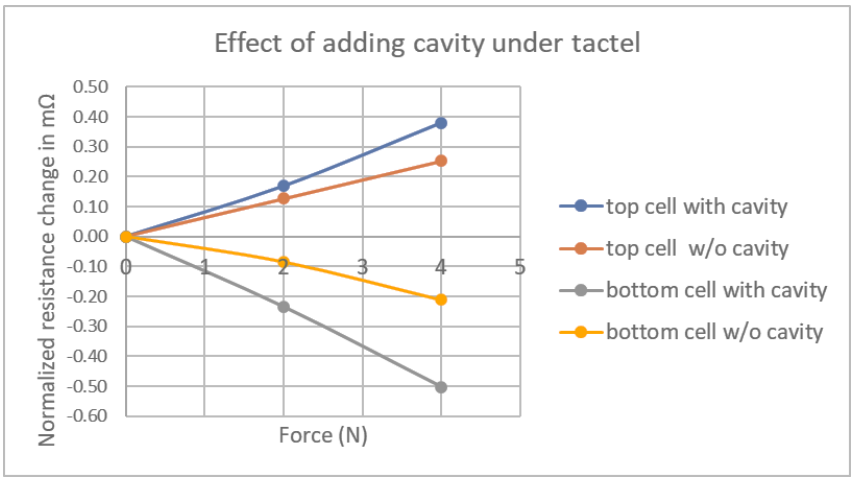

Figure 44 Comparison among sensor sheets with or without cavity

Sensor that is sensitive to temperature such as PEDOT:PSS [38], measurement in a constantly changing environment, especially strain sensing, temperature compensation is necessary. The two layers of laminated sensor are connected in series with the half bridge, our simulation shows that the collective resistance change in this configuration increases by 91% compared to one layer of sensor. Simulation results shown in Figure 45.

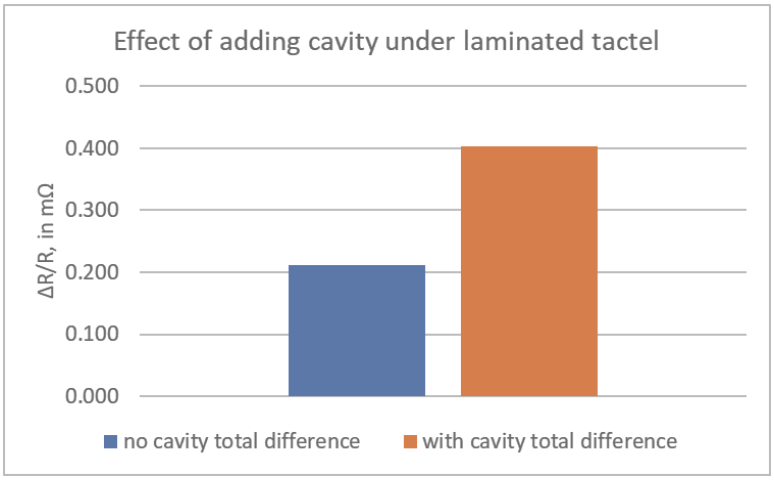

Figure 45 Sensitivity comparison between Sensor patches with and without cavities

The indenter size is optimized for the sensor design, however there are other factors that will affect the sensitivity of the sensor. In the simulation, the sensitivity increases as the

cavity radius either approaches to the outer diameter or the inner diameter of the sensor. In both cases, it is suggested that greater strain in the sensor were induced on the edge of the cavity. For optimization of the design, there are existing challenges in the simulations, several points of simulation encounter nonconverging and unstable issues, especially when the diameter of the top cavity approaches to the outer dimeter of the sensor and close to be zero diameter in cavity. The simulations show that the radius of the cavity in the bedding we used (1.5 mm) was not optimized of the design. Other considerations include the thickness of the membrane, the height of the cavity, the radius of the bottom cavity and the thickness of the cover and the bedding etc. The stiffness of the bedding and the cover can also be improved in the future. With all the material properties and the geometry variables considered it is beyond the scope of this work.

4.2.2 Star shaped Sensor Geometry

The star-shaped tactile sensor design is a 16 individual tactile sensor arrays arranged in a 4×4 format unto a sensor patch having PEDOT: PSS as its base sensing material. The diameter of each sensor is 3.65mm and the 16 sensors are arrayed in a grid with each sensor separated by 7mm spacing. The picture is shown in Figure 46 which also expands the outlook of a single beam in star-shaped structure. Electrical traces are 0.5mm apart and they are 1mm thick. Nine electrodes are interconnected from tactile sensors to both sides of the array. Eight electrodes are for signal lines, and one is for ground. The side electrodes will later be used for interconnection to the electronic circuit. Figure 46 shows a star-shaped design.

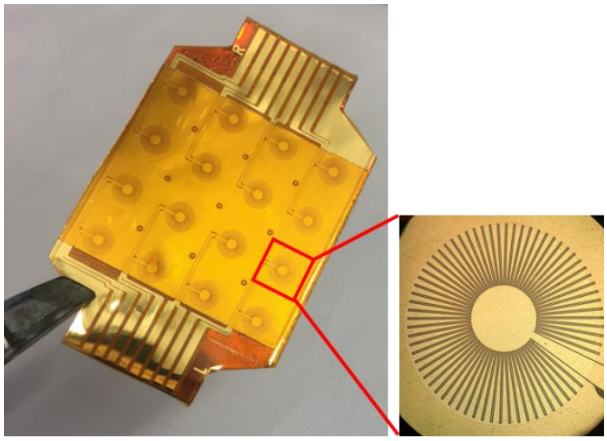

Figure 46 A Star-Shaped Patterned Structure patch

Before doing the lamination of the sensor arrays, each single sensor's resistance is measured and recorded. This step is to prepare for two sensor arrays selection to laminate a double-side (back-to-back) sensor array. The selection is based on the corresponding resistance of sensors which are closed. As a double-side sensor array, two single sensors which are back-to-back laminated together become a pair. For this situation, those pairs are 2-10, 1-9, ... , 7-15, and 8-16 after back-to-back lamination. Figure 47 shows the arrangement of the sensors and electrodes of the sensor array, and the resistance of each sensor is listed in Table 5. Two single sensors' resistance of each pair are close, which is significant for temperature compensation.

Table 8: Resistance Measurement of Two Sensor Arrays of a Pair Before Lamination

No. of sensor	Resistance (Ω)	No. of sensor	Resistance (Ω)
1	40.8	9	62.3
2	56.5	10	43.6
3	39.3	11	43.2
4	35.7	12	60.3
5	43.6	13	60.1
6	37.4	14	60.5
7	34.1	15	41.1

8	34.2	16	35.1
No. of sensor	Resistance (Ω)	No. of sensor	Resistance (Ω)
1	54.4	9	47.1
2	50.8	10	51.4
3	42.3	11	34.9
4	46.8	12	43.7
5	70.8	13	41.9
6	53.3	14	47.4
7	78.9	15	44.6
8	54.6	16	53.5

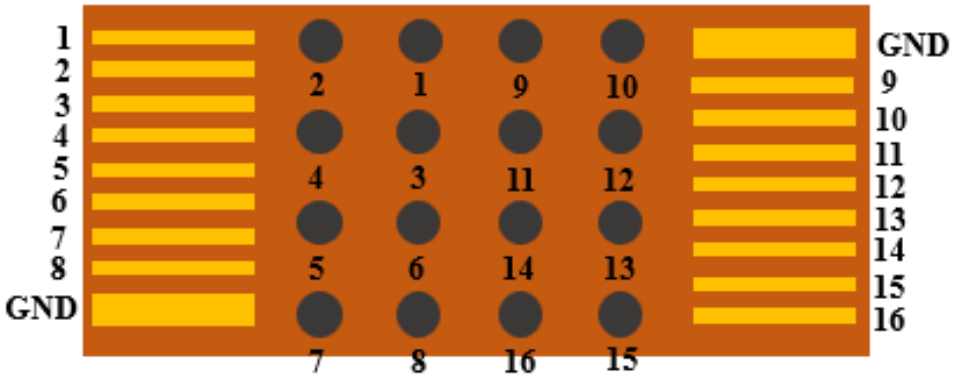

Figure 47 Sensors and Electrodes Arrangement of a Sensor Array

4.2.2.1 Star shaped sensor geometry

The sensor pair was placed on a soft Silicone substrate that deforms when subjected to pressure. When a load is applied on the sensor pair, the pair is squeezed by the pressure, the up-side sensor is compressed inwards, but bottom-side sensor is extended outwards. Strain is developed due to the bottom Silicon layer compliance, in addition to the double side lamination of the sensor.

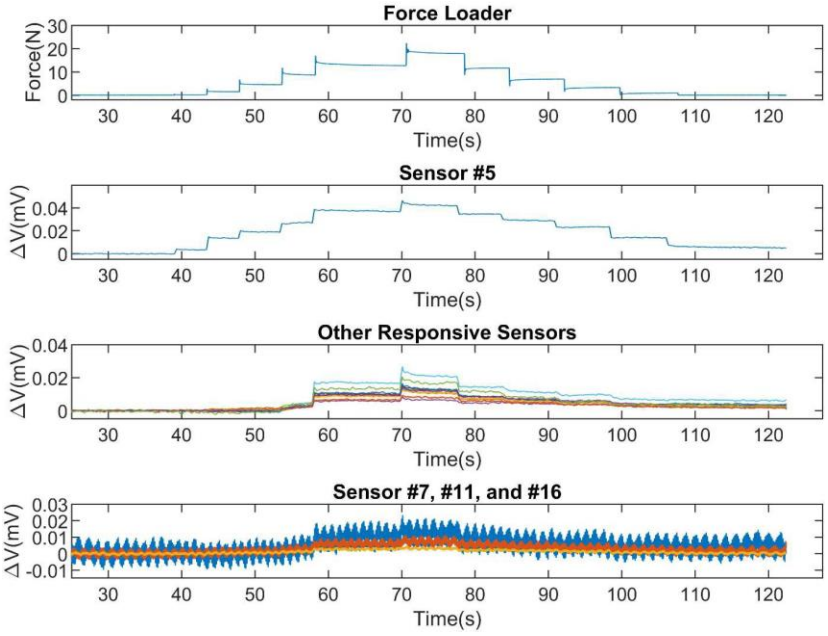

Figure 48 Performance of the star-shaped sensor pairs with variable load

Because of the piezoresistive material PEDOT:PSS between the star-shaped structures of sensor, the resistance of the two sensors of the pair is corresponding increasing (up-side) and decreasing (bottom-side) during the load applying. The ratio of resistance of the sensor pair is changed to make Vo variable, so that the ADC signals from data acquisition board are varied and visualized the performances of the sensor strain gauge. With the variable load (0N-17.5N-0N) applied on the No. 5 sensor pair, the strain gauge performance of the No. 5 sensor pair and surrounding sensor pairs are shown in Figure 48. When the load reaches around 1ON, other sensor pairs start to react with the load variation. Meanwhile, three sensor pairs, 7, 11, and 16 are less sensitive to the pressure of the load. This reduction of sensitivity may be due to the fact that lamination is still a manual process, thus prone to errors from the brayer and adhesive applicator.

4.2.2.2 Star shaped sensor geometry (Tactile calibration result)

Skin sensors are evaluated under a customized automatic testing bench for performance examination and individual sensitivity profile characterization. Details of the testing bench can be found in. We insert different set of static forces that perpendicular to each sensor tactile and traverse all units on the sensor patch. Readings of all tactile are collected and processed on a PC to calibrate sensitivity profile.

In order to interpret voltage measurements into force values comparable between tactile sensors, raw ADC voltage values from each tactile sensor must be calibrated individually. This calibration compensates for variations in manufacturing of the individual strain tactile sensors which may cause differences in resistance at rest and sensitivity to deformation. In the interest of rapid prototyping, we perform all calculations in software on the PC host, so the microcontroller transmits complete raw ADC readings of voltage over serial interface to the host without preprocessing. We wrote a high-speed multi-threaded serial communication tool for Linux in C that processes raw ADC readings for calibration and smoothing. Through a Python extension, the in-memory data structures are exposed to Python, which we use for simple visualizations of live data.

In the test, an encapsulated tactile sensor is attached onto the motorized X-Y stage for raster scan. An indenter with a force sensor is mounted to a motorized Z stage to apply force onto each tactile. The indenter is covered by a 3D printed spherical tip to protect the Skin sensors. Initial alignment is done visually, and the rest of indentations are done automatically according to the designed distance between each tactile. A close-up look of such setup can be seen from Figure 28 in chapter 3.

The calibration experiment sequentially presses each individual tactile while recording the force applied by the indenter onto the sensor and the stream of raw ADC voltage measurements from all tactile sensors. Temporal information of the force must be identified to compare with the collected sensor reading. Force baseline was established by leaving the system static for 30 seconds before engaging, then a threshold higher than baseline average is selected. A Python script is developed to automatically achieve the following: a rising or falling edge on the force reading is identified as indenter – sensor pressing or releasing phase respectively; the relative flat region at the top is identified as force holding phase and its average is taken to calibrate the sensor reading. Figure 49 (a) shows calibrated sensor reading and indenter's force feedback when aligned in the same plot, (b) shows hysteresis of sensor reading vs. indenter force from 0 to 1.5 Newton of the same sensor. The baseline "zero" value for a tactile is the average when the indenter is not pressing. The calibration profile for each Skin Cell tactile consists of three values: i.) a baseline value reading when the tactile sensor is "at rest" or not been pressed, ii.) an average "active" reading when the tactile is pressed, along with iii.) the force in newtons associated with this "active" state. We can see that as the tactile is pressed (blue), the sensor reading increases and remains steady in the hold region (red). As the indenter releases (cyan), the sensor value goes back down. The other gray plots in (b) show the behavior when other tactile were pressed, with adjacent tactile sensors being slightly more highlighted in black.

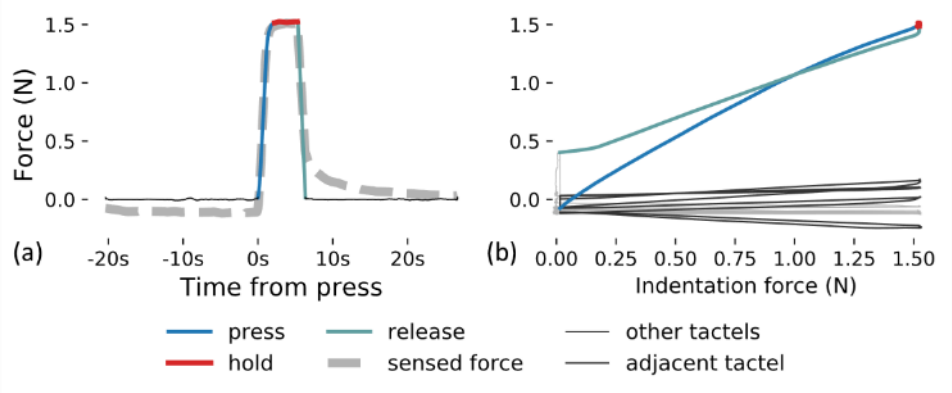

Figure 49 (a) Indenter response identification in 1.5N test for tactile sensor 4. The dashed line represents sensor reading, the solid line represents indenter force feedback. (b) Hysteresis plot for tactile sensor 4. In both, blue – rising edge, red – force holding, cyan – failing edge. In (b), black – adjacent sensor response, gray – response from all other sensors

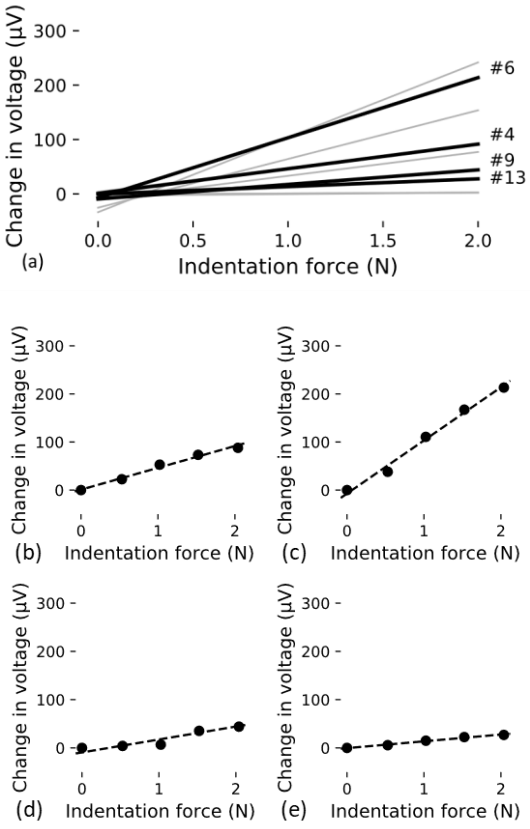

Figure 50 Sensitivity calibration profile for the tactile sensors. Sensitivity profile b) c) d) and e) represent graphs for tactile sensors 4,6,9 and 13 respectively

The two streams of data are synchronized by their timestamps. From this calibration profile, the host subtracts the baseline value (“zero” calibration) and linearly scales ADC readings based on sensitivity to force ("span" calibration). A linear relationship can be used to describe the calibration:

$$F(j) = a_j(v_j - b_j) \tag{4-1}$$

Predicted force F(j) can be calculated from ADC’s raw reading of v_j, with baseline adjustment b_j, and a linear coefficient a_j. For the moment, linear model is used since the current sensor works best at small forces. It can be expanded to a quadratic model by adding a quadratic term. The calibration findings for all sensors are shown in Figure 50, along with further analysis for sensors 4, 6, 9, and 13.

4.2.2.3 Skin Sensor spatial Resolution Evaluation

One of the design goals of using the silicone rubber encapsulation is to define the spatial resolution of the sensor as stated in Section II. B. Indentation offset experiment was conducted to evaluate such claim.

Under the same evaluation condition as Section V. A, we applied 1N force to the center of a tactel then shift the indentation 4 times by step size of 0.7mm. ±X and ±Y directions are all tested to evaluate the tactel response. The experiment results are shown in Figure 51. The first peak in each plot represents aligned indentation, and the second to the fifth represent the shifted responses. The first three indentations have very similar responses for all four directions. However, responses on +X and +Y have shown reduced readings on fourth and fifth peak, which are 2.1mm and 2.8mm away from the center, by 30% to 50%

reduction. The readings from the negative directions shown less reduction, by 30% maximum.

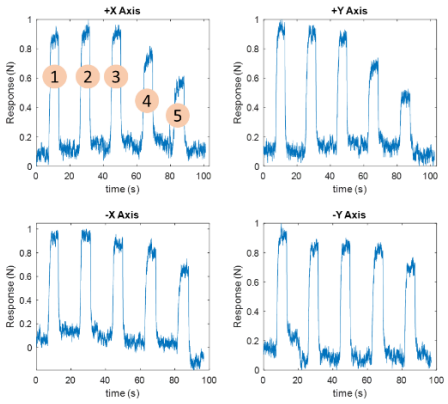

Figure 51 Results of a single skin sensor offset experiment under 1N force loading. The center of the tested tactile is where the initial peak is located.

A possible reason of the uneven attenuation is because of the indenter misalignment, which is visually aligned with the center of the tested tactile. However, this experiment indicates that each tactile sensor reading decreases as indentation force gets away from its geometric center. This effect may be used to improve spatial resolution of a tactile sensor.

4.2.3 Circular Tree Sensor Geometry

In this study, the tactile sensor design proposed is a circular tree structure that is fabricated in the cleanroom on a flexible polyimide substrate otherwise known as a Kapton Sheet. In comparison to traditional interdigitated or serpentine structured strain gauge sensor designs, the topology of the circular tree also known as unbalancing binary tree as depicted in Figure 52c is made to avoid directional effect of strain on the sensor. That is, under the same amount of strain applied, the interdigitated or serpentine sensor topology will produce different values of resistance when measured at x and y axes of the sensors. In our previous work, we proposed a star-shaped design to reduce the directional effect,

through simulation and experiment. The design proved effective but the constraint, microstructure patterning and spatial density efficiency proved hard to improve given the specific fabrication process. Hence, we introduced the circular tree design to improve on the spatial resolution of the star-shaped design, efficiently utilizing the space create with the center of the sensor geometry. Also upgrading the fabrication technique using Gold Etching as discussed in chapter 3 section 3.1.3 rather than a lift-off process to ensure the effective patterning of the structure. This topology which expands recursively in circular patterns forms the sensor. These robotic skin sensors patterned structure are strain gauges fabricated in the cleanroom on 50μm flexible Kapton substrate. Its principle of operation is based on the piezoresistive characteristics of the organic sensing polymer which is the PEDOT: PSS or poly(3,4-ethylenedioxythiophene) polystyrene sulfonate.

These strain gauges which comprises of 300nm micro-patterned structure of Gold is layered with an evenly spread of PEDOT of about 135nm, laminated with Kapton polymer to increase its durability and ease of handling. The overall thickness of the sensor, which is about 125 microns, combines the gold micro patterns and PEDOT: PSS to form a conductive pair that displays varying values of resistance when subjected to strain or deformation. This change in resistance and the measure of the sensitivity of the robotic skin patches is based on the piezoresistive nature of the organic polymer. The geometric design of the patterned structure in terms of length and width of the circular tree design is shown in Figure 52 below.

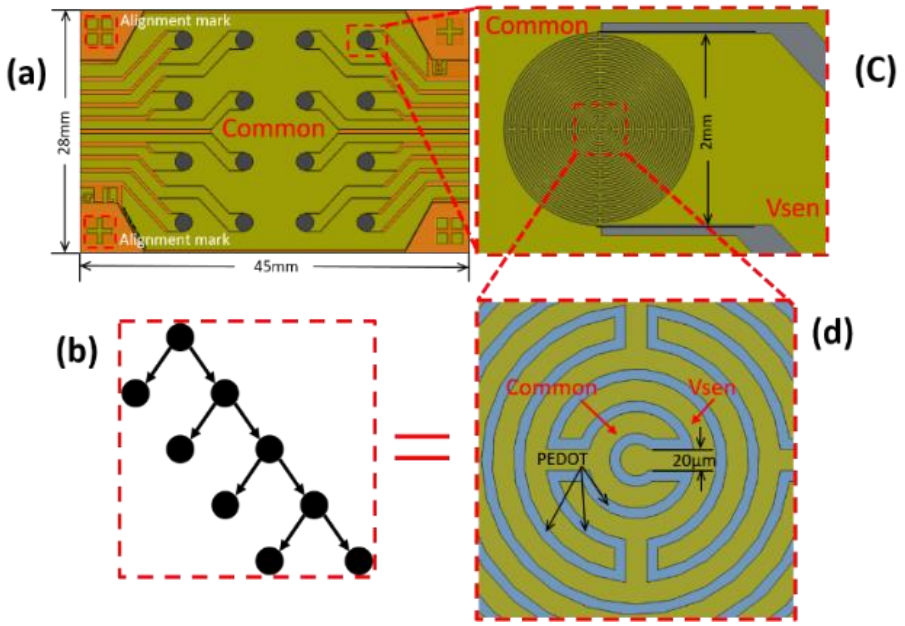

Figure 52 A Circular Tree Patterned Structure

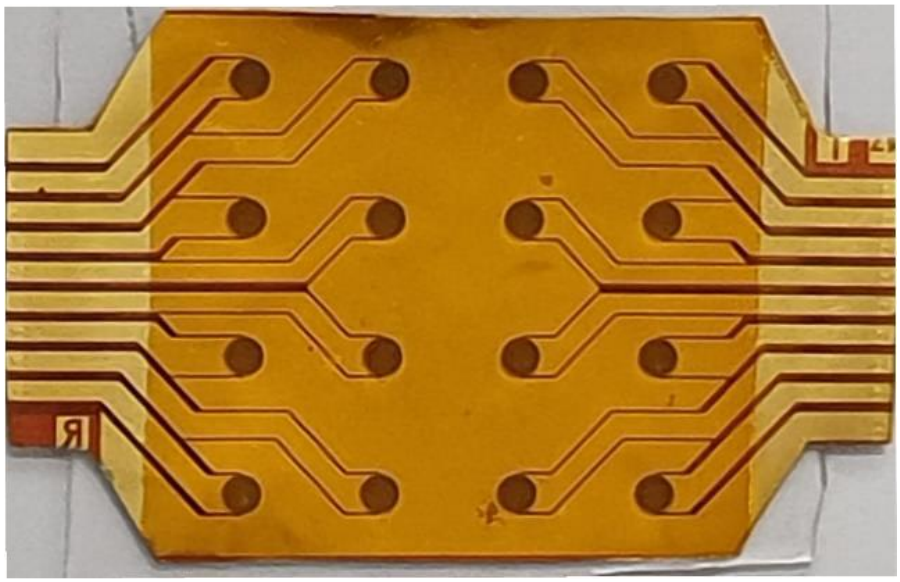

Figure 53 Laminated Circular-Tree Skin Sensor Array

After the conclusion of the fabrication process, prior to the lamination process, each sensor's resistance on the skin sensor patch is measured and recorded. This step is important as it determines the pairing of sensor patches with the closely related readings.

Once the resistance is measured and selection process is done then the lamination process is carried. Table 6 presents the resistance values of the two laminated pairs.

Table 9: Resistance Measurement of Two Sensor Arrays of a Pair Before Lamination

No. of sensor	Resistance (KΩ)	No. of sensor	Resistance (KΩ)
1	18.8	9	8.0
2	11.2	10	25.0
3	14.9	11	26.2
4	21.1	12	10.6
5	13.0	13	7.1
6	26.0	14	10.3
7	20.1	15	23.0
8	27.7	16	13.5
No. of sensor	Resistance (KΩ)	No. of sensor	Resistance (KΩ)
1	29.3	9	20.6
2	55.2	10	139.0
3	123.0	11	34.1
4	46.0	12	61.7
5	59.4	13	77.8
6	21.8	14	22.5
7	64.9	15	138.8
8	49.0	16	36.4

This laminated robotic skin sensor patches pair as shown in Figure 48 is characterized between the varying force of 2-10N for all the sensors, but 4 of the 16 sensors randomly picked is presented in this work. The data visualization graphs show the response of four randomly picked sensors under the influence of exerted force at the center of the skin sensor from the indenter in ladder form. The ladder steps are formed by gradually increasing the strain on the sensors by increasing the force applied by the indenter and holding still for about 5 seconds before increasing the applied force. It is observed that the

skin sensors appear to be very sensitive to strain caused by the impact force ranging from 0-8N and reduces sensitivity as the impact force exceeds the 7.5-8N mark.

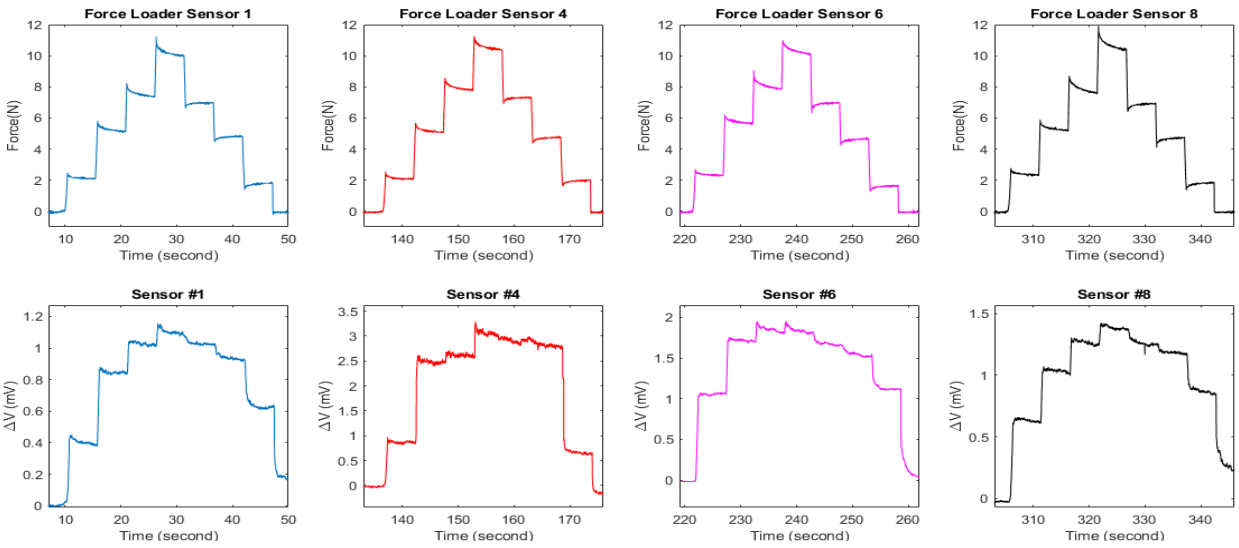

Figure 54 The Performances of Skin Sensors 1, 4, 6, 8 With Variable Force Load Of 2-10N

The ADC signals received from the data acquisition board translates the piezoresistive nature of the PEDOT: PSS under pressure from the indenter into voltage responses shown in Figure 54. The sensitivity exhibited is an average 0.2mV/N for force ranging from 0-2.7N and about 0.07mV/N for a force ranging from 2.7-10N. This in retrospect means the circular tree robotic skin sensor design presented in this compared to that reported previously, the star-shaped design was shown to be around 0.0051mV/N while in Nasser et al, it was stated to be about 1125nV/N in the range of 0-0.5N, and 412nV/N in the range of 0.5-2.3N. This indicates a major improvement of over 1000 times more with our proposed design. It is important to note that the fabrication technique used for realizing the circular tree sensor design is the process employing gold etchant instead of the wet lift-off photolithography process we once adopted. This improved the structure patterning of the sensors, maintaining the yield at 100% as the features became even smaller.

4.2.4 Sensor Patch with Different Geometries with Inkjet Printed PEDOT:PSS

The sensitivity of fabricated robot skin sensor patches is dependent on the piezoresistive nature of PEDOT: PSS, upon the impact of different force-load profiles. This means the resulting strain on the organic polymer based on the force applied varies the resistance output of the sensors accordingly. The geometry of the sensor design also plays a significant role in determining the sensitivity of the robot skin sensors. A 3.65 mm star-shaped skin sensor design fabricated in a cleanroom resulting in a feedback response of about 1.125mV/N. Subsequent progress made improving its spatial resolution with a different design of about 2mm in diameter, called the circular tree improved the skin sensor feedback response to 0.2mV/N. More so, is the importance of having topology such as those of the above-mentioned skin sensor designs as compared to the traditional interdigitated or serpentine kind of strain gauges because of the presence of directional effect of strain producing different measured response along the x and y axes regions of the skin sensors. The entire fabricated microstructure including the flexible polyimide substrate or Kapton sheet has a thickness of roughly about 125micron, consisting of a 300nm patterned gold layer serving as the sensor electrodes, 135nm thick PEDOT: PSS, 50μm protection layer of Kapton tape all situated on 50 microns thick Kapton sheet.

From previous studies, we have designed two types of skin sensor microstructure; spoke shape structure and circular tree structure comparing the performance of these two structures and studied how the design parameters variation influences the performance. Figure 55 displays the circular tree skin sensor patch design and a sensor patch with skin sensors having different geometries and their dimensions.

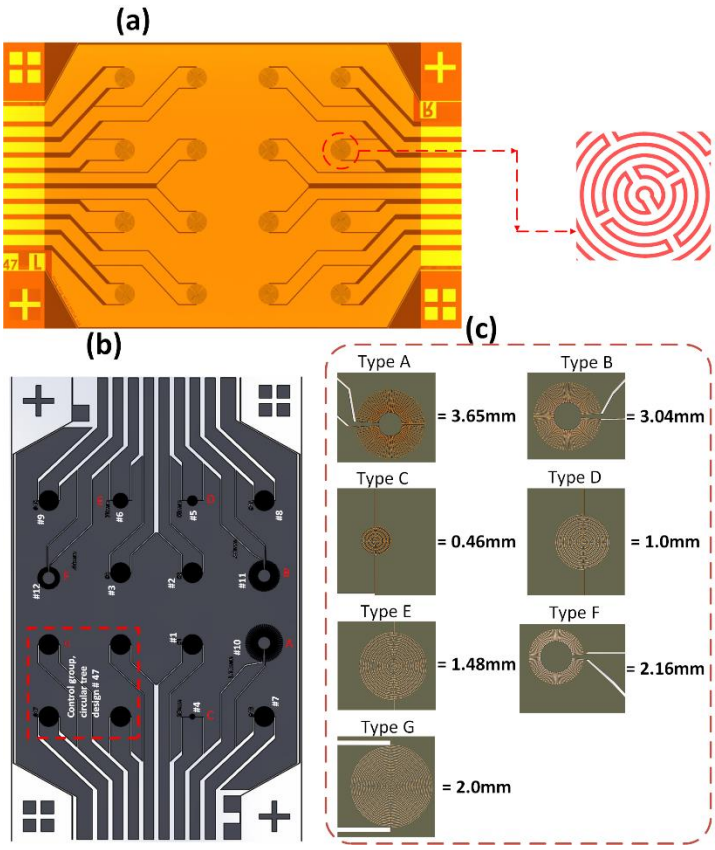

Figure 55 A) Circular Tree Design B) & C) Robot Skin Sensors Array Design with Different Geometries and Topology

Type A and B are based on the same spoke shape topology with trace width of 10um and gap of 20um, but different diameters as shown in Figure 55c and spoke lengths of 1.18mm and 0.88mm respectively. Type C, D, and E have the same topology, gold trace width to be 20um and gap 10um but different diameters. Type F has the same topology as A and B but has a spoke length of 0.44m and a diameter of 2.16mm. while Type G represents the design of the remaining sensors on the sensor patch in Figure 4-17b which is the circular tree design similar to those in Figure 55a.

4.2.4.1 PICO PULSE® Inkjet Printing Results

The PEDOT:PSS deposition procedure can be carried out outside of the cleanroom thanks to the inkjet system. By eliminating the need for cleanrooms, this lowers manufacturing costs and cuts the time needed for deposition from a 5-hour process to just 5 minutes. The result of the Pico Pulse direct write inkjet printing is stated below.

Table 10: Resistance Values of First Circular Tree Design Skin Sensor Patch

Sensor Number	1	2	3	4	5	6	7	8
Resistance Value (Ω)	36.7	34.5	61.4	33.5	50.0	34.1	32.8	31.9
Sensor Number	9	10	11	12	13	14	15	16
Resistance Value (Ω)	32.5	35.3	35.5	30.0	33.8	39.9	34.7	41.3

Table 11**:** Resistance Values of Second Circular Tree Design Skin Sensor Patch

Sensor Number	1	2	3	4	5	6	7	8
Resistance Value (Ω)	33.5	34.1	44.4	41.1	38.7	39.8	38.3	44.2
Sensor Number	9	10	11	12	13	14	15	16
Resistance Value (Ω)	44.4	40.0	35.0	59.7	43.4	36.2	36.1	49.0

Table 12: Resistance Values of First Skin Sensor Patch with Different Geometries

Sensor Number	1	Type F	Type E	4	5	Type D	7	Type B
Resistance Value (Ω)	309.4	194.1	88.2	203.6	66.3	185.8	176.7	341.2
Sensor Number	9	Type A	Type C	12	13	14	15	16
Resistance Value (Ω)	143.8	128.7	445.3	208.1	125.2	139.3	126.6	119.7

Table 13: Resistance Values of Second Skin Sensor Patch with Different Geometries

Sensor Number	1	2	3	4	5	Type C	Type A	8
Resistance Value (Ω)	228.4	159.1	155.1	197.6	146.0	258.0	93.8	110.2
Sensor Number	9	Type B	Type D	12	13	Type E	Type F	16
Resistance Value (Ω)	495.1	52.0	190.0	96.9	136.0	143.6	239.3	662.0

The resistance of each sensor on the robot skin sensor patch is measured and recorded after the conclusion of each fabrication before the lamination. Tables 7 & 8 represent the resistance values of the circular tree sensors within 30-60 **Ω** while Tables 9 & 10 display the resistance values of the sensors with 6 different geometries represented by type a, b, c, d, e, f as shown in Figure 50. The rest of the sensors on the patch is of the circular tree design. The robot skin sensor patches are characterized by force ranging from 0.5N to 6N. Figure 56a displays a graph comparing the sensitivity of the robot skin sensor patch made in our previous study[95], which is represented by the red line using the previous PEDOT: PSS deposition technique in the cleanroom with the new inkjet printing technique described in this paper. The new sensor patch which has an average sensitivity of 11.42mV/N and 22.84mV at 2N is a significant improvement to the sensor patches described in our previous studies which is an average of 0.2mV/N and 1.13N for a force range of 0-2.7N. The sensitivity begins to drop at forces beyond 2.7N while in this study the sensitivity increases almost linearly and begins to dip at forces beyond 6N.

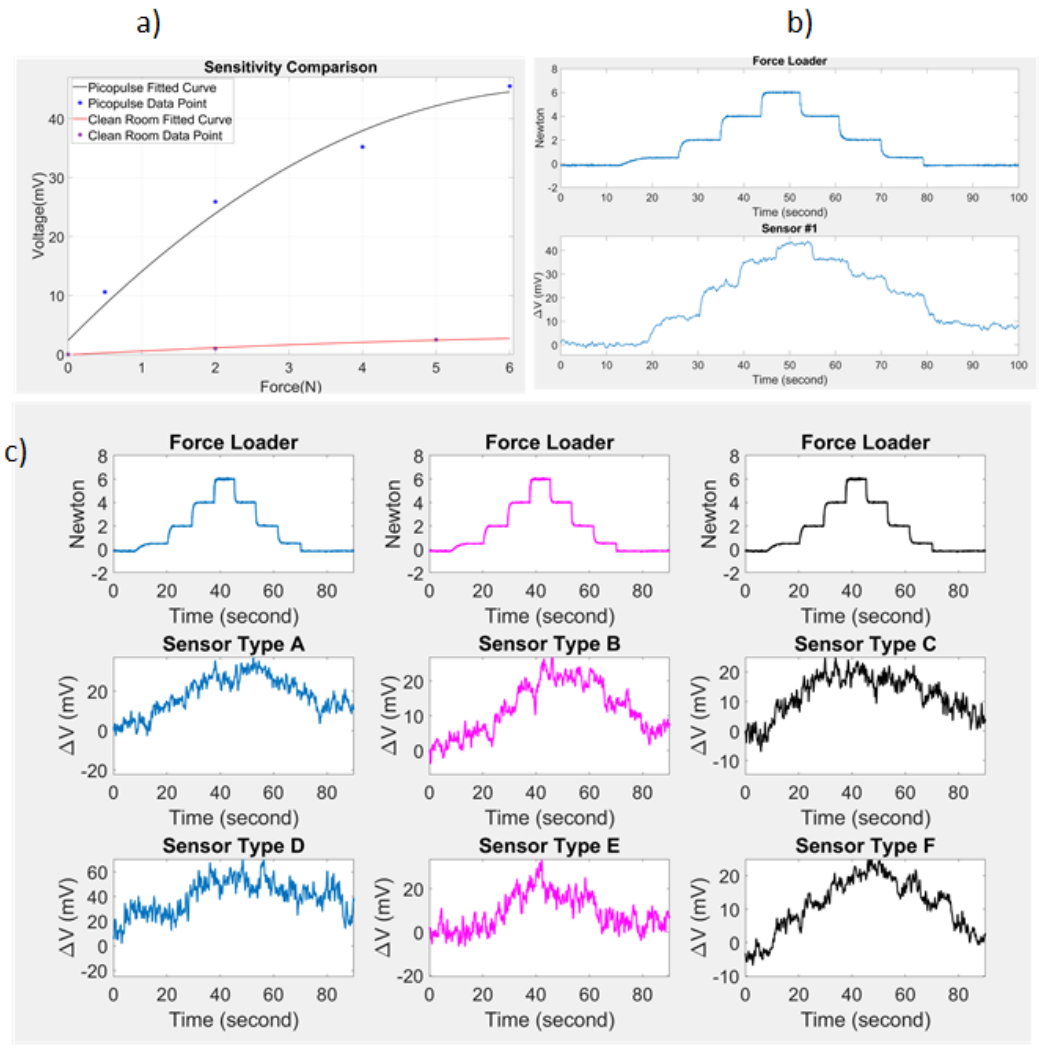

Figure 56 A) Sensitivity Between the Previous and New Skin Sensor Patches B) Response Graph of The Circular Tree Sensors C) Response Graph Of Skin Sensors With Different Geometries.

This observation makes the inkjet printing technique desirable not only to reduce fabrication time but also to increase the sensitivity for robot skin sensors making it applicable for measuring strain-induced from small forces applied. Figured 56b, shows the graph response of the newly fabricated robot skin sensors under the influence of a force indenter increasing the force in steps from 0.5-6N. In comparison with Figure 56c, we can see the response of other sensor types, they all appear to be equally sensitive based on the

application of the inkjet printing technique, but the circular design depicted as type G in Figure 56 appears to be much better due to its ability to properly replicate the force ladder and settle back at zero in a similar fashion.

4.2.4.2 Optomec Aerosol jet printing results

In this paper, we investigated a new method of depositing PEDOT: PSS through aerosol jet printing, replacing the technically challenging and time-consuming techniques applied in the cleanroom. Aerosol jet printing reduces the number of steps and time required to realize the robot skin sensor fabrication process, reducing the process time from about 5 hours to 26 mins for a laminated paired skin sensor patch. It also diminishes the likelihood of human error in the patterning of the PEDOT: PSS on the skin sensor structures, as indicated in its characterized sensitivity of 6.2μV/N as compared to 0.4μV/N and 5.1μV/N of cleanroom fabricated ones.

Resistance measurement of the fabricated skin sensor patches is taken and documented, determining the pairing of patches with similar readings to be laminated together. Tables 11 and 12 show the resistance values of two skin sensor patches laminated together. The resistance of the skin sensor patches is within the range of 40Ω to 5kΩ. The sensitivity of the sensors was determined based on the electrical response measurements conducted with the help of our automated testing bench. To this purpose, controlled deformation of the PEDOT structures was realized by applying strain with indenter at the specific location of each sensor on the sensor patch.

Table 14: Resistance Values of First Circular Tree Design Skin Sensor Patch

Sensor Number	1	2	3	4	5	6	7	8
Resistance Value (Ω)	4.9k	450	105	143	40	137	538	3.0k
Ave. Sensitivity (μV/N)	8.6	10.1	3.6	3.5	3.8	6	10.3	**16.2**
Sensor Number	9	10	11	12	13	14	15	16
Resistance Value (Ω)	92.0	80	103	108	189	273	413	96
Ave. Sensitivity (μV/N)	4.5	4.8	4.6	8.9	1.8	10.9	7.8	9.4

Table 15**:** Resistance Values of Second Circular Tree Design Skin Sensor Patch

Sensor Number	1	2	3	4	5	6	7	8
Resistance Value (Ω)	4.4k	886	105	166	47	157	845	5.8k
Ave. Sensitivity (μV/N)	9.5	8.5	3.8	4.2	2.6	5.0	6.4	8.6
Sensor Number	9	10	11	12	13	14	15	16
Resistance Value (Ω)	104	724	111	237	126	337	367	158
Ave. Sensitivity (μV/N)	5.2	3.6	3.8	3.7	3.3	7.5	6.3	3.0

This deformation, with respect to varying force load profiles, induces corresponding varied voltage responses of each skin sensor. Different electrode geometries of sensors (Figure 55) are responsible for varying resistance measurements - Tables 11 and 12. Each of the sensor responses shown in Figure 55 corresponds to the skin sensor's resistance values in Tables 11 and 12. Figure 52 shows the response of the three skin sensors, sensors 9, 12 and 8 from the newly fabricated skin sensor patch representing skin

sensors within the low, mid, and high-performance range respectively for each force profile from 1N-6N in step ladder form. It evaluates the sensitivity of the PEDOT: PSS skin sensors by recording voltage changes across the given sensor in response to the applied force. The results show the newly fabricated skin sensor patches sensitivity is in range of 1.8–16.2 μV/N, while sensors fabricated through cleanroom techniques have a sensitivity of 0.4μV/N and 5.1μV/N as stated by Saadatzi et al and Wei et al respectively. The majority of sensors can be grouped in two sets with respect to the range of sensitivity values:

- 2 – 6 μV/N for sensors with numbers 3 – 6 and 9 – 13.
- 6 – 11 μV/N for sensors # 1, 2, 7, 8 14 – 16.
- exception - sensor 8 (patch 1) with sensitivity 16.2 μV/N.

Observed distribution of sensitivity values is most likely due to the different geometries of the sensors.

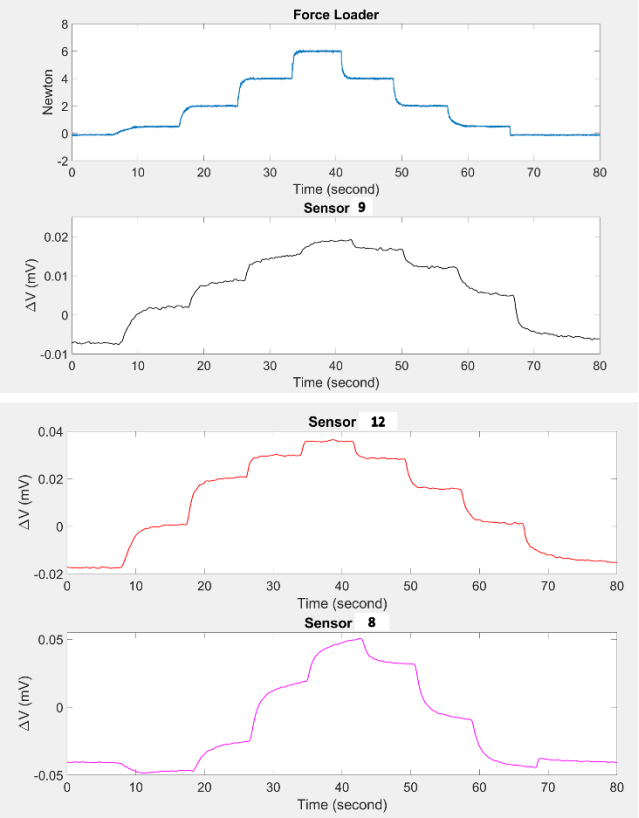

Figure 57 Response graphs of aerosol jet printed PEDOT: PSS skin sensors for sensors #: 9, 12 & 8

4.2.5 Tactile Strain Gauge

The studied tactile sensor design is location-sensitive, which means that the sensor geometry and pressure point position have an impact on its sensitivity. On a soft surface, the strain is uniform around the circumference and increases at the pressure point before decreasing in the radial direction. The circular design serves as an analog to the rectangular serpentine pattern found in the majority of common one-dimensional metal foil strain gauges.

The purpose of the study is to determine how the following design components, when applied to a set of inner and outer silver pattern diameters, affect sensitivity. 1) The diameter of the dimple; 2) The size of the cavity's top surface; and 3) The thickness of the membrane beneath the sensor. Consequently, is needed an ideal encapsulation design for the given silver pattern geometry should be drawn. The top diameter and height of the cone-shaped cavity will change, but the bottom diameter will remain 12 mm, greater than the silver pattern. We anticipate that this design modifies the deformation and stiffness. The PDMS cover is 2 mm thick and has a circular cutout that is 1 mm deep with a 14 mm clearance. As the indentation to the sensor surface, the cylindrical dimple is situated in the cutout's center. As seen in Figure 58. All the domain pieces are attached as boundary condition to one another in the simulations before a boundary force of 5 mm diameter is imposed on top of the cover.

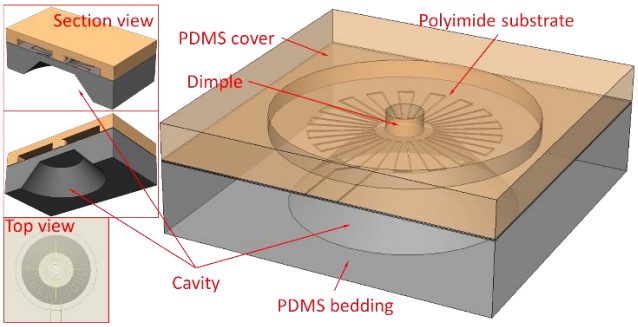

Figure 58 Illustration of tactile sensor for FEA simulation

4.2.5.1 Simulation Results

Sensitivity is defined as the change of resistance ΔR with respect to the nominal resistance R, as in equation (4-2).

$$\text{sensitivity}=\Delta R/R \qquad (4\text{-}2)$$

Figure 59 displays the first simulation results. Without the bedding cavity, sensitivity is displayed against different dimple widths and applied pressures from 0 to 2 Newtons (N). By varying the dimple's diameter, we observed the various sensitivities. Red dots indicate the outcomes of the simulation; the rest of the curve, is interpolated using MATLAB's "pchip" approach[96], shown in Figure 59

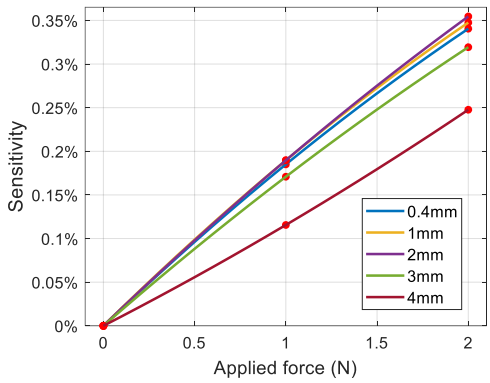

Figure 59 Comparing sensitivity to various dimple widths and forces.

According to Figure 60, among the possibilities, the dimple with a 2mm diameter had the highest sensitivity. Using data taken from Figure 59 and a 2N force, Figure 60 demonstrates how the sensitivity varies by 29 percent depending on the diameter of the dimples.

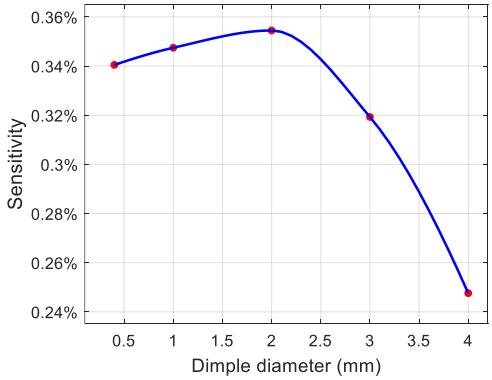

Figure 60 Sensitivity vs. dimple diameter at 2N force.

The top diameter and sensitivity of the cavity are then depicted in Figure 61, with the maximum sensitivity of the dimple's diameter set at 2mm. Variations in sensitivity amount to 22%.

The top diameter can be used to estimate the size of the cone-shaped cavity since the bottom diameter of the cone is designed to be greater than the outside diameter of the sensor structure. The top diameter is better positioned between the outside and inner diameters of the sensor pattern for maximum sensitivity, according to simulation results, which is also a more notable improvement than without the cavity.

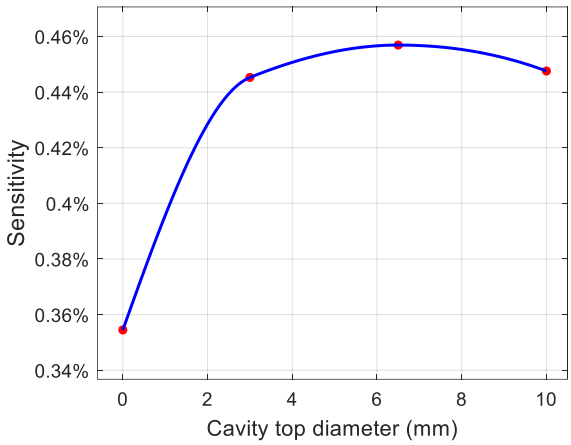

Figure 61 Cone cavity top diameter against sensitivity

The effect of different membrane thicknesses on sensitivity is depicted in Figure 62 after the diameters of the cavity and the dimple have been tuned. Sensitivity is almost inversely proportional to membrane thickness, unlike the other parameters for which there is an ideal size. The rigidity of the membrane diminishes with increasing membrane thickness. Higher deformation and consequently strain are induced around the same sensor area with the same applied force, increasing sensitivity. The sensitivity is also more strongly influenced by

thickness. The sensitivity variation changes by 33 percent for every 1 mm change in thickness.

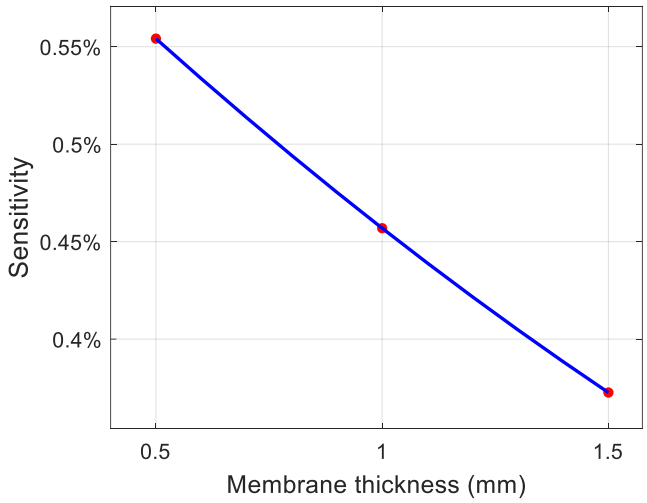

Figure 62 The membrane thickness vs sensitivity

4.2.5.2 Tactile Sensors Test Result Analysis

The tactile sensor fabrication procedure we developed, printed a patterned star shape tactile structure successfully onto an FPC substrate, using the aerosol jet printer and the samples are cured by the IPL and oven, which are all part of a custom-built NeXus microfabrication platform. The entire process requires the characterization of printing resolution giving a precisely measured width of the printed silver lines to be 60 microns and the evaluation of the silver ink conductivity during the sintering process. Figure 3-25 shows the complete tactile sensor fabrication after the curing process. After the fabrication process is carried out and the sintering process is concluded, the resistance values of the tactile sensors under the influence of measure weights are taken.

Table 16: Tactile Sensors Load – Resistance Values

Load (g)	***3-IPL Cycles(Ω)***	***4-IPL Cycles(Ω)***	***Oven cure (6hrs)***	***Oven cure (20hrs)***
0	400.501	65.651	441.74	188.39
28	400.684	65.656	441.806	188.444
44	400.694	65.664	441.855	188.5
72	400.712	65.67	441.93	188.564
84	400.717	65.675	442.004	188.624
112	400.735	65.681	442.065	188.69
128	400.74	65.689	442.153	188.75
156	400.755	65.698	442.208	188.821

As shown in Table 13, it is observed that the resistance measurement varies based on the curing duration of the tactile sensor in the oven and the number of impulse cycles ran on the tactile sensor with the IPL. With an increase in the number of impulse cycles, the resistances of the tactile sensors decrease, showing significant differences between the measured resistance between different cycles and the length of time the tactile sensor spends in the oven.

The graphs shown in Figure 63 show the relationship between the load profile and resistance measured. It shows the near-linear characteristics as the resistance increases with respect to the varying load. This depicts the effectiveness of the aerosol jet printed tactile sensors irrespective of the curing technique.

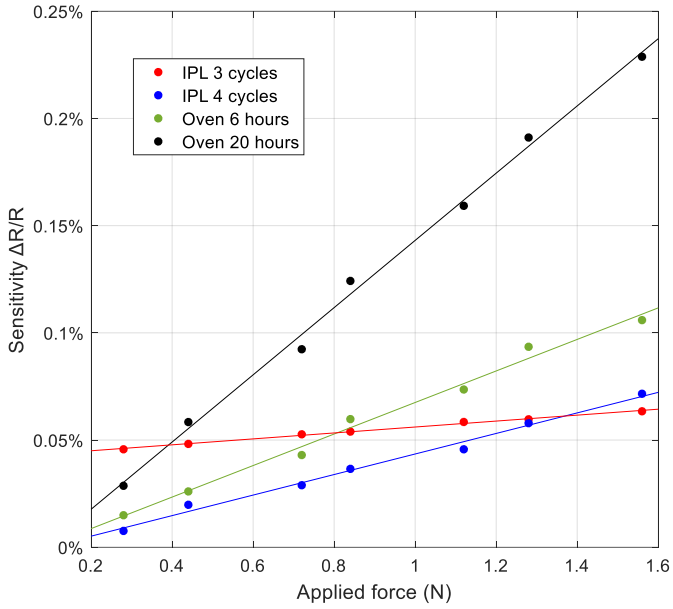

Figure 63 Graphic relationship between the applied load on the sensors (Newton) vs. the change in resistance

We have conducted characterization of the tactile sensor with respect to sensitivity and its dependence on the applied load, in order to experimentally validate proposed sensor's design and its fabrication method. Furthermore, we desired to demonstrate our approach enabling tuning of the tactile sensor's properties depending on the sintering conditions – specifically the duration times. Set of five types of sensors were tested, taking the average of 5 sample readings, the properties of sensors differed depending on sintering duration time – varied from 2 to 20 hours at 200^{o}C in all the cases.

Results presented in Figure 64A demonstrate that overall, the tactile sensors' resistance decreases as the thermal annealing time increases - with significant change from 1.6 kΩ to around 560 Ω, for 2 and 16 hours respectively (Figure 64A). There is minor reduction of resistance for sintering times above 16 hours. The lowest resistance of 528 Ω was measured for the samples cured in the oven for 20 hours. Such improvement of

sensor's conductivity is expected with the longer sintering times, as initially individual silver nanoparticles of the printed lines form continuous structure during thermal treatment.

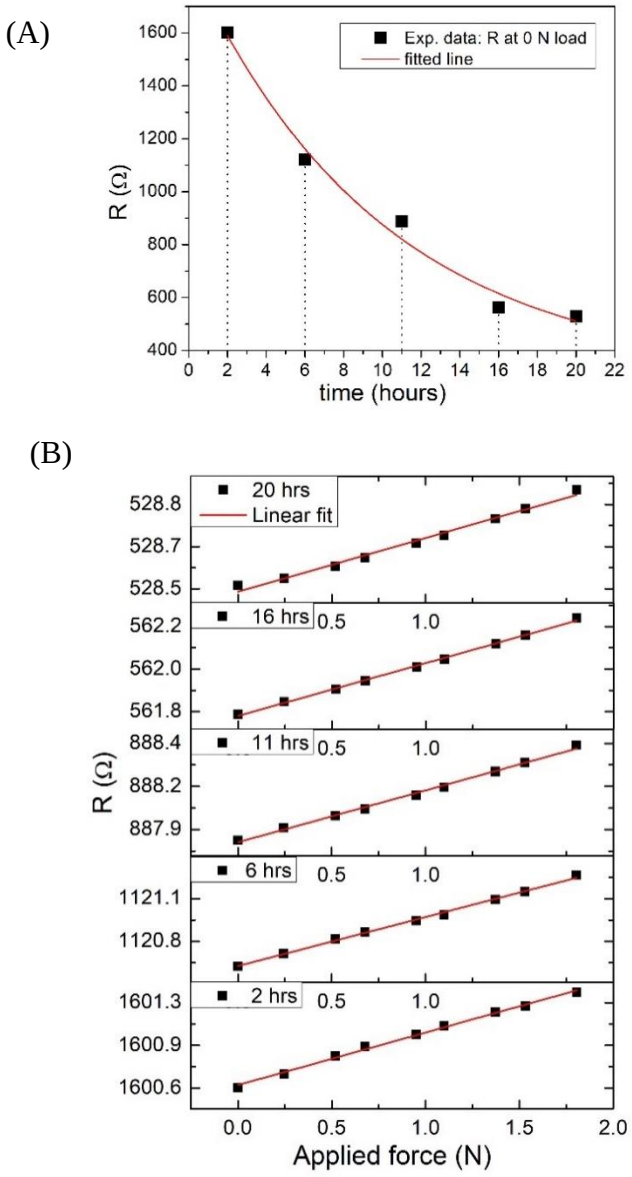

Figure 64 Tactile sensor characterization: A) Sensor' resistance dependance on sintering time. B) Resistance vs applied force for different sintering times

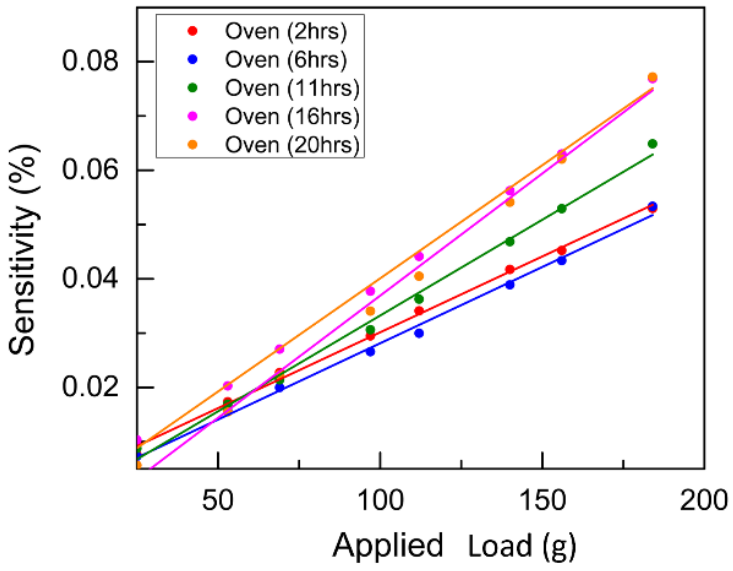

Figure 65 Sensitivity dependance on applied load.

Characteristic feature of the fabricated sensors is that resistance exhibits linear and directly proportional dependence on the applied load in case of all the sintering times (Figure 64B). Consequently, similar relation was observed in the combined linear data fit of the tactile sensors for the sensitivity as a function of the applied load (Figure 65). More importantly, it is apparent that sensor's sensitivity exhibits consistent behavior with respect to sintering duration – with increase of thermal treatment time, slopes for sensitivity vs load trend lines become steeper (Figure 65). Therefore, by adjusting sintering time at given temperature, it is possible to produce sensor with desired sensitivity profile. The best sensitivity (around 0.07%) was observed for the sensors sintered for 16 and 20 hours - with the lowest resistance values (Figure 64B). Interestingly unlike in case of the resistance of the sensors, sensitivity does not experience such dramatic change with respect to sintering time. Resistance decreased almost 3 times for sintering duration between 2 and 16 hours – from ~1600 Ω to ~562 Ω (Figure 64A). Whereas for sensitivity in the same time range, we

have observed increase approximately from 0.05% to 0.07% for maximum load (Figure 65).

Linear dependence of the resistance on the load, indicates that the phenomenon governing sensor's response is similar independently of the sintering time duration (Figure 64B). Combined with observed complementary character of resistances and sensitivity dependance on the thermal annealing times and applied force, it can be claimed that discussed mechanism is related to nano/microscale properties of the printed and cured silver lines.

4.2.6 System Identification for Tactile Sensors

System identification could be referred to as an approach to understanding the behavior of a dynamic system based on the measurement data (input and output). This could be trying to determine mathematical relations between the system responses and input without actually going into many details of the system as described in a black-box approach. Or a grey-box model where the peculiarity of the system is not entirely known. Here, certain insight into the system with observed experimental data with sufficient accuracy would be required into formulating a model.

The system identification procedure of the dynamic system is characterized by the following components illustrated in Figure 66:

The Data: this is the required information source of the input and output needed for the selection of a model. This will impact on the quality of the resulting model based on the signals to be measured, how the input is to be configured, and the collection of the data with a suitable sampling procedure

The Model structure: The selection of a model seems relatively easy in linear identification in contrast to nonlinear identification because this is driven by a range of possibilities that could be user-defined or determined by the nature of the system response or behavior. In other words, the selection of a model structure can be realized based on the ability of the model to replicate the observable behavior of the system which could be hysteresis or shifting resonance. The other consideration would be the structure aspects, will the model be robust enough to provide a true description of the system.

The estimation method: This requires picking the model that best describes the observed data based on a given data set and model set. This can often lead to seeking out prior knowledge that will be needed to compute one-step-ahead prediction at time t-1 of the given model set and data at disposal.

Model Validation: This deals with the evaluation of the estimated model, making inquiry into its efficiency in solving the problem at hand without possible conflict with the data or prior knowledge.

The characteristics of the above components will appear to be more involved for a nonlinear identification compared to a linear identification. As we will be dealing with the complex manifold in a high dimensional space, possible structural model errors and optimization problems resulting from process noise.

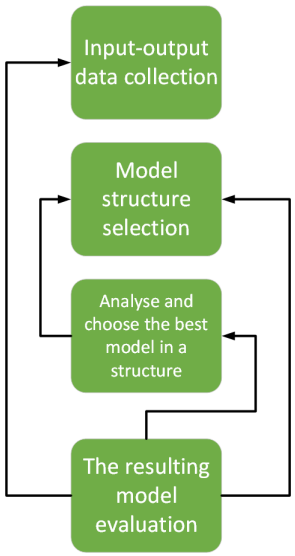

Figure 66 Identification Process

4.2.6.1 System Identification Toolbox

The MATLAB System identification toolbox is a graphic user interface that emerges at the prompt of the command "ident" on MATLAB. The toolbox constructs mathematical models from imported measured input and output data in this case, force, and voltage from the MATLAB workspace. This can be done in the time-domain or frequency-domain for identifying discrete-time and continuous-time transfer functions, state-space models or process models using parameter estimates algorithms present within the toolbox. The toolbox allows preprocessing of data with operations such as filtering, resampling, detrending, and analysis of data within a specified range. Model estimation and validation are done from the measured input and output data, comparing identified models, analyzing their properties, and validating the data set. Figure 67 below shows the system identification toolbox interface.

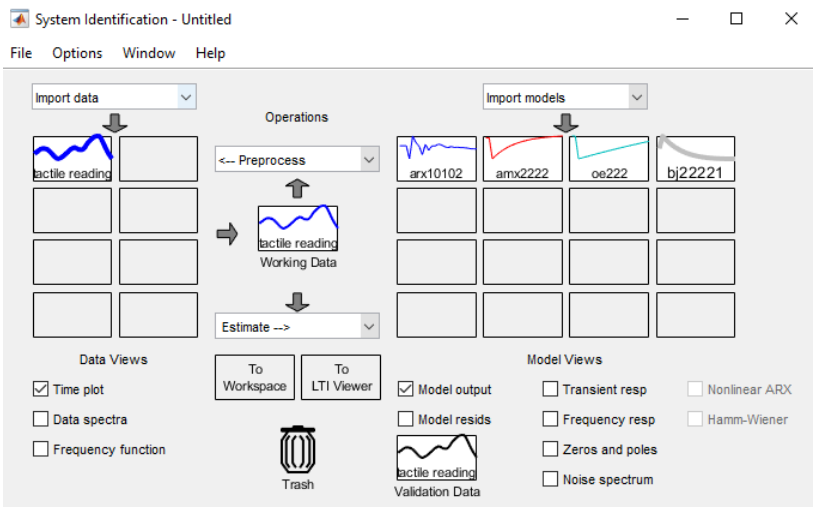

Figure 67 System identification toolbox interface

4.2.6.2 Skin sensors system identification

The fabricated tactile skin sensor was placed in a force-controller mechanical indenter setup developed in-house as discussed in chapter 3. The testbench system was controlled by the cRIO-9074 Real-Time controller with the 9205 and 9516 peripherals used in general-purpose I/O ports. Each 9516 was connected to a Newport travel stage to allow linear motion in a single direction. The first stage was aligned vertically, with the plunger and load cell fastened. This allowed for force testing by controlling the motor positioning based on a feedback loop from the load cell. This setup interfaces with an electronic circuit board and a LabVIEW® front panel designed to automate the testing process and characterize the tactile sensor. This LabVIEW® front panel generates a force-load profile in real-time as the loadcell controlling the force and sensor response is measured using an ADC board then sent to a host PC that logs the current response value in a visualizer, for active test data reading, and a CSV file for post-processing.

The input is a sinusoidal force profile varying with a corresponding voltage response from the tactile sensor. The graph illustrating this relationship with respect to time is shown in Figure 68 below.

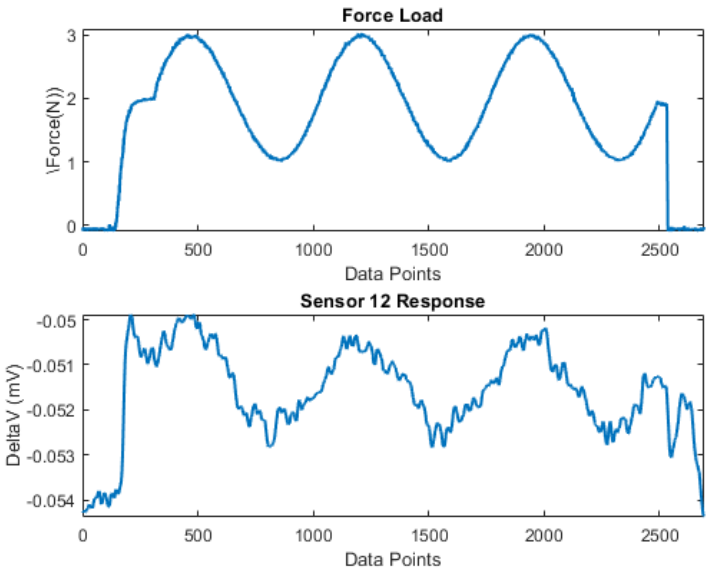

Figure 68 Sinusoidal force input with respective voltage response

4.2.6.2.1 Polynomial model – Box Jenkins

For the Box Jenkins model structure, it's a second order model structure gave the best fit with the input and output relationship obtained with parameters below.

$$\text{BJ model: } y(t) = \frac{B(q)}{F(q)}u(t) + \frac{C(q)}{D(q)}e(t)$$

$$B(z) = 1.438e^{-5}z^{-2} - 1.566e^{-6}z^{-3} \quad (4\text{-}3)$$

$$C(z) = 1 - 0.03134z^{-1} + 0.1313z^{-2} \quad (4\text{-}4)$$

$$D(z) = 1 - 1.874z^{-1} + 0.874z^{-2} \quad (4\text{-}5)$$

$$F(z) = 1 - 1.696z^{-1} + 0.7142z^{-2} \quad (4\text{-}6)$$

Parameterization:

Polynomial Orders: nb=2, nf=2, nk=2

Number of free coefficients: 4

FPE: $1.495e^{-10}$ MSE: $1.482e^{-10}$

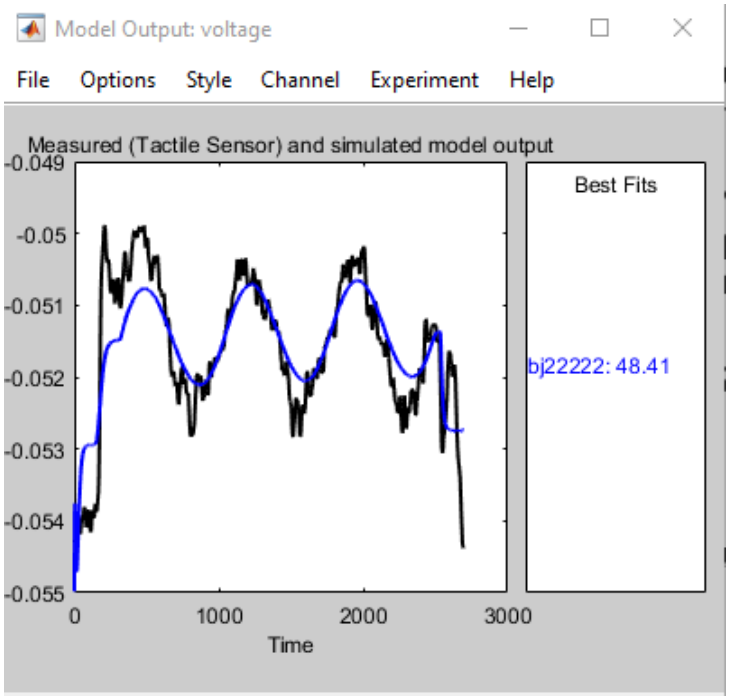

Figure 69 Box Jenkins model output Fit

4.2.6.2.2 Polynomial model – OE

For the OE model structure, it is a second order model structure gave the best fit with the input and output relationship obtained with parameters below.

$$\text{OE model: } y(t) = \frac{B(q)}{F(q)}u(t) + e(t)$$

$$B(z) = 3.236e^{-5}z^{-2} - 3.236e^{-5}z^{-3} \quad (4\text{-}7)$$

$$F(z) = 1 - 1.971z^{-1} + 0.9707z^{-2} \quad (4\text{-}8)$$

Parameterization:

Polynomial Orders: nb=2, nf=2, nk=2

Number of free coefficients: 4

FPE: $2.974e^{-7}$ MSE: $2.969e^{-7}$

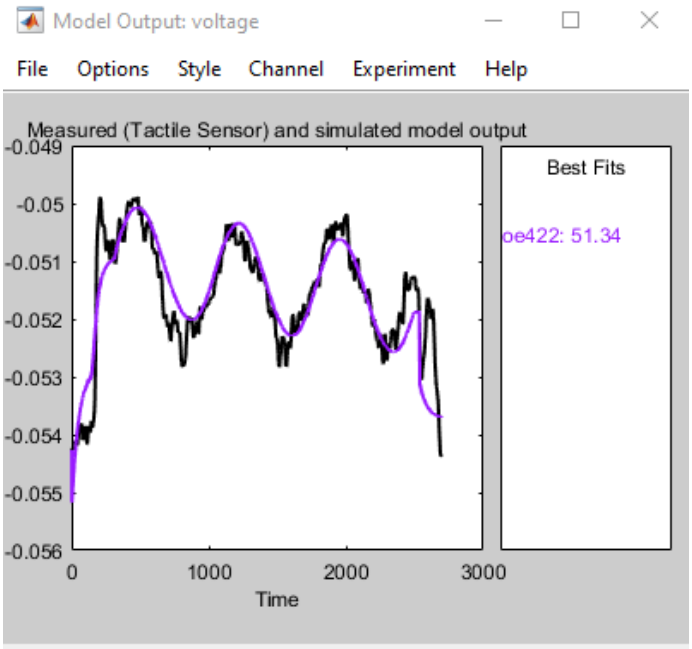

Figure 70 OE model output Fit

4.2.6.2.3 Polynomial model – ARMAX

For the ARMAX model structure a fourth order model structure gave the best fit with the input and output relationship obtained with parameters below.

ARMAX model: A(z)y(t)=B(z)u(t)+C(q)e(t)

Polynomial orders: na=4, nb=4, nc=2, nk=2

Number of free coefficients:10

FPE: 1.384×10^{-10} MSE: 1.369×10^{-10}

$$A(z) = 1 - 1.906z^{-1} + 0.09396z^{-2} + 1.573z^{-3} - 0.7604z^{-4} \quad (4\text{-}9)$$

$$B(z) = 1.256 \times 10^{-5}z^{-2} + 3.829 \times 10^{-7}z^{-3} - 4.885 \times 10^{-6}z^{-4} - 8.118 \times 10^{-6}z^{-5} \quad (4\text{-}10)$$

$$C(z) = 1 - 0.08796z^{-1} - 0.6644z^{-2} \quad (4\text{-}11)$$

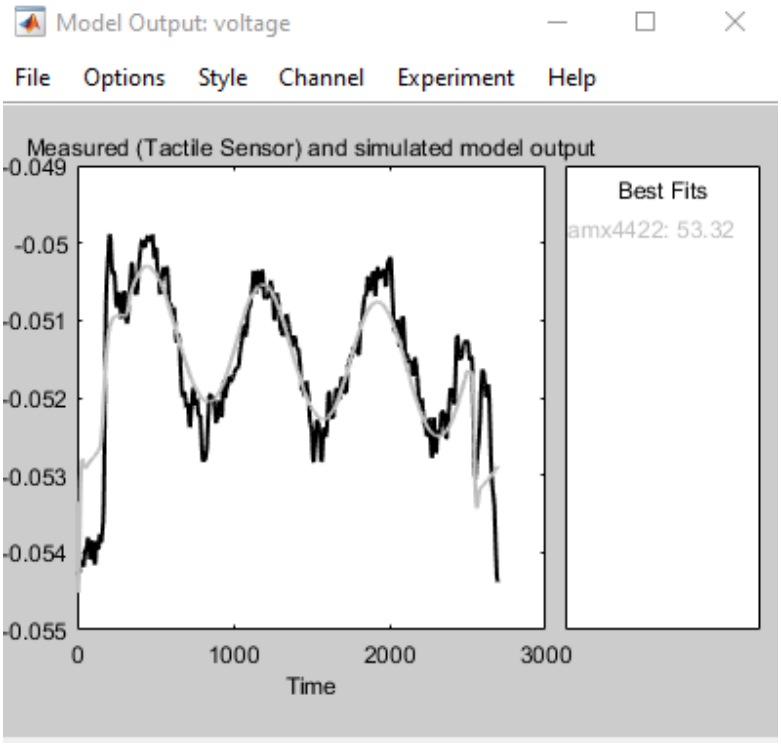

Figure 71 ARMAX model output Fit

4.2.6.2.4 Polynomial model – ARX

For the ARX model structure a 10th order model structure gave the best fit with the input and output relationship obtained with parameters below.

ARX model: $A(z)y(t) = B(z)u(t) + e(t)$

$$A(z) = 1 - 1.891z^{-1} + 0.8053z^{-2} + 0.2861z^{-3} - 0.4843z^{-4} + 0.5272z^{-5} - 0.3728z^{-6} + 0.198z^{-7} - 0.1282z^{-8} + 0.1377z^{-9} - 0.07779z^{-10} \quad (4\text{-}12)$$

$$B(z) = 9.419 \times 10^{-6}z^{-1} + 6.808 \times 10^{-7}z^{-2} - 1.21 \times 10^{-6}z^{-3} - 3.504 \times 10^{-6}z^{-4} + 1.271 \times 10^{-5}z^{-5} + 9.905 \times 10^{-6}z^{-6} - 2.264 \times 10^{-5}z^{-7} + 7.266 \times 10^{-6}z^{-8} - 1.883 \times 10^{-5}z^{-9} + 6.02 \times 10^{-6}z^{-10} \quad (4\text{-}13)$$

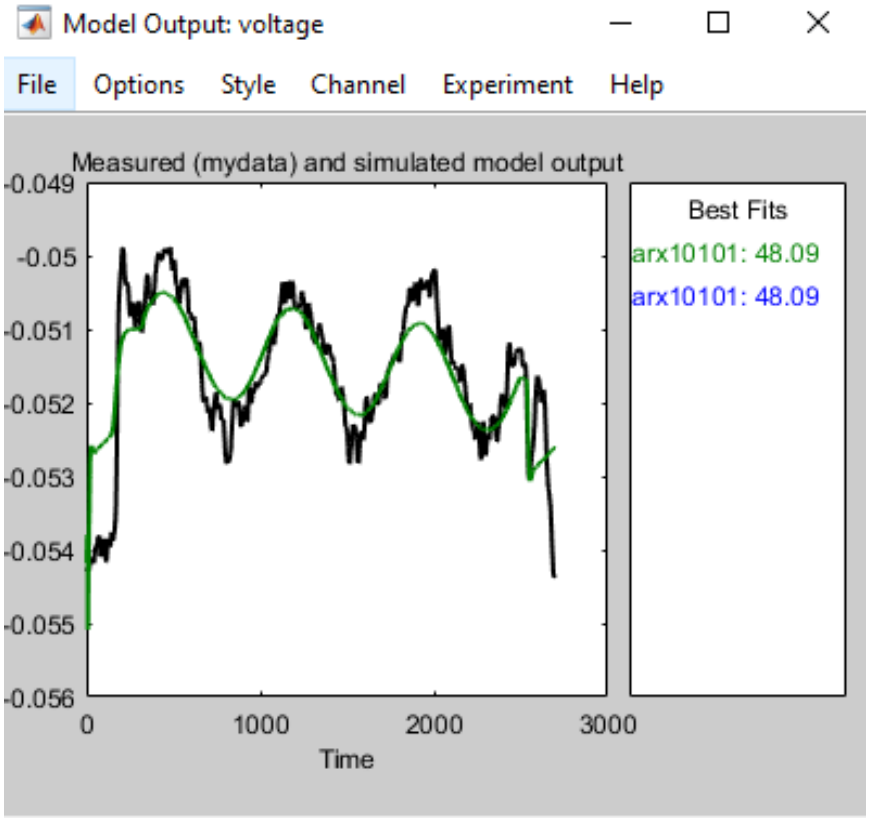

Figure 72 ARX model output Fit

4.2.6.2.5 Transfer Function Estimate

The second order transfer function estimate gives the best model fit at 62.6% for a robot skin sensor.

$$z^{-12} \times \frac{0.00101 - 0.0022011z^{-1} + 0.001002z^{-2}}{1 - 1.99z^{-1} + 0.9897z^{-2}} \quad (4\text{-}14)$$

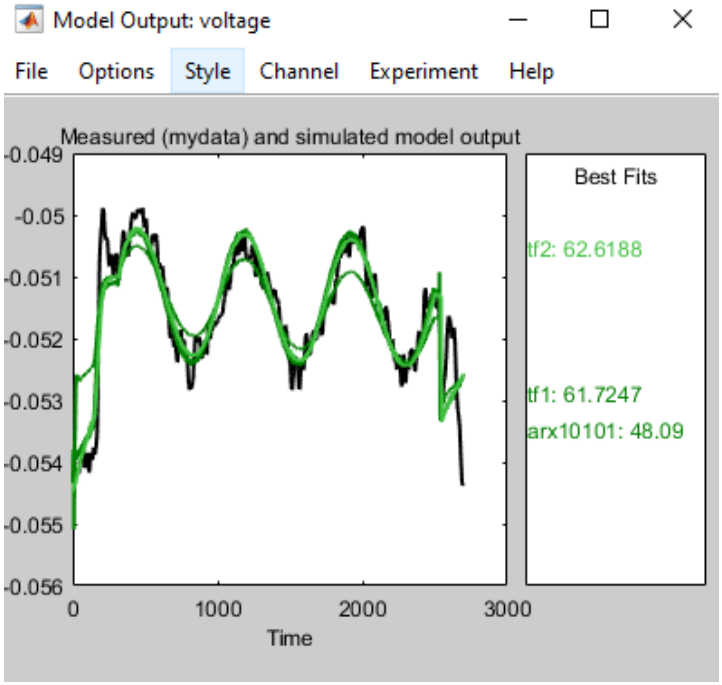

Figure 73 TF model output

4.2.6.3 Tactile Star-Shape Strain Gauge System Identification

The mathematical model of the tactile sensor based on the measured output response in resistance with respect to the force input signal in a linear time-invariant system is analyzed using the System Identification Toolbox in MATLAB. Figure 74 shows the applied force input signal in discreet step ladder profile against the tactile resistance varied response below . The black box modeling estimates parameters in the trial-and-error process and compares the results. The model structure could be configured in the transfer function, expressed in the number of poles and zeros, Linear ARX model, a simple input-output polynomial model, or state-space model estimate specified by the number of model states. The experiment for black-box identification is mostly carried out using discrete

measurement data and the discrete model form is considered and is expressed in the transfer function below:

$$G(s) = \frac{B(s)}{A(s)} = \frac{b_m s^m + \cdots + b_1 s + b_0}{(a_n s^n + \cdots + a_1 s^1 + a_0)} \quad (4\text{-}15)$$

$$A(s) = a_n s^n + \cdots + a_1 s^{-1} + a_0 \quad (4\text{-}16)$$

$$B(s) = b_m s^m + \cdots + b_1 s + b_0 \quad (4\text{-}17)$$

Using a linear transfer function model in continuous time, we looked at how well it can produce the estimation data which is a good fit to the data used to fit the model. Implementing a sixth order (6 poles, 4 zeros), fourth order (4poles, 4 zeros) and second order (2 poles 1 zero) transfer function model and the estimation data fit produced is at 93.63%, 86.43% and 78.95% respectively. A more crucial test is the validation data fit that validates the model on a new set data generated from the same system. As shown in Figure 74B, the black step ladder curve represents the true measured output from the tactile response while the green curve represents the model response to the same input. And the simulated model output response results in 81%, 84.69% and 78.95% validation data fit, respectively. The 4th order transfer function model represents a relatively better model fit. The continuous time identified transfer function of the model is given below.

$$\mathrm{G(s)} = \frac{0.1711\mathrm{s}^4 + 0.2417\mathrm{s}^3 + 0.0008343\mathrm{s}^2 + 0.0002603\mathrm{s} + 2.258\mathrm{e}^{-07}}{(\mathrm{s}^4 + 0.8174\mathrm{s}^3 + 0.002888\mathrm{s}^2 + 0.0008586\mathrm{s} + 1.76\mathrm{e}^{-08})} \quad (4\text{-}18)$$

A)

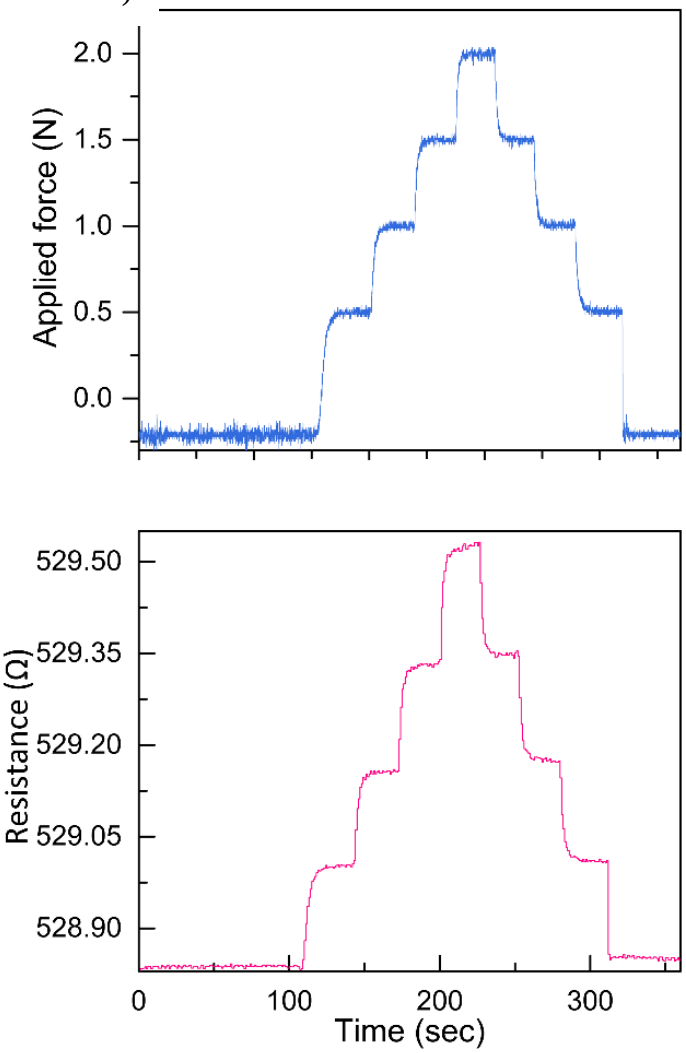
Applied force (N)
2.0
1.5
1.0
0.5
0.0
Resistance (Ω)
529.50
529.35
529.20
529.05
528.90
0
100
200
300
Time (sec)

B)

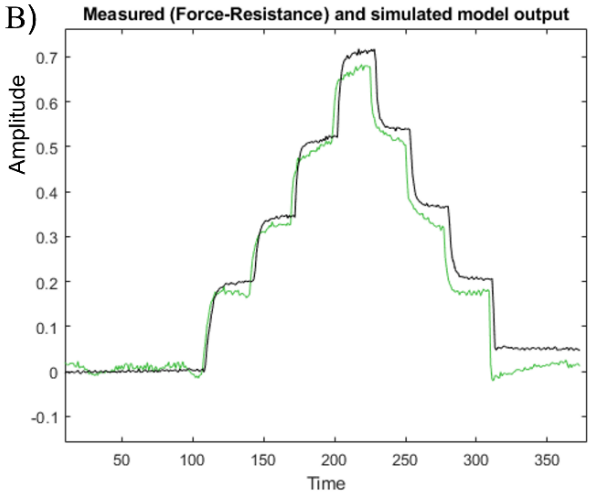
Measured (Force-Resistance) and simulated model output
Amplitude
0.7
0.6
0.5
0.4
0.3
0.2
0.1
0
-0.1
50
100
150
200
250
300
350
Time

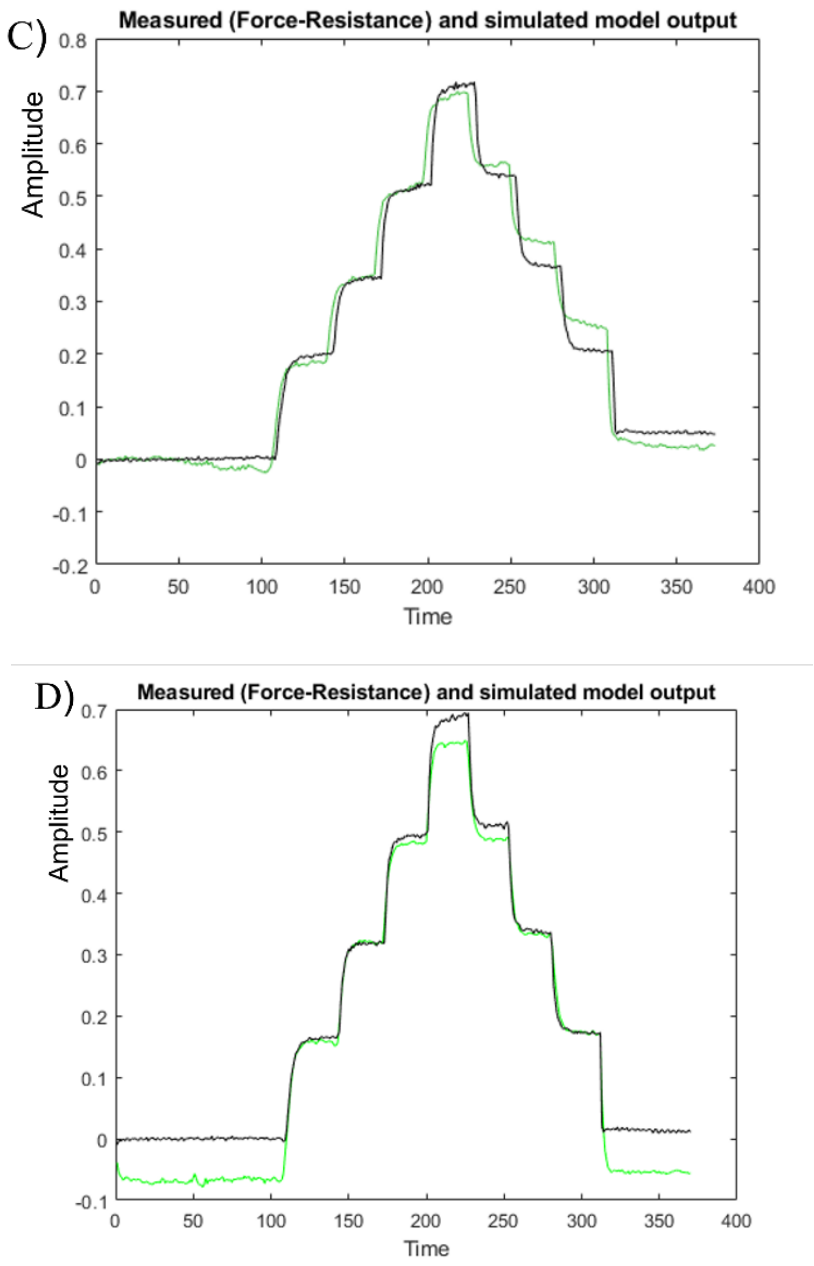

Figure 74 A) Force ladder profile (0.5-2N) and tactile sensor resistance response. Simulated model output of (B) 6th order model, (C) 4th order model (D) 2nd order model, validation data set at 81%, 84.69%, 78.95% respectively

CHAPTER 5

DEPLOYMENT OF TACTILE ROBOT SKINS ON ROBOTIC MANIPULATOR

Robots can become more aware of their environment and become safer to be around by being given the ability to feel external forces, temperature, and proximity. This improves the quality of human-robot interaction. We prototyped robot skins using off-the-self sensors (Flexiforce sensors) in this chapter and mounted them on last robot joint of the end effector. Numerous trials were performed to confirm the need for the robot skin to provide HRI of higher quality. In this work, the methodical approach to the implementing force control and accentuating its directions of application is reviewed. The problem can be defined in two ways 1) how do we integrate tactile sensor to issue out commands to robot joints within cartesian space 2) the need to implement position control to the movement of the joints as orientation of the end-effector changes. This demonstration of the RESquared robot arm equipped with an Octocan sensorized with robot skin patches is proposed to be featured in ROS visualization and experimental setup, to enhance safety and achieve intuitiveness of physical Human-robot Interaction for both intention and unintentional contacts. The Octocan which acts like a placeholder for Skin sensor patches is fabricated to hold on to 8 pairs of the robot skin patches. These laminated pairs of skin sensor patches already fabricated through a cleanroom process contains 16 sensors of about 3.6mm in diameter. The overall steps involved in carrying out this demonstration as highlighted in several texts could be established in the following order. Understanding the working principles, creating the robot arm kinematic model, hardware designs, integration

on the robot arm, for achieving the movement of the robot arm in response to the contact force on the Octocan.

This chapter is organized as follows: Section 5.1 describes hardware, software setup and kinematic modeling of the Resquared robot arm with the Octocan. Section 5.2 introduces the integration of the off-the -shelf force sensing resistor known as Flexiforce sensor. Section 5.3 introduces and describes a physical human-robot interactive component, “Octocan”. It’s hardware component and present work done to integrate it to the Resquared Arm is discussed.

5.1 Resquared Arm – A Robotic Arm

The HEBI robot arm demo model' Resquared arm® as shown in Figure 75 is a 6 degree of freedom manipulator designed exclusively for research institutions and universities, where they may quickly integrate their own controller and application concepts. Exploring Physical Human-Robot Interaction (pHRI) applications was our main goal.

Figure 75 6-DOF RESquared robot arm

In recent years, the dynamic trend in sectors such as product manufacturing, automobile, health and so many others have laid an increasing demand on the production of utility robots suited for their kind of operations thereby increase the concerns of safety as it relates to human-robot co-existence. Dynamical modelling of robot within its typical environment have been studied in recent times however the force control and its direction in contact proximity is still much studied today to increase the safety of operation and enhance physical huma-robot interaction. Position control and force control are the two categories the control of a robot can be analyzed and ascertain in.

Although drawing attention recently, yet the application isn't broad across all regions as it should be. However, in the near future, we hope to witness the adoption of more enhanced robot dexterity in several environment such as hospitals, entertainment, assembly and space. Understanding the behavior of physical or robotic systems is key to evaluating and investigating the performance of models and designed prototypes. That is, the analysis of kinematics and dynamical equation are crucial studies that should be carried out in considering the motion of the robot before the forces its dependent on.

The properties of the robot arm relative to timed based motion and geometry of how it links move in respect to one another is explained in its kinematic modelling. This is the description of the position and orientation between the end-effector and its joint variables. The information of its kinematic modelling makes it possible to simulate in computational software such as Robo-analyzer. In addition to this is, a URDF, Universal Robot Description Format could be created for a more detailed description of the robot. The URDF could then be used in RVIS and ROS-Gazebo simulation environment for further analysis of the robot's motion. Kinematic modelling is divided into the forward and inverse, the forward kinematics evaluates the cartesian position and orientation after been given the mechanism's joint coordinates. While the inverse takes account of the end-effector position relates to the fixed frame to produce the joint variables and this could be quite complex.

5.1.1 Hardware setup

Assembling the hardware to function as intended, a power supply unit with the specification of 4A input current, producing an output of 14.6 A at 240volts is connected to a voltage regulator that in-turn provides a steady DC power at a voltage threshold Vth of 75volts. Setting up the communication port, a wireless router, TP-link 450Mbps connect the system software interface with the Robot arm through a LAN cable. The connection is displayed in Figure 76.

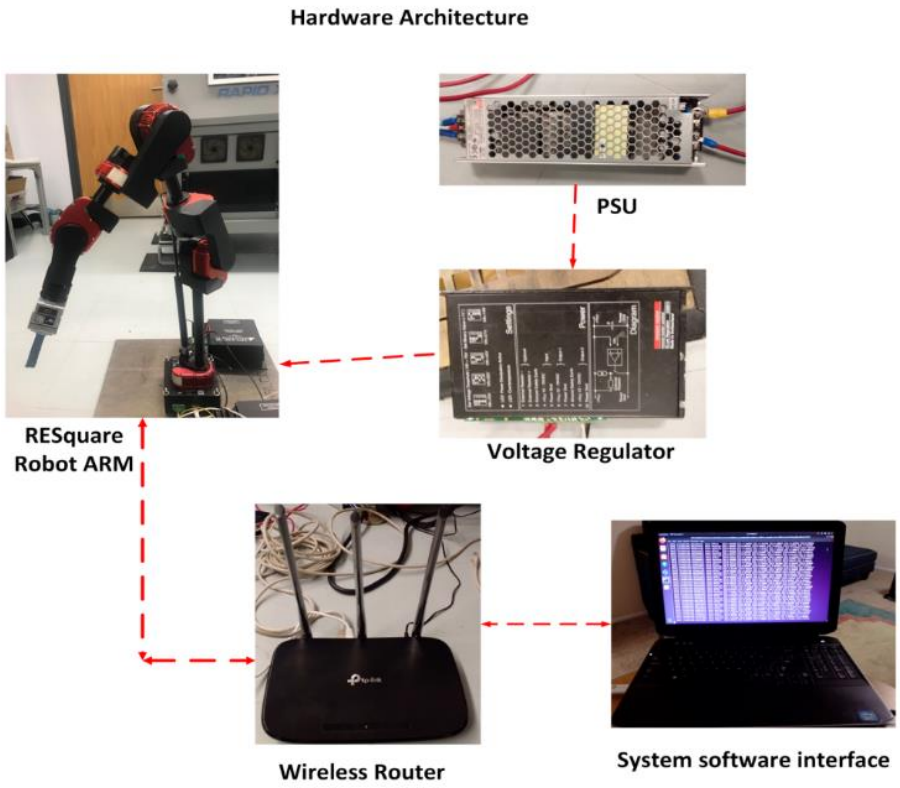

Figure 76 Hardware Components connected with the RESquared Robot Manipulator

5.1.2 Software Framework

There are three distinct portions in the framework. The collection of Data, processing, and transformation of sensor data into required manipulator angle to accomplish desired orientation. Figure 77 shows the block diagram for the software framework implemented.

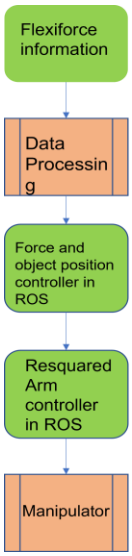

Figure 77 Block diagram of the software framework

The Resquared arm is running Ubuntu 16.04 Xenial Xerus. It operates on a high-level C++ API as well as low-level control of the robot. Resquared arm has an onboard pc running Robot Operating System (ROS) to control manipulator. ROS nodes was created to handle the sensor inputs and provide control messages for the manipulator. It also supports ROS (Robot Operating System) Kinetic Kame and offers a ROS wrapper based on the C++ API. Data are immediately published into topics. In order to construct the manipulator position angle, a subscriber processes the data and publishes it to a topic whose subscriber is the joint state publisher node that influences the robot's motion in the desired coordinates. ROS manages kinematics calculations. The "tf" (transformation) and "KDL" libraries are used to compute the transformation matrix from axis to axis (i.e., Kinematics and Dynamics Library).

5.1.3 Kinematic modelling (Denavit–Hartenberg Parameters Method)

Any robot articulation contains a certain connection between each joint and link regardless of the robot's appearance. In 1955, Jacques Denavit and Richard Hartenberg

proposed a method to reveal this internal relationship by assigning four parameters to each articulation: two angles relate rotation axis and rotation motion, two lengths indicate distance of each link and displacement if the joint is prismatic. Later, a modified DH parameter method is proposed, instead of assigning each coordinate frame to the end of each link, modified method fix the coordinate frame to the starting of each link. In some scenarios, modified parameter has the advantage to be more intuitive. In this report, conventional DH parameter method is used.

Before filling the DH parameter table, each articulation should be assigned with a coordinate frame. The Z axis of each frame is aligned with the rotation axis if the joint is rotational or aligned with the translational axis if the joint is prismatic. Frames are numbered from zero for the base (the world frame) to the last link (the end-effector) with the number of links. The origin of each frame is located at the end of each link except the frame 0, which located at the starting end of first link. The X axis is the common perpendicular between each Z axis, starting from Z_0: if the Z axes are parallel, choose X axis to simplify the overall structure. To finish frame assignment, assign Y axes by right hand rule.

To represent a robot in conventional DH parameters a conventional DH parameters assignment is done as shown in Figure 78. A base frame is assigned at the root of the first link, also it's the first joint, named as frame 0. However, to fulfil the simplification purpose, X_0 is chosen to be the same with X_1. Figure 5 shows all the assigned frames. The DH table contains N rows, N is the number of articulations, from 1 to N; and four columns. Each row corresponding to one articulation and the four columns are: α – the angle between previous Z axis and the current Z axis along current X axis by right hand rule; a – the length

of the common perpendicular between the current and previous Z axis. The above two are fixed, which means the structure of the robot decides their value. d – the distance between current X axis and previous X axis, along previous Z axis. For a prismatic joint, it is one of the joint variables; for a revolute joint, it is a constant. θ – the angle between previous X axis and the current X axis, along previous Z axis. For a revolute joint, this is the joint variable.

Since RE-Squared has six articulations with all revolute joints, parameter d in the table is constant and θ is the joint variable. A complete DH parameter table is shown in Table I.

Table 17: Complete DH table for REsquared robot

	α	a	d	θ
1	90	0	0	θ1
2	-90	0	0	θ2
3	90	a3	0	θ3
4	-90	a4	0	θ4
5	90	a5	0	θ5
6	-90	a6	0	θ6

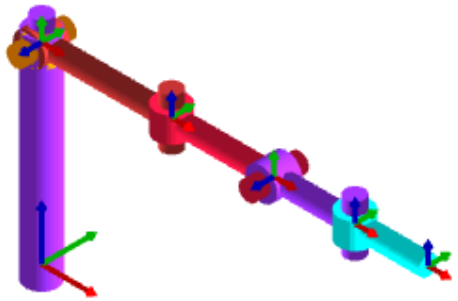

Figure 78 Conventional DH parameters assignment. The frame colored in purple is the base frame. The last one is assigned at the end-effector

Each row from the DH table can forming a standalone transformation matrix by the following equation:

$$A_i = \begin{bmatrix} c_{\theta_i} & -s_{\theta_i}c_{\alpha_i} & s_{\theta_i}s_{\alpha_i} & a_i c_{\theta_i} \\ s_{\theta_i} & c_{\theta_i}c_{\alpha_i} & -c_{\theta_i}s_{\alpha_i} & a_i s_{\theta_i} \\ 0 & s_{\alpha_i} & c_{\alpha_i} & d_i \\ 0 & 0 & 0 & 1 \end{bmatrix} \quad (5\text{-}1)$$

Similarly, the homogeneous transformation matrix derived from DH parameter is:

$$T = A_1 \cdot A_2 \cdot A_3 \cdot A_4 \cdot A_5 \cdot A_6 \quad (5\text{-}2)$$

5.1.4 Kinematic modelling (Product of Exponential (POE) Method)

Instead of revealing the essential relationship hidden within the articulation and assign frames under certain rules, the POE method defines the axis of rotation and a single point on the axis to relate each joint and link.

The end-effector's orientation and translation are also considered by comparing with the base frame. Each rotation axis is selected by its direction defined by the base frame – in order to acquire the same result with DH parameter method, the definition of the base frame for POE method must be the same with DH method – and start numbering from 1 until the last one. By apply Rodrigues' formula and POE calculation, each rotation axis can drive an exponential term $e^{\hat{\zeta}\theta}$. The end-effector's relative orientation and translation to the base frame forms a T_0 matrix. Here, one should notice that the rotation of the end-effector frame contains all three axes. The overall homogeneous transformation matrix T is acquired by multiplying all above elements together:

$$T = e^{\widehat{\zeta_1}\theta} \cdot e^{\widehat{\zeta_2}\theta} \cdot e^{\widehat{\zeta_3}\theta} \cdot e^{\widehat{\zeta_4}\theta} \cdot e^{\widehat{\zeta_5}\theta} \cdot e^{\widehat{\zeta_6}\theta} \cdot T_0 \quad (5\text{-}3)$$

5.2 Sensors [Flexiforce sensors]

The likelihood of physical human-robot interaction increases, as do safety issues, as robots begin to perform well outside of small, factory settings. Even though recent research has made great use of vision systems, pHRI calls for quick and immediate action. Despite all of its benefits, the visual servo system's performance is constrained by the camera's processing delay. When it comes to ensuring human safety, simply having one set of environmental awareness is insufficient. The skin that covers a vast percentage of the human body has the ability to feel force, temperature, and touch. If we wish to improve the pHRI system's efficiency, robots also need a sizable sensory system. For interaction with the environment, eyesight alone is insufficient. The dispersed sensor skin can enhance a robot's perception of its surroundings, which enhances pHRI performance. In order to interpret haptic information from humans in the sense of pushing force, four piezo-resistive force sensors were mounted on the robot. The Force Sensing Resistor (FSR), an off-the-shelf piezoresistive pressure sensor from Tekscan known as Flexiforce as shown in Figure 79, is a force sensor whose resistance value changes under mechanical stress. It is more accurate linearity (3%). They are reasonably priced and strong enough to withstand most situations. With a maximum 5-sec response time, the resistance can adjust from infinity to 50K and can support up to 100lbs. A thin, flexible substrate serves as the foundation for the sensor. Resistance varies as pressure is applied to the circular region. The sensor measures approximately 2.25" in length over".

Figure 79 Tekscan's Flexiforce Sensor

Usually, a series resistor is used with these sensors to create a voltage divider. Depending on the force applied on the sensor, voltage across series resistor will change. In order to find an optimal resistor, we used:

$$\left(\frac{f(x)}{g(x)}\right)' = \frac{f'(x)\cdot g(x) - f(x)\cdot g'(x)}{g^2(x)} \tag{5-4}$$

The difference *VMAX- VMIN* has an extremum:

$$\frac{d}{dR_x}\left(\frac{R_{MAX}}{R_{MAX}+R_x} - \frac{R_{MIN}}{R_{MIN}+R_x}\right) = 0 \tag{5-5}$$

Solving for R_x gives

$$R_x = \sqrt{R_{MAX} \,.\, R_{MIN}} \tag{5-6}$$

5.2.1 Hardware Setup

The Flexiforce integration setup consists of four Flexiforce mounted on to end effector of the robot arm, a connecting cable ran through the symmetry of the robot till it reaches the fixed base and then onto the circuit board. Also included are the resistor, bread board, Arduino mega 2560 and jumper wires(colors red, grey and Blue). The red jumper wire with the 5V source on the Arduino, the grey wire is connected with the ground, the blue is connected to the analog pin. The voltages are read with the Arduino's analog pin

A0 Inserting the Flexiforce sensor and the resistor(10K) into the bread board, they are connected in series. With this connection between the Flexiforce and resistor, it makes the circuit a voltage divider as shown in Figure 80. By establishing the connection, there is varying voltages for different force or pressure values generated with the Flexiforce sensors. With one leg connected in series with the resistor the other is connected to the 5V supply. With the blue wire coming from the analog pin A0 of the Arduino, the other end connected between the Flexiforce sensors and resistor (Note: to measure higher pressure or force a smaller value of resistor can be used). And then connect the ground jumper wire with the remaining leg of the resistor. Finally, we connect the capacitor in parallel to the resistor to prevent drifts and inconsistency with the readings.

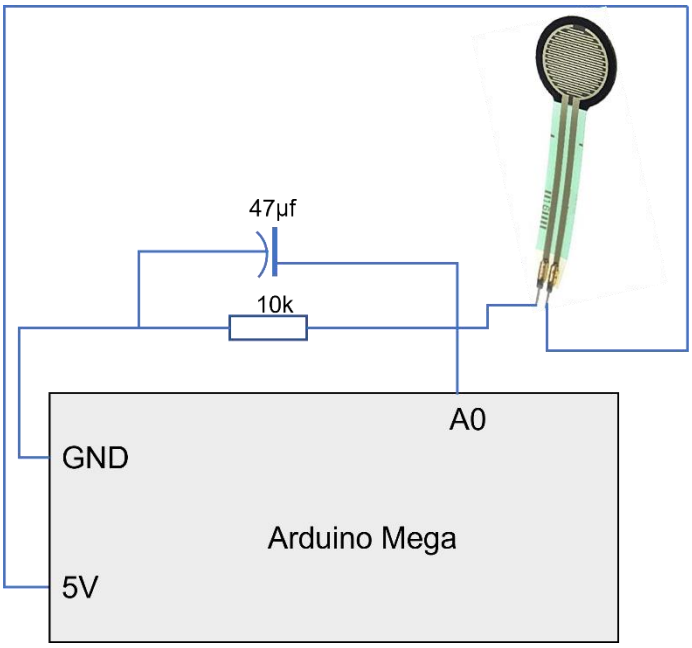

Figure 80 Flexiforce connection circuit

5.2.2 Kinematic

The Flexiforce Sensors is placed at locations we termed as the points of interaction "P," which can be found anywhere along the chain but presently placed at the end effector.

The forward kinematics map from the robot base to a point P of application of the force is provided by Q×R3→SE(3) using the product of exponentials formula is given by.

$$g_{st}(q,p) = (\prod_{i=1}^{j} e^{\xi_i q_i})\, g_{st}(0,p) \qquad (5\text{-}4)$$

If q_i's are joint coordinates, ξ_i's are the link twists, and j is the robot link where the force is applied are the link twists given by:

$$\xi_i = \begin{bmatrix} -w_i \times v_i \\ w_i \end{bmatrix} \qquad (5\text{-}5)$$

where $v_i \in \mathcal{R}^3$ is a point on the twist axis and $w_i \in \mathcal{R}^3$ is a unit vector in the direction of the axis. The base to end-effector transformation matrix often has the following definitions:

$$g_{st}(q,p) = \begin{bmatrix} R(q)_{j+1}^{0} & p(q) \\ 0 & 1 \end{bmatrix} \qquad (5\text{-}6)$$

To achieve change in position from a current position x to the next position $x + 1$ as shown in Figure 81. Where F_s is the force applied to point S changing the initial positions of x to x', $y\ to\ y'$ or $z\ to\ z'$.

$$[x' - x\ y' - y\ z' - z] = \varepsilon \cdot F_s \qquad (5\text{-}7)$$

$$x' = x + \varepsilon \cdot F_s \qquad (5\text{-}8)$$

$$\theta_{x+1} = \theta_x + \alpha J^{-1} F_s \qquad (5\text{-}9)$$

Where ε is equals to αJ^{-1}, α is the gain factor and J^{-1} is the inverse kinematics Jacobian while θ_{x+1} is the new angle of change with the next position $x + 1$ from the initial position x and angle θ_x

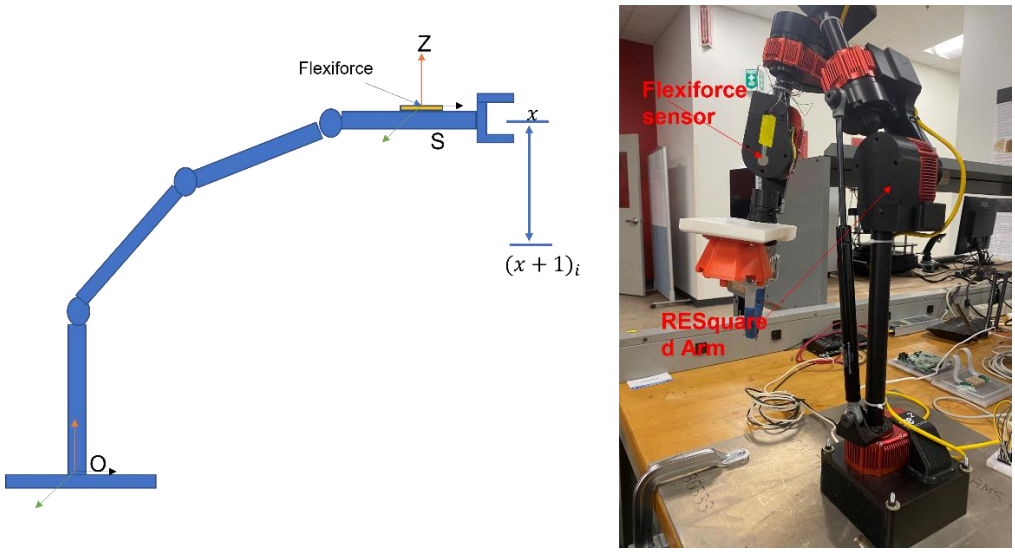

Figure 81 block diagram illustration of Flexiforce sensor on a robot arm

Using orientation model the Position change will be given as :

$$q(x+1) = q(x) + q_r(x) \qquad (5\text{-}10)$$

where $q(x)$ denotes the joint's current position, $q(x+1)$ denotes its next position, and q_r denotes the joint's intended position as determined by the admittance model and inverse kinematics.

Since $q(x+1) \approx q(x)$, q_r must be as minimal as feasible, which is simple to do by raising the admittance model's parameters. The robot's inverse kinematics is used to determine the position q_r. The use of an orientation model in the robot's present position, however, allows us to avoid it. This orientation model, which does not require the use of the robot's inverse kinematics because the joint displacements are modest, helps to establish a direct relationship between the orientations and the joint angles.

Each orientation component in the present pose can be written as a linear combination of the joint angles using robot geometric relations. The Flexiforce force-sensor torques (τx,

τy, τz) are used to derive the three orientations (α, β, γ). These three orientations make up the joint angles. In order to satisfy the linear combination of the orientation given below, the other joint angles can be calculated from the forces of the Flexiforce sensor (F_x, F_y, F_z)[97].

$$\alpha = \sum_{i=1}^{j} (p_i q_i + h_i), \beta = \sum_{i=1}^{j} (p_i g_i + h_i), \gamma = \sum_{i=1}^{j} (p_i g_i + h_i) \quad (5\text{-}11)$$

Where q_i is given as the i-th joint angle, q = [q_1 ... q_n], p_i and h_i are the orientation offset that is determined by the robot configuration.

We can show the calculation method for the orientations of the 5 dof Resquared arm configurations in relation with the joint angles.

$$\alpha = q_1 \, , \beta = -q_2 - q_4 - q_6 \, , \gamma = \, q_3 + q_5 \quad (5\text{-}12)$$

A linear combination is observable in the β and γ orientation and can be divided in the following terms for $\gamma = q_1 + q_5, \ \beta = \ \beta_2 + \beta_4$. Then the force and torque component of the Y and Z direction can be used to generate the terms

$$q_3 = \ \gamma_{q3}, \ \ \gamma_{q3} = admit(\tau_x) \quad (5\text{-}13)$$

$$q_2 = -\beta_{q2}, \ \beta_{q2} = admit(f_x) \quad (5\text{-}14)$$

$$q_1 = \alpha, \ \alpha = admit(f_y) \quad (5\text{-}15)$$

$$q_4 = -\beta_{q4}, \ \beta_{q4} = admit(f_x) \quad (5\text{-}16)$$

$$q_5 = \gamma_{q5}, \ \gamma_{q5} = admit(\tau_x) \quad (5\text{-}17)$$

$$q_6 = -\beta_{q6}, \ \beta_{q6} = admit(f_x) \quad (5\text{-}18)$$

.

5.2.3 ROS Implementation

Integrating the Flexiforce sensor with the Resquared arm requires the implementation of ROS communication protocol for receiving physical contact data metrices in actual real time coordinates, processing them using orientation model, robot dynamic information and robot arm configuration data expressed in it URDF. To establish this software connection aside the hardware set up connection earlier described in section 5.1.1, the complete URDF must be known. The joint state publisher and robot state publisher should be created and ascertained for the transfer and exchange of data in joint coordinates or transforms via topics through the nodes. This allows us to find the orientation and position of sensors relative to the base frame. The Joint state publisher created publishes the current positions of every joint, sends to the robot state publisher. While the robot state publisher node taking the URDF that completely describes the robot arm in detail gets the transformation from the base link to end effector attached to the 6^{th} link and publishes to the TF topics in ROS, returning the results in quaternions, roll, pitch, yaw and rotational matrix. Figure 82 shows a physical contact of a Flexiforce sensor attached to the Resquare arm.

Figure 82 Physical contact with mounted Flexiforce sensors

Mapping out the force vector components (F_x, F_y, F_z) responsible for movement the arm to the next pose or position from the base frame of the Resquare arm to the Flexiforce sensors attached to the end effector is very crucial. The vector components are determined by the multiplication of the perpendicular force component acting on the Flexiforce sensor and rotational matrix from the base frame O to the location of the Flexiforce sensors at the end effector S as shown in Figure 75 is given as:

$$R_S^o \cdot \begin{bmatrix} 0 \\ 0 \\ F_z \end{bmatrix}_s = \begin{bmatrix} F_x \\ F_y \\ F_z \end{bmatrix}_o \tag{5-19}$$

Where $R_s^o \in \mathcal{R}^{3\times3}$represents the rotational matrix from the base to the location of the Flexiforce sensor, $F_z \in \mathcal{R}^{1\times3}$is the perpendicular force or torque component interacting with the Flexiforce sensors.

This perpendicular force component exerted by human interacting with the robot arm via the Flexiforce sensors is directly proportional to the float voltage generated from the analog-digital conversion of the ADC reading.

$$\begin{bmatrix} F_x \\ F_y \\ F_z \end{bmatrix}_o = \begin{bmatrix} v_x \\ v_y \\ v_z \end{bmatrix}_o \tag{5-20}$$

This float voltage reading is processed by the C++ control script (Admittance model) to sending commands through the Robot Operating System to the Hebi joint motor to new orientation and position based on the extent of interaction with the sensors. The ADC reading to float voltage conversion is given as:

$$float\ voltage\ (v) = ADC\ reading \times \frac{5\text{V}}{1024} \tag{5-21}$$

This leads us to equating force components to ADC reading and its conversion to its proportional voltage that is required to move the robot arm to the new pose or position. Using measured weights in grams, 10, 20, 50, 100, 200, 500, ADC value was recorded, the corresponding force in newton was calculated using equation (5-25) and corresponding voltages were recorded and shown in the table below.

$$F = \frac{Mass\ (grams)}{1000} * 9.8\ \frac{Meters}{Sec^2} \qquad (5\text{-}22)$$

Table 18: measured weight voltage equivalence

Mass(grams)	ADC Value	Force (Newtons)	Voltage
10	40	0.098	0.04887586
20	50	0.196	0.09775171
50	160	0.49	0.24437928
100	180	0.98	0.48875855
200	260	1.96	0.97751711
500	350	4.9	2.44379277

It is important to note that the ROS default format for expressing orientation and positional vectors is in quaternions and so the first step to implementing the force components derived from physical contacts with the Flexiforce sensors either for translation or rotation is to first convert from quaternions to rotation matrices. To do this we implement the TF ROS library utilizing the KDL rotational matrix tags and executables under the heading "*tf::quaternionToKDL(link2base_transform.getRotation(), rot);"*. And this converts all the quaternions into rotation matrices recognizable by ROS to implement the subsequent written codes.

Setting up the force vector components which is directly proportional to the generated voltages as shown in equation (5-25) in a 1×3 matrix is represented in the Y and Z axis in the quantity of our Flexiforce sensors. And it is given as $[0,0,voltage], [0,0,-voltage]$ for the Z axis component and $[0,voltage,0], [0,-voltage,0]$ for the Y axis component. These voltage matrices also equivalent to the 1×3 force matrix $[Force_x, Force_y, Force_z]$ is summed up in all the Y component and summed in all the Z components to give direction to the magnitude of force contact as shown in the equation (5-27) & (5-28)below:

$$Force_{sum\,y} = Force_{1,y} + Force_{2,y} + Force_{3,y} + Force_{4,y} \quad (5\text{-}23)$$

$$Force_{sum\,z} = Force_{1,z} + Force_{2,z} + Force_{3,z} + Force_{4,z} \quad (5\text{-}24)$$

In Figure 82, the result shows the change of orientation of the end effector in respect to the accumulate magnitude of the voltage converted based on the impact of force applied to the tactile sensors.

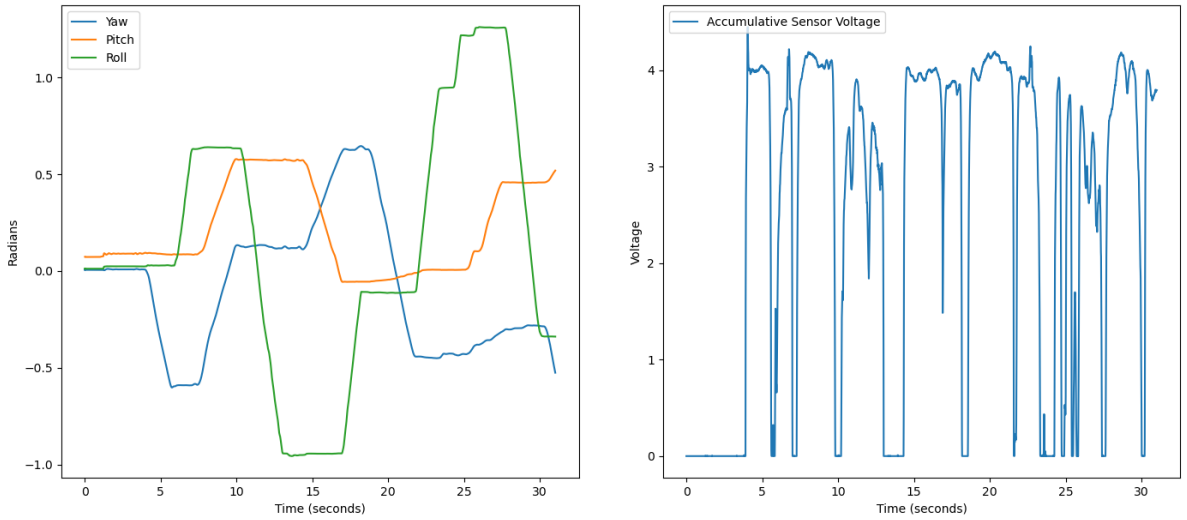

Figure 83 change of orientation with respect to force impact in terms of voltage

While Figure 83, shows the results of the change of orientation of the end effector presented in radian and also the designated input of each of the four Flexiforce sensors attached to the Resquared arm.

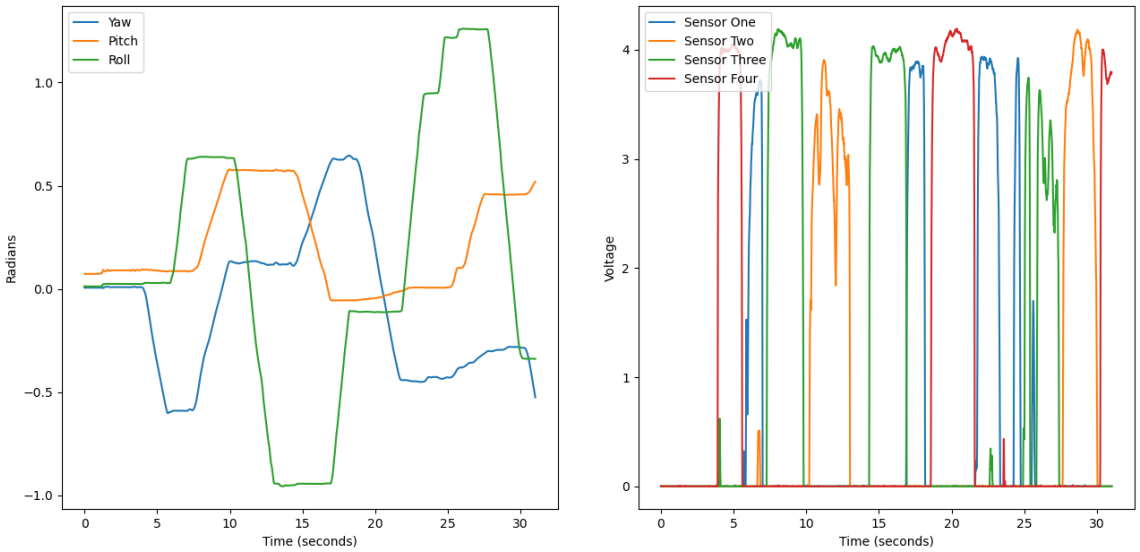

Figure 84 The tactile response of the Flexiforce sensors with respect to the change in orientation

5.3 Octocan For Physical Human Robot Interaction

The demonstration of physical human-robot interaction with the RESquared arm consists of a force sensor integration through a hardware interface known as the Octocan The "Octocan" as the name implies is an eight sided 3-D Printed can made of PLA. The printing specifications is defined at an extruding temperature of 220°C, Bed Temperature of 65°C, layer thickness of 0.32inches, layer width is 0.5inches and a print speed of 120mm/s. The print time for a complete 3-D printed can is 9hours. Shown below in Figure 85 is the picture of a complete octocan.

Figure 85 3-D Printed Octocan

The Octocan an integrated hardware component as shown in the illustrative design in Figure 85 to fit the last joint right beside the end effector to guide the trajectory of the Resquare arm enhancing the collaboration with humans as seen in Figure 86.

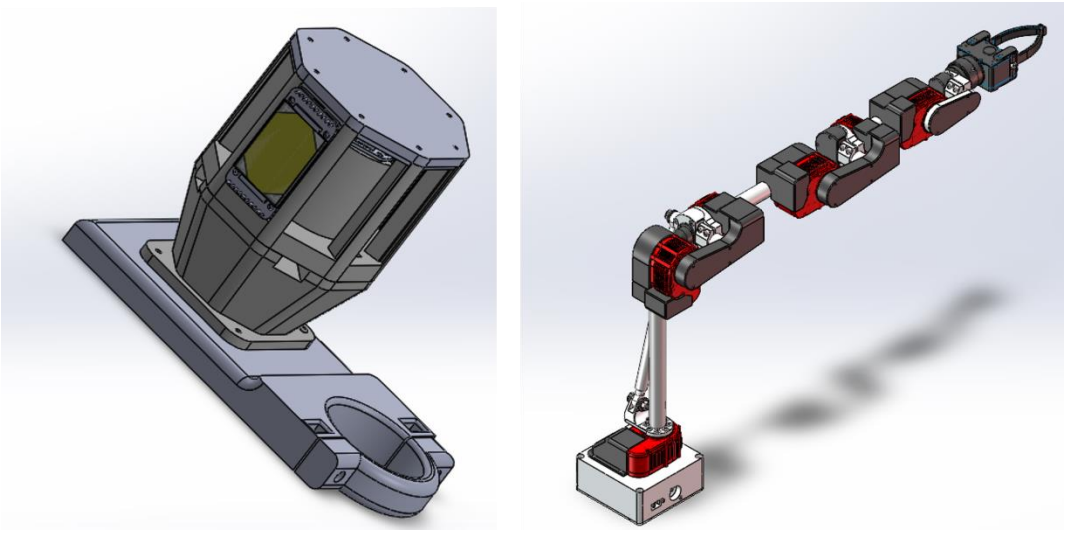

Figure 86 Octocan and Resquared arm solidworks design

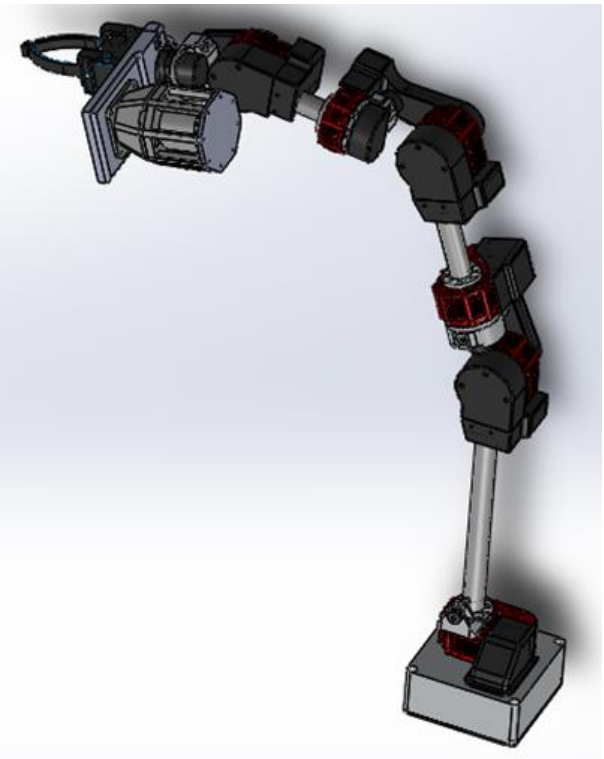

Figure 87 Octocan and Resquared robot arm assembly

The model of the Octocan and Resquared arm were designed in solid works and assembled as shown in Figure 86. The integrated hardware component houses eight skin sensor patches which is shown in Figure 87 which is responsible for the force control within its contact environment. OctoCan's surface has eight openings and slots that can fit eight encapsulated SkinCell sensors. Each sensor has a separate circuit board that handles power supply, signal conditioning, and analog-to-digital conversion. Figure 88 (a) depicts an exploded view of a complete SkinCell sensor and its circuit board, while Figure 88 (b) depicts the OctoCan, which consists of a body with eight sensors and a detachable base that can be screwed onto a surface. To coordinate A/D conversion and serial data transmission to a PC, a microcontroller unit (MCU) board and master power supply circuit

are concealed inside the OctoCan body. Each sensor circuit is connected to the MCU using flexible flat cables (FFC).

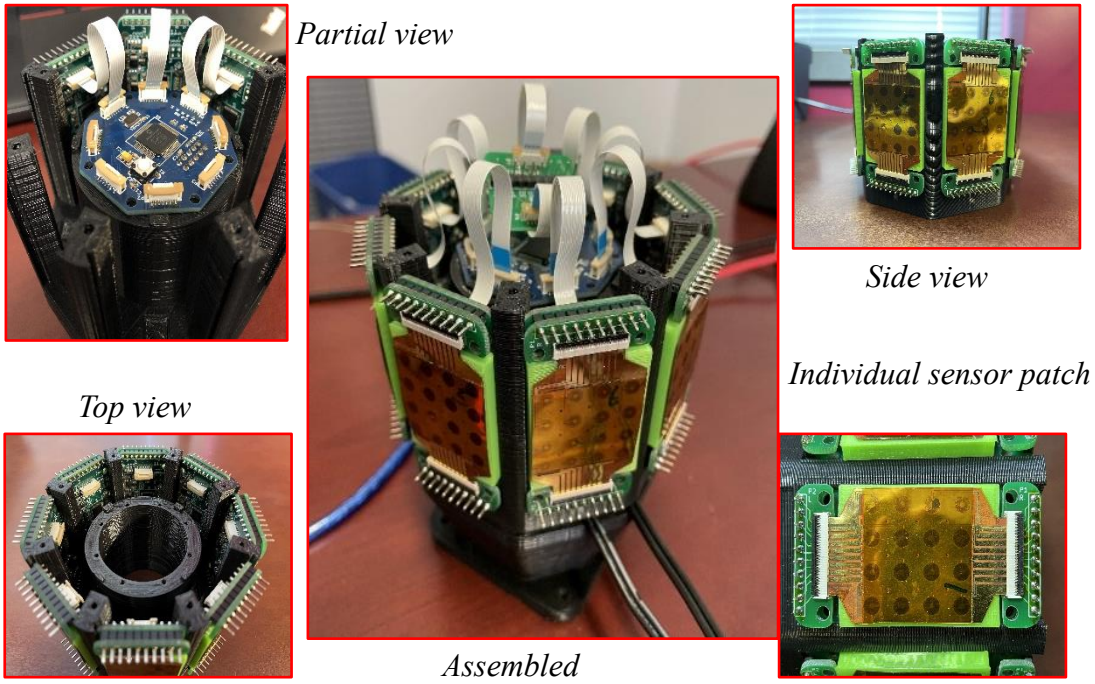

Figure 88 Complete assembly of an Octocan integrated with Robot skin sensors

Data from each of the eight sensor patches is collected round-robin style by an MCU running a bespoke firmware. Through a Serial Peripheral Interface (SPI) bus and serial connection with a USB dongle connected to the PC, the MCU communicates with each ADC chip. Registers can be used to set the ADC conversion rate, SPI transmission rate, and serial transmission rate. The OctoCan electronics perform two key functions: first, they digitize sensor readings, and second, they gather and communicate the newly transformed data back to the PC for processing and viewing. As the workload is split between the ADC chips and the MCU, Figure 89 illustrates their respective workloads using two timelines. We implemented eight ADC chips because there are eight patches.

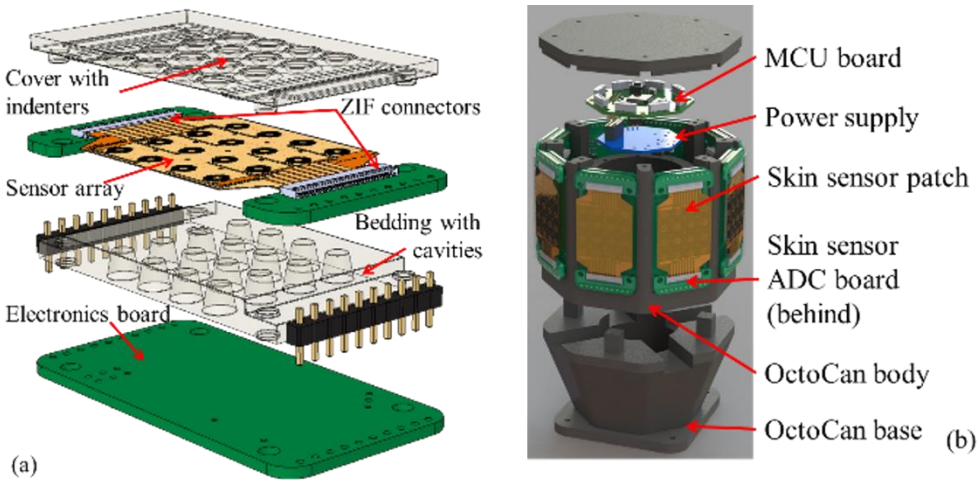

Figure 89 a) the skin sensor patch supporting electronics b) octocan electronic circuit

Each ADC requires 108 seconds to complete a sample and conversion cycle in order to guarantee conversion accuracy. The timeline is separated according to it because it takes longer to complete than other tasks. Each job slot is identified by the ADC number and is designated as Windows 1, 2, 3..., 8. The MCU gathers digitalized data from the ADC(n) and transmits it back to the PC at the window (n+1), parallelizing the two timelines. For instance, windows receive and send data from ADC.

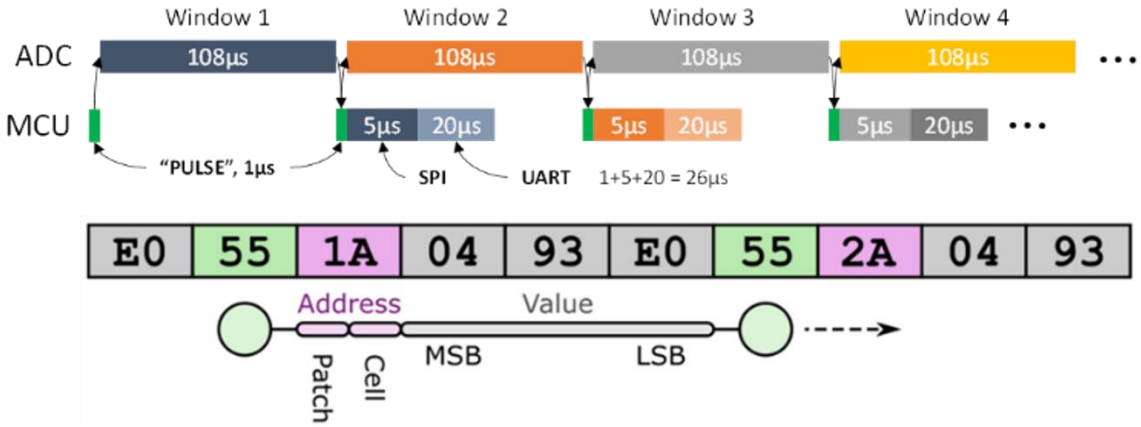

Figure 90 Octocan ADC and MCU timelines implemented in its electronics

We designate sensor tactile (T) on each patch as 0 to 15 (0x0f) and sensor patches (P) as 1 to 8 (0x08), allowing them to be integrated into a single byte. For instance, "(P1 T1)" is the name of the second sensor tactile on the first sensor patch. If all of the digits are hexadecimal, the 128-sensor tactile are scanned in the following order: (P1 T0), (P2 T0), (P3 T0)..., (P1 T1), (P2 T1), (P3 T1), till (P8 Tf). With this numbering scheme, we are able to align the communication between the MCU and the PC by adding an address byte and a starting byte of 0x55 to the beginning of each transformed data. Simply put, the address byte combines the patch number and unit number, as in Figure 89, where "1A" denotes patch 1 and tactile 0xA.

5.3.1 Octocan Kinematic modelling (Denavit–Hartenberg Parameters Method)

Integrating the Octocan to Resquare robot arm, changes the kinematic modelling of the assembly. So therefore, is it important to revise the DH parameters in order to achieve its correct homogenous transform. Earlier express is the DH notation of the Resquared arm in section 5.1.3 expanding that would require the addition of two link. The base frame of the octocan extending from its attachment to the Resquared’s end effector link and finally the last link upholding the mounting of the robot skin sensor patch. The Denavit–Hartenberg is expressed below.

Table 19: Complete DH table for REsquared robot

	α	a	d	θ
1	90	0	0	θ1
2	-90	0	0	θ2
3	90	a3	0	θ3
4	-90	a4	0	θ4
5	90	a5	0	θ5
6	-90	a6	0	θ6
Complete DH Table for Octocan				
7	-90	a6	0	Θ7
8	0	a7	d1	180

The homogeneous transformation matrix derived from DH parameter will be expressed as:

$$T = A_1 \cdot A_2 \cdot A_3 \cdot A_4 \cdot A_5 \cdot A_6 \quad (5\text{-}25)$$

$$To = A_7 \cdot A_8 \quad (5\text{-}26)$$

$$T_t = T \cdot To \quad (5\text{-}27)$$

$$T_t = A_1 \cdot A_2 \cdot A_3 \cdot A_4 \cdot A_5 \cdot A_6 \cdot A_7 \cdot A_8 \quad (5\text{-}28)$$

Where T is the transform for the Resquare arm, To is for the added links from the Octocan. The new transform for the eventually assembly will be defined as the multiplication of all of them together represented by T_t.

5.3.2 Octocan Kinematic modelling (Product of Exponential (POE) Method)

Deriving the kinematic modelling using product of exponential method requires defining the axis of rotation and a single point on the axis to relate each joint and the link includes those of the octocan with the Resquare arm.

Where the Resquare arm configuration is represented as:

$$T_{RES} = {}^{6}_{0}T = e^{\widehat{\zeta_1}\theta} \cdot e^{\widehat{\zeta_2}\theta} \cdot e^{\widehat{\zeta_3}\theta} \cdot e^{\widehat{\zeta_4}\theta} \cdot e^{\widehat{\zeta_5}\theta} \cdot e^{\widehat{\zeta_6}\theta} \cdot T_0 \tag{5-29}$$

Where T_0 is the transform at zero configuration, $e^{\widehat{\zeta_i}\theta}$ is the term representing the exponential for rotation axis of each link. So therefore, integrating the two presumed joints of the Octocan to the Resquared arm will give an expression shown below assumed one of the joint is a revolute based on its attachment to the last robot's rotating joint and the other a stationary joint where octocan is attached to the plate:

$$T_{oct} = {}^{7}_{6}T . {}^{8}_{7}T \tag{5-30}$$

Where ${}^{7}_{6}T$ is the transform from 6th link of the Resquared arm to the first link of the Octocan and ${}^{8}_{7}T$ is representing the transform of the last link of the Octocan.

$${}^{7}_{6}T = e^{\widehat{\zeta_7}\theta_7} \tag{5-31}$$

$${}^{8}_{7}T = e^{\widehat{\zeta_8}\theta_8} \tag{5-32}$$

$where\ \zeta_7 = \begin{bmatrix} w_7 \\ v_7 \end{bmatrix}\ w_7 = \begin{bmatrix} 0 \\ 0 \\ 1 \end{bmatrix}, v_7 = \begin{bmatrix} 0 \\ 0 \\ 0 \end{bmatrix}, \qquad \theta_7 = 0, \qquad \zeta_8 = \begin{bmatrix} w_8 \\ v_8 \end{bmatrix}\ w_8 = \begin{bmatrix} 0 \\ 0 \\ 0 \end{bmatrix}, v_7 = \begin{bmatrix} 0 \\ 0.127 \\ 0 \end{bmatrix}, \theta_8 = 0, 45, 90, 135, 180, 225, 270, 315.$ Where θ_8 represents the 45° degrees angle displacement of each of the eight-skin sensor patch of the Octocan in respect to the origin.

So, the total homogeneous transform of Resquared arm + Octocan at point of origin to the sensor patch will be given as:

$$T_{total} = T_{RES} \cdot T_{Oct} = {}^{6}_{0}T \cdot {}^{8}_{6}T. \begin{bmatrix} 0 \\ 0 \\ 0 \\ 1 \end{bmatrix} \quad (5\text{-}33)$$

While the total homogeneous transform of Resquared arm + Octocan at a vector perpendicular to the sensor patch will be given as:

$$T_{total} = T_{RES} \cdot T_{Oct} = {}^{6}_{0}T \cdot {}^{8}_{6}T. \begin{bmatrix} 0 \\ 0 \\ 1 \\ 1 \end{bmatrix} \quad (5\text{-}34)$$

5.4 ROS Visualization of Resquared Arm and Octocan Integration

To visualize the robot arm assembly of the Resquared arm and the Octocan, the complete solid works model must be defined in format understood by the Robot Operating system (ROS). The model attributes of the robot arm are described in the Unified Robot Description Format (URDF) presenting a model file consisting of its joint, link and transmission mechanism. The URDF model is a collection of files that describe a robot's physical description to ROS. These files are used by ROS (Robot Operating System) to tell the computer what the robot actually looks like in real life and to create its visualization in ROS and control in gazebo. The link attributes give details of the robot link in aspects of visual, collision and inertial properties, the joint attributes dwell on the joints range of motions and its limitation. The transmission attributes focus on the transmission mechanism and gear ratio. Present in the model files is the system Semantic Robot Description Format (SRDF), this is responsible for loading model files, commands implementation, receiving parameters and result planning as shown in Figure 90. The final

attribute is the Config Formats, this is responsible for sending command prompts to the terminal and performing analysis of data such as acceleration and speed.

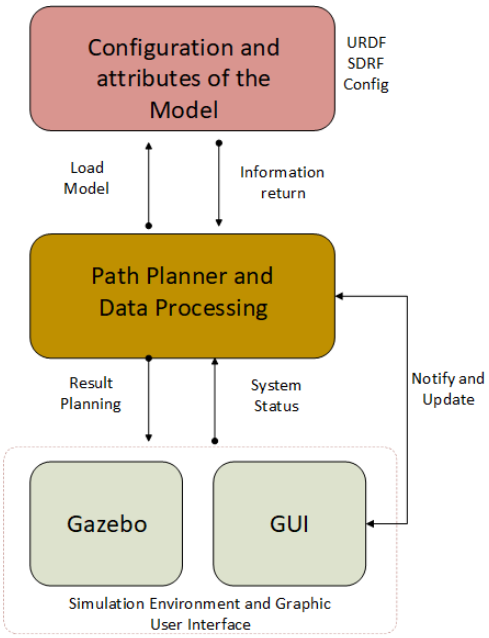

Figure 91 Model configuration and attributes in ROS-Gazebo simulation environment

Robots, sensors, and algorithms can all be shown in 3D using the software program known as Rviz (short for "ROS visualization"). It allows you to observe how the robot sees the outside environment (real or simulated). Rviz's goal is to make it possible for you to visualize a robot's status. It makes an effort to accurately represent what is happening in the robot's environment using sensor data. It incorporates a list of plugins to enable one view the robot state information, the sensor data and even visualize in hierarchy the position and orientation of the frames of a robot. Shown below in Figure 91 is the assembly of the Octocan filled with the skin sensor electronics and the Resquared arm.

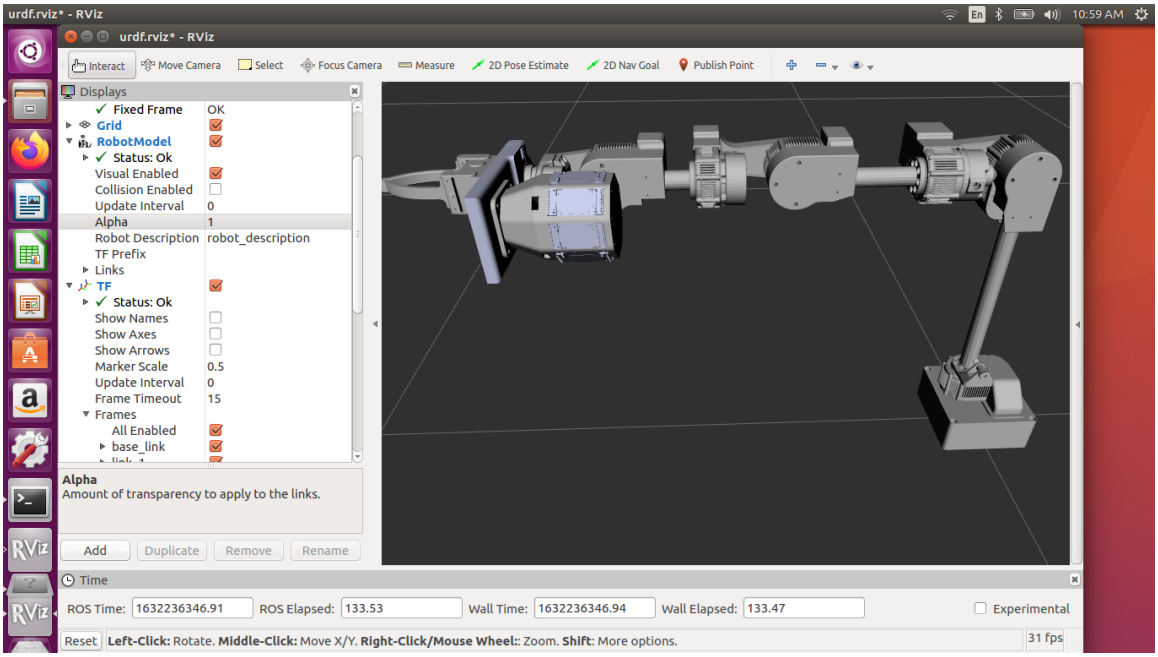

Figure 92 Octocan and Resquared Integrated in ROS with the Skin sensor circuit

Integrating the Octocan to ROS after the connection of the hardware requires a configuration as shown in Figure 92. The Octocan is connected to serial port of a Linux kennel device through a USB serial. The robot skin sensors attached to the Octocan are calibrated in the Skintalk module with a preinstalled calibration profile that defines the boundary limits of contacts and the depth of contact on each sensor patch. The calibrated signal is then sent to Skinvis python program to be visualized.

On the other hand, the calibrated signal is received through the hardware interface and delivered to the ROS node (Joy node) that then delivers the optimized signals to a subscribing node activated through the ROScore via a control script programmed in C++. This subscribed node delivers the information to the ROS controller in topics to process the information and identify the unique force-position control command sent from the

octocan to the specific joint(which controlled by the Resqaure hebi motors). Figure 93 shows a table mounted Octocan used to control selective joints of the robot arm.

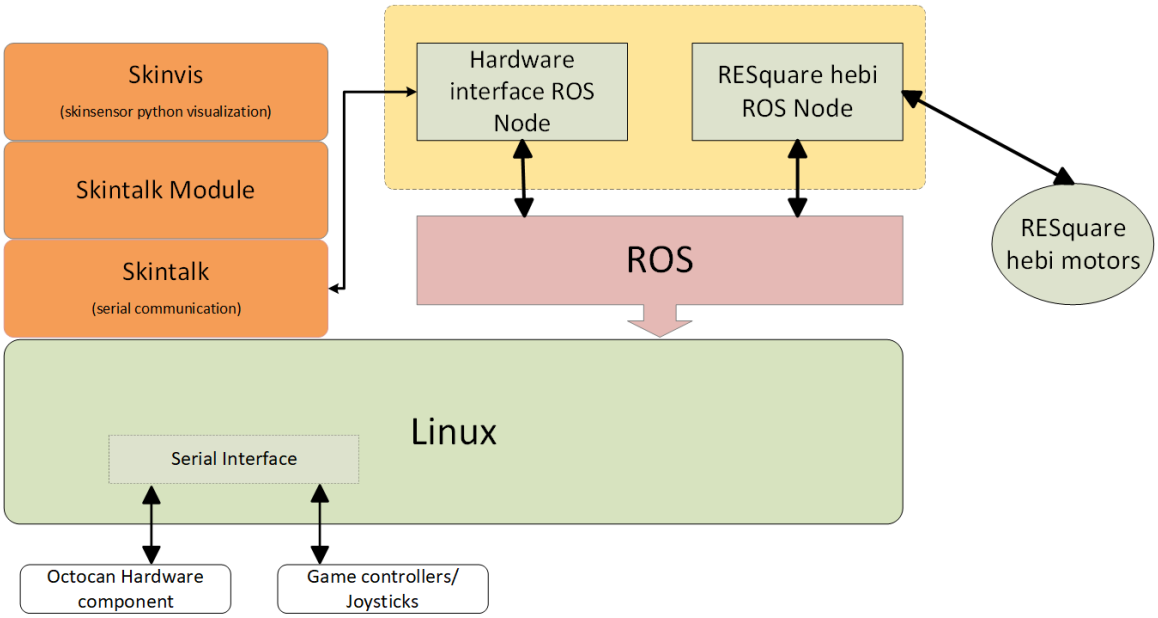

Figure 93 Octocan, Resquared Arm and ROS integration

Figure 94 Table mounted Octocan controlling the Resquare arm joints

CHAPTER 6

DESIGN, FABRICATION, AND CHARACTERIZATION OF NOVEL INKJET-PRINTED ORGANIC PIEZORESISTIVE TACTILE SENSOR ARRAYS

6.1 Introduction

In this chapter, a new design is proposed imitating the human finger print to fulfill the design criteria in [95] of increased spatial resolution achievable using inkjet printers in the NeXus microfabrication platform. As a result, our new sensors are half the size of what was previously possible. This completely substitutes the entire photolithographic fabrication process in the cleanroom with aerosol jet printing that can deposit solvent or water-based ink droplets up to 30cp in viscosity for extruding silver printed lines as sensor electrode and ink-jetting instrument for the deposition of PEDOT:PSS which is the base sensing organic polymer responsible for piezoresistive nature of the tactile sensor. We describe the fabrication procedures, including the curing of the samples in the oven, and the 4-point probe method to assess the performance of the printed sensors. As discussed in previous publications[95], [16], the organic polymer PEDOT:PSS undergoes a process preparation involving the mixture of solvents and compounds such as DMSO (Dimethyl sulfoxide) and PVP (Polyvinylpyrrolidone) to improves its wettability and reduces its viscosity making it applicable for spin coating which is not necessary with the use of Inkjet printers within the NeXus. In view of this, a suitable PEDOT:PSS stock (Clevios PH 1000) is obtained from Heraeus adaptable to the direct write jetting technique is used eliminating

the need for the preparation of PEDOT:PSS recipe and further reducing the time taken and improving the ease of manufacturing the tactile sensors. The tactile sensor described in this paper, increases the possibility of a higher spatial resolution due to its small and compact structure increasing its ability to be condensed in given area as compare to[98]. Finally, to establish the dynamic relationship between the sensor output and the measured indentation force, we employed system identification analysis on the tactile response data. We also indented the SkinCell array in 29 number of points by scanning the sample under the force load applicator tip. The experimental testing bench used for this purpose was custom designed in our laboratory. Results demonstrate the SkinCell has an average spatial resolution of 827 microns, a 1.795μV/N average sensitivity at 2.365PSI.

The article is organized as follows: section II discusses the design, fabrication and sintering process of fingerprint tactile structure, section III describes the experiment setup and electronics for testing the tactile sensor arrays and its durability. Section IV present the results and system identification of the tactile sensor and section V concludes the work discusses future work.

6.2 Design of Fingerprint single tactile sensor and arrays

A 3.80mm diameter fingerprint design tactile sensor inspired by design of the human fingerprint shown in Fig.1 is proposed in this study based of the performance simulation study of the miniaturized and compact spatial structure in. The sensor is manufactured by printing a nominal trace width of 60 microns and a printable aerosol inkjet nozzle tip of 300 microns. created . The conductivity of the NovaCentrix® silver ink is 7.05×10^6 S/m, which is comparable to the conductivity of bulk silver, which is 6.3×10^6 S/m. Equation (1) below can be used to derive the conductance of the ink conductors of our sensors.

$$G = \sigma \frac{TW}{L}, \tag{6-1}$$

In which the length of the fingerprint tactile structure printed on the flexible substrate is L=55.26 mm[99], T is the thickness of the deposited silver ink measured at 8microns, σ is the conductivity of the silver ink, and w is the width of the conductive silver line measured to be 60µm. The tactile sensor's design is depicted in Figure 95a with a diameter of 3.80mm. The conductance of the ink conductors of the tactile sensor is approximately 3.94×10^{-5} S.

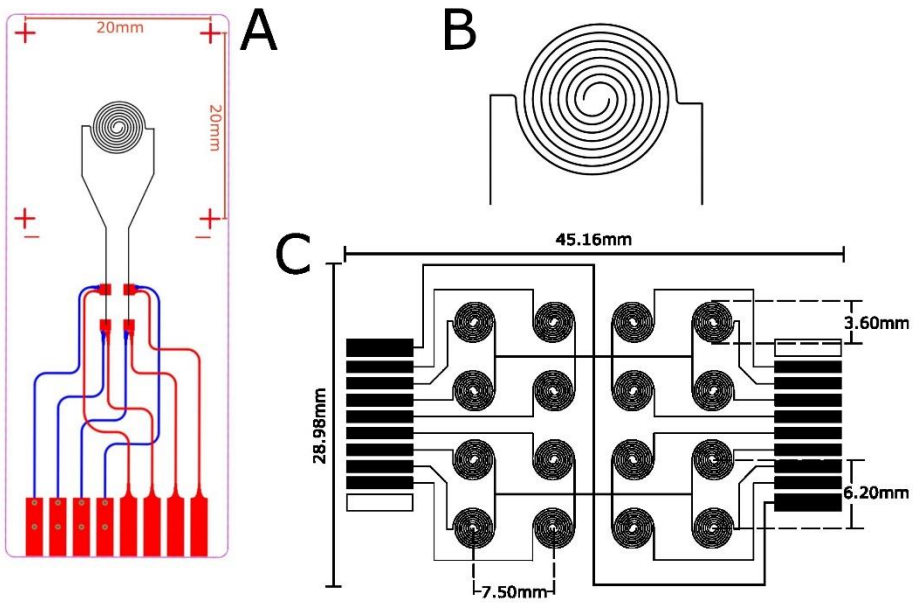

Figure 95(a) Single Fingerprint tactile on a flexible substate; b) Single tactile sensor; c) 4x4 Sensor Structure

Figure 95b on the other hand, shows the computer aided design of a 4 by 4 fingerprint structure design replicating the single tactile structure. The structure which has an overall length of 45.16 mm and a width of 28.98mm is referred to as a SkinCell consists of 16 identical sensors, all connected with a common ground and individually patterned

electrodes to corresponding connectors. These parameters were chosen in accordance with COSMOL simulation in, which highlights the significance of designs with improved spatial density and features that allow for flexibility in defining various sensor structures and resolutions. The connectors of the sensor patches are electrical pins located on the left and right side of the sensor patch accommodating eight pins each and a pin for the ground. The empty box required on each of the sides is situated somewhat as an alignment mark, not only to properly align and facilitate the back-to-back assembly of two closely match sensor patches but also to complete the half Wheatstone bridge configuration of a functional pair. These paired individual sensors referred to as "tactel" send signal response to the connectors transferring external stimulus through the connectors to electronics testing setup for data acquisition.

6.3 Fabrication of Fingerprint single tactile sensor and arrays

6.3.1 Inkjet Print System

To carry out the fabrication process as indicated in the flowchart presented in Fig. 6 a unique robotic system named NeXus is used for multiscale additive manufacturing, and it includes the OPTOMEC® Aerosol inkjet print system[100]. The inkjet printing system includes the IPL, inspection station, aerosol jet printing station and also included in the inkjet print system is a custom-built direct write inkjet printer called the Nordson EFD Pico Pulse®. A control cabinet for controlling the ink streaming process through the print head, KEWA process control software, and a 6DOF positioner for aligning the substrate to the 100 microns-nozzle tip with a 3-5 mm standoff distance make up the aerosol jet printing station. The substrate (which is either a FPC Kapton for a single sensor fabrication or a blank Kapton sheet for 4 by 4 sensor patch fabrication as shown in Fig. 96a) is positioned

on the 6DOF positioner as seen in Fig. 96b and is lined up with the print head for printing. According to the process parameters described in Table 20. The Nordson EFD Pico Pulse® used for the purpose of depositing the organic polymer responsible for the piezoresistive behavior of the tactile sensor as shown in Fig. 96f. This ink-jetting instrument has a controller that actuates the piezoelectric actuator print head attached with a 50 microns nozzle and fluid syringe. The controller was tuned to the following parameters shown in Table 21 to produce an even overlapping overlay of PEDOT:PSS.

The following dispensing parameters are typically adjusted during the print process:

- Waveform times (open/close/pulse).
- Cycle - drop dispense period corresponding to dispensing Frequency, f_d. Defines the frequency of during the printing process (1 - 250 Hz).
- Stroke - force of ink droplet ejection. Expressed in %, where maximum force equals 100%.
- Deposit Height, h (3 mm): Distance from the print head nozzle to the substrate.
- Temperature, T_f (40 °C): Temperature of the ink.
- Air Pressure, Pa (20psi): Fluid pressure in the print head valve Assembly.

Table 20: Parameters for Aerosol Jet Printing.

Sheath Flow Rate	135sccm	Print Speed	10mm/s
Atomizer Flow Rate	15sccm	Atomizer Bath Temperature	27℃
Atomizer Current	400mA	Stand-off Distance	3mm

6.3.2 Tactile sensor Inkjet Printing Trajectory

Motion and ink deposition control for the inkjet systems is realized through the LabView control interface developed for the NeXus system. The conductive fingerprint design, printed by the Optomec using NovaCentrix® JS-A426 silver ink, is realized through Line-Arc Trajectories, a machine control language unique to the Newport controllers built into the NeXus system that control the 6DOF positioner. These trajectory files enable printing of a continuous line at a constant velocity producing smooth curved features and a constant line width throughout the structure. The PEDOT:PSS thin film, realized by the Pico Pulse®, is controlled through an integrated Gcode parser built into the LabView control interface. Through this parser both deposition control and motion control are dictated. For the thin film deposition, an overlapping serpentine structure is used to efficiently and reliably deposit the PEDOT:PSS ink into a film on top of the conductive structure.

6.3.3 Tactile Sensor Sintering and Plasma Treatment

To get rid of the solvent and increase the compactness of the silver nanoparticles, the silver ink must be cured after being deposited. The particles combine and adhere firmly during the curing process, improving the conductivity. The curing procedure was carried out using a thermal scientific Lindberg vacuum oven as shown in Fig. 96c. The fabricated tactile sensor is cured in the oven for 20 hours at the temperature of 200°C[94]. The substrate upon which the tactile sensor is fabricated determines how long the thermal cure takes to complete and, in this case, the Kapton substrate is best suited for the required number of curing cycles. The oven-cured sample is depicted in the Fig. 96d below. After

oven drying, the substrate's color darkens, this is probably because the extended curing period changed the adhesive properties used to assemble the flexible printed circuit.

Table 21: Parameters For PEDOT:PPS Deposition.

f_d[Hz]	Stroke	$\boldsymbol{P_a}$ [psi]	$\boldsymbol{T_f}$ [°C]	h [mm]	$\overline{\boldsymbol{d_d}}$ (μm)	$\boldsymbol{S_d}$ (μm)
3.3	80%	20	40	3	400	10

6.3.4 PEDOT:PSS Deposition

The cured sample at this point before the deposition of PEDOT:PSS should be tested as open circuit before placing in a vacuum plasma chamber shown in Fig. 96e in preparation for the PEDOT:PSS deposition. The PEDOT: PSS is the material responsible for the tactile sensor sensitivity to strain. The reason for the Plasma treatment is to improve the wettability of the Kapton substrate. A Harrick® Plasmer Cleaner device was used to administer the plasma treatment. The substrate is placed inside the chamber, evacuated,

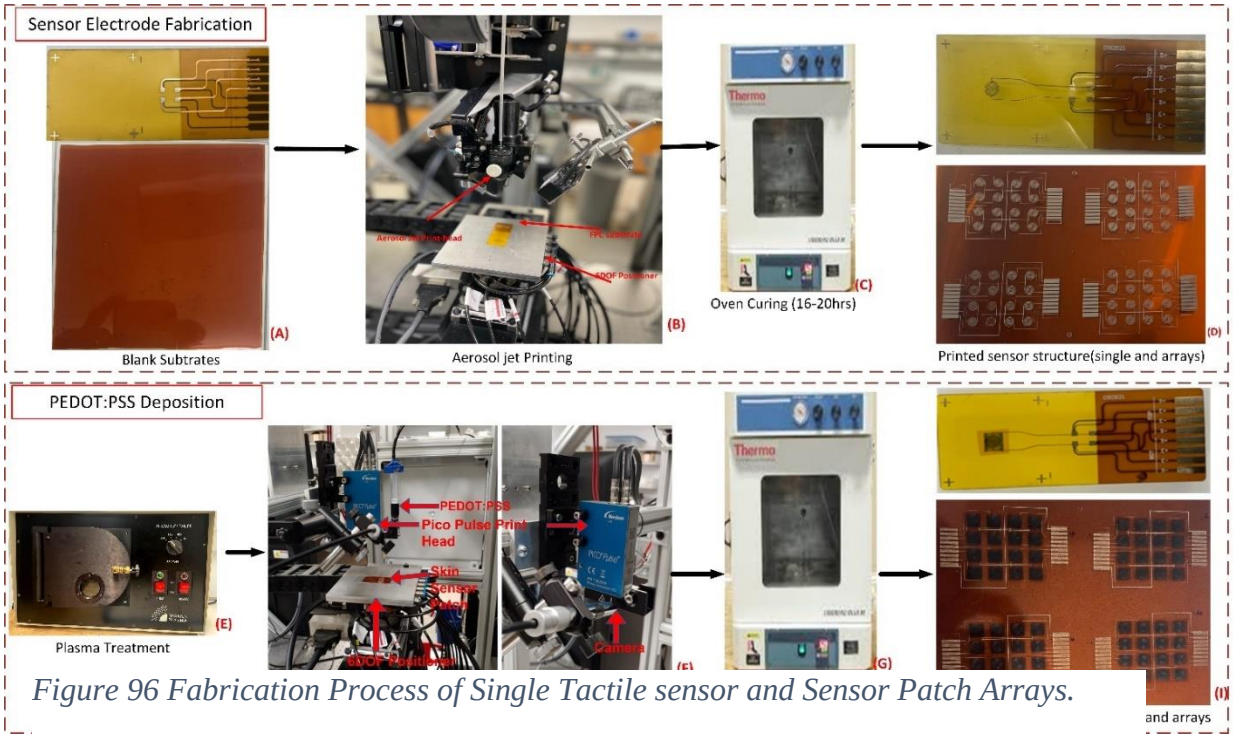

Figure 96 Fabrication Process of Single Tactile sensor and Sensor Patch Arrays.

and subjected to air RF plasma at 30W for two minutes after reaching low vacuum. The tactile sensor patterned substrate is prepared for Pico Pulse® jet printing with the PEDOT: PSS organic polymer for an effective time of 30 minutes[93], this setup is displayed in Fig. 96f. Immediately the deposition is completed the sample in placed within the oven as seen in Fig. 96g for additional curing for duration of 30-45 mins leaving the PEDOT: PSS effectively attached to the tactile sensor electrode as seen at end of the fabricating procedure in Fig. 96i

6.3.5 Sensor Patch Lamination

A pair of double-sided pieces with two entirely manufactured and bonded skin sensor patches make up a functionally constructed robot skin sensor patch. Each sensor patch is laminated with Kapton tape to make handling easier, prevent the silver electrode connections from breaking and the PEDOT:PSS from wearing off, as well as to protect the sensor area from ambient moisture. The two fully constructed sensor patches are paired and positioned back-to-back with the sensor region facing outward during this operation. To account for temperature drift of the sensors, the sensor patches are attached on both sides. Importantly, the lamination keeps the sensor patches well fastened to the connectors on the circuit board, enabling a constant and consistent feedback response. The process of lamination depicted in Fig. 97. is described in detail below:

1. Completely fabricated sensor patch: The square shaped Kapton sheet with four completely fabricated sensor patches is placed on a flat surface ready to be the processed.

2. Detached Sensor Patches: The square Kapton sheet is cut to detach the four sensor patches are. Choosing two closely match pair for processing based on the measured resistance of the tactile sensors.
3. Protect sensor electrode connectors: To laminate the closely matches pairs the sensor electrode is protected by covering them with sticky notes on either side of the sensor patch.
4. Protect with Kapton tape: The closely matched sample pair requires carefully handling to avoid touching on the sensor surface. The surface is covered with the Kapton adhesive tape. The Kapton tape covers the sensor regions leaving the electrode open to making connection with the circuit for testing.
5. Double sided tape for alignment: One of the matching pair is turned upside down and taped to the flat surface with a double side tape in preparation for alignment with the other patch.
6. Matching pair alignment: With the first patch held down firmly with a double-sided tape, the other sensor patch is aligned properly utilizing the rectangular alignment box on the end of the connectors.
7. Apply adhesive spray to aligned pair: The double-layer sensor array is placed on the flat substrate, put wiping paper in the middle of the pair and separated them. Then we sprayed 3M® contact adhesive evenly in between the pairs.
8. Smoothen the adhered pair: The wiping paper was removed, and the pair was closed together, then the clip was removed, another wiping paper was placed on the top of the laminated sensor arrays and the brayer was used to create a double-sided structure.

9. Cured and trimmed outline: Laminated double-layer sensor array is put between two flat substrates, placed a heavy metal block on the top and moved them into the conventional oven at 75°C under vacuum for 10 minutes to cure the adhesive. Finally, the laminated sensor array is moved out and trimmed the outline to make its edge flush with the bottom for inserting two ZIF connectors, which are now ready to interconnect with our conditioning electronic circuit.
10. Clean the laminated paired sensor patch: The resulting laminated pair is cleaned of any adhesive residue using Acetone and IPA and ready for test connection.

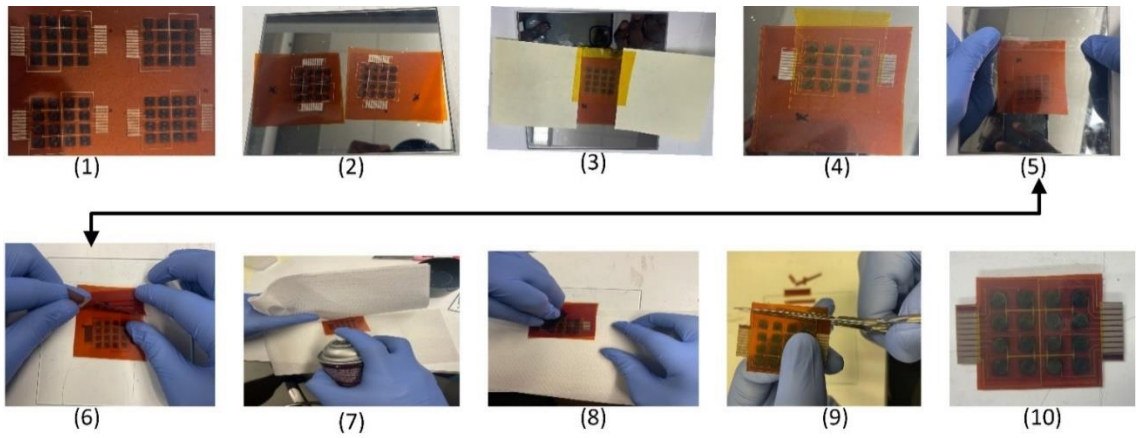

Figure 97 Lamination Process for double-layer skin sensor array

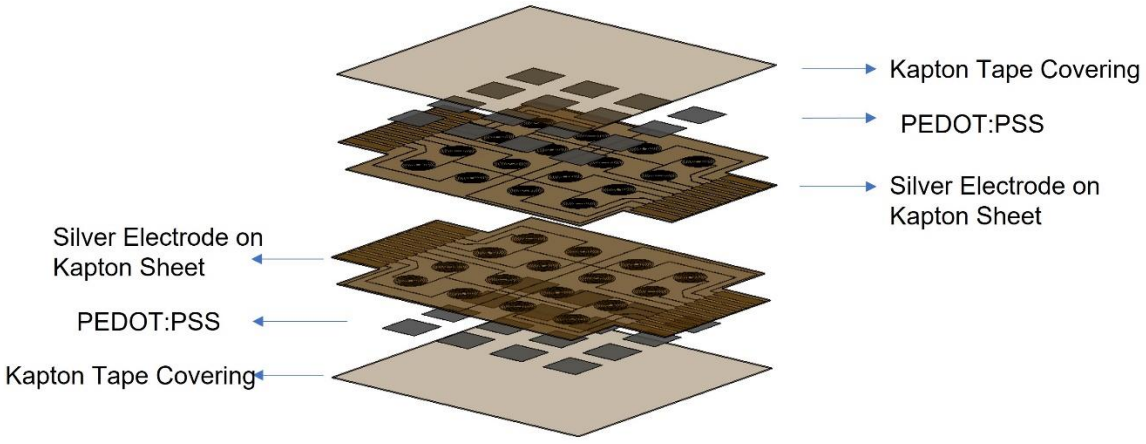

Figure 98 Overview of the arrangement of a single sensor patch unit

6.3.6 Fabrication Duration Analysis

The complete fabrication of a tactile sensor patch is predicated on two main processes. These processes are the fabrication of the sensor electrode, which involves the inkjet printing of a conductive metal in a specific design. The second process involves the deposition of the organic material responsible for the piezoresistive behavior of the tactile sensors and in our case, it is the deposition of PEDOT:PSS. In past publications[13, 15], we carried out the entire fabrication process in the cleanroom using sputtering and photolithographic techniques to pattern the sensor electrodes and ensure the deposition of PEDOT:PSS on the sensor region. The drawbacks experienced with the cleanroom process is the high cost of processing, low design adaptability, longer time taken associated with it as compared to the inkjet printing processes within the NeXus. Making it cumbersome, requiring high level of precision to maintain high yields of working sensors. Analyzed below is the time taken to complete fabrication using Cleanroom techniques and the direct write inkjet processes within the NeXus.

1. Sensor Electrodes: For the patterning of sensor electrode with conductive metals such as gold in the cleanroom, a photolithographic technique for creating the window for metal deposition, coupled with metal sputtering and wet etching process for approximately "*2 hours 53 minutes"* are required to pattern the electrodes. While for the inkjet printing process, the metal ink is loaded into the OPTOMEC® Aerosol Jet printer and optimized using the printing parameters specified in table 1. The approximated print time is "*1 hour 5 minutes"*.

2. PEDOT:PSS Deposition: For the deposition of the PEDOT:PSS, it is required it is present on only the sensing area surface to avoid shorting the circuit. To execute this in the cleanroom as described in [15], spin coating of the PEDOT:PSS is carried out but since the PEDOT:PSS covers the entire surface a series of steps are required to preserve the PEDOT:PSS on only the sensor surface removing the rest from the unwanted regions. The average time to perform the entire process is approximated to be *"7 hours 24 minutes"* For the Inkjet printing process within the Nexus, the PEDOT:PSS is loaded in the direct write inkjet printing tool called the Pico Pulse® earlier described depositing the organic polymer precisely on the sensor surfaces for an approximated time of *"45minutes"*.

In summary, the cleanroom process for fabrication of skin sensor patches averages a total of *"10 hours 17 minutes"* while using direct write inkjet printing techniques averages a total of *"1hours 50 minutes"*. This is indicated below in the pie chart.

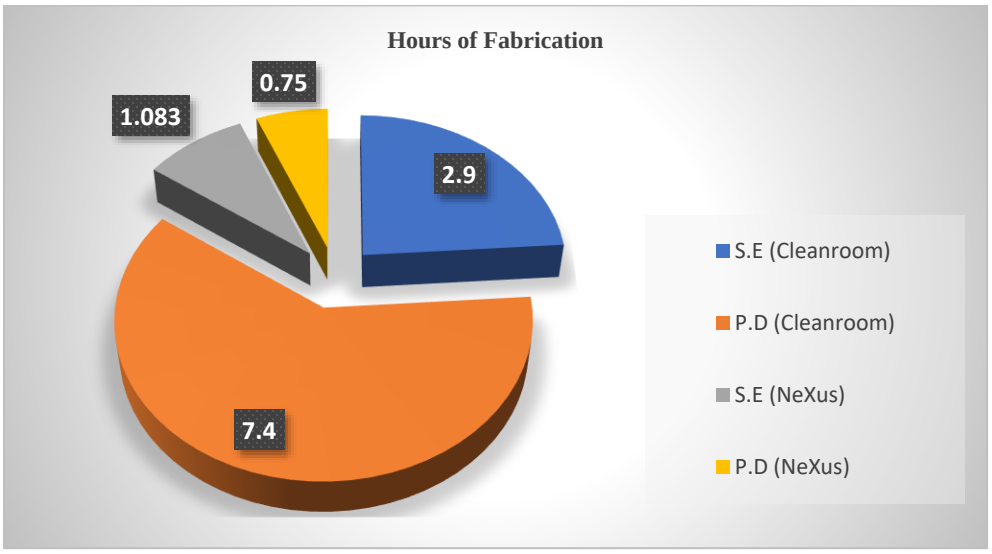

Figure 99 Fabrication duration analysis of cleanroom and NeXus Inkjet printing fabrication process where S.E represents sensor electrode and P.D is PEDOT:PSS deposition.

6.4 Experimental Test Setup and Results

The experimental test setup is described in our previous studies[15, 16, 98] and makes use of a plunger and a load cell to evaluate how well each patch's sensors work when subjected to varied forces. The testbench is controlled by the cRIO-9074 Real-Time controller from National Instruments®, and the NI9205 and NI9516 devices are installed in the general-purpose I/O ports. For one-way linear motion, the NI9516 units are coupled to Newport® travel stages. The first stage is positioned vertically, and the plunger and load cell are fastened. Testing with force is possible by modifying the motor position in response to feedback from the load cell. The system is connected to an electronic circuit board and LabVIEW® interface, which automate the testing and evaluation of the tactile sensor. The load cell regulates the force applied to the tactile sensor as the LabVIEW® front panel generates a real-time force-load profile.

6.4.1 Spatial Response for a Single Tactel

The characterization of the tactile sensor based on applied load to the varying locations on geometry of the manufactured fingerprint tactile structure on the Kapton substrate is carried out. As shown in Fig. 99, we tested 16 sub-indenter positions at each of the following angles: 0°, 45°, 90°, 135°, 180°, 225°, 270°, and 315° including the center. Tactile responses to indentations from 5mm and 10mm distance to the center were recorded. Three seconds were spent keeping the indenter in place at every location, with 1N applied at each sub-indenter location separately measured Using an Agilent® 34970A and an Agilent® 34901A 20-channel multiplexer, a 4-wire resistance measuring approach is used to gather resistances. Fig. 100. shows the response of the tactile sensor. In Fig.100a.

it is noticed at the center of the tactile sensor, the response of the sensor to the indentation is at the highest. The sensor response from the other locations appears to follow the same trendline with a reduced sensitivity in comparison to the center as the location get further from the center with the exception of the response from the angle 270°. This is due to the presence of the printed connecting silver lines beneath the sub-indenter impacted by the applied force. The linear and quadratic fit between the sensitivity with respect to the applied force is determined with 30 samples taken. The mean baseline resistance is recorded as 493.678Ω with a standard deviation of 0.058550. The resulting sensor demonstrated a linear relation between relative resistance change ($|\Delta R|/R_0$) and force F with a sensitivity of approximately $0.328 {}^{m\Omega}/_{\Omega}/N$ as shown in Fig.100b. In Fig.100c. the elastic hysteresis

of the tactile sensor based on the increasing and decreasing load is determined within the quadratic fit.

6.4.2 Repeatability of Sensor Measurements

A custom 3D-printed reciprocating mechanism was designed and manufactured to perform dynamic testing on soft sensors at a desired frequency and amplitude as shown in

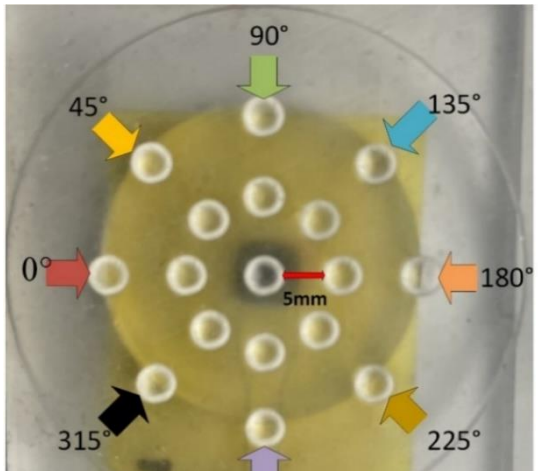

Figure 101 Characterization of a tactile sensor printed on a Kapton® substrate with 8 separate sub-indenter location marked for 0°, 45°, 90°, 135°, 180°, 225°,270°, 315° orientations.

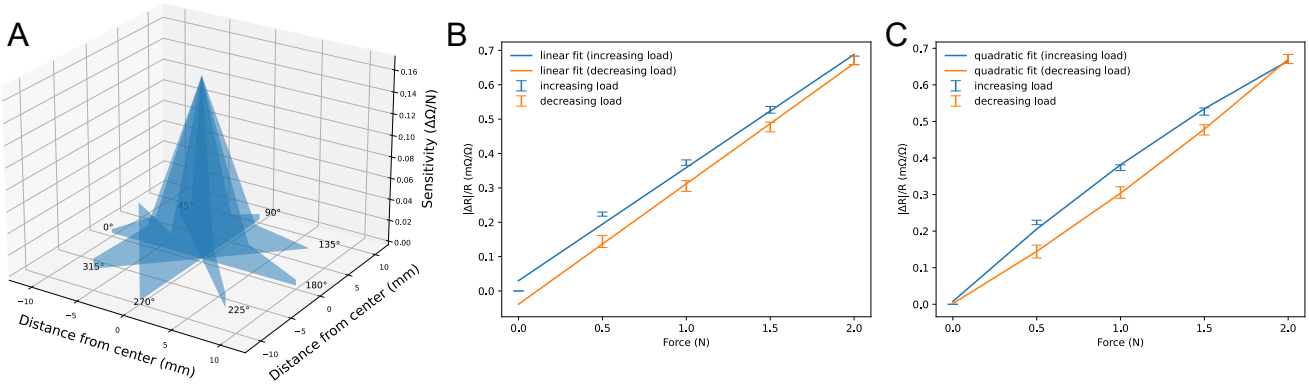

Figure 100 Relationship between resistance and force applied to the sensor (0-2N). (a) shows the magnitude of the force response from various locations indicating a Gaussian shaped response with a peak at the center and almost no response as we get further from the center; (b) shows the absolute linear fit of the sensitivity with respect to applied load; (c) this is a quadratic fit describing the hysteresis of the tactile sensors based on the load and unloading of applied force.

Fig.101a. At its core, the unit utilizes the Scotch-Yoke mechanism and consists of a sliding track connected to a rod (yoke) that moves back and forth in a straight line along with a rotating disk (crank) that provides the rotary motion. The yoke is connected to the crank through a pin and bearing which freely moves in the slot. As the crank rotates, the pin pushes the yoke back and forth along the slot, translating the rotary motion into linear motion. Here, the distance of the pin forms the center determines the range of motion of the rod(stroke), and the spin speed of the DC motor defines the cycle frequency. On of the novel feature of this design is that the distance of the pin forms the center can vary from 0.1 mm to 10 mm using a built-in set screw and washer, allowing to operate the unit with a desired amplitude. With obtaining calibration curve for Motor speed vs voltage, we hence were enabled to operate the machine and test the sensors subject to desired frequency and amplitude. The unit also has other adjustable screws to approach the sample at various height and to secure the device at the bench for long operation. The sensor pad was placed on a digital scale to monitor pressing force delivered by the end point of the reciprocating rod. The maximum force applied on the sensor was set around 100g under the frequency of 1 Hz. Fig. 101b. depicts the tactile sensor's durability profile for about 1N across a significant number of force indentation cycles, making it relevant in comparison to silicon micromachined sensors' brittleness[42]. Compared to[101], it is less stiff, more flexible, and less expensive, allowing it to conform to non-planar surfaces. Fig. 101b. illustrates cycling indentation or bending characterization of the tactile sensor investigated under continuous application of stress for more than 180000 cycles to test for its durability with the aim of bendable and flexible application. Measuring the minimum rolling window which functions as a high pass filter for the sample size, which eliminates temperature

fluctuations. The graph displays the change in resistance from the baseline in relation to the sensor response.

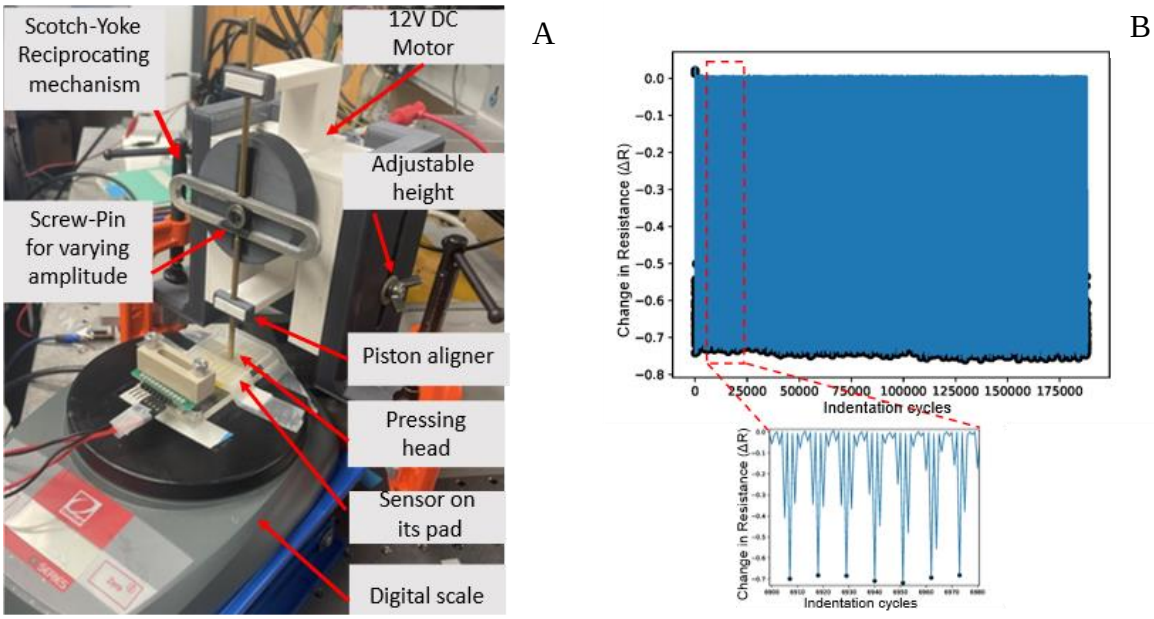

Figure 102 (a) Durability and repeatability test setup; (b) Tactile sensor durability test for more than 180000 cycles of indentation.

6.4.3 Resistance and Sensitivity Measurement of Sensor Patch

The resulting sample is sintered in the oven separately for 20 hours after the patterning of the silver electrodes and 30—45mins after PEDOT:PSS deposition. Each sensor's resistance on the skin sensor patch is measured and recorded after the fabrication process is complete but before the laminating procedure having a mean resistance 143ohms and standard deviation: 17ohms. This process is crucial because it selects the sensor patches with closely similar readings for pairing. After the selection procedure and resistance measurement are completed, the lamination process is carried out. The resistance values of the two laminated pairs are shown in Table 22. The top of the sensors experiences an inward compression when strain is applied to the laminated sensor pair immediately

with the indenter, whilst the opposite pair of sensors experience an outward expansion. A soft rubber silicone is positioned beneath the sensor patch on the testing station platform, which allows for its deformation as pressure is applied to the sensors. Fig 102 shows the

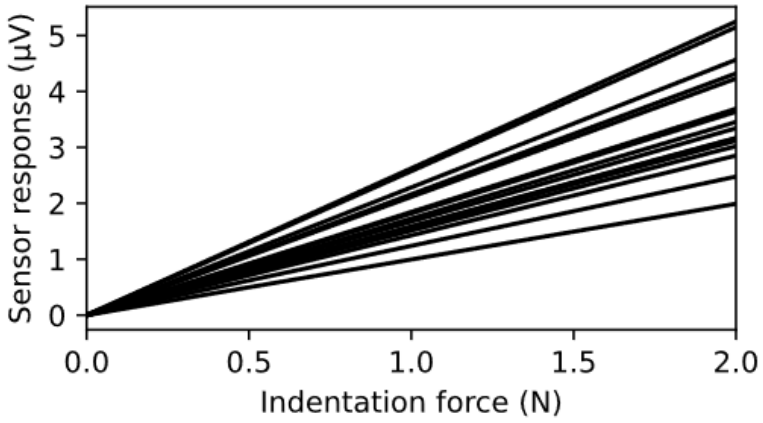

Figure 103 Indentation responses of all 16 tactels to increase load as measured by conditioning electronic circuit.

sensitivity of the 16 sensors on the patch, indicating the response of the sensors from 0.5-2 N. The mean sensitivity of the tactile sensor patch is gotten to be 1.795 μV/N with a standard deviation of 0.45 μV /N.

Table 22: Resistance measurement of two paired sensor patches.

Number of Sensor	Resistance (Ω)	Number of Sensor	Resistance (Ω)
1	159	1	184
2	145	2	169
3	137	3	160
4	142	4	165
5	122	5	148
6	121	6	152
7	128	7	158
8	136	8	167

Number of Sensor	Resistance (Ω)	Number of Sensor	Resistance (Ω)
1	151	1	151
2	133	2	145
3	130	3	135
4	146	4	134

5	141	5	120
6	124	6	117
7	141	7	115
8	165	8	124

6.4.4 Sensor Array Spatial Indentation Results

Fig 103 shows the distributed point of force indentation for the study of the sensor patch spatial resolution using responses of 4 tactile sensors located at the center of the sensor patch based on the force distribution of 2 Newtons applied to the sensors. The force is evenly applied to 29 points distributed along the X and Y axis of the four centered tactile sensors include the centers of each sensor. In Fig.104, the circles represent the location of the 16 tactile sensors on the sensor patch. The Gaussian shape across the 4 center sensors shows the behavior of the tactile sensors under the influence of force distribution at the center of the sensors and pressure points away from the center of the sensors. We fit an elliptical Gaussian model to measured sensor values using nonlinear least squares fit, specifically using Python's SciPy implementation of the Levenberg-Marquardt algorithm ("curve_fit"). The Gaussian prediction model of sensor *I, Si(x,y),* depends on the location of the indentation at *x, y* coordinates, and can be expressed as:

$$S_i(x,y) = h_i \exp\left(-\frac{\left(x_i-\mu_{x_i}\right)^2}{2{\sigma_{x_i}}^2} - \frac{\left(y_i-\mu_{y_i}\right)^2}{2{\sigma_{y_i}}^2}\right) \quad (6\text{-}2)$$

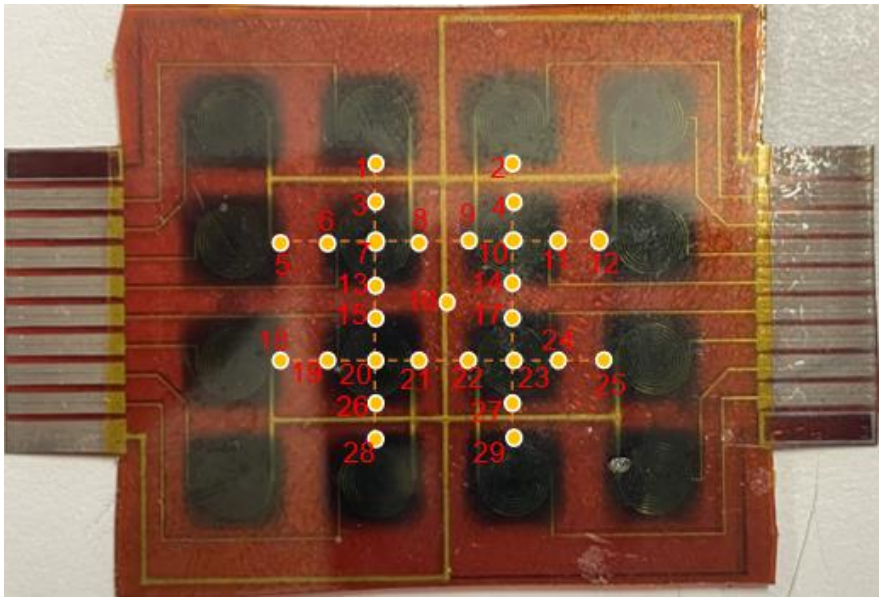

Figure 105 Sensor response to 2 Newtons force distribution along the x and y axis determine its spatial resolution.

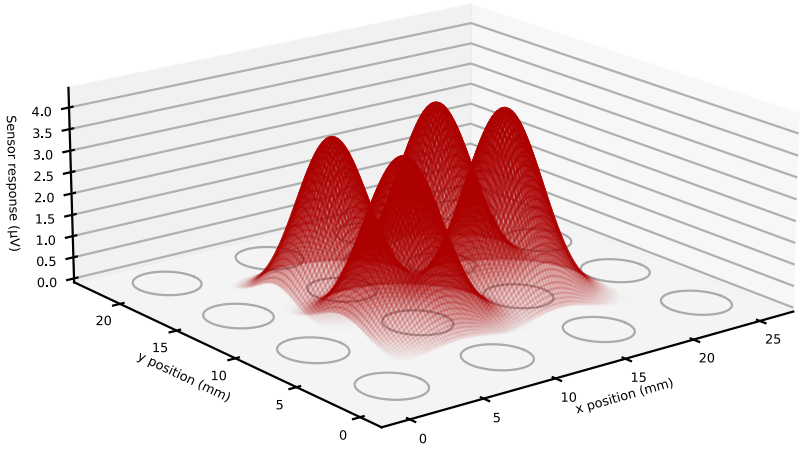

Figure 104 Gaussian curve fit of the four centered tactile sensor responses

Where h_i is the height of the Gaussian peak for sensor i, centered at (μ_x, μ_y) and a standard deviation width of σ_x (in the x-direction) and σ_y (in the y-direction).

$$R^2 = 1 - \frac{RSS}{TSS} \tag{6-3}$$

The quality of fit is determined by the coefficient of determination denoted by R^2 , with range from 0 to 1, according to Equation (3) where RSS is the sum of squares of residuals,

and TSS is the total sum of squares of the individual measurements. R^2 shows how well the measured data fits the gaussian model and how to predict a measurement given this model [102]. The closer the value of R^2 to 1, the more the ability of the model to explain all the variability of the response data around its mean.

For the four tactile sensors in the center of the SkinCell in this study we were able to estimate a very good coefficient of determination as shown in Table 23 along with the Gaussian model parameters of the four central sensors in the array and the offset of the peak of their Gaussian from the peak of the measure response.

Table 23: Estimated parameters For the Gaussian Model in Figure 103.

Skincell	R^2	height	μ_x	μ_y	σ_x	σ_y	offset (mm)
1	0.966	357	8.35	14.1	2.08	1.64	0.887
2	0.964	384	15.8	14.1	2.19	1.72	0.804
3	0.978	371	8.60	8.62	2.17	1.92	0.761
4	0.958	429	15.7	8.47	2.14	1.97	0.855

6.4.5 Spatial Resolution Estimation for Sensor Array

Using the interpolated Gaussian model, we estimate the spatial resolution of the sensor array. Specifically, given an indentation with known force at a particular target location, the x and y coordinates of the indentation point can be estimated from the sensor responses measured at the four adjacent corner tactels. The difference between the actual load application point and the estimated point is defined as the spatial resolution of our sensor array. Proposed and evaluated are two estimation methods for determining the load

application point, namely weighed averaging method and elliptical intercept predicted by the model as described in this Section.

6.4.5.1 Weighted Averaging Method

This method implements a "weighted averaging" technique, similar to the ones proposed in [103], [104]. The fundamental concept of this approach is to combine the measured response at the centers of the Gaussian distributions at each of the four corner sensors adjacent to the (x,y) coordinate. Weights of each contribution are the measured responses S_i, and then, we can compute the estimated indented location as the weighted average of the corner locations (μ_{xi}, μ_{yi}) of each sensor's Gaussian distribution shown in Figure 103b, according to:

$$x = \frac{\sum(S_i \mu_{xi})}{\sum W_i} \tag{6-4}$$

$$y = \frac{\sum(S_i \mu_{yi})}{\sum W_i} \tag{6-5}$$

After total of 20,000 iterations of randomly picking load application points taken at two separate times of 10,000 iterations each, the x and y coordinates of the estimated weighted averaged method of determining these unknown indentations had some points precisely accurate to the target locations while some were off at certain distances from the target locations. The mean distance of the estimated coordinates for the two separate iterations appears to be the same at 1.1mm off the target location. Using 13 of the already known indented locations of the measured data, the estimated location was calculated using the weighted average technique as shown in fig.105a. It is seen that 6 out of 13 of the estimated

coordinates specified by the smaller circles "°"aligns with the indentation points in crosses "+"while the rest are of varying distances off the mark.

6.4.5.2 Elliptical Intercept Method

This method uses the Gaussian model equations to estimate x and y coordinates of unknown force indentation. As a result, it is more precise, but also more complicated. To solve for the precise coordinate of force indentation, the intersections of the ellipses representing the responses of the four sensors is the method used. The gaussian model is inversed to mirror the formular of a shifted ellipse having different width and depth representing the response to each sensor. This is expressed below derived for each sensor from equation 6-2 for some given modeled response Si.

$$\frac{{\sigma_{yi}}^2(x-\mu_{xi})^2+{\sigma_{xi}}^2(y-\mu_{yi})^2}{2{\sigma_{xi}}^2{\sigma_{yi}}^2} = \ln\frac{h_i}{S_i} \tag{6-6}$$

$${\sigma_{yi}}^2(x-\mu_{xi})^2 + {\sigma_{xi}}^2\left(y-\mu_{yi}\right)^2 = 2{\sigma_{xi}}^2{\sigma_{yi}}^2\ln\frac{h_i}{S_i} \tag{6-7}$$

Let $C_i = 2{\sigma_{xi}}^2{\sigma_{yi}}^2\ln\frac{h_i}{S_i}$, then

$$\frac{(x-\mu_{xi})^2}{\frac{C_i}{{\sigma_{yi}}^2}} + \frac{(y-\mu_{yi})^2}{\frac{C_i}{{\sigma_{xi}}^2}} = 1 \tag{6-8}$$

Since the width of an ellipse centered at (μ_{xi}, μ_{yi}) is define by "2a" and the depth as "2b".

$$\text{Width } (w_i) = \frac{2\sqrt{C_i}}{{\sigma_{yi}}^2} \tag{6-9}$$

$$\text{Depth } (d_i) = \frac{2\sqrt{C_i}}{{\sigma_{yi}}^2} \tag{6-10}$$

To determine indented location x and y, the equation is expressed and simplified in the formula of a shifted ellipse for the four sensors i=1,2,3, and 4:

$$\frac{(x-\mu_{xi})^2}{(w_i/2)^2} + \frac{(y-\mu_{yi})^2}{(d_i/2)^2} = 1 \tag{6-11}$$

This gives rise to four elliptical equations with two unknowns (x,y).

$$d_i{}^2(x-\mu_{xi})^2 + w_i{}^2(y-\mu_{yi})^2 = \frac{1}{4}w_i{}^2 d_i{}^2 \tag{6-12}$$

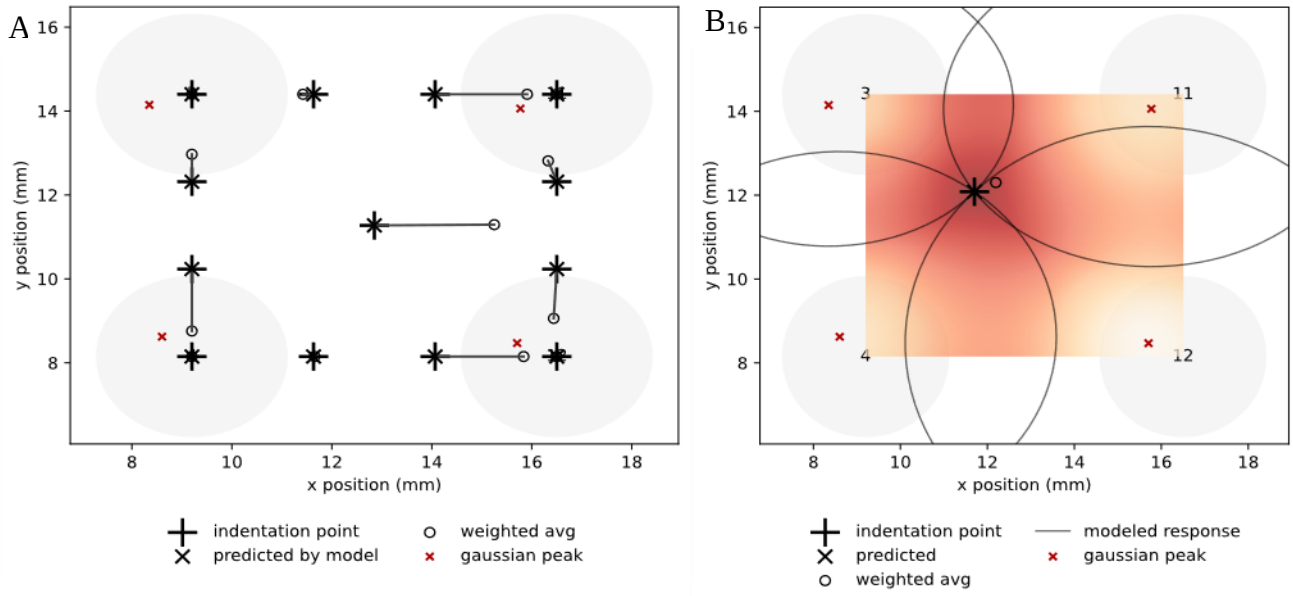

Figure 106 (a) Using the measure data on the sensor patch the weighted average is compared with elliptical model predicted response; (b) The intersecting ellipses predicts the point of indentation compared with a weighted average.

The intersection of these four ellipses (x, y) is found using their equations and known values (Table 23) with Python's SymPy symbolic solver. In Figure 105b, we present an example of one iteration. The predicted estimated location is denoted by the symbol '×,' perfectly aligned with the '+' symbol representing the unknown indented location.

Meanwhile, the '°' shape indicates the weighted average, estimated to be at a certain distance from the indented location. To verify the accuracy of the elliptical intersect method, we used the known measured force indented location in Figure 105a and estimated it using the elliptical intersect of the nearby four sensors. The results show an exact match for all locations compared to the weighted average method. Considering that the force indenter used in this study has a 3.86mm diameter, the weighted average technique falls within the indenter's sphere of influence. The mean distance off the precise target location is 1.1mm, which is less than the indentation tip's radius at 1.93mm. Consequently, the weighted average method proves to be faster in estimating force-indented locations. The spatial resolution is defined by the difference between the peak of the Gaussian model and the peak of the measured response, which amounts to 827 microns.

6.4.6 Dynamic Response Characterization of Tactile Sensors

To understand the dynamical response of our sensors, we employ system identification techniques defining the mathematical relationships between sensor responses and changing input force signals. The system identification modeling of the tactile sensor can be used as an alternative to finite element analysis model (FEA) as it takes a long time to execute, and the results of the models occasionally do not converge, necessitating the simplification of the initial design. This might provide us with an observable trend on its own, but in contrast to a model for system identification, it cannot provide precise insight into the description of the model.

To identify the dynamical response of our sensors, we used the System Identification Toolbox in MATLAB ®. by using a sampling procedure to get synchronized input and output data. The response of the system, assumed to be approximately linear can

be represented using a variety of model structures, including input-output polynomial models, transfer functions, and autoregressive models. In order to evaluate the observed output response in resistance with regard to the force input signal for tactile sensors, a linear time-invariant system, the Auto-Regressor with eXtra input model was used. As seen in Fig. 106, a discrete step ladder profile represents the applied force input and sensor response of a single tactile sensor on a flexible printed substrate. The performance of the sensor was evaluated using a force step ladder profile from 0.5-2 Newtons, and the results shown in Fig106A & B displays a negative inversion in sensor response. It is seen that the sensor response is inverted negatively depicting clearly that resistance of the sensor and specifically of the PEDOT:PSS layer is reduced when the applied force increases. The discovered model is represented by a state-space model with a predetermined number of states, starting at 1 and progressively increasing it to 3. The continuous-time identified state-space model is represented by the mathematical expression below:

$$dx/dt = Ax(t) + Bu(t) + Ke(t) \tag{6-13}$$

$$y(t) = Cx(t) + Du(t) + e(t) \tag{6-14}$$

The process of system identification heavily depends on measurement data, and the identified model is subsequently evaluated for correctness and validity using model validation procedures. This means that a portion of the data was used for identification of the unknown parameters, and the rest of the data was used for validation.

Three states were added in the third-order model, resulting in a 3x3 matrix (A) that characterizes system dynamics, a 3x1 matrix (B) that maps input to state, a 1x3 matrix (C) that maps state to output, and a scalar (D) that maps input to output. Bias terms or system

disturbances were represented by an additional 3x1 vector (K). The requirement to take into account for any intermediate states in the system, such as mechanical deformation or temperature changes brought on by the force applied to the sensor, led to the use of a second-order model. A more thorough knowledge of the system dynamics and the tactile sensor's reactions to diverse force inputs was made possible by the second-order model.

The first-order state-space model formulated only takes into account one state variable as a means of comparison. A condensed view of the system dynamics is provided by the first-order model. The state could indicate an instantaneous deformation or change in the sensor as a result of the applied force, suggesting a direct relationship between the applied force and the resulting resistance.

Using the state space model in continuous time, we were able to produce the model with the best estimation data fit, implementing a third order and first order state model. This produced an estimation data fit of 94.9%, 86.75%and 95.58% respectively. The models are validated by a validation data set from the system, producing a simulated validation data fit of the of 65.1%, 63.02% and 63.92% for both the third order, second order and first order respectively as shown in Fig.107. The continuous-time identified state-space model for both second and first order is given below.

A third-order state-space model:

	A		B	K	C		D
-4.116e-07	8.157e-05	-1.141e-06	2.05e-05	0.0002261	-2494	0.1928	0.01798	-0.09251
-0.133	-14.9	1.485	-2.828	-7.695				
-0.02731	-7.206	-1.572	-3.067	8.4				

A second-order state-space model:

A				B	K	C	D
-7.625e-07	4.753e-05	5.109e-05	-0.0003617	-2712	0.1262	-0.09251	
-0.04459	-3621	-3.972	-0.6717				

A first-order state-space model:

A	B	K	C	D
-1.032e-06	-1.641e-07	-0.0001816	-2494	-0.1363

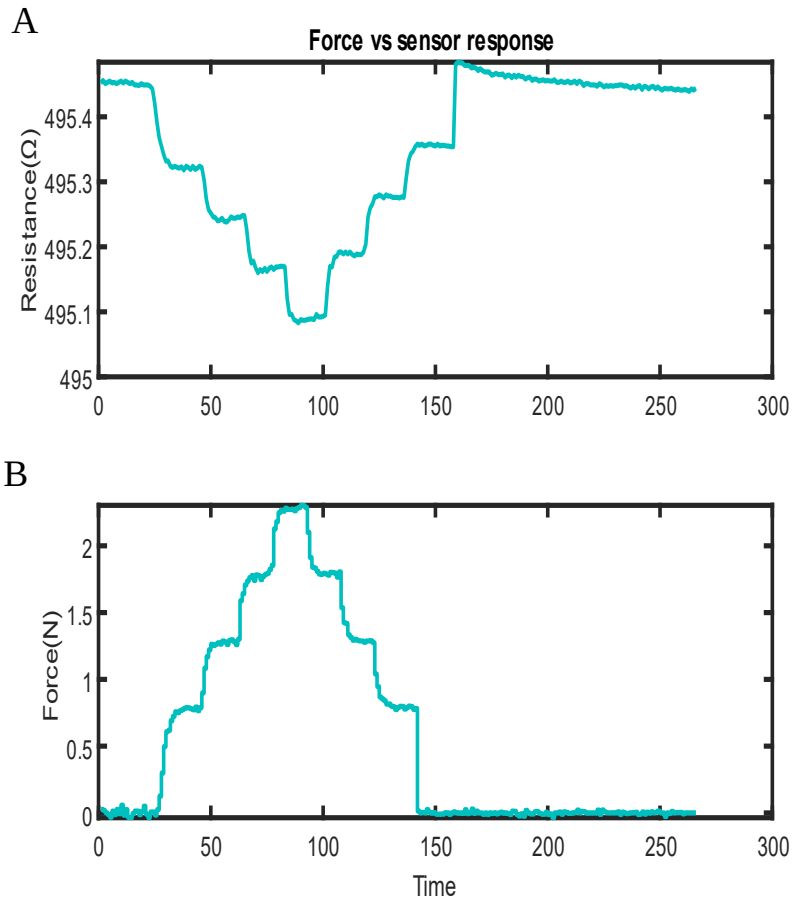

Figure 107 Step ladder response of the tactile sensor to the change in applied force (0-2N), (a) resistance change of the sensor, (b) Applied force from (0-2N)

Results indicate that the first order model has a good validation data fit compared to the others, and it is also the simplest, therefore we selected it. This model reveals that the

tactel response had a time constant of approximately 63ms, indicating great performance for human-robot-interaction.

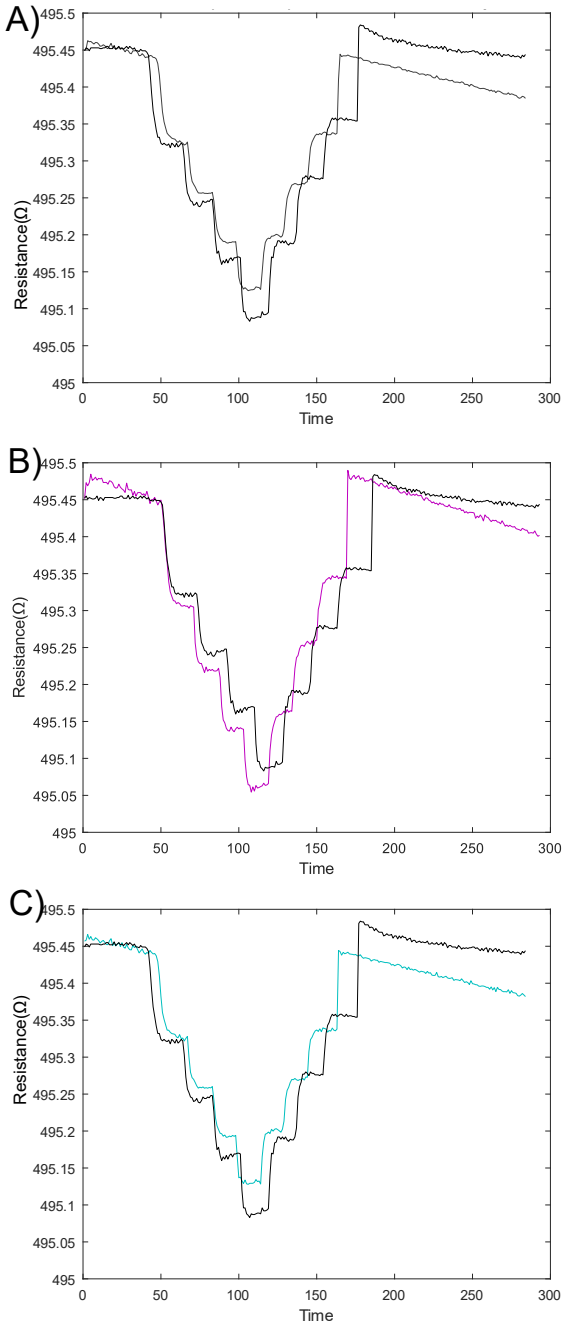

Figure 108 Model output from simulations of the (a) 3rd order model, (b) second order model, (c) First order model, with validation data fit at 65.1%, 63.02 and 63.92 respectively.

CHAPTER 7

CONCLUSION AND FUTURE WORK

Applications for robots are expanding across all facets of human life. Concerns about human and robot safety increase as it grows quickly. The world is full of dynamic environments after the robots leave the factory's orderly surroundings. Everything can no longer be pre-programmed in advance. The robots must independently comprehend their environment and adjust to them with the use of sensors. Multi-modal sensors combined with robotic skin can be quite effective in this situation. It will give robots access to real-time sensory data that will make safe for humans and robots to interact in an unstructured environment. In this thesis, we presented robot skin sensor designs, optimized fabrication techniques, spatial resolution approaches and integration with a robot.

7.1 Conclusion

There have been several tactile designs and structures conceived and created to optimize the response of robot skins, however the fabrication techniques needed to be upgraded alongside to scale up its production and manufacture. This is crucial for the skin sensor patches production to meet up with the potential application with increasing robot manufacture. For this reason, the NeXus micro-fabrication platform has been instrumental in replacing completely the fabrication processes previously carried out in the cleanroom, thereby reducing the time taken in completing the fabrication of skin sensor patches. Direct write ink jet printing equipment within the NeXus such as the Aerosol jet printer and Pico

Pulse have been instrumental in the patterning of skin sensor structures and deposition of the organic based sensing material, PEDOT:PSS. These have helped limiting errors due to human interventions or equipment malfunction that is observable during cleanroom fabrication techniques.

After the fabrication of robot skin sensors, and tactile strain gauge sensors, a comprehensive test on the test station is conducted using the force controller. We can fairly evaluate the sensors in a cell by developing repeatable force testing. The information made available by this enables us to test and characterize our sensors against one another in order to compare their performance as well as that of sensors created in batches or using other production processes. With the use of this knowledge, we can choose the geometry and deposition methods to test and develop in the future.

We can correctly compare both the sensors and the cells by using the automated test bench to the sensors created by the NGS team. Testing sensors with the circular tree structure revealed an increase in sensitivity of around 1000 times over the basic star shaped structure. Both the Optomec and Pico Pulse printing systems, which are used in the updated printing processes, exhibit advantages over the earlier sensors fabricated in the cleanroom in various ways. The sensors produced by Pico Pulse had a lot more sensitivity than the clean room sensors producing responses that mirrored the force indented waveform used.

In chapter 5, the deployment of tactile sensor on a robot arm is discussed. The integration of commercially obtained Flexiforce sensors is achieved and introduction of a 3-D printed placeholder for 4×4 skin sensor patches known as the Octocan is described. The Octocan is made to improve the physical human robot interaction with Resquare robot arm. The result from the integrated tactile sensor shows a change in the orientation of the end effector

as indicated by a change in the voltage signal determined by applied pressure on the tactile sensor.

In chapter 6, the successful creation of a novel fingerprint sensor structure is fabricated using our robotic additive microfabrication platform NeXus. Fabrication with the NeXus reduces lengthy cleanroom processes by a factor of 10, from 10 hours to less than 2. This structure is completely fabricated outside the cleanroom using direct write ink jet printing equipment within the NeXus such as the Aerosol jet printer and Pico Pulse fabrication of the sensor electrodes to the deposition of organic polymer PEDOT:PSS. Single tactile and 4×4 arrays sensor patch is achieved and characterized to determine static, dynamic performance, its reliability, resolution and sensitivity. In this chapter the two methods used to determine target location of load application namely weighted average and elliptical intercepts is described. These tactile sensor patches were successfully deployed on a robot arm for demonstration.

The sensor has a distinctive "fingerprint" design which allows it to be manufactured in a compact footprint of 3.8mm x 3.8mm. The sensor contains silver electrodes and an organic polymer film PEDOT:PSS printed in successive layer. Two layers of silicone elastomer with precise protrusions and inner chambers surround the sensor array in order to improve the consistency and detection resolution of the center of force. We performed numerous characterization tests on the tactile sensor to fully assess its capabilities. To evaluate durability and repeatability, these tests employ single force, ladder force, and several indentation cycles totaling more than 180,000 cycles. The sensor's capacity to record fine spatial details is shown by the results, which have an average spatial resolution of 827 microns. Additionally, the sensor displays an average sensitivity of 1.795 μV/N in the 0.5-

2N force range, demonstrating its capacity to successfully detect minute force fluctuations. The study does system identification analysis to get additional insights into the behavior and reaction to external stimuli of the sensor. The dynamic relationship between applied forces and sensor output is described by this analysis showing a time constant of 63 ms. The information on the dynamic response is crucial for improving the sensor's performance in dynamic situations and adjusting to changing forces over time. In connection with Skinsim, a simulation program made to simulate large sensor arrays for robot applications, the system identification of the tactile sensor offers its model for next level application[105]. The proposed tactile sensor has a lot of promise for use in a wide range of fields, especially in robotics, prosthetics, and human-machine interfaces. It is a desirable option for situations calling for precise tactile feedback and force sensing due to its high spatial resolution, sensitivity, and dynamic nature. The discovery paves the way for more complex and natural human-machine interactions, enhancing user experience across a range of fields.

7.2 Future Work

In the future, based on successful creation of tactile sensors in this work, for maintainability, aside from the need for easy repair or replacement, maintaining the functionality of the tactile sensors in a robotic system requires constant calibration as the sensors might drift off calibrated profile as time goes on. So, it is important to maintain its functionality making sure it doesn't stray off the mark during use. It would even be more desirable to manufacture these skin sensors and to make these tactile sensors maintainable by integrating them directly without calibration and that can be made possible with the introduction of a Neuroadaptive controller (NAC). While the re features the astonishing

possibilities of the original material sensor, there are a few roads for future investigation. Addressing difficulties connected with versatility, large scale manufacturing, and cost-viability through the use of direct write inkjet printing technology could prompt more extensive reception and arrangement of the innovation in certifiable applications. Additionally, the sensor's capabilities could be further validated, and its potential applications expanded by examining its performance in dynamic and complex environments.

REFERENCES

[1] L. A. Ballard, S. Sabanovic, J. Kaur, and S. Milojevic, "George charles devol, jr.[history]," *IEEE Robotics & Automation Magazine,* vol. 19, no. 3, pp. 114-119, 2012.

[2] V. Fountain, "The father of the robot," *Electronics and Power,* vol. 33, no. 4, pp. 232-233, 1987.

[3] REUTERS. "Robots marched on in 2021, with record orders by North American firms." REUTERS. https://www.reuters.com/technology/robots-marched-2021-with-record-orders-by-north-american-firms-2022-02-02/#:~:text=Companies%20across%20North%20America%20laid,surge%20in%20the%20automotive%20sector. (accessed.

[4] L. Liu, F. Guo, Z. Zou, and V. G. Duffy, "Application, development and future opportunities of collaborative robots (cobots) in manufacturing: A literature review," *International Journal of Human–Computer Interaction,* pp. 1-18, 2022.

[5] M. Javaid, A. Haleem, R. P. Singh, S. Rab, and R. Suman, "Significant applications of Cobots in the field of manufacturing," *Cognitive Robotics,* vol. 2, pp. 222-233, 2022.

[6] A. C. Simões, A. L. Soares, and A. C. Barros, "Factors influencing the intention of managers to adopt collaborative robots (cobots) in manufacturing organizations," *Journal of engineering and technology management,* vol. 57, p. 101574, 2020.

[7] B. Gates, "A robot in every home," *Scientific American,* vol. 296, no. 1, pp. 58-65, 2007.

[8] G. Westling and R. S. Johansson, "Factors influencing the force control during precision grip," *Experimental brain research,* vol. 53, no. 2, pp. 277-284, 1984.

[9] J. Erp and H. Veen, "Touch down: The effect of artificial touch cues on orientation in mircogravity," *Neurosci. Lett,* vol. 404, pp. 78-82, 2006.

[10] G. J. Gerling and G. W. Thomas, "The effect of fingertip microstructures on tactile edge perception," in *First Joint Eurohaptics Conference and Symposium on Haptic Interfaces for Virtual Environment and Teleoperator Systems. World Haptics Conference*, 2005: IEEE, pp. 63-72.

[11] T. A. Quilliam, "The structure of finger print skin," *Active touch,* vol. 1, 1978.

[12] M. T. Francomano, "Microtechnologies for compliant interfaces between manipulated objects, hand prostheses and the nervous system," 2013.

[13] D. Wei, R. Zhang, M. N. Saadatzi, O. O. Olowo, and D. O. Popa, "Organic Piezoresistive Pressure Sensitive Robotic Skin for Physical Human-Robot Interaction," in *International Design Engineering Technical Conferences and Computers and Information in Engineering Conference*, 2020, vol. 83907: American Society of Mechanical Engineers, p. V001T01A013.

[14] M. N. Saadatzi and D. O. P. Joshua R. Baptist Zhong Yang, "Modeling and fabrication of scalable Tactile Sensor," *IEEE SENSORS JOURNAL*, vol. 19, no. 17, pp. 1558-1748, 2019.
[15] O. O. Olowo, R. Zhang, Z. Yang, B. Goulet, and D. O. Popa, "Organic Piezoresistive Robotic Skin Sensor Fabrication, Integration and Characterization," in *International Manufacturing Science and Engineering Conference*, 2021, vol. 85079: American Society of Mechanical Engineers, p. V002T08A013.
[16] O. Olowo *et al.*, "INKJET PRINTING OF PEDOT: PSS INKS FOR ROBOTIC SKIN SENSORS," in *Proceedings of the ASME 2022 17th International Manufacturing Science and Engineering Conference (MSEC2022) unpublished, West Lafayette, Indiana, USA*, 2022, vol. 80989.
[17] R. S. Dahiya, G. Metta, M. Valle, and G. Sandini, "Tactile sensing—from humans to humanoids," *IEEE transactions on robotics*, vol. 26, no. 1, pp. 1-20, 2009.
[18] T. Kanda, H. Ishiguro, T. Ono, M. Imai, and R. Nakatsu, "Development and evaluation of an interactive humanoid robot" Robovie"," in *Proceedings 2002 IEEE International Conference on Robotics and Automation (Cat. No. 02CH37292)*, 2002, vol. 2: IEEE, pp. 1848-1855.
[19] J. Rajruangrabin and D. O. Popa, "Enhancement of manipulator interactivity through compliant skin and extended kalman filtering," in *2007 IEEE International Conference on Automation Science and Engineering*, 2007: IEEE, pp. 1111-1116.
[20] A. Schmitz, P. Maiolino, M. Maggiali, L. Natale, G. Cannata, and G. Metta, "Methods and technologies for the implementation of large-scale robot tactile sensors," *IEEE Transactions on Robotics*, vol. 27, no. 3, pp. 389-400, 2011.
[21] Tekscan. "Pressure Mapping, Force Measurement & Tactile Sensors." https://www.tekscan.com/ (accessed.
[22] H. Iwata and S. Sugano, "Design of human symbiotic robot TWENDY-ONE," in *2009 IEEE International Conference on Robotics and Automation*, 2009: IEEE, pp. 580-586.
[23] PPS. "Capturing The Sense Of Touch: The TactArray Tactile Pressure Sensor." https://pressureprofile.com/sensor-systems/sensors?hsCtaTracking=9783058c-f7e7-413f-821f-b5c6e6b74658%7Cd1623b2b-9404-4476-979a-9f61f606ac1b (accessed.
[24] F. Lorussi, W. Rocchia, E. P. Scilingo, A. Tognetti, and D. De Rossi, "Wearable, redundant fabric-based sensor arrays for reconstruction of body segment posture," *IEEE sensors Journal*, vol. 4, no. 6, pp. 807-818, 2004.
[25] V. Duchaine, N. Lauzier, M. Baril, M.-A. Lacasse, and C. Gosselin, "A flexible robot skin for safe physical human robot interaction," in *2009 IEEE International Conference on Robotics and Automation*, 2009: IEEE, pp. 3676-3681.
[26] V. Lumelsky, M. S. Shur, S. Wagner, and M. Ding, *Sensitive skin*. World Scientific, 2000.
[27] K. Fukuda *et al.*, "Fully-printed high-performance organic thin-film transistors and circuitry on one-micron-thick polymer films," *Nature communications*, vol. 5, no. 1, pp. 1-8, 2014.

[28] M. TANAKA, T. OKUYAMA, M. SONE, Y. TANAHASHI, and S. CHONAN, "Development of an endoscopic tactile sensor using PVDF films," in *Nano-Biomedical Engineering 2009*: World Scientific, 2009, pp. 245-254.
[29] G. Cannata, M. Maggiali, G. Metta, and G. Sandini, "An embedded artificial skin for humanoid robots," in *2008 IEEE International conference on multisensor fusion and integration for intelligent systems*, 2008: IEEE, pp. 434-438.
[30] P. Mittendorfer, E. Yoshida, T. Moulard, and G. Cheng, "A general tactile approach for grasping unknown objects with a humanoid robot," in *2013 IEEE/RSJ International Conference on Intelligent Robots and Systems*, 2013: IEEE, pp. 4747-4752.
[31] R. S. Dahiya, A. Adami, C. Collini, and L. Lorenzelli, "Fabrication of single crystal silicon micro-/nanostructures and transferring them to flexible substrates," *Microelectronic Engineering*, vol. 98, pp. 502-507, 2012.
[32] E. Kolesar, C. Dyson, R. Reston, R. Fitch, D. Ford, and S. Nelms, "Tactile integrated circuit sensor realized with a piezoelectric polymer," in *1996 Proceedings. Eighth Annual IEEE International Conference on Innovative Systems in Silicon*, 1996: IEEE, pp. 372-381.
[33] D. Polla, W. Chang, R. Muller, and R. White, "Integrated zinc oxide-on-silicon tactile-sensor array," in *1985 International Electron Devices Meeting*, 1985: IEEE, pp. 133-136.
[34] K. Suzuki, K. Najafi, and K. Wise, "A 1024-element high-performance silicon tactile imager," in *Technical Digest., International Electron Devices Meeting*, 1988: IEEE, pp. 674-677.
[35] Z. Chu, P. Sarro, and S. Middelhoek, "Silicon three-axial tactile sensor," *Sensors and Actuators A: Physical*, vol. 54, no. 1-3, pp. 505-510, 1996.
[36] B. L. Gray and R. S. Fearing, "A surface micromachined microtactile sensor array," in *Proceedings of IEEE International Conference on Robotics and Automation*, 1996, vol. 1: IEEE, pp. 1-6.
[37] R. J. De Souza and K. D. Wise, "A very high density bulk micromachined capacitive tactile imager," in *Proceedings of International Solid State Sensors and Actuators Conference (Transducers' 97)*, 1997, vol. 2: IEEE, pp. 1473-1476.
[38] M. Leineweber, G. Pelz, M. Schmidt, H. Kappert, and G. Zimmer, "New tactile sensor chip with silicone rubber cover," *Sensors and Actuators A: Physical*, vol. 84, no. 3, pp. 236-245, 2000.
[39] M. Raibert, "An all digital VLSI tactile array sensor," in *Proceedings. 1984 IEEE International Conference on Robotics and Automation*, 1984, vol. 1: IEEE, pp. 314-319.
[40] H. Takao, K. Sawada, and M. Ishida, "Monolithic silicon smart tactile image sensor with integrated strain sensor array on pneumatically swollen single-diaphragm structure," *IEEE Transactions on Electron Devices*, vol. 53, no. 5, pp. 1250-1259, 2006.
[41] B. Choi, H. R. Choi, and S. Kang, "Development of tactile sensor for detecting contact force and slip," in *2005 IEEE/RSJ International Conference on Intelligent Robots and Systems*, 2005: IEEE, pp. 2638-2643.

[42] B. J. Kane, M. R. Cutkosky, and G. T. Kovacs, "A traction stress sensor array for use in high-resolution robotic tactile imaging," *Journal of microelectromechanical systems,* vol. 9, no. 4, pp. 425-434, 2000.
[43] L. Liu, X. Zheng, and Z. Li, "An array tactile sensor with piezoresistive single-crystal silicon diaphragm," *Sensors and Actuators A: Physical,* vol. 35, no. 3, pp. 193-196, 1993.
[44] S. Sugiyama, K. Kawahata, M. Yoneda, and I. Igarashi, "Tactile image detection using a 1k-element silicon pressure sensor array," *Sensors and Actuators A: Physical,* vol. 22, no. 1-3, pp. 397-400, 1990.
[45] X. Wang *et al.*, "Dynamic pressure mapping of personalized handwriting by a flexible sensor matrix based on the mechanoluminescence process," *Advanced Materials,* vol. 27, no. 14, pp. 2324-2331, 2015.
[46] D. Hughes, J. Lammie, and N. Correll, "A robotic skin for collision avoidance and affective touch recognition," *IEEE Robotics and Automation Letters,* vol. 3, no. 3, pp. 1386-1393, 2018.
[47] C. Domenici and D. De Rossi, "A stress-component-selective tactile sensor array," *Sensors and Actuators A: Physical,* vol. 31, no. 1-3, pp. 97-100, 1992.
[48] L. Persano *et al.*, "High performance piezoelectric devices based on aligned arrays of nanofibers of poly (vinylidenefluoride-co-trifluoroethylene)," *Nature communications,* vol. 4, no. 1, pp. 1-10, 2013.
[49] T. Sharma, S.-S. Je, B. Gill, and J. X. Zhang, "Patterning piezoelectric thin film PVDF–TrFE based pressure sensor for catheter application," *Sensors and Actuators A: physical,* vol. 177, pp. 87-92, 2012.
[50] W. Wu, X. Wen, and Z. L. Wang, "Taxel-addressable matrix of vertical-nanowire piezotronic transistors for active and adaptive tactile imaging," *Science,* vol. 340, no. 6135, pp. 952-957, 2013.
[51] G. Buchberger, R. Schwödiauer, and S. Bauer, "Flexible large area ferroelectret sensors for location sensitive touchpads," *Applied Physics Letters,* vol. 92, no. 12, p. 123511, 2008.
[52] Q. Sun, W. Seung, B. J. Kim, S. Seo, S. W. Kim, and J. H. Cho, "Active matrix electronic skin strain sensor based on piezopotential-powered graphene transistors," *Advanced Materials,* vol. 27, no. 22, pp. 3411-3417, 2015.
[53] S. Park *et al.*, "Stretchable energy-harvesting tactile electronic skin capable of differentiating multiple mechanical stimuli modes," *Advanced Materials,* vol. 26, no. 43, pp. 7324-7332, 2014.
[54] S. C. Mannsfeld *et al.*, "Highly sensitive flexible pressure sensors with microstructured rubber dielectric layers," *Nature materials,* vol. 9, no. 10, pp. 859-864, 2010.
[55] J. Y. Sun, C. Keplinger, G. M. Whitesides, and Z. Suo, "Ionic skin," *Advanced Materials,* vol. 26, no. 45, pp. 7608-7614, 2014.
[56] L. Viry *et al.*, "Flexible three-axial force sensor for soft and highly sensitive artificial touch," *Advanced materials,* vol. 26, no. 17, pp. 2659-2664, 2014.
[57] C. Pang *et al.*, "A flexible and highly sensitive strain-gauge sensor using reversible interlocking of nanofibres," *Nature materials,* vol. 11, no. 9, pp. 795-801, 2012.

[58] X. Wang, Y. Gu, Z. Xiong, Z. Cui, and T. Zhang, "Silk-molded flexible, ultrasensitive, and highly stable electronic skin for monitoring human physiological signals," *Advanced materials,* vol. 26, no. 9, pp. 1336-1342, 2014.
[59] H. B. Yao *et al.*, "A flexible and highly pressure-sensitive graphene–polyurethane sponge based on fractured microstructure design," *Advanced Materials,* vol. 25, no. 46, pp. 6692-6698, 2013.
[60] T. Li *et al.*, "From dual-mode triboelectric nanogenerator to smart tactile sensor: a multiplexing design," *ACS nano,* vol. 11, no. 4, pp. 3950-3956, 2017.
[61] Z. L. Wang, "Triboelectric nanogenerators as new energy technology for self-powered systems and as active mechanical and chemical sensors," *ACS nano,* vol. 7, no. 11, pp. 9533-9557, 2013.
[62] M. T. Hongbo Wang, Lucia Beccai, "Development of fully shielded soft inductive tactile sensors," Center for Micro-BioRobotics, Istituto Italiano di Tecnologia (IIT), Italy, 2019.
[63] J.-S. Heo, J.-H. Chung, and J.-J. Lee, "Tactile sensor arrays using fiber Bragg grating sensors," *Sensors and Actuators A: Physical,* vol. 126, no. 2, pp. 312-327, 2006.
[64] X. Wang, L. Dong, H. Zhang, R. Yu, C. Pan, and Z. L. Wang, "Recent progress in electronic skin," *Advanced Science,* vol. 2, no. 10, p. 1500169, 2015.
[65] V. E. Abraira and D. D. Ginty, "The sensory neurons of touch," *Neuron,* vol. 79, no. 4, pp. 618-639, 2013.
[66] A. Chortos, J. Liu, and Z. Bao, "Pursuing prosthetic electronic skin," *Nature materials,* vol. 15, no. 9, pp. 937-950, 2016.
[67] I. Birznieks, P. Jenmalm, A. W. Goodwin, and R. S. Johansson, "Encoding of direction of fingertip forces by human tactile afferents," *Journal of Neuroscience,* vol. 21, no. 20, pp. 8222-8237, 2001.
[68] J. M. Wolfe *et al.*, *Sensation & perception*. Sinauer Sunderland, MA, 2006.
[69] R. D. Howe, "Tactile sensing and control of robotic manipulation," *Advanced Robotics,* vol. 8, no. 3, pp. 245-261, 1993.
[70] M. H. Lee and H. R. Nicholls, "Review Article Tactile sensing for mechatronics—a state of the art survey," *Mechatronics,* vol. 9, no. 1, pp. 1-31, 1999.
[71] P. Dario and D. De Rossi, "Tactile sensors and the gripping challenge: Increasing the performance of sensors over a wide range of force is a first step toward robotry that can hold and manipulate objects as humans do," *IEEE spectrum,* vol. 22, no. 8, pp. 46-53, 1985.
[72] J. Dargahi and S. Najarian, "Human tactile perception as a standard for artificial tactile sensing—a review," *The international journal of medical robotics and computer assisted surgery,* vol. 1, no. 1, pp. 23-35, 2004.
[73] B. Jayawant and J. Watson, "Array sensor for tactile sensing in robotic applications," in *IEE Colloquium on Solid State and Smart Sensors*, 1988: IET, pp. 8/1-8/4.
[74] H. Zhang and E. So, "Hybrid resistive tactile sensing," *IEEE Transactions on Systems, Man, and Cybernetics, Part B (Cybernetics),* vol. 32, no. 1, pp. 57-65, 2002.

[75] J. R. Baptist, R. Zhang, D. Wei, M. N. Saadatzi, and D. O. Popa, "Fabrication of strain gauge based sensors for tactile skins," in *SPIE Commercial + Scientific Sensing and Imaging*, Anaheim, 2017.
[76] D. J. Beebe, A. S. Hsieh, D. D. Denton, and R. G. Radwin, "A silicon force sensor for robotics and medicine," *Sensors and Actuators A: Physical*, vol. 50, no. 1-2, pp. 55-65, 1995.
[77] M. Wolffenbuttel and P. Regtien, "Polysilicon bridges for the realization of tactile sensors," *Sensors and Actuators A: Physical*, vol. 26, no. 1-3, pp. 257-264, 1991.
[78] M. Mokhtari, T. Tiberghien, J. Biswas, and A. Aung, "Futuring Digital Health and Wellness," in *2014 IEEE 11th Intl Conf on Ubiquitous Intelligence and Computing and 2014 IEEE 11th Intl Conf on Autonomic and Trusted Computing and 2014 IEEE 14th Intl Conf on Scalable Computing and Communications and Its Associated Workshops*, 2014: IEEE, pp. 892-896.
[79] S. Miyazaki and A. Ishida, "Capacitive transducer for continuous measurement of vertical foot force," *Medical and Biological Engineering and Computing*, vol. 22, no. 4, pp. 309-316, 1984.
[80] P. A. Schmidt, E. Maël, and R. P. Würtz, "A sensor for dynamic tactile information with applications in human–robot interaction and object exploration," *Robotics and Autonomous Systems*, vol. 54, no. 12, pp. 1005-1014, 2006.
[81] J. R. Flanagan and A. M. Wing, "Modulation of grip force with load force during point-to-point arm movements," *Experimental brain research*, vol. 95, no. 1, pp. 131-143, 1993.
[82] J.-i. Yuji and C. Sonoda, "A PVDF tactile sensor for static contact force and contact temperature," in *SENSORS, 2006 IEEE*, 2006: IEEE, pp. 738-741.
[83] E. S. Kolesar Jr, R. R. Reston, D. G. Ford, and R. C. Fitch Jr, "Multiplexed piezoelectric polymer tactile sensor," *Journal of Robotic Systems*, vol. 9, no. 1, pp. 37-63, 1992.
[84] J. Dargahi, M. Parameswaran, and S. Payandeh, "A micromachined piezoelectric tactile sensor for an endoscopic grasper-theory, fabrication and experiments," *Journal of microelectromechanical systems*, vol. 9, no. 3, pp. 329-335, 2000.
[85] Y. Yamada, T. Maeno, I. Fujimoto, T. Morizono, and Y. Umetani, "Identification of incipient slip phenomena based on the circuit output signals of PVDF film strips embedded in artificial finger ridges," in *Proceedings of the SICE Annual Conference*, 2002, pp. 3272-3277.
[86] P. Mittendorfer, "From a Multi-modal Intelligent Cell to a Self-organizing Robotic Skin-Realizing Self and Enriching Robot Tactile Interaction," Technische Universität München, 2015.
[87] A. Sherehiy, A. Montenegro, D. Wei, and D. O. Popa, "Adhesive Deposition Process Characterization for Microstructure Assembly," in *International Manufacturing Science and Engineering Conference*, 2021, vol. 85079: American Society of Mechanical Engineers, p. V002T08A012.
[88] E. B. Secor, "Principles of aerosol jet printing," *Flexible and Printed Electronics*, vol. 3, no. 3, p. 035002, 2018.
[89] A. Mette, P. Richter, M. Hörteis, and S. Glunz, "Metal aerosol jet printing for solar cell metallization," *Progress in Photovoltaics: Research and Applications*, vol. 15, no. 7, pp. 621-627, 2007.

[90] D. Ratnayake, A. Curry, and K. Walsh, "Demonstrating a new ink material for aerosol printing conductive traces and custom strain gauges on flexible surfaces," in *2021 IEEE International Conference on Flexible and Printable Sensors and Systems (FLEPS)*, 2021: IEEE, pp. 1-4.
[91] A. H. Ghahremani, D. Ratnayake, A. Sherehiy, D. O. Popa, and T. Druffel, "Automated Fabrication of Perovskite Photovoltaics Using Inkjet Printing and Intense Pulse Light Annealing," *Energy Technology*, vol. 9, no. 10, p. 2100452, 2021.
[92] D. Wei *et al.*, "Precision Evaluation of NeXus, a Custom Multi-Robot System for Microsystem Integration," in *International Manufacturing Science and Engineering Conference*, 2021, vol. 85079: American Society of Mechanical Engineers, p. V002T07A008.
[93] O. O. Olowo *et al.*, "PEDOT: PSS Polymer Aerosol Jet-printing for Robotic Skin Sensors," in *2022 IEEE International Conference on Flexible and Printable Sensors and Systems (FLEPS)*, 2022: IEEE, pp. 1-4.
[94] O. O. Olowo, R. Zhang, D. Wei, D. Ratnayake, D. Jackson, and D. O. Popa, "Aerosol Jet Printed Tactile Sensor on Flexible Substrate," in *2022 IEEE International Conference on Flexible and Printable Sensors and Systems (FLEPS)*, 2022: IEEE, pp. 1-4.
[95] O. O. Olowo and Z. Y. Ruoshi Zhang, Brian Goulet, Dan O. Popa, "Organic Piezoresistive Robotic Skin Sensor Fabrication, Integration and Characterization," in *International Manufacturing Science and Engineering Conference (MSEC 2021)*, 2020.
[96] R. Zhang, J.-T. Lin, and D. O. Popa, "Finite Element Analysis of a Flexible Tactile Sensor with Circular Pattern," in *2022 IEEE International Conference on Flexible and Printable Sensors and Systems (FLEPS)*, 2022: IEEE, pp. 1-4.
[97] W. Yu and A. Perrusquía, "Simplified stable admittance control using end-effector orientations," *International Journal of Social Robotics*, vol. 12, no. 5, pp. 1061-1073, 2020.
[98] O. O. Olowo *et al.*, "Design and Fabrication of an Aerosol Jet Printed Tactile Sensor on Flexible Substrate," *IEEE Journal on Flexible Electronics*, 2023.
[99] A. Hollinger and M. M. Wanderley, "Evaluation of commercial force-sensing resistors," in *Proceedings of the International Conference on New Interfaces for Musical Expression, Paris, France*, 2006: Citeseer, pp. 4-8.
[100] D. Wei, "Design, evaluation, and control of nexus: a multiscale additive manufacturing platform with integrated 3D printing and robotic assembly," 2022.
[101] C.-Y. Huang, W.-L. Sung, and W. Fang, "Develop and implement a novel tactile sensor array with stretchable and flexible grid-like spring," in *2017 IEEE SENSORS*, 2017: IEEE, pp. 1-3.
[102] N. J. Nagelkerke, "A note on a general definition of the coefficient of determination," *biometrika*, vol. 78, no. 3, pp. 691-692, 1991.
[103] A. V. Oppenheim, A. S. Willsky, S. H. Nawab, and J.-J. Ding, *Signals and systems*. Prentice hall Upper Saddle River, NJ, 1997.
[104] Y. Huang, K. Jiang, and N. Yi, "Some weighted averaging methods for gradient recovery," *Advances in Applied Mathematics and Mechanics*, vol. 4, no. 2, pp. 131-155, 2012.

[105] S. Cremer, M. N. Saadatzi, I. B. Wijayasinghe, S. K. Das, M. H. Saadatzi, and D. O. Popa, "SkinSim: A Design and Simulation Tool for Robot Skin With Closed-Loop pHRI Controllers," *IEEE Transactions on Automation Science and Engineering*, vol. 18, no. 3, pp. 1302-1314, 2020.

APPENDIX A: List of Journal and Conference Publications

List of Publications

Journal Publication

1. Ruoshi Zhang, Ji-Tzuoh Lin, Olalekan Olowo, Brian Goulet, Bryan Harris, Dan O. Popa. “skincell: a modular tactile sensor patch for physical human-robot interaction” in 2022 IEEE Sensors Journal.
2. Olalekan O. Olowo, Ruoshi Zhang, Ji-Tzouh Lin, Danming Wei, Andriy Sherehiy, Douglas Jackson, Dilan Ratnayake, Dan O. Popa. “Design and fabrication of an aerosol jet printed tactile sensor on flexible substrate” in 2022 IEEE J-FLEX.
3. Olalekan O. Olowo, Bryan Harris , Daniel Sills, Ruoshi Zhang , Andriy Sherehiy , Alireza Tofangchi , Danming Wei and Dan O. Popa. “Design, fabrication, and characterization of inkjet-printed organic piezoresistive tactile sensor on flexible substrate” MDPI sensors Journal 2023.

Conference Papers:

4. Wei, Danming, Ruoshi Zhang, Mohammad N. Saadatzi, Olalekan O. Olowo, and Dan O. Popa. "Organic piezoresistive pressure sensitive robotic skin for physical human-robot interaction." In *International Design Engineering Technical Conferences and Computers and Information in Engineering Conference*, vol. 83907, p. V001T01A013. American Society of Mechanical Engineers, 2020.
5. Olowo, Olalekan O., Ruoshi Zhang, Zhong Yang, Brian Goulet, and Dan O. Popa. "Organic piezoresistive robotic skin sensor fabrication, integration and characterization." In *International Manufacturing Science and Engineering*

Conference, vol. 85079, p. V002T08A013. American Society of Mechanical Engineers, 2021.

6. Olowo, Olalekan O., Ruoshi Zhang Andriy Sherehiy, Brian Goulet, Alexander Curry, Danming Wei, Zhong Yang, Moath Alqatamin, and Dan O. Popa. "Inkjet printing of pedot:pss inks for robotic skin sensors." In *Proceedings of the ASME 2022 17th International Manufacturing Science and Engineering Conference (MSEC2022) unpublished*, West Lafayette, Indiana, USA, vol. 80989. 2022..
7. Olowo, Olalekan O., Ruoshi Zhang, Danming Wei, Dilan Ratnayake, Douglas Jackson, and Dan O. Popa. "Aerosol jet printed tactile sensor on flexible substrate." In *2022 IEEE International Conference on Flexible and Printable Sensors and Systems (FLEPS)*, pp. 1-4. IEEE, 2022.
8. Olowo, Olalekan O., Danming Wei, Dilan Ratnayake, Brian Goulet, Alexander Curry, Andriy Sherehiy, Ruoshi Zhang, and Dan O. Popa. "PEDOT:PSS polymer aerosol jet-printing for robotic skin sensors." In *2022 IEEE International Conference on Flexible and Printable Sensors and Systems (FLEPS)*, pp. 1-4. IEEE, 2022.
9. Wei, Danming, Ruoshi Zhang, Ji-Tzuoh Lin, Dilan Ratnayake, Olalekan O. Olowo, Andrew S. Nimon, Moath Alqatamin, Andriy Sherehiy, and Dan O. Popa. "Automated fabrication of tactile sensors using a custom additive manufacturing platform." In 2022 *International Conference on Manipulation, Automation and Robotics at Small Scales (MARSS)*, pp. 1-6. IEEE, 2022.

10. Wei, D., Zhang, R., Lin, J.T., Ratnayake, D., **Olowo, Olalekan**, Nimon, A., Alqatamin, M., Sherehiy, A. and Popa, D., 2023. Precise fabrication of tactile sensors using a custom additive manufacturing platform

APPENDIX B: COMPLETE TESTING RESULTS FOR SKIN SENSOR

B1: 2020 Cleanroom Circular Tree Geometry Design

Sensor#	2N response(mV)	6N response(mV)	8N response(mV)	10N response(mV)	Sensitivity average(mv/N)
1	0.375	0.835	1.021	1.141	0.1141
2	0	0	0	0	0
3	0	0	0	0	0
4	0.647	1.21	1.435	1.81	0.181
5	0	0	0	0	0
6	1.052	1.71	1.81	1.93	0.193
7	0	0	0	0	0
8	0.619	1.03	1.25	1.43	0.143
9	0	0.52	0.81	0.93	0.093
10	0	0.558	0.861	1	0.1
11	0.629	0.953	1	1.07	0.107
12	0	0.67	0.985	1.09	0.109
13	0	0.438	0.589	0.746	0.0746
14	0	0.727	0.975	1.15	0.115
15	0	0	0	0	0
16	0.7477	0.947	1.03	1.136	0.1136

Table 24: Average Response Value of sensors: 0 indicates nonfunctioning sensors

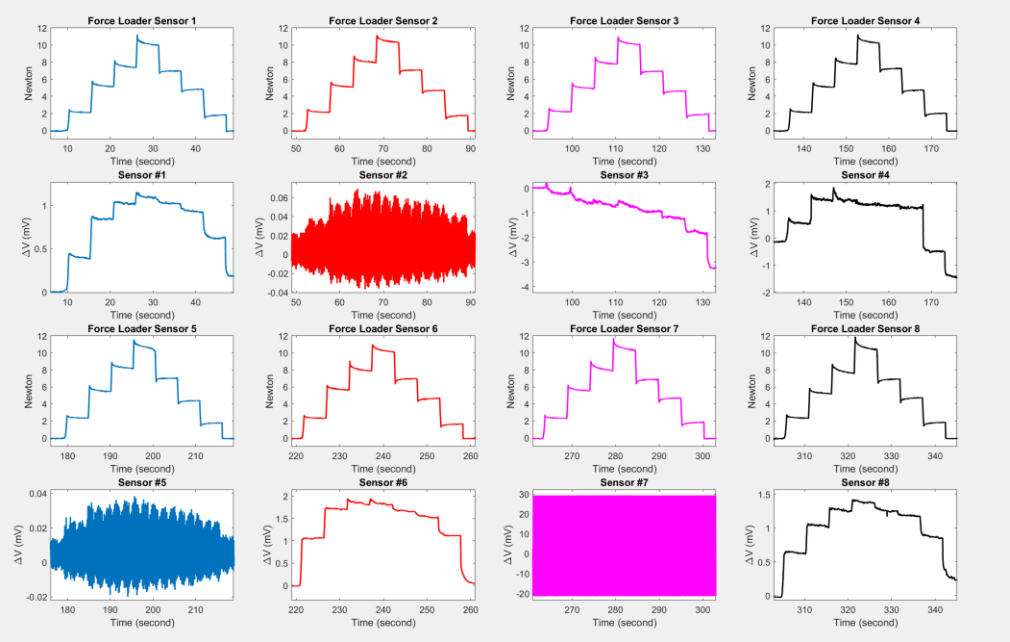

Figure 109: Visualization of Force load and sensor response for sensors 1-8

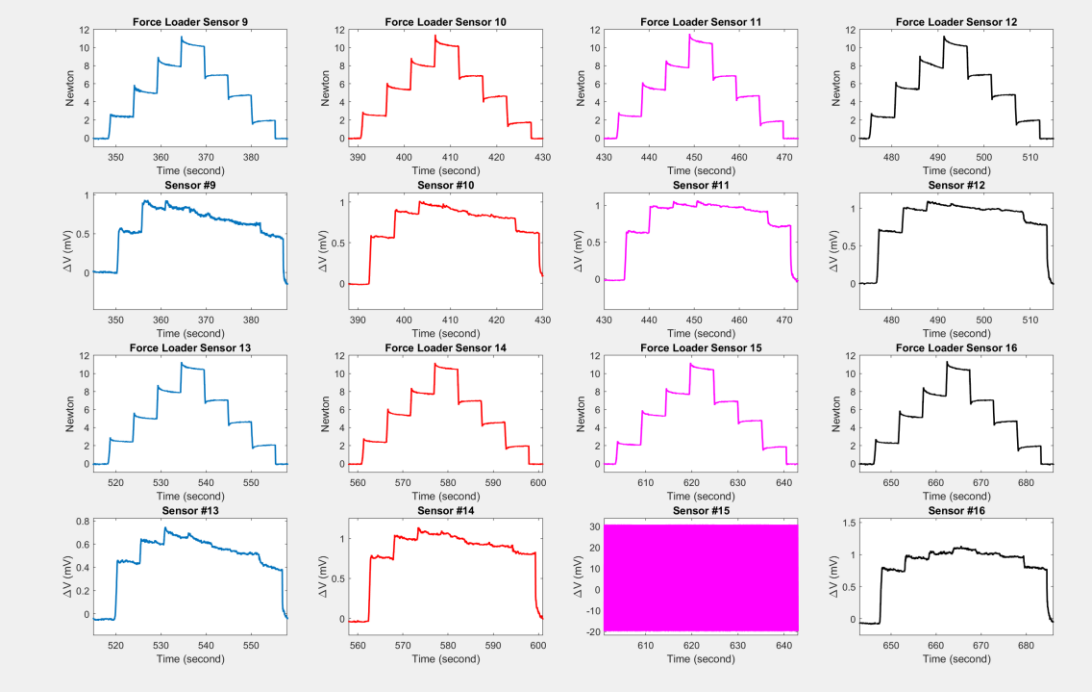

Figure 110: Visualization of Force load and sensor response for sensors 9-16

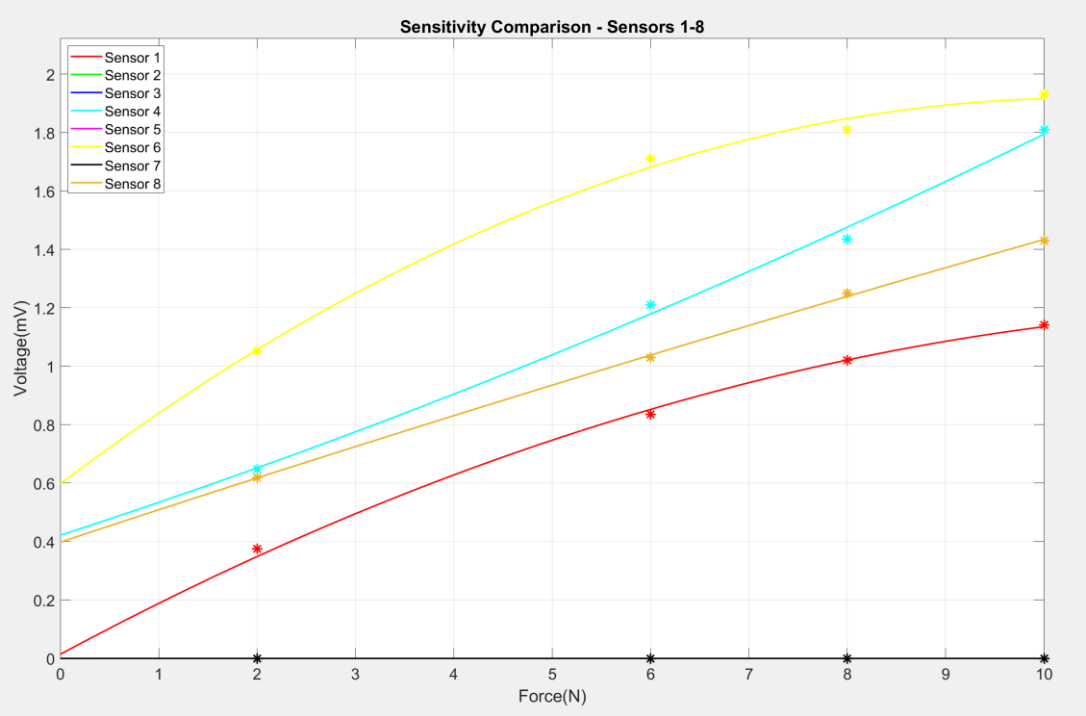

Figure 111: Comparison of working Sensitivity, Voltage with Respect to Force, Across Sensors 1-8 including a poly fitted line of best fit.

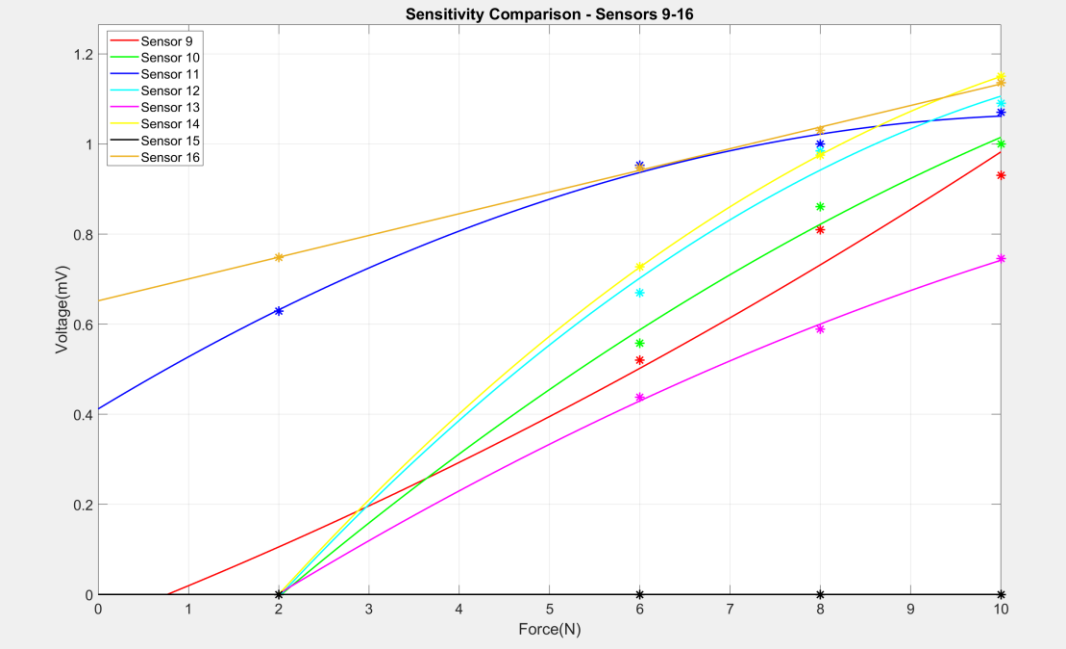

Figure 112:Comparison of working Sensitivity, Voltage with Respect to Force, Across Sensors 1-8 including a poly fitted line of best fit.

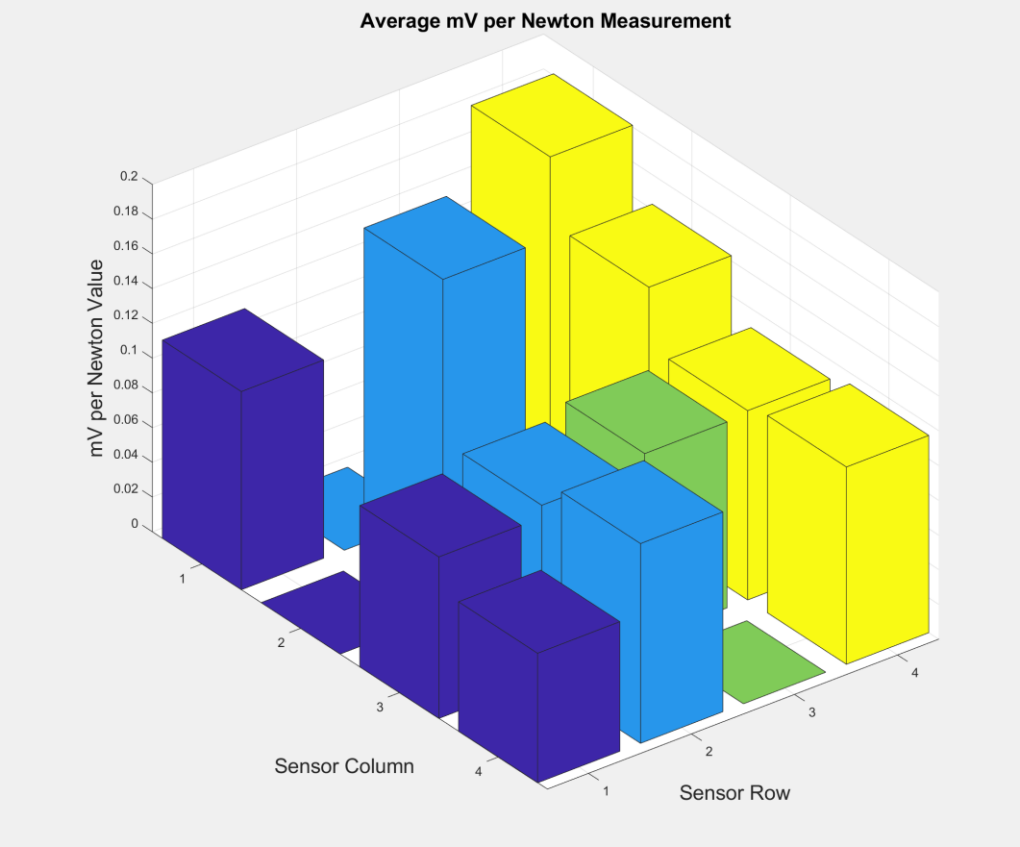

Figure 113: Average mV per Newton Measurement visualization

B2: 2021 IEEE Skin Sensor Publication Measurements

Sensor #	0.5N response(mV)	1N response(mV)	1.5N response(mV)	2N response(mV)	Sensitivity average(mv/N)
1	0.06565	0.059	0.0716	0.0868	0.0434
2	0	0	0	0	0
3	0	0.00132	0.03589	0.042	0.021
4	0.0251	0.0642	0.0813	0.0924	0.0462
5	0.1752	0.9517	2.035	2.151	1.0755
6	0.0475	0.104	0.186	0.212	0.106
7	0	0	0	0	0
8	0	0	0	0	0
9	0.00435	0.0312	0.0626	0.0806	0.0403
10	0.0241	0.0528	0.071	0.0846	0.0423
11	0	0.0112	0.0163	0.031	0.0155
12	0.00684	0.01673	0.0235	0.0278	0.0139
13	0.0122	0.124	0.124	0.124	0.062
14	0.0355	0.1513	0.185	0.2022	0.1011
15	0.0164	0	0.691	0.631	0.3155
16	0	0	0	0	0

Table 25: Average Response Value of sensors: 0 indicates nonfunctioning sensors

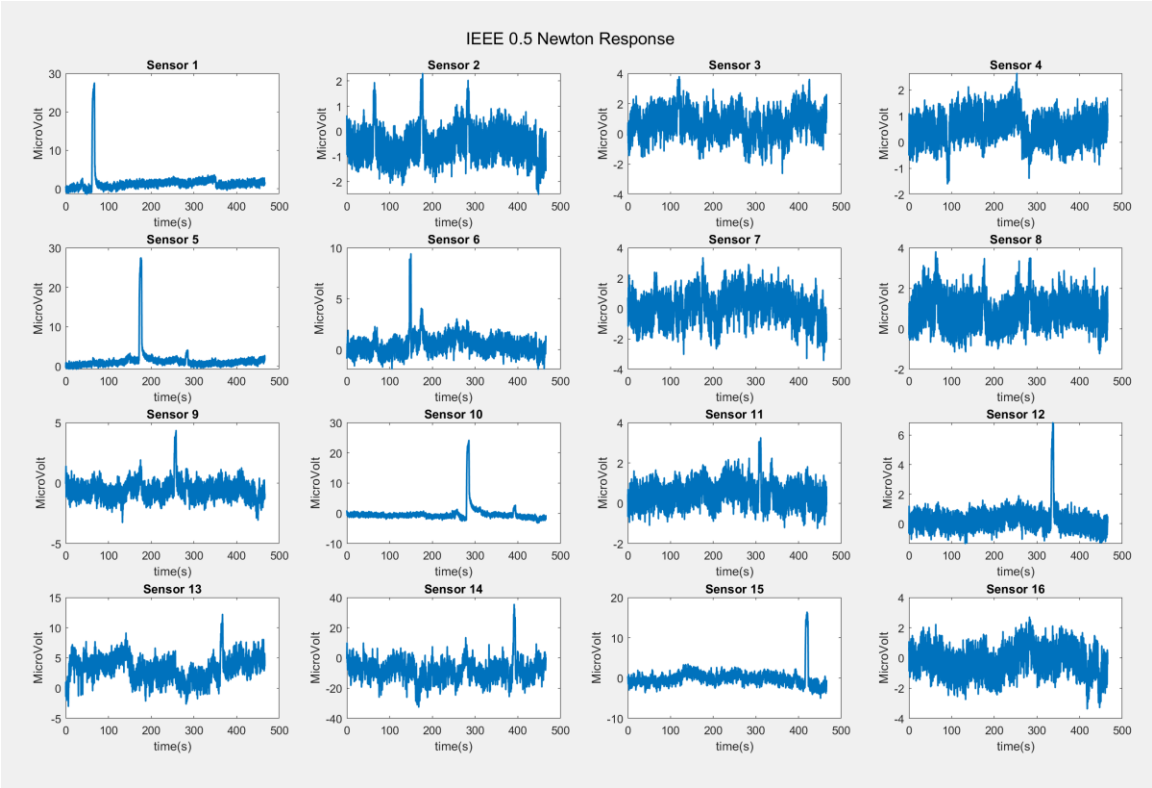

Figure 114: Visualization of 0.5 Newton Test Raw Response Data

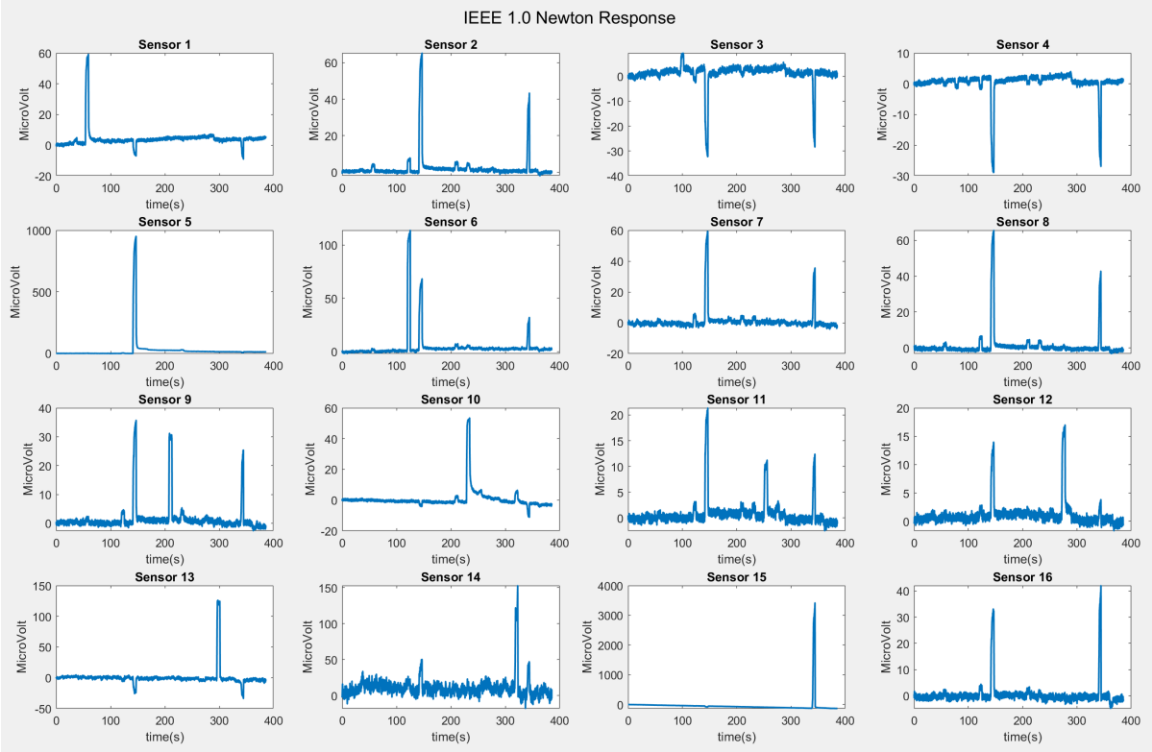

Figure 115: Visualization of 1.0 Newton Test Raw Response Data

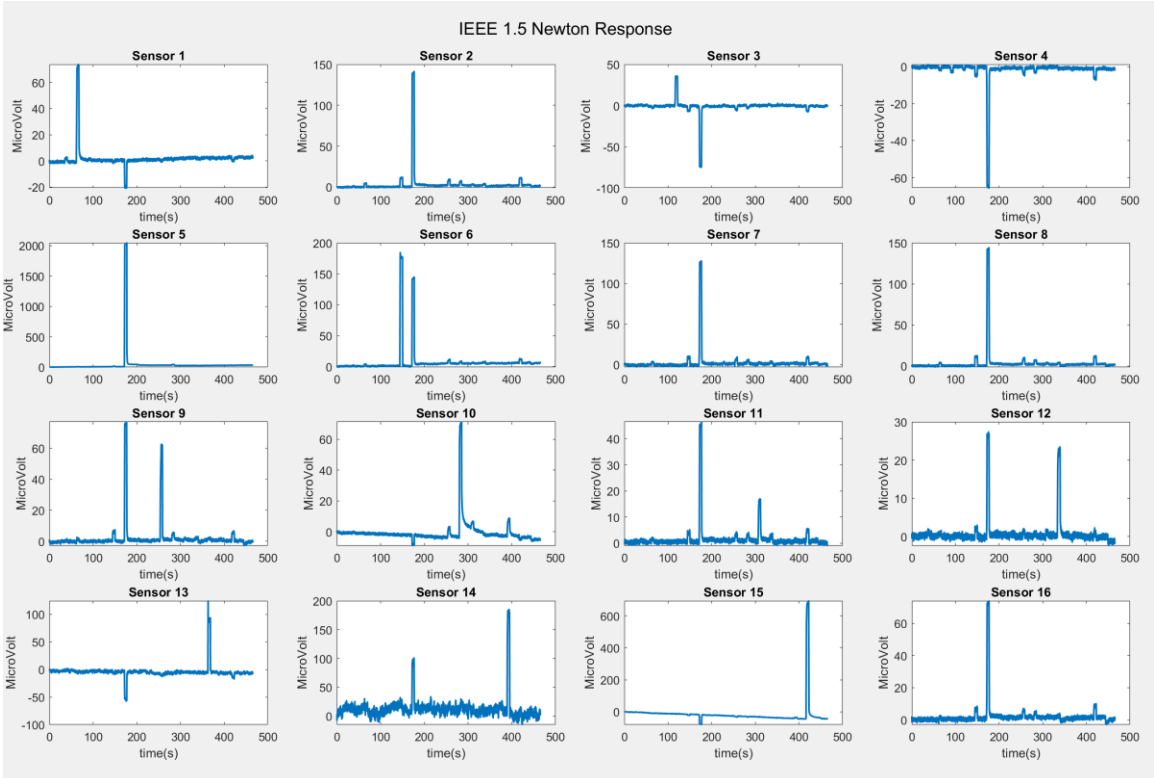

Figure 116: Visualization of 1.5 Newton Test Raw Response Data

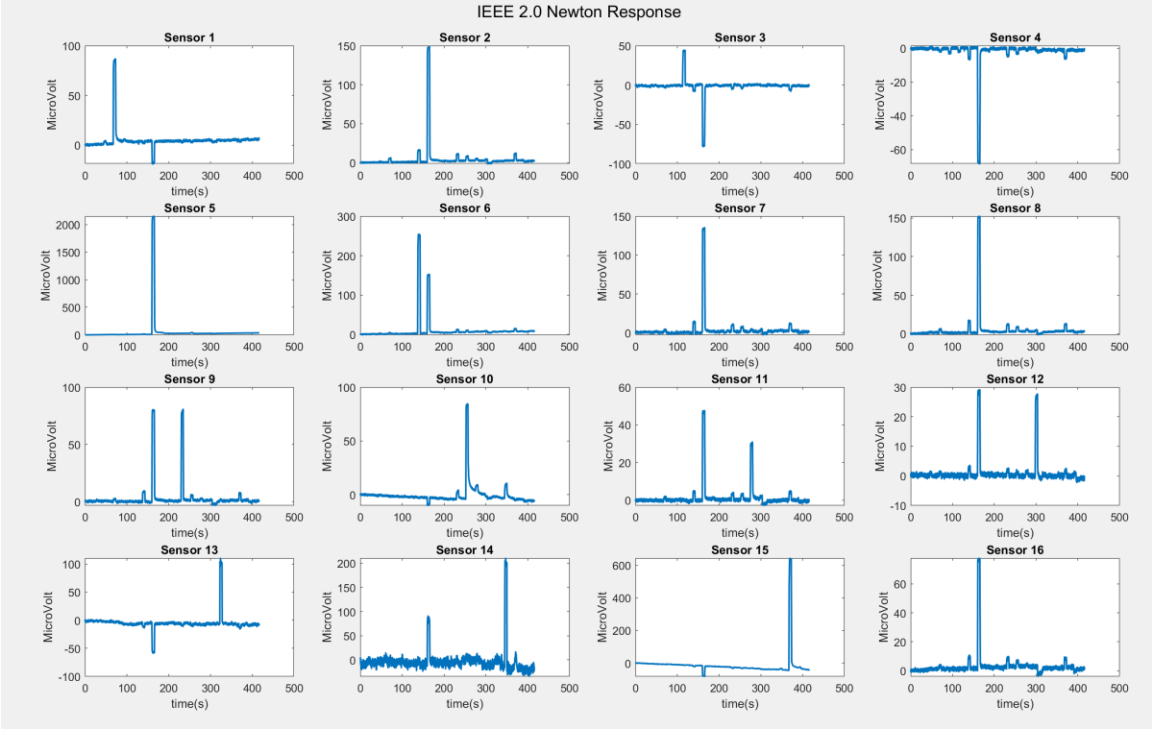

Figure 117: Visualization of 2.0 Newton Test Raw Response Data

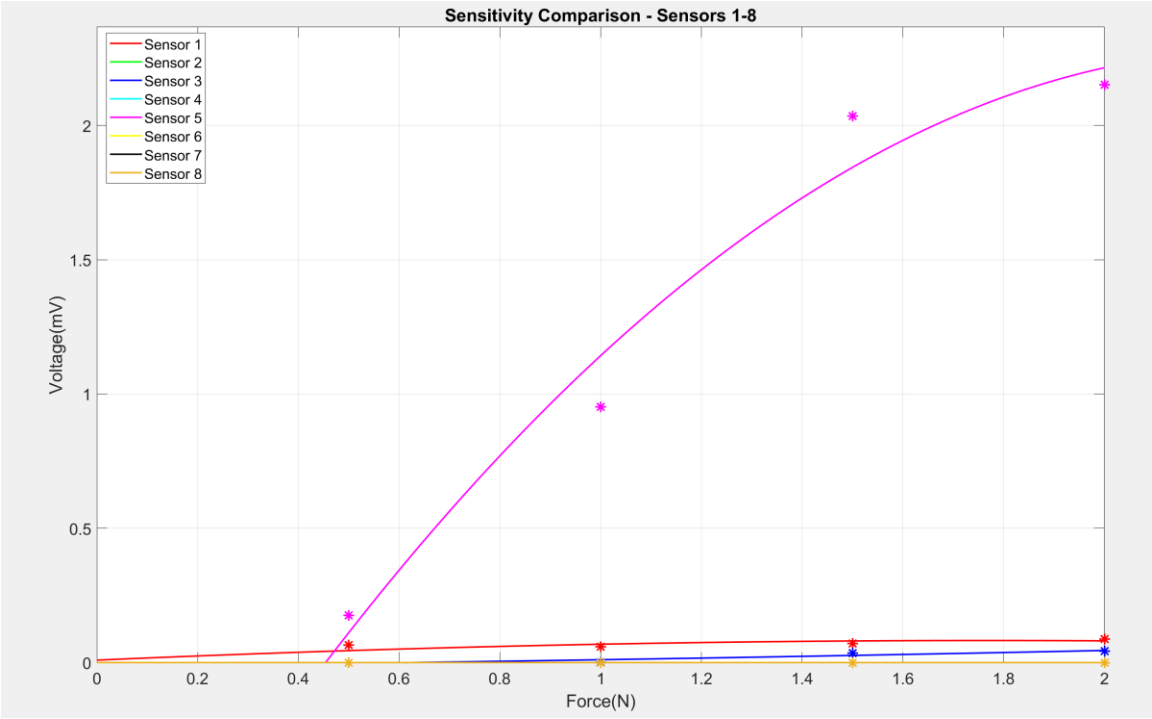

Figure 118: Comparison of working Sensitivity, Voltage with Respect to Force, Across Sensors 1-8 including a poly fitted line of best fit.

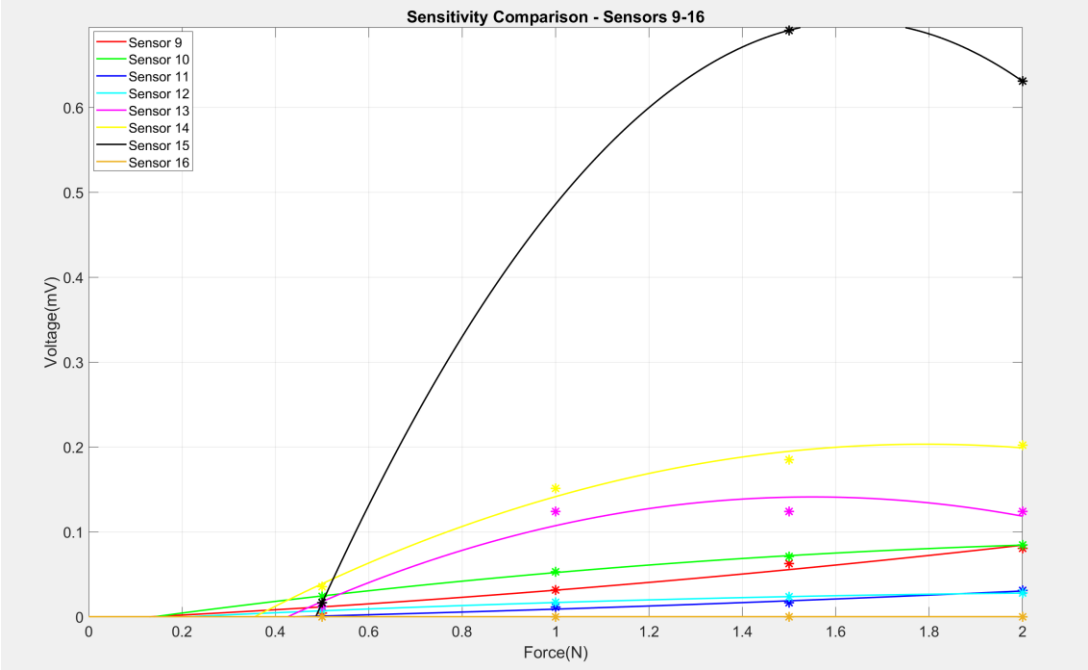

Figure 119: Comparison of working Sensitivity, Voltage with Respect to Force, Across Sensors 1-8 including a poly fitted line of best fit

Figure 120: Average mV per Newton Measurement visualization

B3: PicoPulse Deposited Circular Tree with Differing Structures

Sensor #	0.5N response(mV)	2N response(mV)	4N response(mV)	6N response(mV)	Sensitivity average(mv/N)
1	8.875	18.57	34.461	45.55	7.591666667
2	0	0	0	0	0
3	6.39	11.64	17.71	24.2424	4.0404
4	8.59	18.899	31.15	37.838	6.306333333
5	0	0	0	0	0
6	0	0	0	0	0
7	4.724	11.012	15.686	24.85	4.141666667
8	8.5	15.96	21.14	30.84	5.14
9	7.08	11.14	15.06	23.2	3.866666667
10	0	0	0	0	0
11	5.976	10.67	20.491	31.32	5.22
12	11.91	25.11	50.122	67.47	11.245
13	0	0	0	0	0
14	10.61	19.66	23.56	34.01	5.668333333
15	5.5	11.72	18.3	25.71	4.285
16	6.55	12.07	17.5	24.19	4.031666667

Table 26: Average Response Value of sensors: 0 indicates nonfunctioning sensors

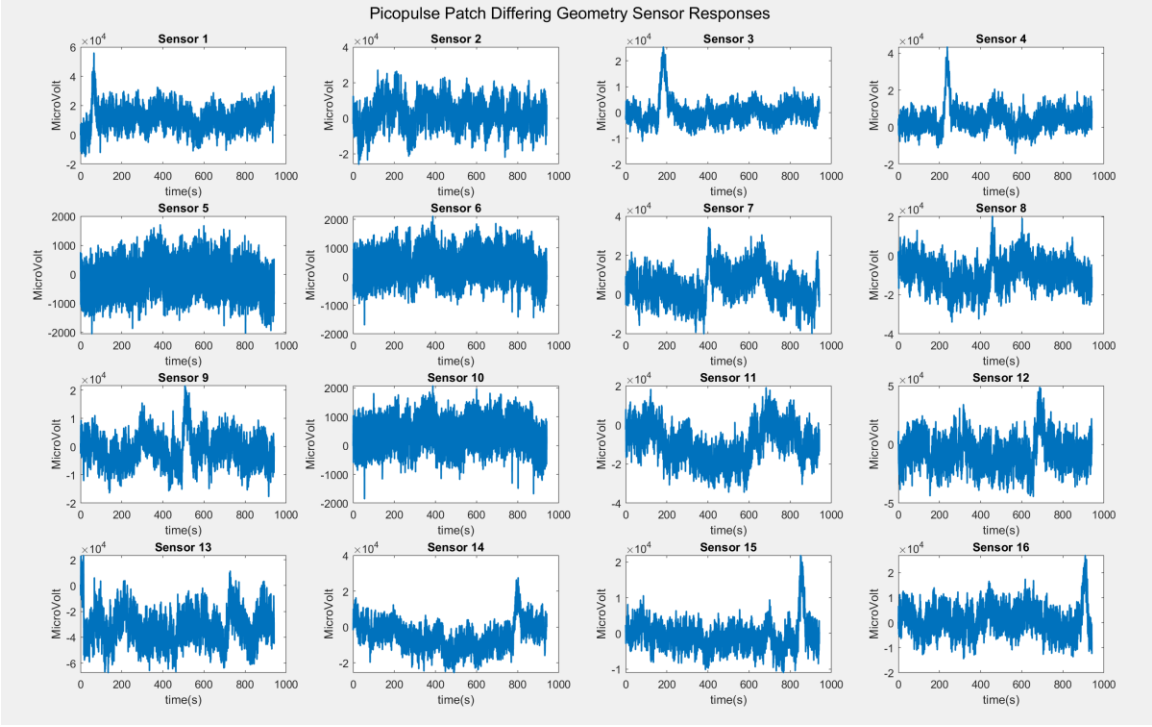

Figure 121: Visualization of Test Raw Response Data Across the Entire Test

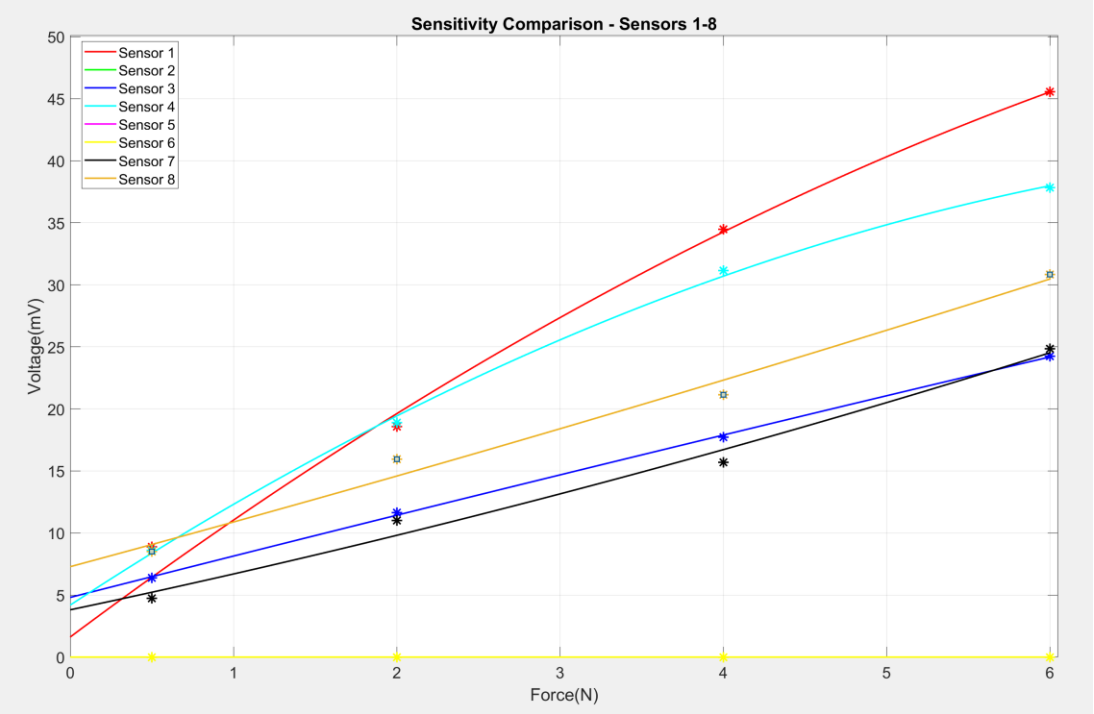

Figure 122: Comparison of working Sensitivity, Voltage with Respect to Force, Across Sensors 1-8 including a poly fitted line of best fit.

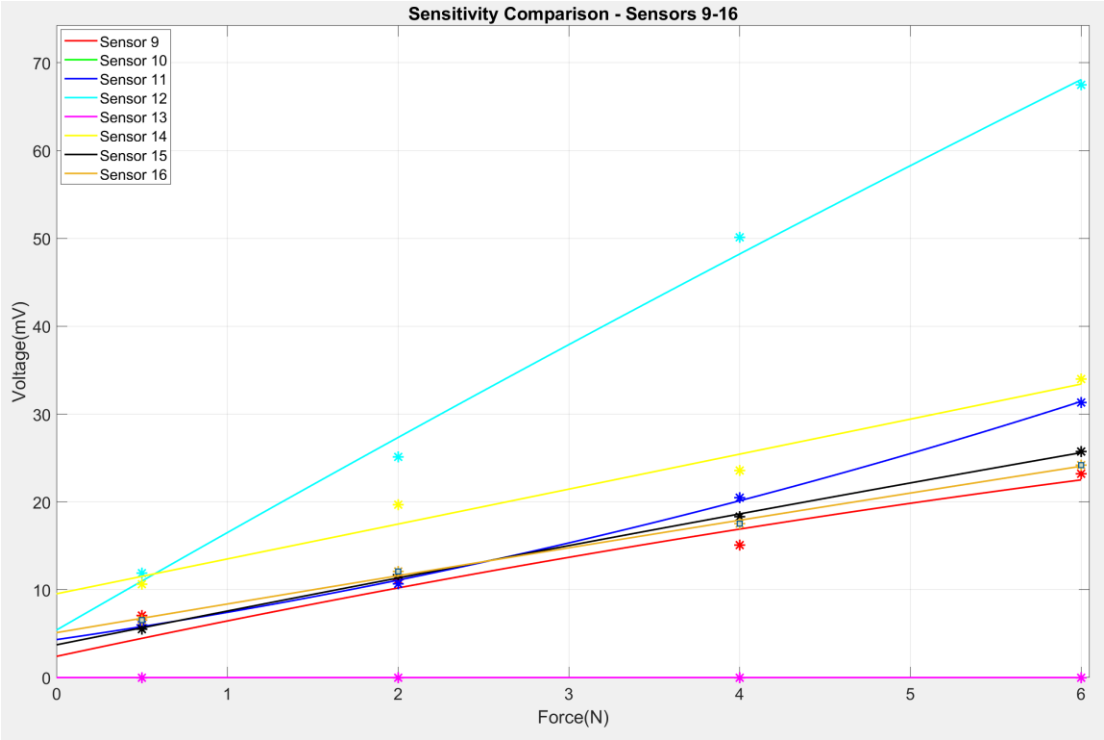

Figure 123: Comparison of working Sensitivity, Voltage with Respect to Force, Across Sensors 9-16 including a poly fitted line of best fit.

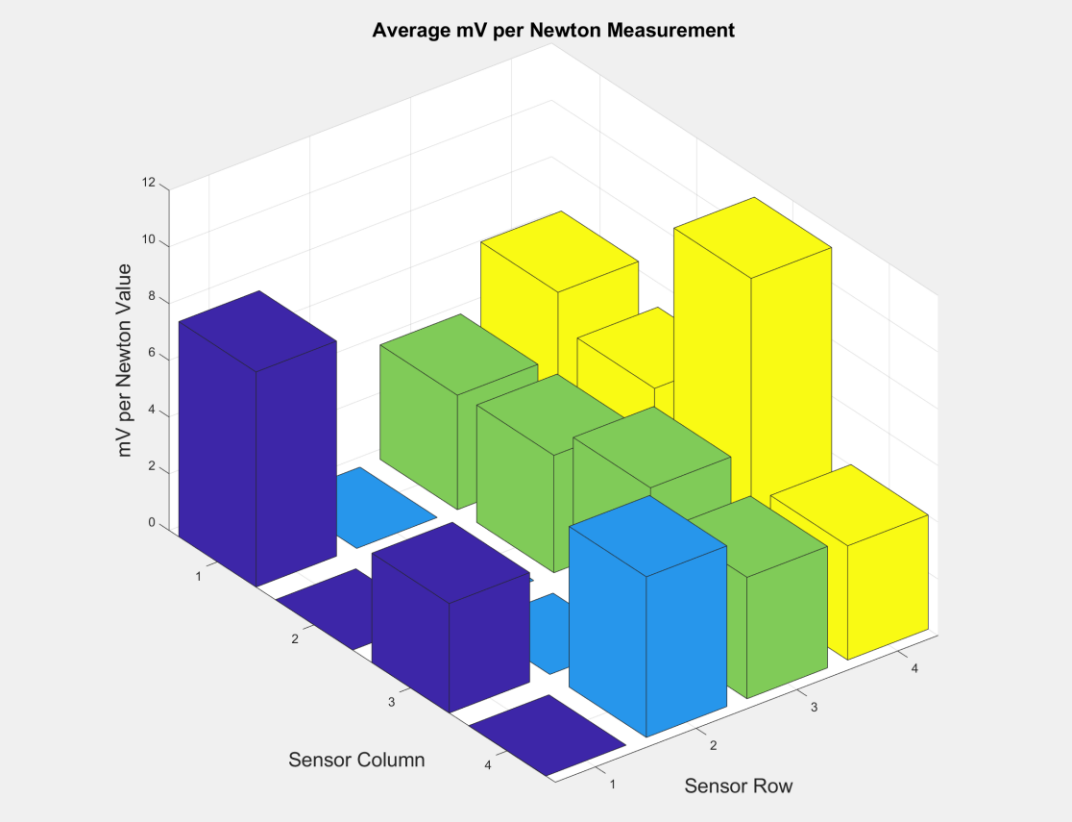

Figure 124: Average mV per Newton Measurement visualization

B4: PicoPulse Deposited Circular Tree with Similar Structures

Sensor #	0.5N response(mV)	2N response(mV)	4N response(mV)	6N response(mV)	Sensitivity average(mv/N)
1	12.11	24.51	35.32	42.68	7.113333333
2	0	0	0	0	0
3	9.37	17.35	48.77	67.21	11.20166667
4	0	0	0	0	0
5	8.08	13.6	17.23	33.01	5.501666667
6	6.1	12.47	21	38.21	6.368333333
7	6.91	13.71	17	21.15	3.525
8	0	0	0	0	0
9	9.5	15.2	19.87	25.75	4.291666667
10	6.48	14.65	19.94	41.7	6.95
11	0	0	0	0	0
12	3.54	8.66	15.12	28.74	4.79
13	0	0	0	0	0
14	10.61	14.5	21.73	65.5	10.91666667
15	8.57	16.82	51.68	60.38	10.06333333
16	0	0	0	0	0

Table 27: Average Response Value of sensors: 0 indicates nonfunctioning sensors

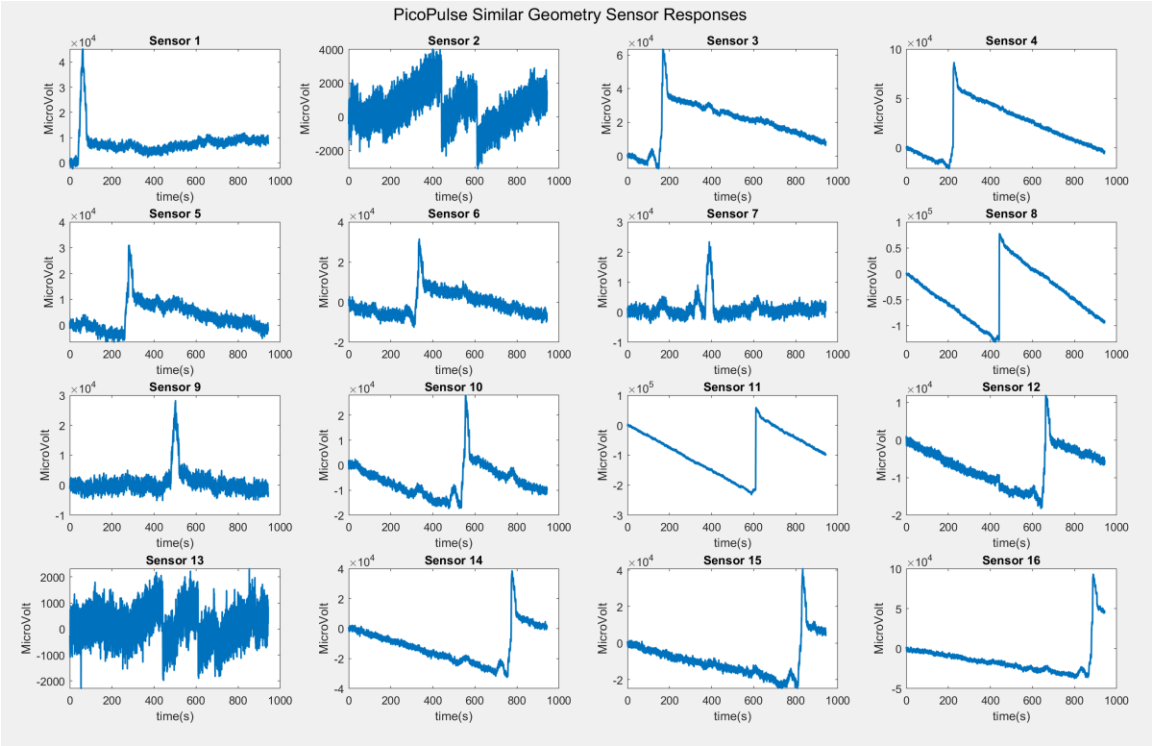

Figure 125: Visualization of Test Raw Response Data Across the Entire Test

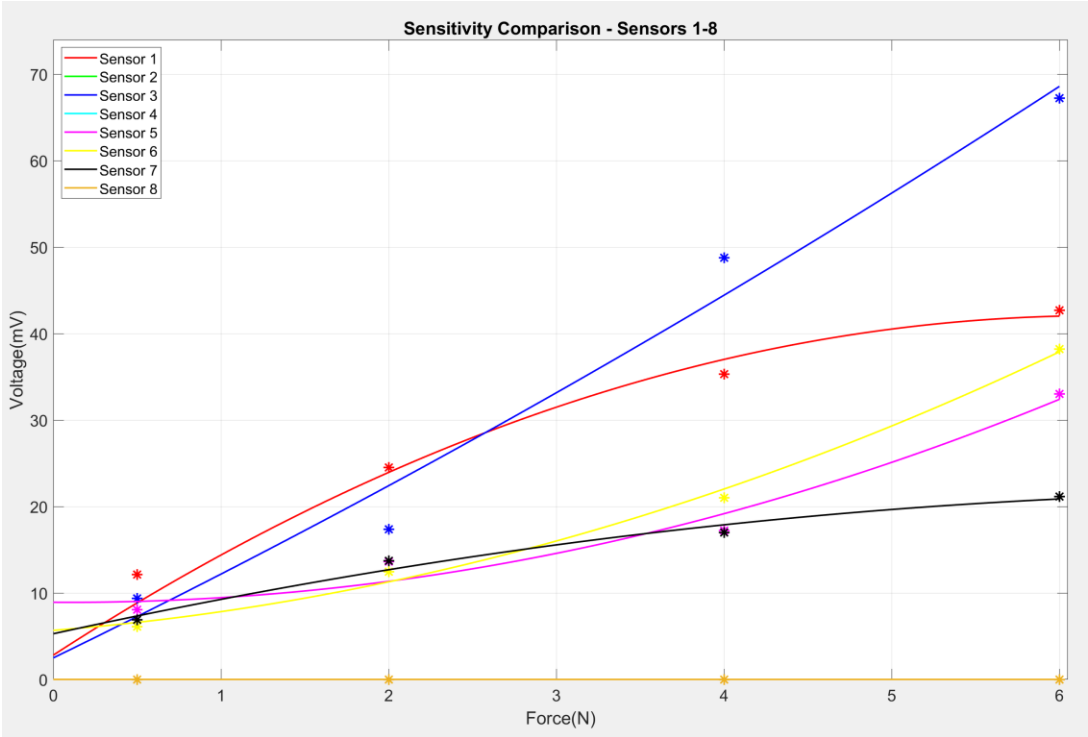

Figure 126: Comparison of working Sensitivity, Voltage with Respect to Force, Across Sensors 1-8 including a poly fitted line of best fit.

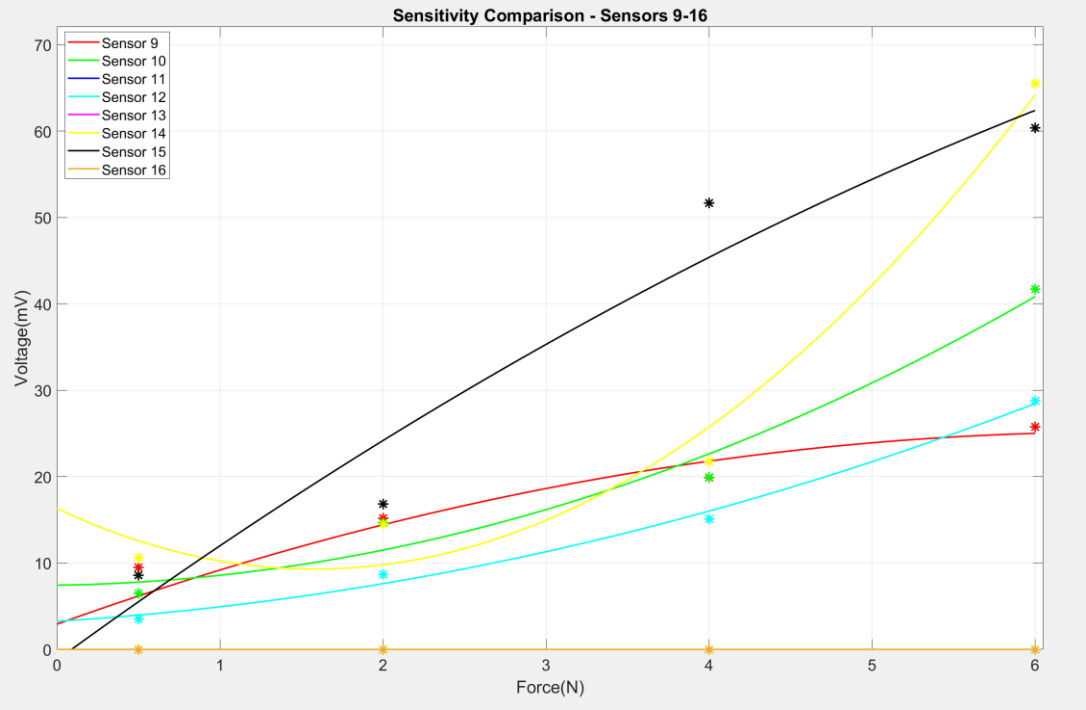

Figure 127: Comparison of working Sensitivity, Voltage with Respect to Force, Across Sensors 9-16 including a poly fitted line of best fit

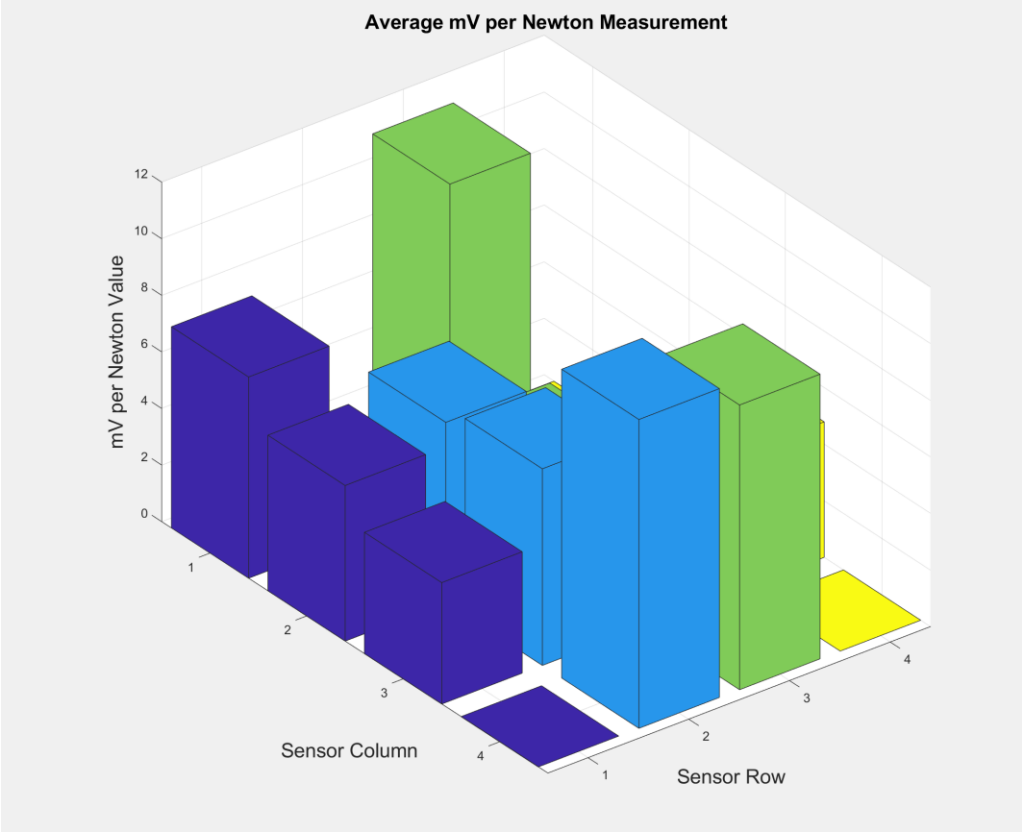

Figure 128: Average mV per Newton Measurement visualization

B5: Optomec Fabricated Sensor –SkinCell 1

Sensor #	0.5N response(mV)	2N response(mV)	4N response(mV)	6N response(mV)	Sensitivity average(mv/N)
1	0.01144	0.02454	0.03694	0.05164	0.008606667
2	0.0366	0.0446	0.05505	0.06085	0.010141667
3	0.0041	0.0142	0.0229	0.0291	0.00485
4	0.010805	0.01774	0.02347	0.02727	0.004545
5	0.009098	0.01333	0.017715	0.021995	0.003665833
6	0.00855	0.01435	0.01805	0.02115	0.003525
7	0.018	0.036	0.047	0.0537	0.00895
8	0.012	0.0198	0.025	0.0278	0.004633333
9	0.01891	0.02815	0.0337	0.036	0.006
10	0.009235	0.01558	0.0193	0.0233	0.003883333
11	-0.009	-0.00445	0.0026	0.0112	0.001866667
12	0.03243	0.04495	0.0531	0.0659	0.010983333
13	-0.004655	0.0237	0.06625	0.09735	0.016225
14	0.033	0.046	0.054	0.062	0.010333333
15	0.026	0.0331	0.0396	0.0471	0.00785
16	0.02	0.0355	0.0465	0.0565	0.009416667

Table 28: Average Response Value of sensors: 0 indicates nonfunctioning sensors

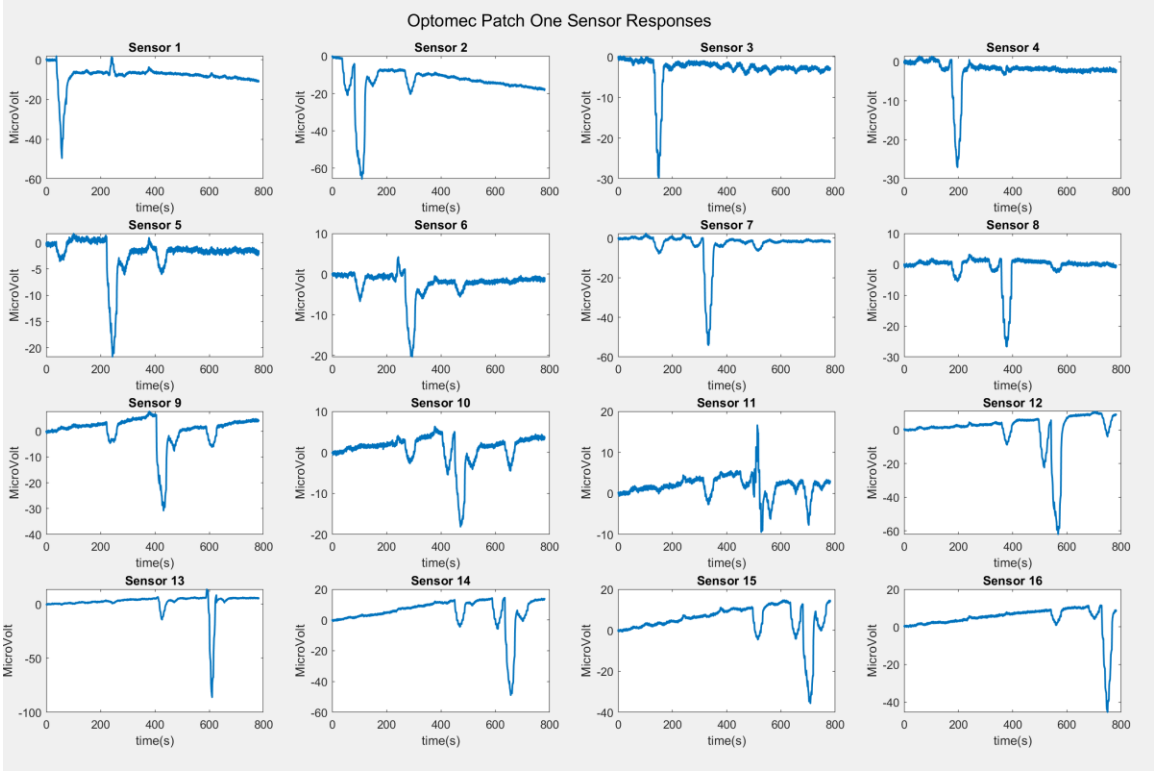

Figure 129: Visualization of Test Raw Response Data Across the Entire Test

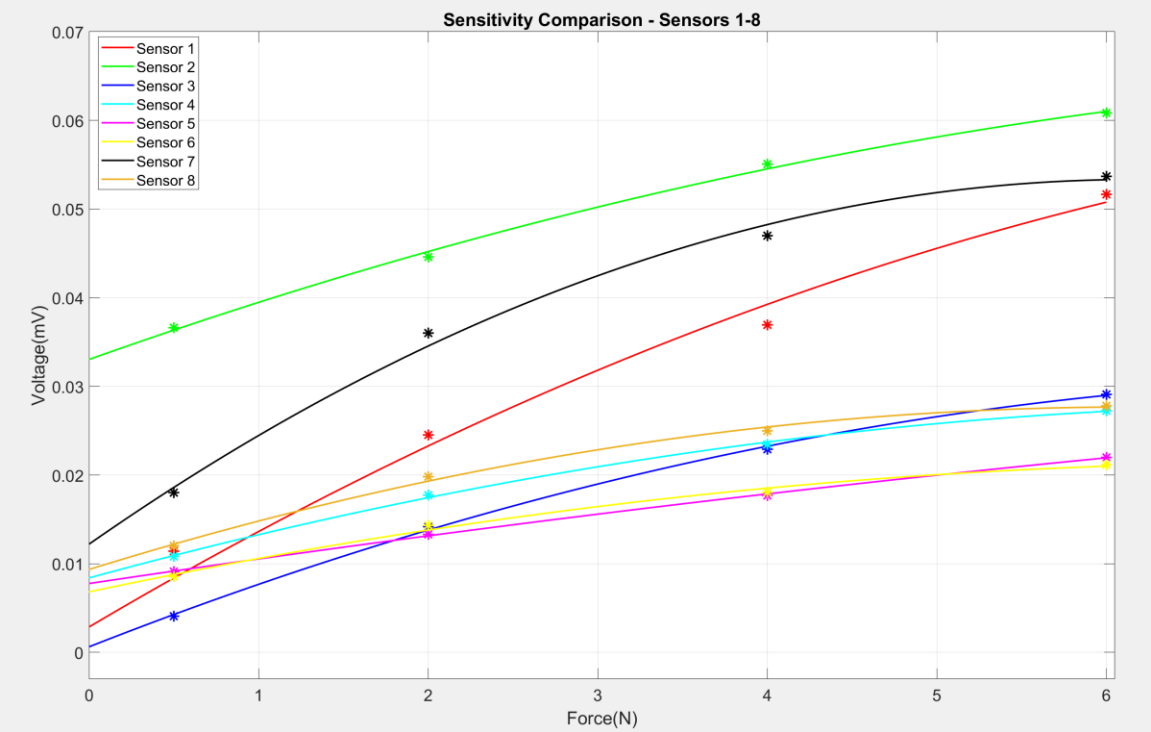

Figure 130: Comparison of working Sensitivity, Voltage with Respect to Force, Across Sensors 1-8 including a poly fitted line of best fit

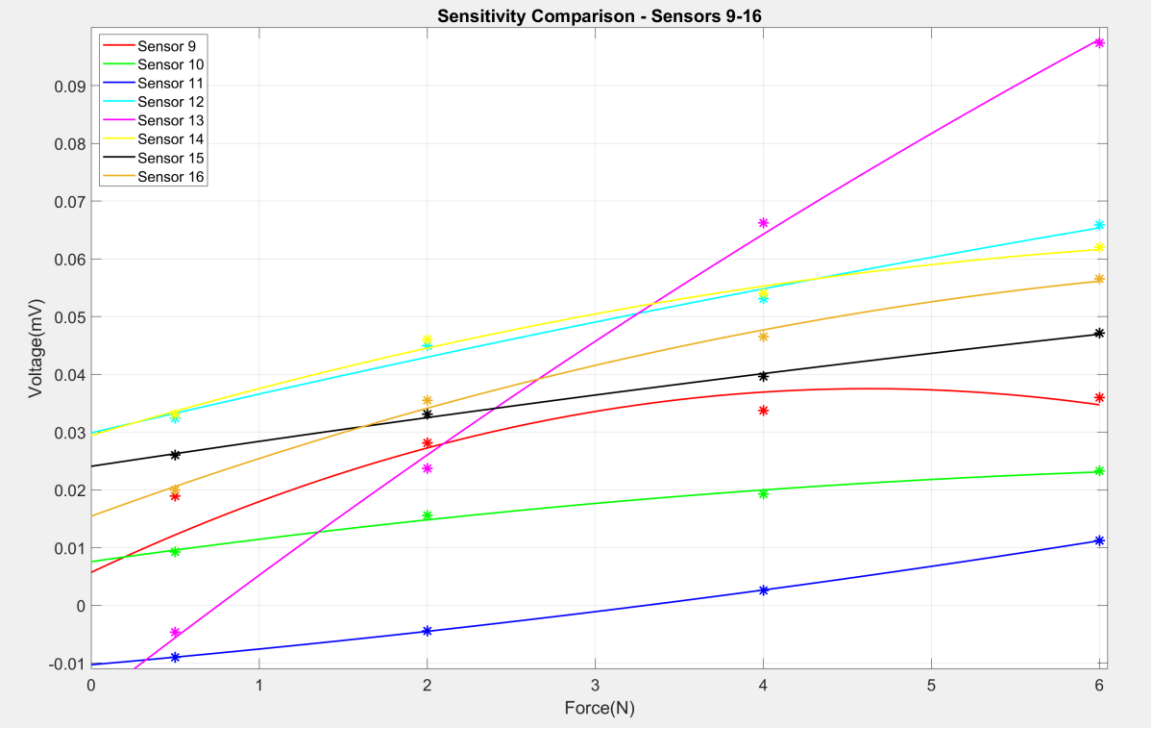

Figure 131: Comparison of working Sensitivity, Voltage with Respect to Force, Across Sensors 9-16 including a poly fitted line of best fit

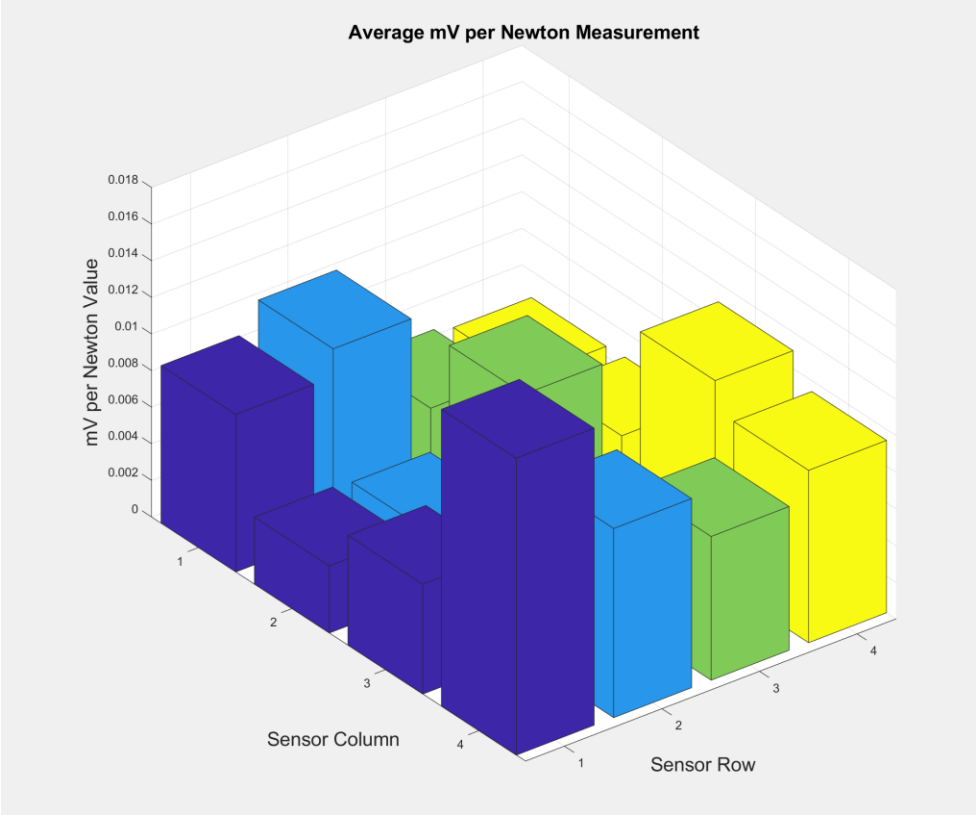

Figure 132: Average mV per Newton Measurement visualization

B6: Optomec Fabricated Sensor –SkinCell 2

Sensor #	0.5N response(mV)	2N response(mV)	4N response(mV)	6N response(mV)	Sensitivity average(mv/N)
1	0.00995	0.0221	0.0267	0.0315	0.00525
2	0.00682	0.01401	0.017625	0.021835	0.003639167
3	0.02778	0.03748	0.04628	0.05108	0.008513333
4	0.01272	0.02805	0.0418	0.0572	0.009533333
5	0.005	0.012625	0.01919	0.02289	0.003815
6	0.007635	0.01558	0.019465	0.022535	0.003755833
7	0.0086	0.01892	0.02198	0.02562	0.00427
8	0.01152	0.0159185	0.019965	0.023235	0.0038725
9	0.01995	0.03056	0.03935	0.0454	0.007566667
10	0.0046	0.01305	0.017605	0.020165	0.003360833
11	0.007364	0.01066	0.01371	0.01615	0.002691667
12	0.018158	0.02322	0.02715	0.03055	0.005091667
13	0.0058	0.0096	0.01215	0.01815	0.003025
14	0.0154	0.02455	0.0334	0.0381	0.00635
15	0.0229	0.02707	0.0324405	0.0386705	0.006445083
16	0.0175	0.03798	0.04319	0.05204	0.008673333

Table 29: Average Response Value of sensors: 0 indicates nonfunctioning sensors

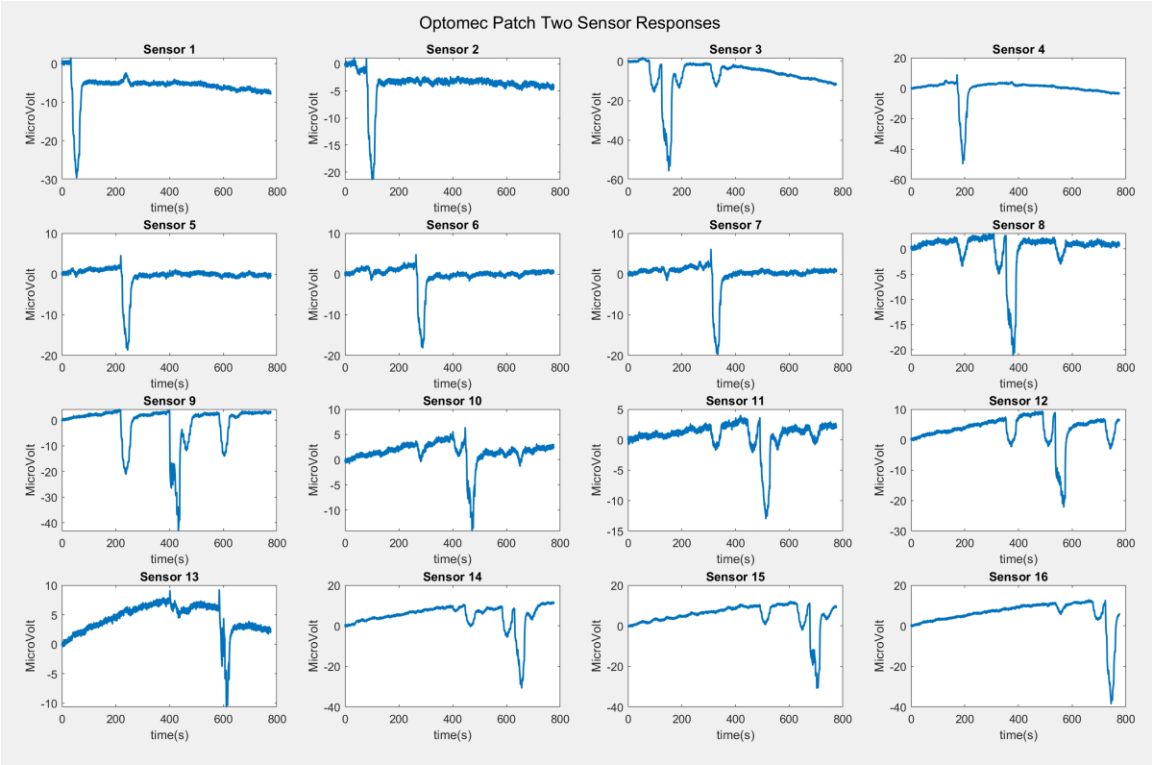

Figure 133: Visualization of Test Raw Response Data Across the Entire Test

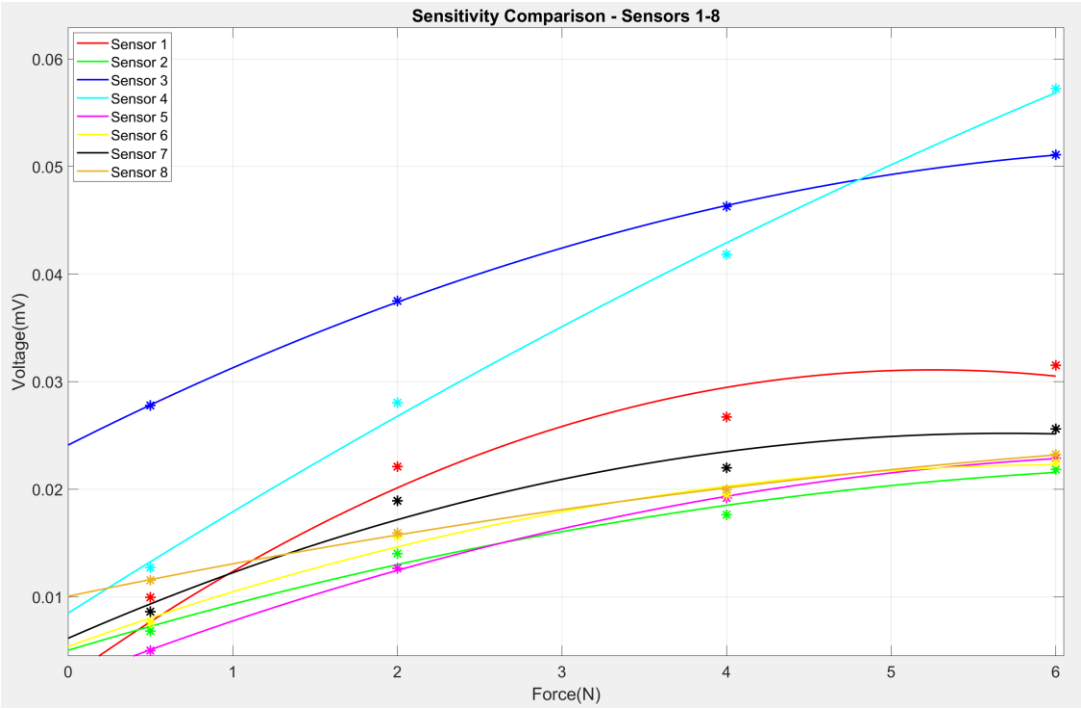

Figure 134: Comparison of working Sensitivity, Voltage with Respect to Force, Across Sensors 1-8 including a poly fitted line of best fit

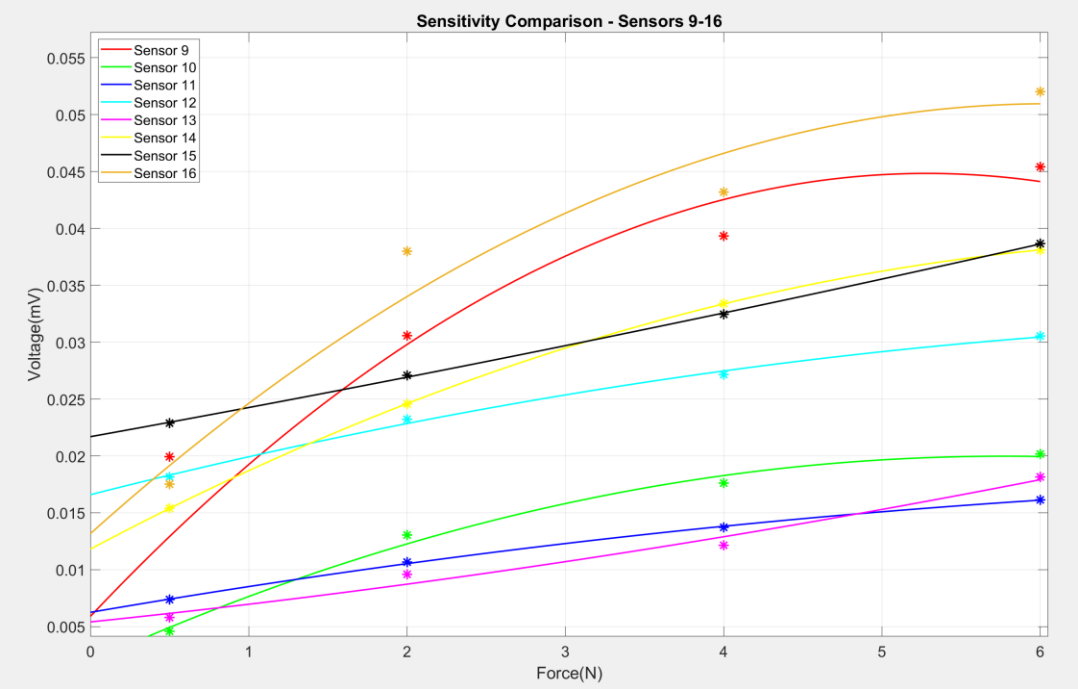

Figure 135: Comparison of working Sensitivity, Voltage with Respect to Force, Across Sensors 9-16 including a poly fitted line of best fit

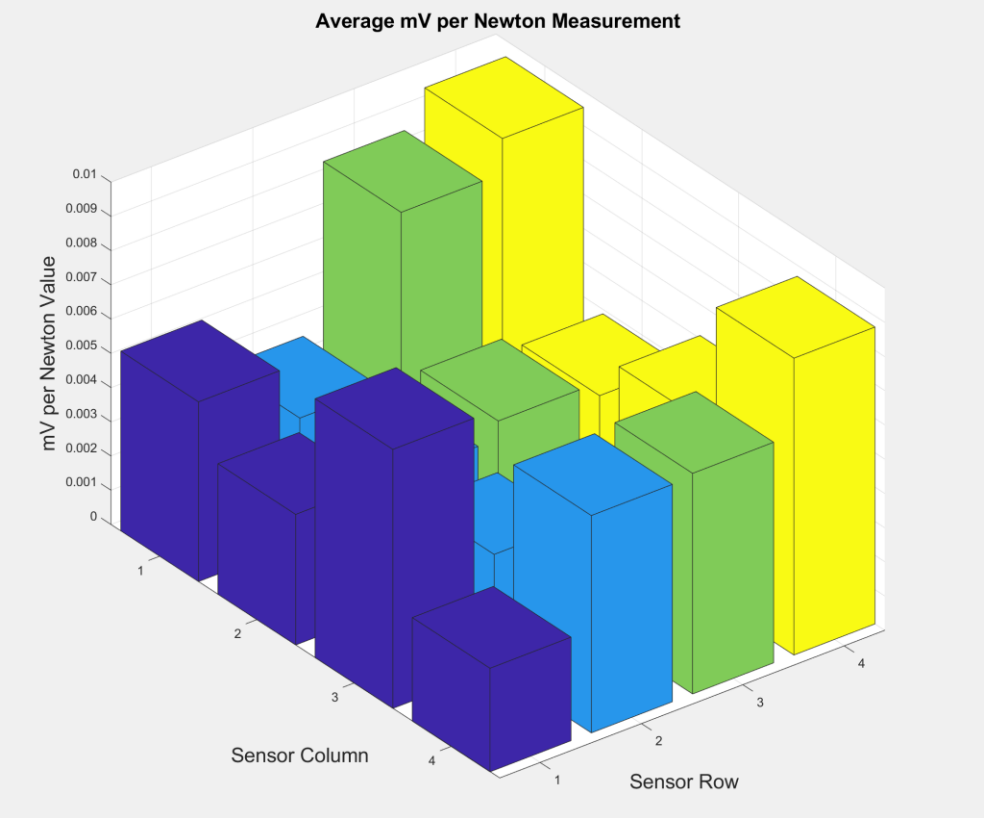

Figure 136: Average mV per Newton Measurement visualization

CURRICULUM VITA

NAME: Olalekan O. Olowo

DOB: Lagos, Nigeria – March 15, 1990

EDUCATION: B.S., M.S., PhD (in View)., Electrical Engineering
University of Louisville